FABRICATION AND APPLICATION OF SHORT AND NOVEL STRUCTURE IN-FIBRE BRAGG GRATINGS

KAREN ELIZABETH CHISHOLM

Doctor of Philosophy

ASTON UNIVERSITY

January 2000

ASTON UNIVERSITY

FABRICATION AND APPLICATION OF SHORT AND NOVEL STRUCTURE IN-FIBRE BRAGG GRATINGS

KAREN ELIZABETH CHISHOLM

Doctor of Philosophy

January 2000

ABSTRACT

This thesis presents details on progress made in the fabrication and application of short and novel structure fibre Bragg gratings. The basic theoretical concepts of in-fibre Bragg gratings and photosensitive mechanisms are introduced together with an overview of fabrication methods and applications presented to date.

The fabrication of fibre Bragg gratings using a quadrupled Nd:YAG laser is presented and some of the issues of grating fabrication using a phasemask are investigated, including the variation of the separation of the fibre and phasemask, and other alignment issues. A new apodisation technique is presented, enabling the production of gratings with a wide range of spectral profiles. The technique is used to investigate the design and fabrication of length limited fibre Bragg gratings for use in telecommunication systems as filters. Application to devices designed for use in WDM systems is presented.

The use of fibre Bragg gratings as high spatial resolution distributed sensors is investigated. Grating sensing arrays comprising very short apodised gratings are demonstrated and Chirped Moiré gratings are implemented as distributed sensors achieving high spatial resolution with miniature point sensing sub-elements. A novel grating sensing element designed to imitate an interferometer is also presented.

Finally, the behaviour of gratings fabricated in Boron-Germania-co-doped fibre is investigated, revealing atypical behaviour of the Bragg wavelength during ageing.

KEY WORDS

Optical fibre, Bragg grating, Optical fibre sensor

To Mum and Dad, for your endless encouragement.

ACKNOWLEDGEMENTS

Acknowledgement is due to the members of the Photonics Research Group at Aston University, particularly my supervisor Ian Bennion, and to John Williams and Lin Zhang who have freely shared their expertise in gratings throughout. Special thanks go to Bert Biggs who provided endless pieces of apparatus, and patience when equipment failed at the most inappropriate moments. Thanks also to my two post-doc supervisors, Kate Sugden and Andy Gloag. Kate in particular provided many hours of encouragement, and got me hooked on grating fabrication. The work on apodisation was carried out with Lorna Everall who, together with Richard Fallon and his humour, kept me going throughout. My two industrial supervisors, Peter Foote (BAe) and Kate Sugden (Oxford Fiber Optic Tools) provided many suggestions. There are also researchers at other institutions to whom I am grateful, mostly for using my gratings or characterising them. Gordon Flockhart (Heriot-Watt University) characterised some of my gratings for me, Ale Iocco (EPFL) included some gratings in his tuneable filter, and Tom Allsop (Plymouth University) implemented the novel strain-sensing element. In addition, Steve Alleston and Des Ryan from the Photonics Research group at Aston University carried out work on the use of gratings for spectral slicing.

Many other people have contributed to the writing of this thesis, particularly my friends and family. Mum and Dad have given me endless support and encouragement over the past three years, particularly when my knee was being fixed. Thanks are due to the medical staff who fixed my knee, to people at St Stephens who have kept on praying for my knee and my thesis, and to all my other friends, in particular Jo, Anita, Kate, Ruth and Neil.

TABLE OF CONTENTS

FIGURE CAPTIONS

1 INTRODUCTION

1.1 Perspective

Optical fibres represent one of the most significant technological advances in the latter 25 years of the 20th century. Their many diverse applications pay credit to the ideal characteristics of fibres: the small size (~125μm diameter), near perfect transmission characteristics, very broad bandwidth capability, reduced susceptibility to electromagnetic interference and reliability. It is because of these incredible properties that optical fibres represent the next generation technology in so many applications such as telecommunications, signal processing, medicine and smart structures. In-fibre Bragg gratings are ideal components in fibre optic systems as they are, as the name suggests, made inside the fibre itself meaning that the integration of the components is simple, with very low loss. The potential for optical fibre systems incorporating Bragg gratings is seemingly endless, as industry is only just beginning to realise their many capabilities in real systems.

Research in fibre Bragg gratings has progressed rapidly in the last 10 years, since the first inscription through the side of the fibre [1]. In recent years, several companies have started making and selling a variety of Bragg gratings, mainly for the telecommunications and sensing industries. Among the first devices to be commercialised were chromatic dispersion compensators – long chirped gratings designed to compensate for the chromatic dispersion experienced by high speed optical data transmitted over the existing fibre network. Other devices, such as filters designed for use as add/drop nodes in wavelength division multiplexed systems, enable vast increases in capacity using the current telecommunications infrastructure. Gratings are also finding application in structural sensing, being embedded in many composite structures during production. Structural sensing can also be performed by bonding the gratings to existing structures, for instance to monitor the degradation of old concrete structures, or the strain on aircraft wings during flight. There are many other applications of gratings, a few of which are touched on in chapter 2.

The many emerging applications for Bragg gratings require research into the behaviour of gratings in different situations: how will they perform in 25 years time? will they survive 20 years of being strained without breaking? Different fibres have been developed over the years in order to enable more effective fabrication of gratings. However, each of these special fibres requires characterisation before being cleared for use in devices. In addition, many different UV laser sources have been trialed, in an effort to harness the full potential of Bragg gratings. The use of gratings in telecommunications systems places increasing demands on the design and fabrication of gratings and there are many trade-offs between many parameters to be considered when designing a grating for a specific device.

1.2 Thesis Overview

The work contained within this thesis addresses a variety of issues involved in the fabrication, characterisation and application of fibre Bragg gratings. The main technological advances presented may be summarised as follows:

- Development of a fibre Bragg grating fabrication utility employing a frequency quadrupled Nd:YAG laser
- A new simple and flexible apodisation technique
- A comprehensive study of the trade offs involved in the design and fabrication of uniform period apodised fibre Bragg gratings
- New insights into the long-term characteristics fibre Bragg gratings fabricated in boron-germania co-doped fibres
- Development of advanced grating structures for sensing applications
- Novel use of chirped Moiré gratings as miniature distributed sensors

Chapter 2 provides the reader with an overview of the development of fibre Bragg grating technology and aims to portray the current status of the field. Since the explosion in worldwide research into fibre Bragg gratings in 1989, the field has developed rapidly, and so only those aspects of fibre gratings relevant to the work contained within this thesis are reported. The coupled mode theory of the propagation of light within fibre gratings is presented, along with an introduction to the growth and decay mechanisms of photosensitive gratings. The vast majority of the gratings fabricated as part of this thesis were inscribed using the phasemask method, and so particular attention is paid to explaining the development of this fabrication technique. As mentioned already, the uses of gratings are diverse, and an overview of the applications of gratings concludes the chapter; the section concentrates on the two main area of application contained within this thesis: WDM telecommunications and sensing.

Many of the gratings investigated here were fabricated using a frequency quadrupled Nd:YAG laser; and much time and effort was expended setting up a fabrication utility using this laser. Chapter 3 introduces some of the fabrication issues encountered during the course of the experimental work in the thesis, particularly using the Nd:YAG. The development of a fabrication utility using a frequency quadrupled Nd:YAG laser is described, together with the advantages and disadvantages of using such a laser for grating fabrication. Aspects of grating fabrication such as the effects of misalignment during grating inscription using a phasemask and Nd:YAG laser are also studied. The methods used for characterising the gratings are also outlined.

Chapter 4 is an in-depth study of the trade-offs involved in the design and fabrication of apodised gratings subject to length constraints. A new flexible method for fabrication of apodised gratings is presented, and then used to fabricate gratings with a wide range of apodisation profiles. The study investigates both the theoretical and experimental spectral profiles of apodised gratings, providing valuable information when designing gratings to meet challenging specifications. Two applications of apodised gratings fabricated using the knowledge gained from this study are presented at the end of the chapter. The first application is a TDM to WDM converter, the second a tuneable fibre grating based filter, suitable for use in WDM systems.

Chapter 5 presents a number of different grating architectures tailored for use as grating sensors. Expertise gained as a result of the work in chapter 4 has been used to fabricate arrays of very short apodised gratings. The use of grating arrays as distributed sensors is presented and discussed. For the first time, the use of chirped Moiré gratings as distributed strain and temperature sensors is presented, with examples of measurements of arbitrary temperature profiles being demonstrated. The design and fabrication of a novel structure apodised grating specially designed as part of a collaborative sensing project, is presented at the end of the chapter.

New insights into variations in the spectral characteristics of gratings over potential device lifetimes are presented in chapter 6. Gratings fabricated in boron-germania co-doped fibres exhibit different long-term behaviour from those fabricated in other fibres. The thermal decay of gratings fabricated in 3 types of fibres is studied: standard telecommunications fibre, hi-germania doped fibre, and boron-germania co-doped fibre. The dependence of the long term grating characteristics on the grating refractive index modulation, fibre composition and annealing temperature are all considered. An empirical model for predicting the wavelength shift of gratings fabricated in boron-germania co-doped fibres is presented.

Chapter 7 presents a summary of the technological advances described in this thesis, and reflects on possible future areas of research involving Bragg gratings, in the light of the developments detailed here. The thesis concludes with a list of the publications resulting from this work.

2 BACKGROUND

2.1 Historical Background

Optical fibre research began as early as the 1920s, when Baird patented uncladded fibres, and cladded fibres did not follow until 1954. These early fibres were largely used for the transmission of images down the fibres and it was not until 1966 that a potential use for telecommunications was suggested [2]. However, fibres at this time were very lossy (~10 000dB/km) and not at all practical for applications such as communications. Following Kao's suggestion, there was much research into reducing the loss in fibres to 20dB/km (Corning, 1970 [3]) and then the acceptable values of <0.2dB/km we know today (Miya, 1979 [4]). The development of Erbium doped amplifiers in 1987 by researchers at Southampton University finally opened up the possibility of transmission over transatlantic distances using fibres [5].

The fabrication of fibre gratings by a photosensitive process was first presented by Hill *et al* in 1978[6]. Hill was investigating second harmonic generation in optical fibres, which at the time was a topic of much interest to researchers. However, Hill made a surprising discovery whilst light from an argon ion laser at 488nm was coupled into a germanosilicate fibre. Gradually, the amount of light reflected back along the fibre increased, until nearly all the light was reflected back along the fibre. A standing wave had been set up between forward propagating light and the 4% reflected back from the other end of the fibre. Investigations pointed to the fact that a Bragg grating had in fact been produced in the fibre core. The light at 488nm had been absorbed by the fibre, resulting in a change in the refractive index of the fibre core. The pattern of the standing wave in the fibre resulted in this photosensitive effect leading to the formation of a periodic variation in refractive index in the fibre core, along the fibre axis. Many researchers realised the potential of this discovery, however, there were limitations to the gratings: there was no control over the wavelength of the grating, because it was formed by a standing wave. It was not until 1989 that research into fibre Bragg gratings exploded, when Meltz and Morey presented a method for fabricating gratings through the side of the fibre, allowing the grating wavelength to be adjusted [1].

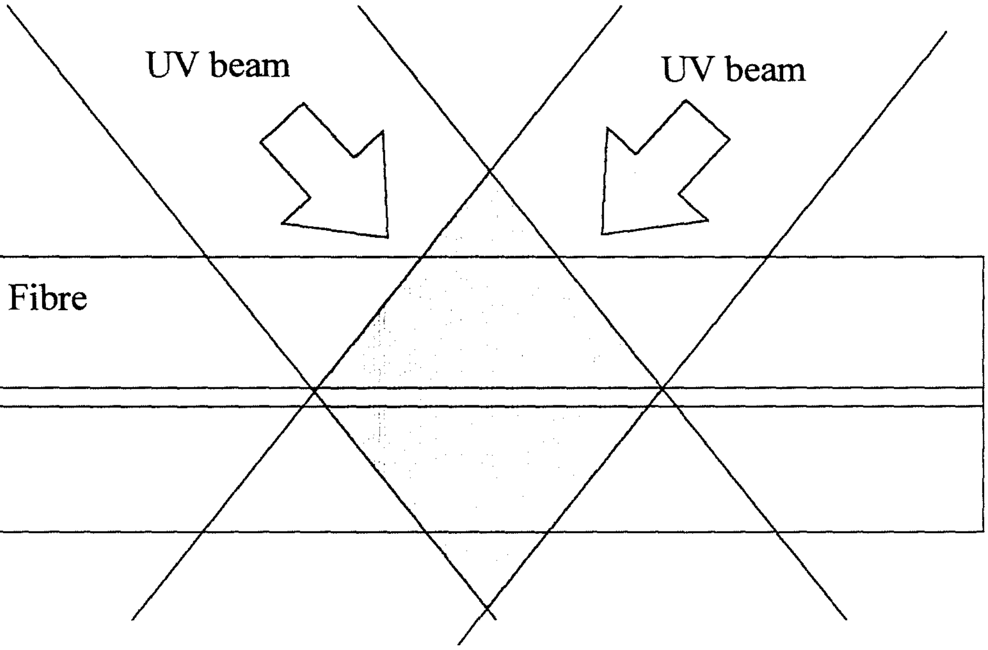

Figure 2.1: Photosensitive grating formation by the side-writing method. The grating wavelength can be adjusted by varying the angle between the two beams.

The side-writing technique first presented by Meltz and Morey is the basis for the vast majority of grating fabrication techniques (though others such as point-by-point writing have been presented [7]). Figure 2.1 shows the basic principle of the fabrication set-up for the fabrication of all photosensitive fibre gratings, by the formation of an interference pattern in the fibre core. Another significant breakthrough in grating formation was made in 1991. Two research groups reported fabrication of gratings by the use of a diffractive element, placed directly next to the fibre, which was used to generate the 2 interfering beams [8,9]. This development eliminated the need for large bulk optics systems previously required in order to generate the 2 interfering beams. The majority of the advanced grating fabrication utilities now in operation make use of this technique. The phasemask technique is discussed in detail in the background chapter and throughout the thesis.

2.2 Theoretical Background

Qualitative Picture

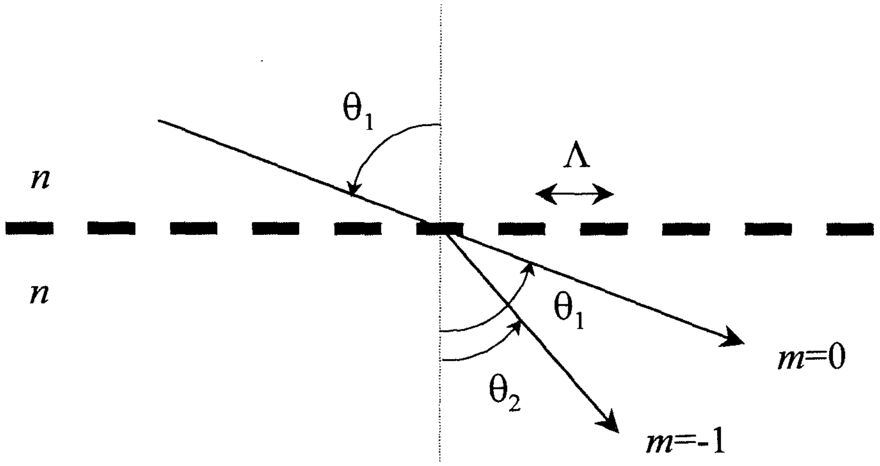

Figure 2.2 : The diffraction of light by a grating

In its simplest form, a fibre Bragg grating is purely an optical diffraction grating and so can be represented by the following relation:

$$n\sin\theta_2 = n\sin\theta_1 + m\frac{\lambda}{\Lambda},$$

Equation 2-1

where the symbols are defined in Figure 2.2, and λ is the wavelength of the diffracted light. In the case of a fibre grating, the grating simply couples light between forward and backward propagating modes in an optical fibre. Equation 2-1 predicts accurately the wavelength of the light diffracted by a fibre grating.

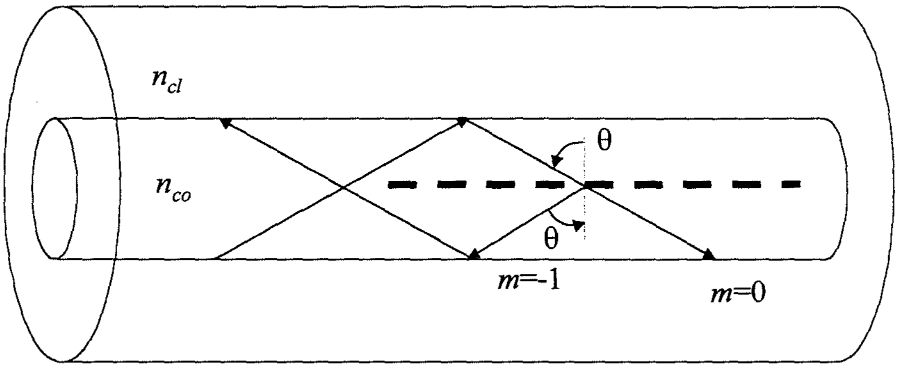

Figure 2.3: Illustration of reflection of a core mode by a Bragg grating

Figure 2.3 shows the reflection of a core mode by a Bragg grating (in simple terms). The incident wave is diffracted by the grating into a mode that propagates in the opposite direction from the incident wave. The propagation constant of an incident wave,

$$\beta = \left(\frac{2\pi}{\lambda}\right) n_{eff},$$

Equation 2-2

where

$$n_{eff} = n_{co} \sin\theta .$$

Equation 2-3

Therefore, we may rewrite Equation 2-1 as:

$$\beta_2 = \beta_1 + m\frac{2\pi}{\Lambda} .$$

Equation 2-4

As is depicted in Figure 2.3, the diffracted order from the grating propagates in the opposite direction from the incident wave and so it has a negative propagation constant. Therefore, if the forward and backward propagating modes are identical, Equation 2-4 may be rewritten

$$\lambda = 2n_{eff}\Lambda ,$$

Equation 2-5

which is the well known relation describing Bragg diffraction.

2.2.1 Coupled Mode Theory

Coupled mode theory provides a good description of the interaction of guided waves and gratings in fibres. Coupled mode theory is the most widely used modelling technique for fibre Bragg gratings [10,11], and is used in the transfer matrix technique for modelling the response of long and complex structure gratings (see Appendix 8.2). Other simulation techniques have been summarised by Erdogan [12] and include integration of the Ricatti equation [13] and inverse Fourier transform techniques [14].

Coupled Mode Equations

First we should consider two electromagnetic modes, propagating the unperturbed medium, with complex amplitudes A and B and frequencies ω_a and ω_b:

$$a(z,x,t) = A\exp\{i(\omega_a \pm \beta_a z)\}f_a(x)$$

Equation 2-6

$$b(z,x,t) = B\exp\{i(\omega_b \pm \beta_b z)\}f_b(x)$$

Equation 2-7

Where $f_a(x)$ and $f_b(x)$ describe the behaviour of the modes in the x direction. In the presence of a perturbation, in our case a refractive index grating, the energy is coupled between these two modes. A and B are no longer constant, and they vary as:

$$\frac{dA}{dz} = \kappa_{ab}B\exp\{-i\Delta\beta z\}$$

Equation 2-8

$$\frac{dB}{dz} = \kappa_{ba} A \exp\{+ i\Delta\beta z\}$$

Equation 2-9

where $\Delta\beta$ is the phase mismatch constant which depends both on the frequency of the two modes and the period of the perturbation; κ_{ab} and κ_{ba} are the coupling constants.

Counter-directional Coupling

Coupling occurs in Bragg gratings both between counter-propagating modes and between co-propagating modes. Coupling between co-propagating modes leads to short wavelength loss as energy is coupled from the core modes to cladding modes for wavelengths below the grating peak. Coupling between counter-propagating modes occurs between two core modes and results in the reflection of light at the Bragg wavelength. In this case, the propagation of two counter-propagating core modes in the unperturbed fibre is described by:

$$a = A \exp\{i(\omega_a t + \beta_a z)\}$$

Equation 2-10

$$b = B \exp\{i(\omega_b t - \beta_b z)\}$$

Equation 2-11

where *A* and *B* are constant. A time-space periodic perturbation results in a power exchange between the modes and the local power is conserved so that:

$$\frac{d}{dz}\left(|A|^2 - |B|^2\right) = 0,$$

Equation 2-12

this condition is satisfied if $\kappa_{ab}=\kappa_{ba}^*$, so that Equation 2-8 and Equation 2-9 become:

$$\frac{dA}{dz} = \kappa_{ab} B \exp\{-2i\Delta\beta z\}$$

Equation 2-13

$$\frac{dB}{dz} = \kappa_{ba}{}^{*} A \exp\{+2i\Delta\beta z\}.$$

Equation 2-14

We take mode b to be incident on the grating at z=0, with amplitude *B(0)*. Mode a is generated by the perturbation, so *A(L)*=0, (the end of the perturbation region is at *z*=*L*). Given these boundary conditions, the solutions to Equation 2-13 and Equation 2-14 are:

$$A(z) = \frac{B(0) i\kappa_{ab} \exp\{-i\Delta\beta z\}}{-\Delta\beta \sinh(SL) + iS\cosh(SL)} \sinh[S(z-L)]$$

Equation 2-15

$$B(z) = \frac{B(0)\exp\{i\Delta\beta z\}}{-\Delta\beta \sinh(SL) + iS\cosh(SL))}\{\Delta\beta \sinh[S(z-L)] + iS\cosh[S(z-L)]\}$$

Equation 2-16

where $S \equiv \sqrt{\kappa^2 - (\Delta\beta)^2}$, and $\kappa \equiv \kappa_{ab}$.

Equation 2-17

Under phase matching conditions, $\Delta\beta$=0:

$$A(z) = B(0)\left(\frac{\kappa_{ab}}{\kappa}\right)\frac{\sinh[\kappa(z-L)]}{\cosh(\kappa L)}$$

Equation 2-18

$$B(z) = A(0)\frac{\cosh[\kappa(z-L)]}{\cosh(\kappa L)}$$

Equation 2-19

Equation 2-18 and Equation 2-19 describe the propagation of counter-propagating modes in fibre Bragg gratings. The variation in the amplitudes of the two modes as they propagate through the grating is shown in Figure 2.4.

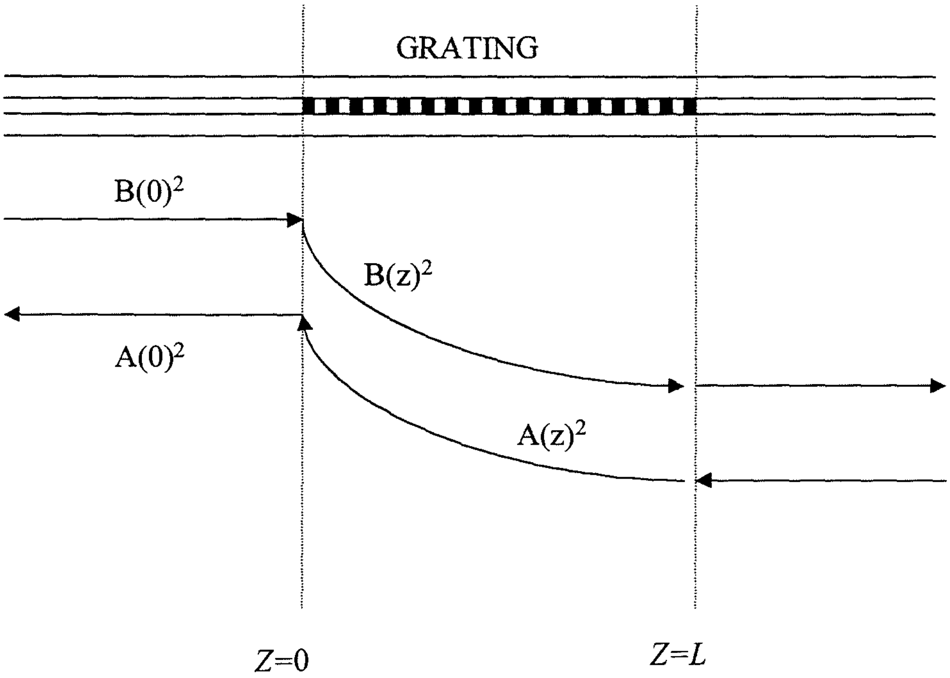

Figure 2.4: The Bragg grating inside the optical fibre causes coupling between forward (B) and backward (A) propagating modes. The variation in intensities of the modes during propagation through the fibre is shown.

The reflection, *R*, and transmission, *T*, of a short section of grating can be described by:

$$R = \left|\frac{A(0)}{B(0)}\right|^2 \quad \text{and} \quad T = \left|\frac{B(L)}{B(0)}\right|^2 .$$

Equation 2-20

$$R(L,\lambda) = \frac{\kappa^2 \sinh^2(SL)}{(\Delta\beta)^2 \sinh^2(SL) + S^2 \cosh^2(SL)}, \qquad \kappa^2 > (\Delta\beta)^2$$

Equation 2-21

$$R(L,\lambda)=\frac{\kappa^2\sin^2(QL)}{(\Delta\beta)^2-\kappa^2\cos^2(QL)},\qquad \kappa^2<(\Delta\beta)^2$$

Equation 2-22

where $$Q=\sqrt{(\Delta\beta)^2-\kappa^2}\,.$$

Equation 2-23

The maximum value of R, R_{max}, occurs when $\Delta\beta=0$ $\therefore S=\kappa$; Equation 2-21 gives an expression for the maximum reflectivity of the grating:

$$R_{\max}=\tanh^2(\kappa L)\,.$$

Equation 2-24

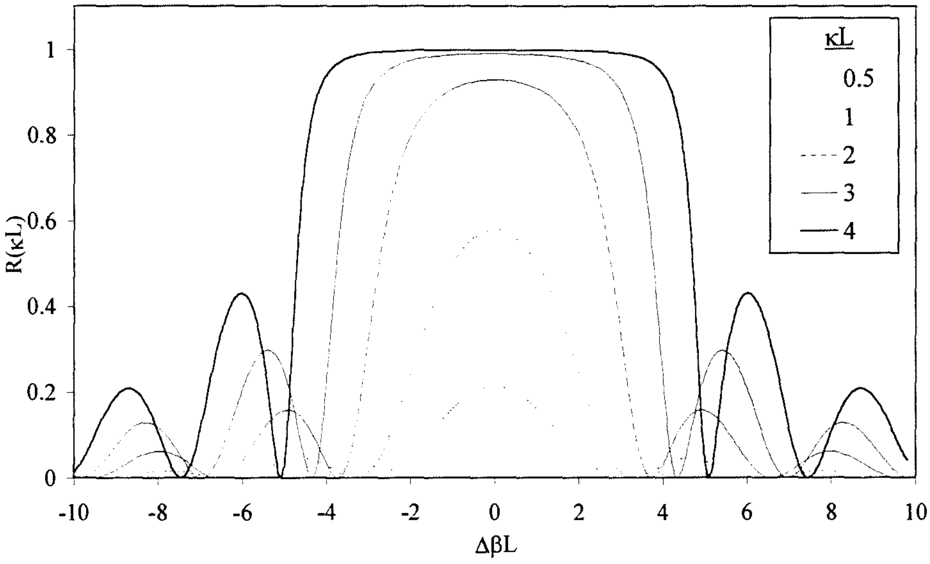

Figure 2.5: Variation of grating reflectivity with κL from Equation 2-24.

Figure 2.5 shows how the reflection characteristics of a short length of grating, L, vary with coupling constant, κ and detuning, $\Delta\beta$. The full bandwidth of the grating measured between the zeros on either side of the grating peak,

$$\Delta\lambda = \frac{\lambda_B^2}{\pi n_{eff} L}\sqrt{(\kappa L)^2 + \pi^2}\ .$$

Equation 2-25

2.3 Photosensitivity

2.3.1 Type I photosensitivity

The photosensitivity of germanosilicate fibres was first observed by Hill *et al*[6], using light with a wavelength of 488nm. Lam and Garside [15] realised that the photosensitive process in this case was a two-photon process and that therefore it would be far more efficient to use light with half of the wavelength – that is, at 244nm, so as to use a one-photon process in the 5eV germania-oxygen-vacancy defect band.

When UV light irradiates a photosensitive optical fibre, the refractive index of the glass is changed. Initially this photosensitive effect was thought to be limited to germanosilicate fibres. However, since then it has been shown that several other dopants in silica fibre result in photosensitive effects [16].

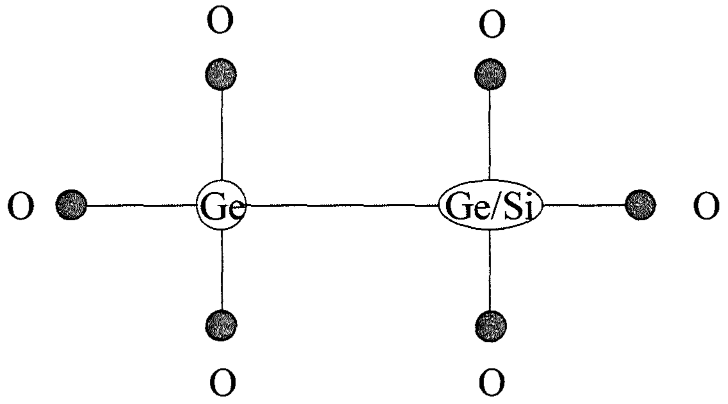

Figure 2.6: The oxygen deficient defect, responsible for the photosensitive effect in germanosilicate fibres.

A common defect found in germanium doped silica is thought to lie behind the photosensitive effect. The material has a characteristic absorption at 240nm and this absorption has been identified to be caused by an oxygen deficient defect. Figure 3 shows this defect. Germanium is usually co-ordinated with 4 oxygen atoms, however in this case Si or Ge has replaced one of the oxygen atoms and has an extra donor electron associated with it. It is this bond which can be broken by photo-excitation, releasing charges which are free to move through the glass network. Free charges are then trapped at hole defect sites. Russell *et al* have shown that the defect population has to be a large proportion of the Ge ion concentration before substantial photo-induced index changes occur [17].

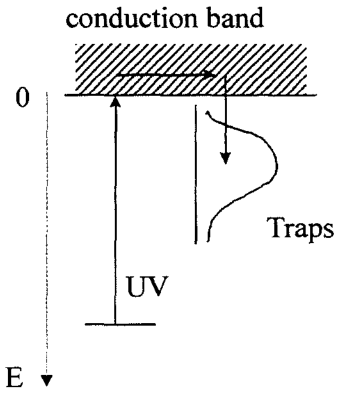

Figure 2.7: Empirical model for growth of fibre gratings [18]

A simple empirical model for grating growth presented by Erdogan [18] is shown in Figure 2.6. The incident UV light excites carriers into the conduction band, from where they then fall into traps where they remain. However, if the carriers become excited (for example thermally), then they can obtain enough energy to escape from the traps and the photosensitive process is reversed and a decay of the photo-induced refractive index is observed[1].

This 'colour-centre model' results in refractive index changes through the Kramers-Kronig relationship [19,20,21]:

---

[1] Thermal decay of fibre gratings is discussed in more detail later in this chapter (see 'Grating Lifetime Issues') and in chapter 5.

$$\Delta n(\omega') = \frac{c}{\pi} P \int_0^{\infty} \frac{\Delta\alpha(\omega) d\omega}{\omega^2 - \omega'^2},$$

Equation 2-26

where P stands for the principle part of the integral, Δα(ω) is the change in the absorption spectrum and Δn(ω) is the corresponding change in refractive index for a given incident optical frequency, ω. This model however, only leads to a rough estimate of the refractive index change. Other models accounting for the phenomenon include stress relief [22] where the UV induces bond breaking, which in turn allows the relaxation of stresses which arise from the drawing process. This 'stress-relief' model however, has been shown not to be dominant [23]. A large part of the UV induced refractive index in non-hydrogen loaded fibres is thought to be caused by densification of the silica. Evidence for this process has been presented using a number of different inspection techniques [24,25,26] and Poumellec *et al* formulated a model describing the origins of the distributed UV-induced strains within the core [25]. Much of the work investigating the origins of photosensitivity has been done by Douay *et al*, who have published a comprehensive review of the different theories for the mechanism [27].

2.3.2 Type IIa photosensitivity

Several researchers have suggested that another type of photosensitive process occurs in fibres [28,29]. Xie *et al* first reported that a long exposure time leads to the photoinscription of a positive refractive index type I grating followed by its complete or partial erasure and then the formation of a new negative refractive index type IIa grating [28]. Another suggestion is that UV exposure leads to formation of Ge(1) and Ge(2) colour centres with absorption bands at 281nm and 213nm[19]. A 3-energy-level model for the formation of negative index gratings following that of positive index gratings has been proposed by Dong *et al* [29]. This model was proposed to fit their experimental findings. They suggested that a positive index change is obtained when a lower level (level 2) is populated by depletion of a ground level (level 1) and a negative index change is achieved when a higher level (level 3) is populated by depletion of level 2. This is a highly simplified model but it can also be used to explain the amplification of a weak grating by uniform post exposure observed by Dyer *et al* [30].

2.3.3 Type II (Damage) gratings

Early on in grating research, the possibility of grating fabrication as newly formed fibre left the draw-tower was investigated. There were several reports of single-excimer-pulse writing of fibre gratings [31,32,33], raising hopes of the possibility of the mass production of gratings. These single pulse gratings have been shown to exhibit different properties from type I gratings. Figure 2.8 shows the transmission spectrum of a typical type II grating (fabricated using a pulsed quadrupled Nd:YAG laser) displaying strong out-coupling of wavelengths below the grating transmission dip. Milhailov *et al* reported evidence of melting and resolidification of the glass, forming a periodic stress pattern in the pure silica cladding as well as the core [34]. The fluence at which type II gratings occur varies according to the absorption characteristics of the fibre at the irradiating wavelength [35,36].

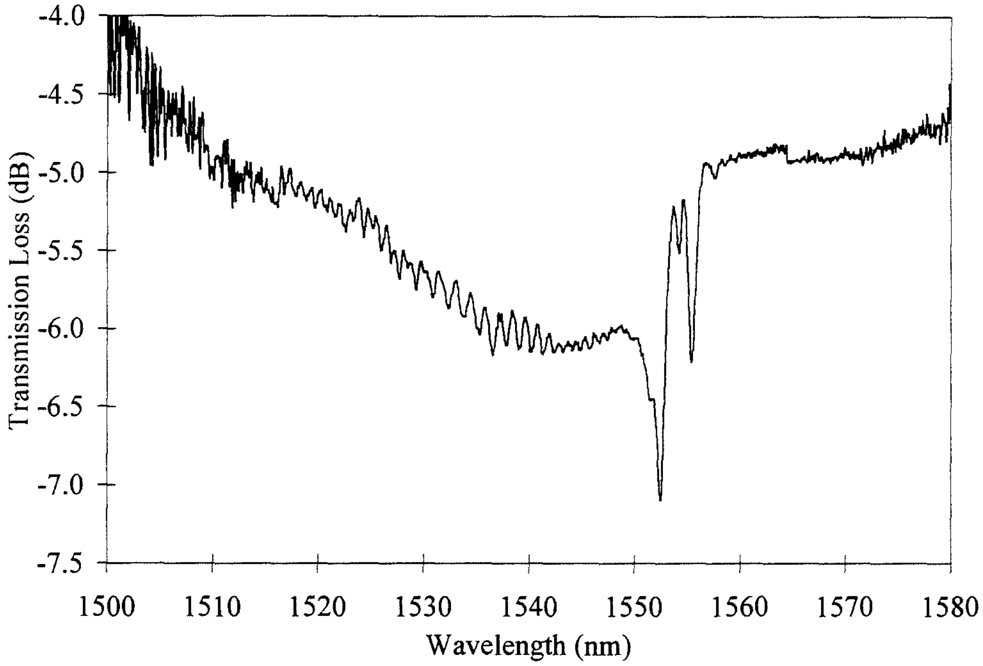

Figure 2.8: Type II (damage) gratings display high short wavelength loss.

2.3.4 Hydrogen loading and other enhancement methods

Increasing the photosensitivity of fibres is an on going issue. Early in the research of UV induced photosensitivity, it was found that the photosensitivity of germanosilicate fibres could be increased by loading the fibre with H_2 at high pressure [37,38]. The hydrogen loading resulted in UV-induced index increases that can exceed the initial core-to-cladding refractive index difference [39]. Loading with hydrogen not only increases the formation of GeE' centres, but also results in an additional contribution to Δn from GeH centres. It is interesting to note that there is no evidence of densification in hydrogen sensitised fibres after grating fabrication [24,26]. It has also been reported that hydrogen loading prevents the formation of negative index (type IIa) gratings [40]. After removal from high-pressure hydrogen, the hydrogen concentration in the fibre core decreases steadily at room temperature. This out-diffusion can be minimised by storage at temperatures <-30°C in order to retain the hydrogen concentration at levels suitable for grating fabrication [41]. Another sensitisation technique involving localised heating of the fibre during UV exposure was presented, but has not been widely implemented as hydrogen loading has [42].

2.3.5 Different types of fibres

The search for ever greater photosensitivity has resulted in the development of fibres specially designed for their photosensitive properties. Some co-dopants have been added to germanosilicate fibres to allow the addition of higher concentrations of germania, whilst keeping the numerical aperture of the fibre at the required value of ~2.4 for telecommunications systems. The earliest of these co-dopants was boron [43]. The addition of boron allowed the fabrication of gratings with $\Delta n > 10^{-3}$ in non-hydrogen-loaded fibres, thought to be caused by an increase in the contribution from densification effects. However, the addition of boron makes the fibre more difficult to draw into a cylindrical core and results in increased loss at the crucial telecommunications wavelength of 1.55μm. Tin-co-doped fibres exhibit a similar photosensitivity to boron co-doped fibres, but do not have the same drawbacks as boron fibres [44]. Other co-dopants have been reported including Cerium [45] and Tantalum [46]. Recently, UV photosensitivity of a germanium free oxynitride fibre has been demonstrated with exposure to a 193nm excimer laser [16]. These fibres have the advantage that they are known to be far more resistant to gamma-radiation than germanosilicate fibres [47].

2.3.6 Photosensitivity at different wavelengths

The 242nm absorption band is not the only region in which it is possible to access the photosensitive properties of fibres. Many different lasers, at a variety of wavelengths, have been used to fabricate gratings. Lasers used for grating fabrication include those at 193nm (ArF excimer laser)[48], 244nm (doubled argon ion) [49], 248nm (KrF excimer laser) [50], 255nm (doubled copper vapour) [51, 266nm (quadrupled Nd:YAG) [52], 351nm[53] and 325-364nm[54] (both Argon ion lasers). Atkins *et al* [53] demonstrated grating fabrication at 351nm using an argon ion laser. The index change in this case was small ($\sim 2\times10^{-4}$) even though the fibre was hydrogen loaded and had previously been exposed using a CO_2 laser in order to increase the concentration of GODC[2] sites. The GODC absorption band utilised in this case is centred at ~330nm[55]. Gratings fabricated at 193nm involve an absorption band, centred at 185nm, which is also due to oxygen deficient bonds [55]. More recently, Davis *et al* have demonstrated fabrication of long period gratings using a CO_2 laser at 10.6μm[56]. Irradiation at this wavelength is thought to induce gratings by densification alone and shows that UV irradiation is not necessary for grating formation.

2.4 Grating Fabrication

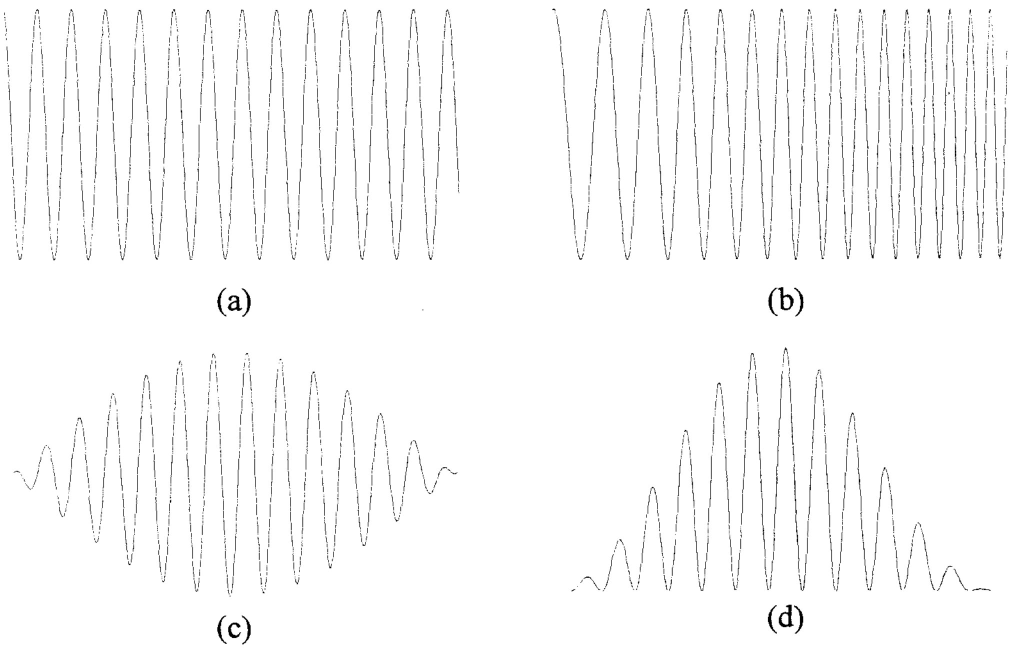

Figure 2.9: Typical grating refractive index profiles: (a) uniform period, (b) chirped, (c) constant refractive index apodised, (d) UV dose apodised

Since the first demonstration of UV side-written in-fibre Bragg gratings by Meltz and Morey [1], many different types of gratings have been presented, some of which are shown in Figure 2.9. Chirped gratings were the first variation to be investigated. In recent years, pursuit of ever more 'perfect' filters has seen the development of

---

[2] Germanium-Oxygen Deficiency Centre

apodisation techniques, amongst the developments in grating profiles. The development of grating writing techniques is summarised in the following sections.

2.4.1 Uniform period gratings

Holographic side exposure

The first side-writing technique for in-fibre gratings, presented by Meltz and Morey, is shown in Figure 2.10. This method has several advantages over that presented by Hill; the wavelength at which the grating reflects light can be controlled, as can the grating length. The wavelength of radiation used by Meltz was in the strong absorption band centred at 242nm.

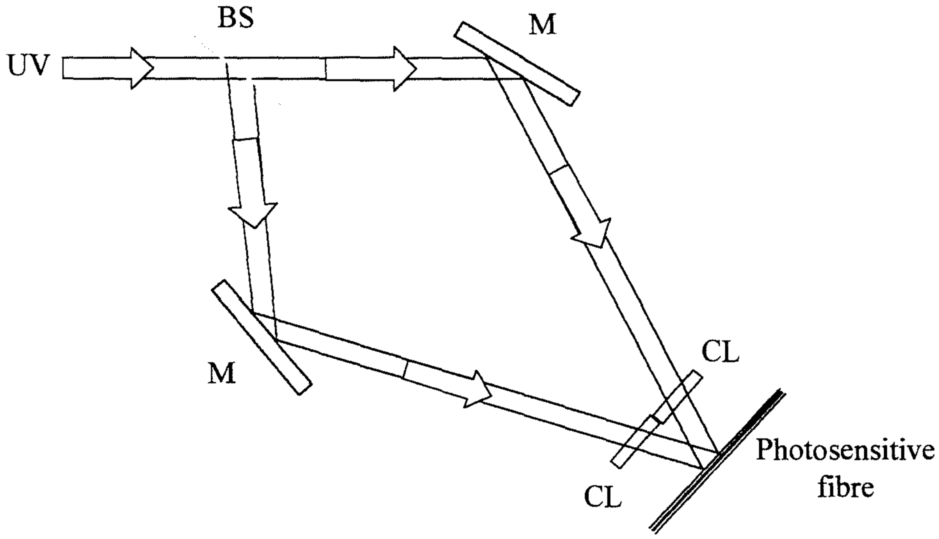

Figure 2.10: Holographic side exposure technique for fabricating uniform period gratings

The incident laser beam is split into 2 equal intensity beams, which are then recombined after being focused down into the fibre core using cylindrical lenses in each arm of the interferometer. Gratings are formed in the bare photosensitive fibre where the 2 overlapping arms form an interference pattern in the fibre core. A periodic variation of refractive index results along the length of the core exposed to the interference pattern. The period of the grating is determined by the wavelength of the incident light and by the included angle between the 2 interfering beams; the length of the grating is determined by the length of the overlap region, which can be increased by expanding the size of the incident beam. This method of grating fabrication requires a laser with a long coherence length and good beam quality. Gratings fabricated using a laser with a Gaussian beam shape are intrinsically apodised by the decrease in beam intensity at the grating edges. Whilst it is not easy to tailor the grating profile using this method, it still provides the greatest flexibility of all the fabrication techniques in the very wide range of grating wavelengths possible (<600nm to >1600nm).

Phasemask method

In 1993, two research groups presented a new, simple method of grating fabrication [57,58]. The schematic diagram of the method is shown in Figure 2.11.

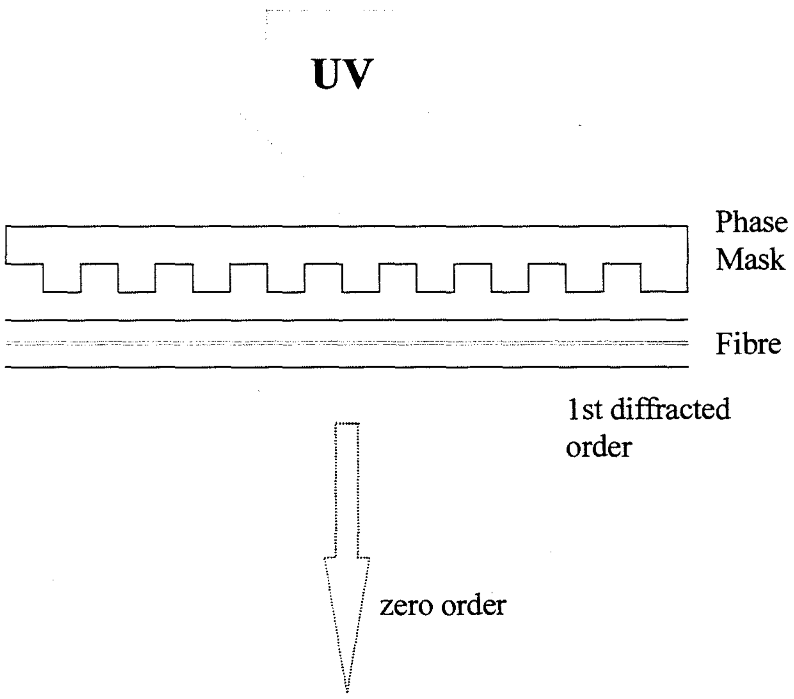

Figure 2.11: The incident UV light is ideally split into +/-1 orders which interfere inside the core of the fibre

A diffractive optical element or 'phasemask' is used to split the single incident UV beam into 2 interfering beams. The fibre is placed as near to the phasemask as is possible and because of this short distance between the point at which the incident beam is split in two and then recombined, the requirement for long coherence length of the irradiating source is significantly reduced. It can however, in the simplest case, only be used to fabricate gratings of a single wavelength.

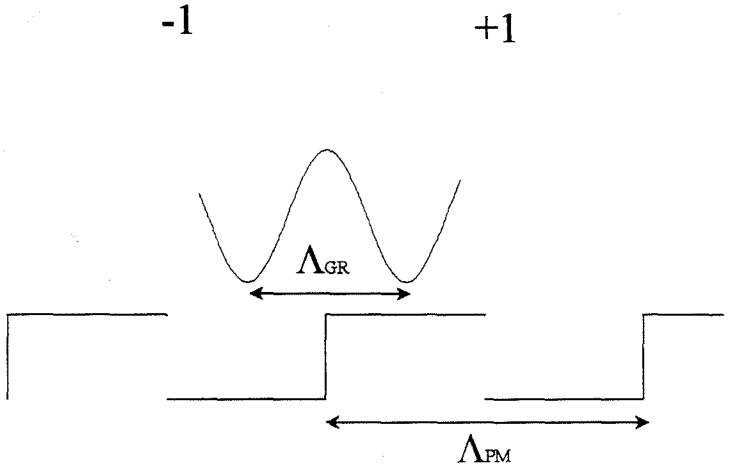

Figure 2.12: Schematic diagram of phase mask and the refractive index profile generated in the fibre core due to intereference of the first orders.

Figure 2.12 shows a simple diagram of a phasemask, period Λ_{PM}, and the interference pattern formed by the overlapping beams, period Λ_{GR}. As can be seen in the diagram, the region of overlap of the two beams is relatively small and so the fibre has to be placed close to the phasemask. The period of the grating in the fibre is determined by the period of the phasemask alone and bears no relation to the wavelength of the illuminating radiation. In the case of normal incidence of the phasemask, the wavelength of the resulting grating,

$$\lambda_B = 2n_{eff}\Lambda_{GR},$$

where

$$\Lambda_{GR} = \frac{\Lambda_{PM}}{2},$$

Equation 2-27

and n_{eff} is the effective mode refractive index of the fibre, which can be approximated to the refractive index of the fibre core for single mode fibre. Phasemasks can also be optimised for irradiation at off-normal incidence, so that the light is split into one of the first orders and the zero order. The two beams again interfere resulting in a grating in the fibre with the same pitch as that of the phasemask [58]. The phasemask is made out of fused silica (quartz) and the illuminating wavelength determines the required etch depth of the corrugations in the phasemask. Though Figure 2.12 shows the ideal phasemask with only +/-1 diffracted orders produced by the phasemask, there is always some light present in the zero order and higher orders. Many factors effect the efficiency of the phasemask, including the etch depth of the corrugations, the phasemask profile (square corrugations are ideal), and the mark-space ratio. The light from other orders results in a decrease in the UV induced fringe visibility of the perturbation in the fibre core, introducing a DC offset for the UV induced refractive index and reducing the refractive index available for grating fringes. Much attention has focussed recently on the affect of the zero order, which interferes with the +/-1 orders, resulting in the formation of a second grating in the fibre core, with a pitch equal to that of the phasemask.

The disadvantage with the phasemask technique compared to the holographic technique described earlier is that the phasemask pitch determines the grating wavelength. However, many techniques have now been presented to overcome this limitation. The early suggestions included placing a lens in front of the phasemask in order to diverge the incident beam and thus increase the Bragg wavelength [59], and stretching the fibre whilst fabricating the grating, resulting in a grating at wavelength shorter than that determined by the phasemask when the fibre tension is released [60]. The type of fibre also determines the grating wavelength. For instance, a grating fabricated in 20 mol% germania doped fibre will have a higher wavelength than a grating fabricated in either standard telecommunications fibre or boron-germania co-doped fibre, due to the higher refractive index of the core of the hi germania doped fibre.

Longer Phasemask Gratings

The introduction of the phasemask technique still did not overcome one of the major limitations of the holographic technique – that the width of the irradiating laser beam limited the grating length. Martin *et al* presented the idea of scanning the laser beam along the fibre and phasemask (which are static) in order to realise longer gratings [61], and demonstration of a 50mm long grating soon followed [62]. However, now the length of the grating was limited by the length of the available phasemasks. The maximum length of a phasemask currently stands at 10cm for those fabricated by both e-beam lithography and holography. Longer gratings have been fabricated using many phasemasks joined together [63], though this is a rather expensive solution.

Recently methods overcoming this limitation have been presented. The grating is fabricated in small sections with the fibre scanned past the beam and phasemask between exposures. The position of the fibre is controlled very precisely by interferometric techniques so that the grating structure is glitch-free [64].

Fabrication Limitations

The importance of good alignment of the fibre relative to the phasemask soon became apparent following the introduction of the scanning phasemask technique. The coherence length required for phasemask fabrication is much reduced compared to that required for the interferometric technique. However, Orthonos and Lee showed that laser sources with poor temporal coherence result in a very high sensitivity of the grating reflectivity to the distance between the phasemask and the fibre [65]. As the distance between the phase mask and fibre is increased, the fringe visibility of the grating refractive index modulation decreases. They also showed that changing the angle between the phasemask and the fibre resulted in a change in the Bragg wavelength of the grating. The effect of poor alignment between the beam and the fibre core has also been demonstrated [66], along with a method for ensuring good control of the beam-fibre alignment by monitoring fluorescence at 400nm.

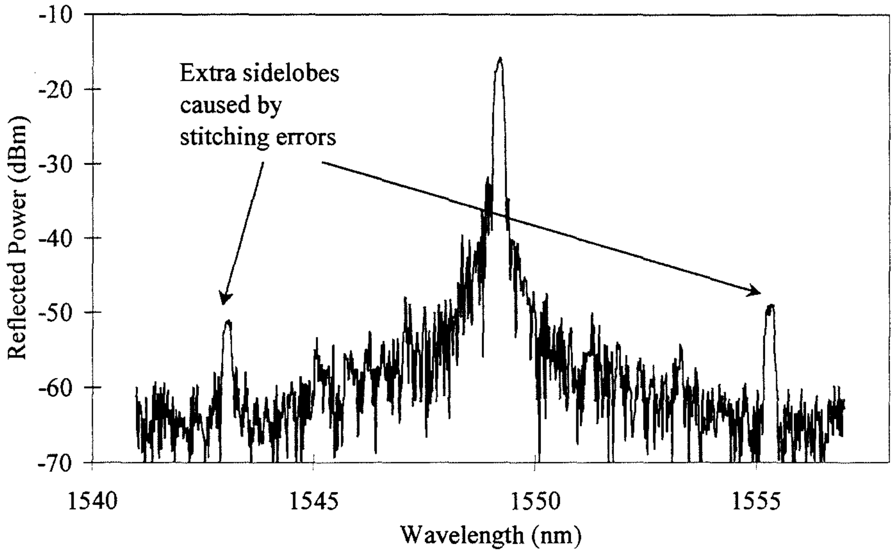

Figure 2.13: Stitching error sidelobes caused by constant phase errors between writing fields of the e-beam.

One of the major problems with long phasemasks is that of 'stitch errors' for those fabricated using electron beam lithography [67,68]. These stitch errors are phase errors that occur when the phasemask is longer than the length of each individual writing field of the electron beam machine used to write the phasemask. The fields have to be stitched together to make a long phasemask, thus a phasemask can have phase errors at the joins of the fields. If the phase errors are constant in magnitude, then distinct peaks can be seen either side of the grating peak, as is shown in the grating spectrum in Figure 2.13. The spectral separation of these peaks caused by stitching errors,

$$\Delta\lambda_p = \frac{\lambda_B^2}{2nM},$$

Equation 2-28

where M is the e-beam phasemask field size.

With care, these phase errors can be minimised, for example by varying the field size over the grating length [69]. Errors in already existing phasemasks can be compensated for at the grating writing stage by carefully altering the relative positions of the fibre and phasemask [70], though this is an involved solution to the problem.

Apodisation

Many applications now require that the spectra of gratings in reflection have flat tops and very low sidelobe levels. The way in which this spectral shaping is achieved for Bragg gratings is using a process called 'apodisation', where the refractive index modulation of the grating is reduced at either end of the grating. There has been much work done in recent years on grating apodisation. Gratings fabricated by the interferometric method are often intrinsically apodised, if the intensity of the irradiating beam falls at the edges. However, using this method, the resulting average refractive index of the fibre core is lower at the edges of the grating than in the centre and so the wavelength of the grating at the edges is lower than the grating peak, resulting in a resonance effect.

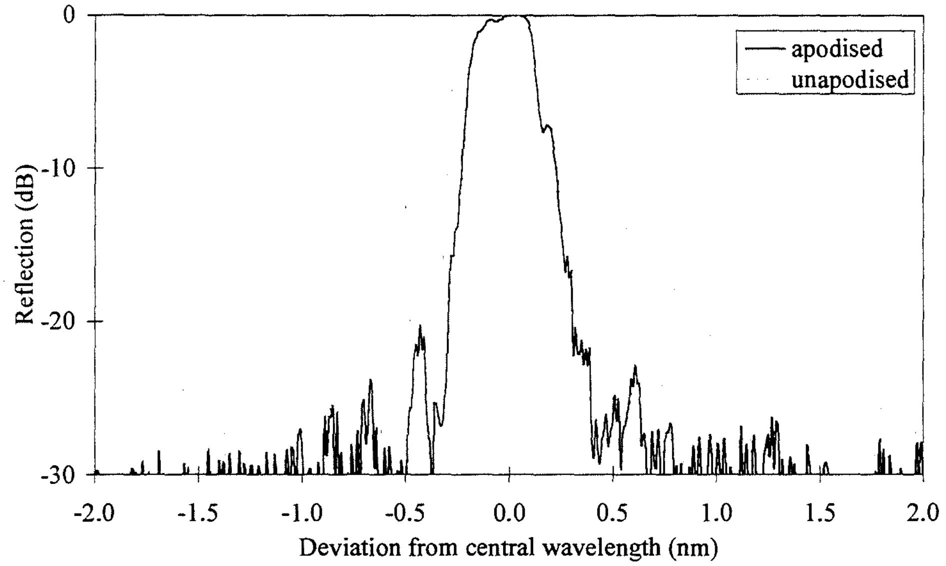

Figure 2.14: The spectra of apodised and unapodised gratings. The apodised grating shows significantly reduced sidelobe levels.

Figure 2.14 shows the effect of apodising a Bragg grating (i.e. gradually decreasing the fringe visibility of the grating structure at either end of the grating). The average UV induced refractive index of the grating is constant along the grating length, so as to avoid any low wavelength resonances and ensure a symmetric grating spectrum. Many methods have been presented for apodising gratings, for example [71,72,73]. A large proportion of the work contained in this thesis is concerned with the design and fabrication of apodised gratings, the work can be found in chapter 4.

2.4.2 Chirped Gratings

Holographic methods

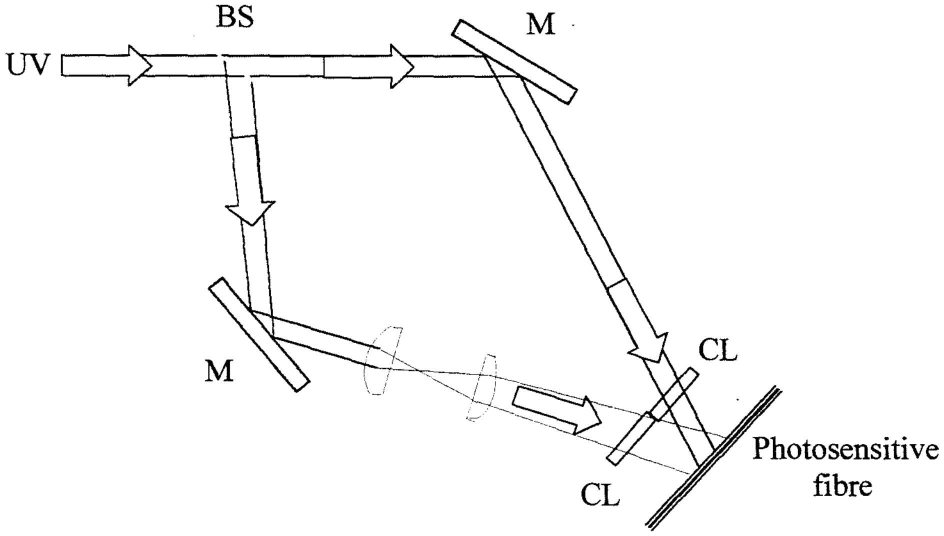

Figure 2.15: The set-up for fabricating chirped fibre Bragg gratings used at Aston University

The first work on the fabrication of chirped fibre Bragg gratings was published by Byron *et al* in 1993 [49]. The gratings were fabricated in fibre tapers, where the spacing of the grating fringes in the fibre remained constant but the waveguiding properties of the fibre along the length of the grating were changed. Methods presented later altered the spacing of the fringes along the length of the grating. Chirped gratings may be formed by bending the fibre during exposure [74], and by a method involving the placement of a defocussed telescope in one arm of the basic interferometer used for grating fabrication, shown in Figure 2.15. The interfering beams have dissimilar curvatures and so the gratings are chirped [75]. This method is very flexible and enables the fabrication of gratings with a wide range of chirps, up to atleast 50nm [76].

Phasemask methods

The advent of phasemask technology introduced a simple and highly reproducible method for fabricating fibre gratings. However, much of the technological future for Bragg gratings lay in telecommunications and the possible use of Bragg gratings for dispersion compensation; thus the ability to mass-produce chirped gratings was important for the future of grating technology. Whilst the methods presented for use with the holographic fabrication technique were able to produce chirped gratings with very broad chirps, there was no guarantee of being able to reliably reproduce many identical gratings. In addition, the requirement for chirped dispersion compensators was a long, slowly chirped grating.

Kashyap *et al* presented the first step-chirped phasemask in 1994 [77] which was constructed by having a different phasemask period for each e-beam writing field, keeping the fields as small as possible. The period of the phasemask gradually increased along the length of the phasemask. It is impossible to make a true chirped grating using the e-beam method of phasemask fabrication because of the finite size of the writing fields. However, gratings fabricated using these masks result in a fair approximation of a chirped grating.

Other methods have been presented using uniform period phasemasks to fabricate chirped gratings. The first method, presented by Hill *et al*, is a dual scan method, fabricating a standard uniform period grating first and then applying a second scan without the phasemask in order to introduce a variation in the average core refractive index along the grating length resulting in a chirp[78]. A single scan technique, presented by Byron and Rourke, involves the gradual stretching of the fibre whilst the laser beam scans across the phasemask, thus introducing a chirp to the grating [79]. By varying the angle between the fibre and the phasemask, Painchaud *et al* showed that it was possible to fabricate linearly chirped gratings by tilting the fibre relative to a uniform period phasemask [80]. Longer chirped gratings can be made by concatenation of shorter chirped gratings [81]. Recently, a technique for producing very long fibre gratings (>1metre long) has been presented for producing dispersion compensators. The technique uses a standard phasemask and the grating is essentially written plane by plane [82].

2.4.3 Bandpass filters and resonators

Fibre Bragg gratings are all fibre devices and therefore have a very low insertion loss meaning that they are ideal for insertion into many fibre optic systems. With the emergence of DWDM technologies, one of the most important devices are bandpass filters. The first bandpass filters for use in transmission were demonstrated by Farries *et al* in 1994, who demonstrated a 44nm stop band incorporating a 2nm passband [75], and Mizrahi *et al* who presented an early fibre grating demultiplexer incorporating bandpass filters for use in transmission [83]. In this example the narrow passband was created by use of an amplitude mask during fabrication of the very broad chirped grating. More recently, high quality, low loss (<2dB) bandpass filters with very broad stop bands and out of band rejection of >30dB have been fabricated by the concatenation of chirped fibre Bragg gratings in depressed cladding fibre [84].

Phase shift gratings

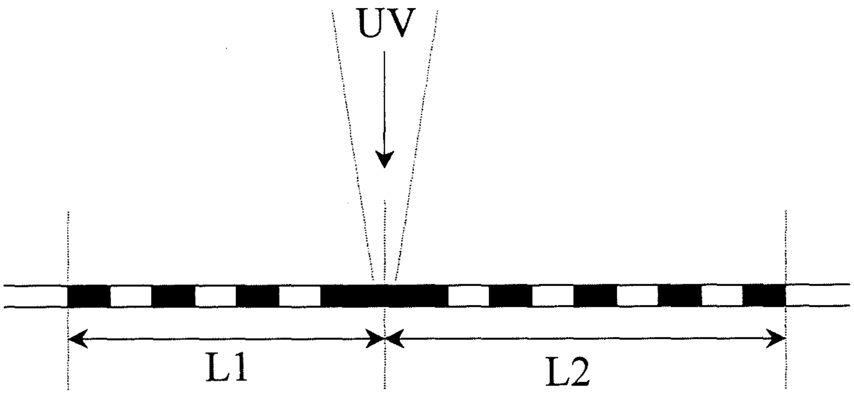

Figure 2.16: Introduction of a phase shift by raising the refractive index at a point along the fibre [85].

A similar technique to that presented by Mizrahi may be used to create both phase-shifted uniform period grating bandpass filters [85] and broad stopband transmission filters [86]. In these two examples rubbing out part of the grating that has already been written creates the passbands or phase shifts, as is shown in Figure 2.16. The position of the passband in the stopband is determined by the size of the phase shift and by the relative phases of the two grating portions L1 and L2. A similar effect may be obtained by thermal post processing, in order to rub out the desired part of the grating [87]. Phase shifts can also be introduced by using phase shifted phasemasks [88], allowing more accurate replication of the phase-shifts. Using this phasemask method, it has been shown to be possible to adjust the width of the passband within the grating structure by inserting multiple $\pi/2$ phase shift at specific points along the grating length [89]. The effect of the positioning and size of phase shifts in phasemasks has been studied in detail by two groups in particular [90, 91]

Moiré gratings

Moiré gratings are fabricated, in general, by the inscription of one grating (chirped or uniform period) followed by a second grating with a very slightly different wavelength in exactly the same position of the fibre. The resulting compound grating has positions along the length where the two gratings are directly out of phase and thus phase shifts are formed.

The refractive index modulation of a Moiré grating, $\Delta n(z)$:

$$\Delta n(z) = \Delta n\left(2 + 2\cos\frac{2\pi z}{\Lambda_C}\cos\frac{2\pi z}{\Lambda_S}\right),$$

Equation 2-29

where Δn is the amplitude of the grating refractive index modulation, z is the position along the grating, Λ_c is the period of the slowly varying envelope, and Λ_s is the period of the rapidly varying fringes within the envelope[3].

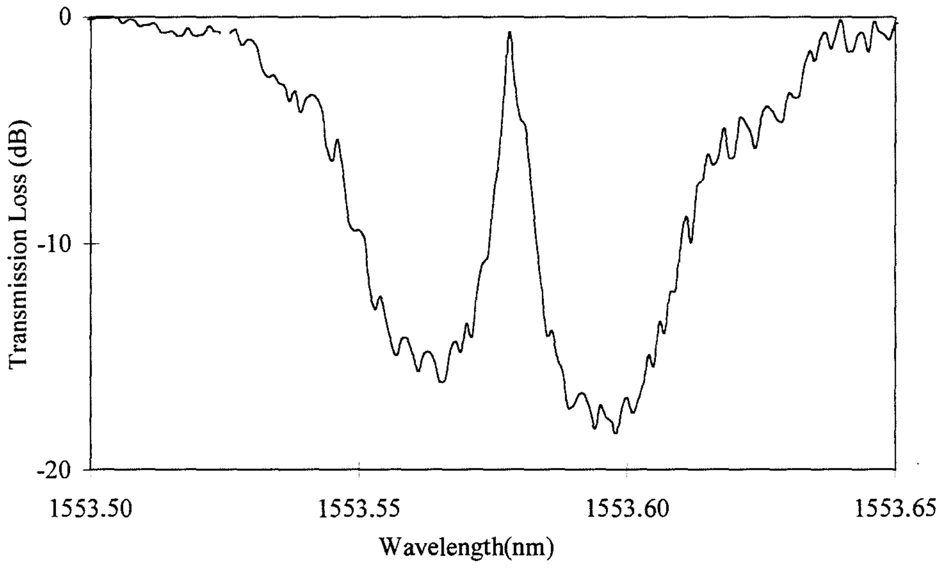

Figure 2.17: A single passband uniform period Moiré grating.

Moiré gratings were originally formed in optical fibres using surface relief gratings [92] and were quickly demonstrated using UV exposure of the fibre [93]. Moiré gratings were also shown to be feasible for producing wide-stopband transmission filters when concatenated with other chirped gratings to form a broad stopband [94]. Figure 2.17 shows the spectrum of a single passband, uniform period Moiré grating, fabricated by dual scan of a uniform period phasemask. The fibre was stretched between two scans of the phasemask, a technique originally demonstrated for chirped gratings [95,96]. The structure of Moiré filters can also be adapted to introduce flattened passbands, by UV bleaching sections of the Moiré grating between the resonances [97].

---

[3] The structure of Moiré gratings is discussed in detail in chapter 7.

Comb Filters

There are other methods of producing multi-passband filters for use in reflection. The disadvantage with transmission based passband filters, is the need for a broad stop band at either side of the passband, combined with the difficulties in controlling the exact shape of the passband, whilst passband filters used in reflection require a costly circulator. Orthonos *et al* showed that it is possible to fabricate superimposed uniform period gratings in order to effect a comb of gratings [98]. However, the disadvantage with this method is that the amount of available refractive index for grating fabrication is limited and so the reflectivity of the gratings is also limited. A solution to this problem, involving the fabrication of arrays of uniform period gratings has been presented [99] (further details on the fabrication of short grating arrays may be found in chapter 7).

Another method of producing a spectral comb function using fibre gratings, is the fabrication of sampled gratings [100]. The spectrum of an unapodised sampled grating is shown in Figure 2.18. In order to make the grating peaks all of the same reflectivity, it is necessary to apodise each sub-grating in the sampled structure with a sinc function, which requires a long grating length [101].

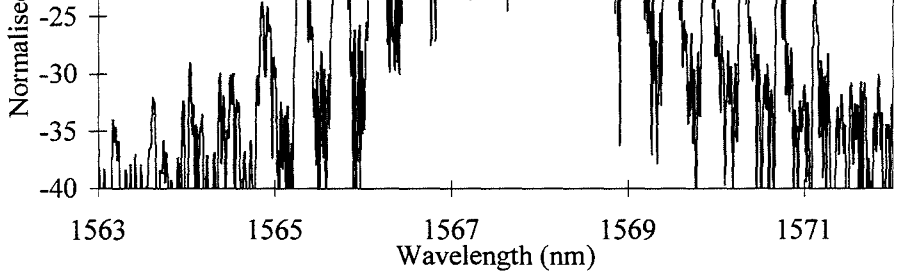

Figure 2.18: A 3cm long sampled grating, the length of the individual samples was 1mm, and the spacing 2mm.

2.5 Grating Characterisation

As the fabrication of fibre gratings has enabled the realisation of more sophisticated spectral characteristics, there has been an increasing need for accurate characterisation methods. An early report on the characterisation of gratings was published by Mizrahi and Sipe, introducing explanations for the basic properties of fibre grating spectra, explained below [102].

2.5.1 Spectral Characterisation of Gratings

There is now a necessity to measure the optical properties of fibre gratings with extreme accuracy. The increasing length of gratings means that the grating bandwidths are becoming narrower. For example, an unapodised 10 cm grating with an index modulation of 1.25×10^{-5}, results in a grating of 95% reflectivity and a 3dB bandwidth of 16pm. A 1m long grating of the same reflectivity has a bandwidth of 1.6pm. There have been many different methods proposed for measuring the optical characteristics of gratings [103,104]. The most recent examples involve modulated tuneable laser sources [105], white light interferometry and spectroscopy techniques [106,107] in order to overcome the resolution restrictions of tuneable lasers (typically 1 to 10pm). The terms often used in grating specifications are illustrated in Figure 2.19 and Figure 2.20. The bandwidth of a grating is usually measured in reflection. In order to measure the sidelobe suppression (or isolation) accurately it is necessary to measure the grating reflection in dBs, rather than using a linear scale.

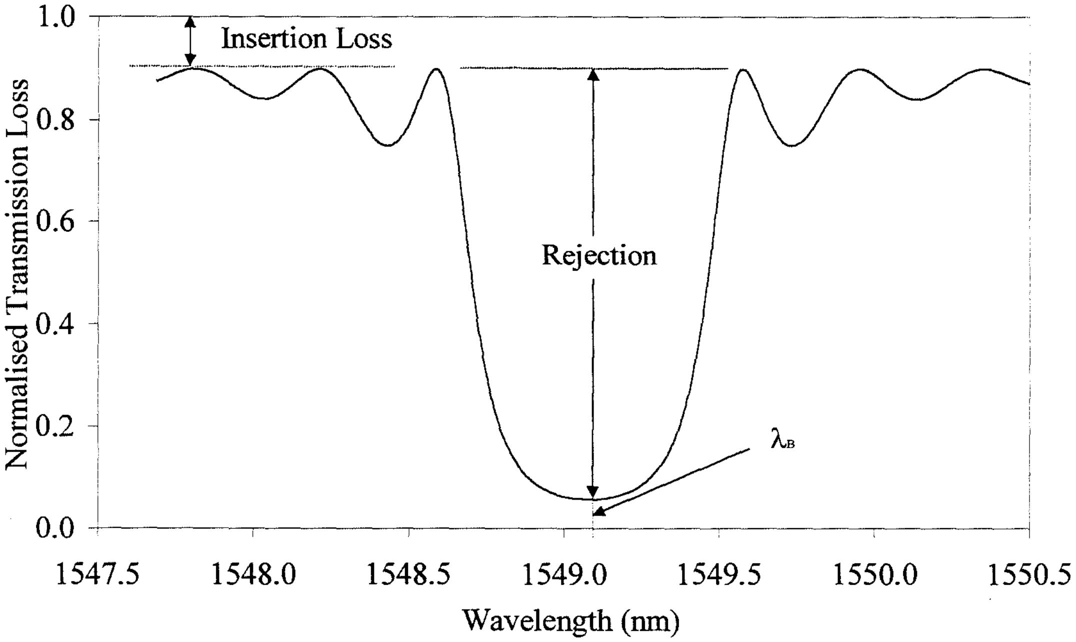

Figure 2.19: Transmission Characteristics of gratings

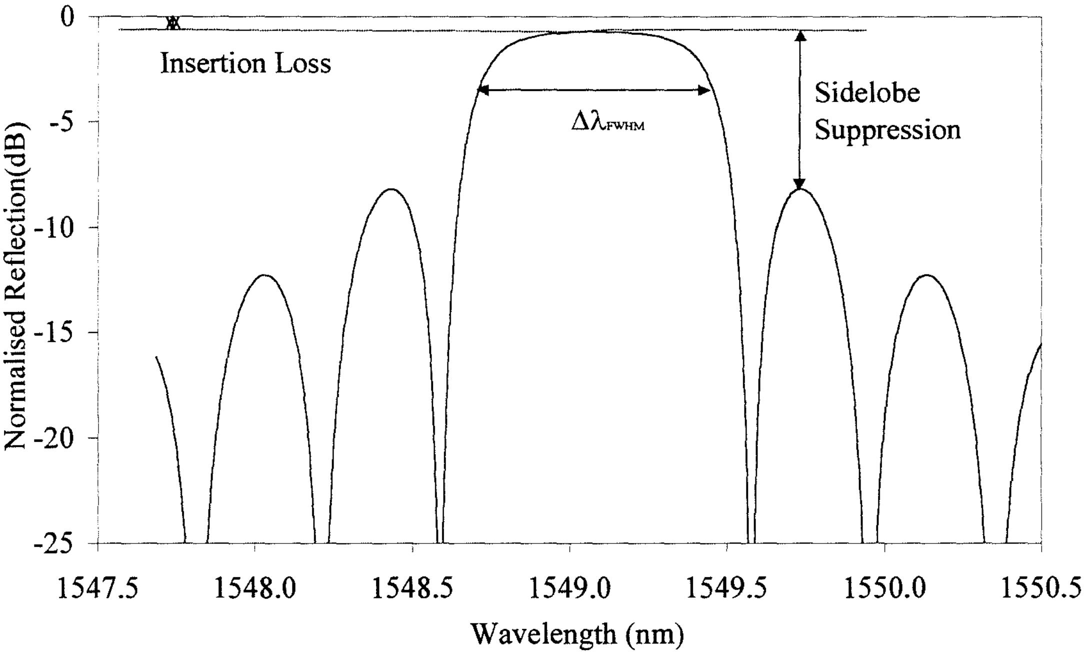

Figure 2.20: Reflection characteristics of gratings

2.5.2 Short wavelength loss

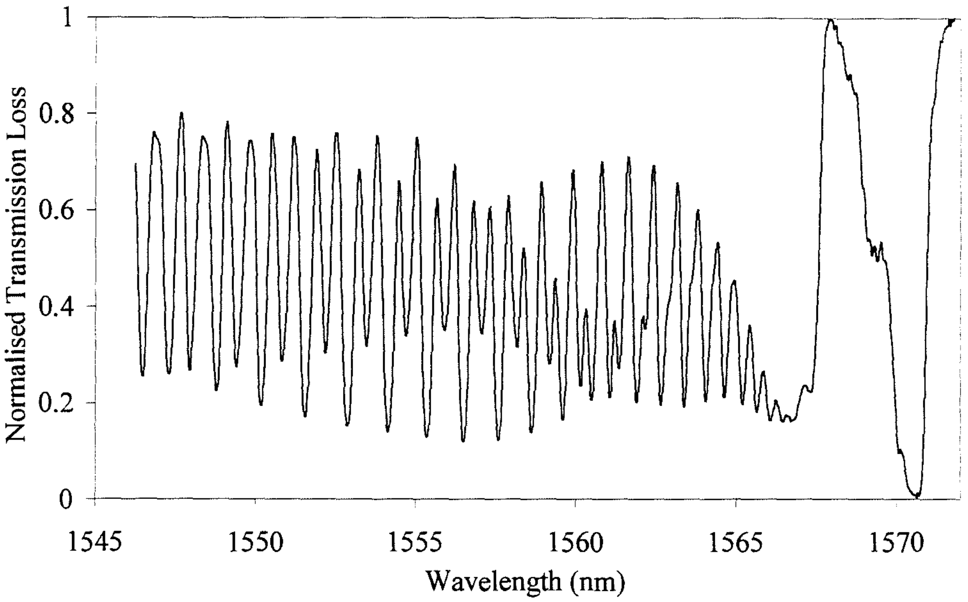

Figure 2.21: Short wavelength loss of a uniform period grating

Bragg gratings fabricated in standard photosensitive fibres exhibit 'short wavelength loss' which is caused by coupling between forward propagating core modes and backward propagating cladding modes [108]. This coupling results in resonances at wavelengths below the Bragg wavelength; a typical grating spectrum exhibiting this loss is shown in Figure 2.21. The resonances can be reduced by dipping the bare fibre containing the grating into index matching gel; whilst this results in a smoother loss spectrum, the loss is still present.

Several examples of depressed cladding fibres have been presented in order to try to overcome this loss [109,110]. However, gratings in these fibres have been shown to exhibit 'ghost' gratings at wavelengths higher than the main Bragg peak [111,112].

2.5.3 Other Grating Characterisation

In order to understand the fundamental mechanisms behind photosensitive grating production, techniques have been developed which interrogate the fibre structure itself. Krug *et al* presented a technique to interrogate the grating from outside the fibre using a probe laser (633nm) [113,114].

It is also important to characterise the polarisation effects caused by the fabrication of gratings. UV fabrication of gratings induces birefringence in the fibres, due to a non uniform absorption of the UV across the fibre core. This birefringence causes polarisation mode dispersion [115], but can be overcome by rotating the fibre during exposure of the grating [116].

2.6 Grating Lifetime Issues

2.6.1 Grating mechanical strength

The consistency of grating properties over timescales equivalent to required device lifetimes is an ongoing area of investigation. There has been much work published on the effect that UV writing of gratings has on the fibre strength. Feced *et al* have suggested that irradiation at 193nm degrades the fibre strength significantly less than irradiation at 248nm [117]. Whilst other evidence indicates that pulsed exposure significantly degrades fibre strength and continuous wave exposure yields fibre breaking stresses close to that for pristine fibre [118].

The treatment of the fibre during the fabrication of Bragg gratings is very important and has an acute effect on the eventual breaking strength of the fibre. Chemical stripping of the fibre coating has been found to preserve the mechanical strength of the fibre significantly [119] compared to the use of mechanical coating removal methods. Many groups have presented fibres with special UV transparent coatings thus removing the necessity to strip the coating from the fibre at all [120,121], though the use of a high power laser is required.

2.6.2 Grating Refractive Index (Thermal) Decay of Gratings

As fibre Bragg grating devices are being considered for integration into real systems, their long-term characteristics become increasingly important. Erdogan *et al* showed that gratings could be made more stable by annealing at temperatures higher than the eventual required operating temperature of the device [18]. This accelerates the grating decay resulting in greater stability of gratings, which can be considered stable over timescales as long as 50 years.

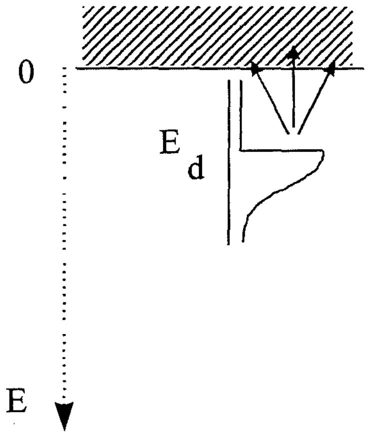

Figure 2.22: Thermal decay of fibre gratings caused by the emptying of traps [18]

Initially, the refractive index modulation decays very rapidly and the rate of decay then decreases as time advances (following a power law). The decay is a strong function of temperature, hence the ability to accelerate the decay by annealing. The decay is caused by the thermal depopulation of traps. The effect of annealing on the trap population is shown as described by Erdogan *et al* in Figure 2.22. When they have been released from the traps, electrons are assumed to repopulate the original level occupied prior to UV excitation. This assumption is supported by measurements made on the 240nm absorption band after thermal erasure, which has been shown to be bleached again [19]. As the refractive index modulation decays, the average refractive index of the fibre core decreases, resulting in a shift to shorter wavelengths of the central grating wavelength [122]. This shift has been shown, in work carried out as part of this thesis, to be affected by the changing properties of the fibre itself in the case of boron-co-doped fibre [123].

There have been differing reports on the decay of gratings fabricated in hydrogen loaded fibres. Some gratings have been shown to exhibit an initial rapid decay followed by relatively little change in the refractive index modulation [124]. Whilst others have been shown to exhibit similar decay to gratings fabricated in unloaded fibre [125]. Gratings fabricated in silica fibres with different dopants have been observed to decay at different rates. Gratings fabricated in boron/germania co-doped fibres are known to decay more rapidly than those fabricated in germania doped fibres [126], whilst those fabricated in tin codoped fibres exhibit a stability similar to those in Ge fibres [44]. In addition, negative index gratings exhibit far superior stability at elevated temperatures when compared to positive index (type I) gratings [6]. The behaviour of gratings fabricated using both pulsed and cw exposure has been studied [127], with no conclusive differences observed.

2.7 Applications

The fabrication of fibre gratings has been very much refined since the early demonstrations. The quality of gratings is now such that they are being employed in many real systems, competing with other photonics technologies. The following section is an illustration of the many and varied uses of fibre gratings.

2.7.1 Sensors

Fibre Bragg gratings can be used to measure a variety of parameters, and are used in many diverse applications, a sample of these applications can be found in Table 2.1. As shown in Table 2.1, the range of applications for fibre Bragg grating sensors is wide and diverse. Nearly all fibre Bragg grating sensors work because the measurand induces a change in the Bragg wavelength. For example, in the case of strain sensors, a compressive strain results in a shift to shorter wavelengths of the Bragg wavelength, and a tensile strain results in a longer wavelength. The first Bragg grating sensors to be demonstrated were temperature and strain sensors [137]. The most common use of grating sensors is for point sensors, where an average reading of the measurand along the grating length is obtained. All of the examples in Table 2.1 involve the use of point sensors. Gratings can be used to make distributed measurements, by deploying an array of gratings, often of different wavelengths, along a length of fibre. Distributed sensing is now used commercially, in many applications, a typical one being the measurement of strain in composite structures, where the gratings can be embedded when the structure is made [128]. The wavelength shift of the grating peak is usually detected using some sort of tuneable filter [129], scanning laser [130], or matched Bragg gratings [131].

FIBRE BRAGG GRATINGS USED FOR SENSING:	REFERENCES:
Acceleration	[132]
Chemicals	[133]
Efficiency of human heart	[134]
Electric current	[135]
Pressure	[136]
Strain	[137]
Temperature	[137]
Ultrasonic field	[138]
Vibration	[139]
Wavelength	[140]

Table 2.1: Sample of applications for fibre Bragg gratings as sensors

One of the main issues concerning the use of Bragg gratings is that of isolating the effect on the grating of parameters which are not being measured. Many papers have been presented concerning the discrimination between strain and temperature effects measured by Bragg gratings [141,142,143,144]. However, methods for measuring both strain and temperature simultaneously currently require two different gratings.

2.7.2 Dispersion Compensation

One of the telecommunications applications, for which fibre gratings have already been used to make competitive devices, is dispersion compensation. In transmission, the chromatic dispersion of the fibre can cause significant broadening of optical pulse, leading to a significant increase in the bit error rate (BER) to above the accepted level of 1 in 10^9.

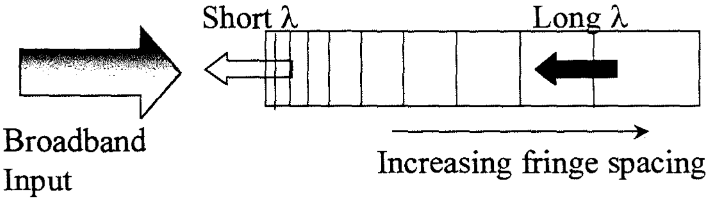

Figure 2.23: A chirped (dispersion compensating) grating reflects different wavelengths at different points along the grating.

Chirped fibre gratings can be used to compensate for this chromatic dispersion, as they themselves have dispersive properties, due to the nature of the chirped grating structure. The grating dispersion,

$$D = \frac{2n_{eff}L}{c\Delta\lambda},$$

Equation 2-30

where n_{eff} is the refractive index of the fibre core at the grating, L is the grating length, and $\Delta\lambda$ is the total grating bandwidth (or chirp). As is shown in Figure 2.23, different points along the grating reflect different wavelengths, meaning that a pulse that has been temporally broadened can be compressed using a chirped grating.

Outelette reported a theoretical presentation of the use of gratings as dispersion compensators [145] and the first experimental demonstrations followed a few years later [146,147]. Gratings were also demonstrated for the compression of pulses broadened by self-phase-modulation [148]. These early demonstrations involved the use of gratings in reflection requiring the use of expensive circulators. More recently, gratings suitable for dispersion compensation in transmission have been reported [149]. In this configuration, the gratings are tapered in strength and are of uniform period.

Successful dispersion compensators have to be carefully designed [150] in order to reduce the inherent ripples on the time delay response of the gratings. Recently, high quality dispersion compensators involving the fabrication of gratings >1metre in length have been demonstrated [151].

2.7.3 Fibre Lasers

It is not surprising that one application for fibre gratings is in fibre lasers, as they provide the obvious choice of highly wavelength selective partially reflecting mirrors required in fibre lasers [152]. They are ideally suited as, in many cases, the gratings can be fabricated directly in the active fibre of the laser itself, thus removing the need for loss-inducing splices between the components. Bragg gratings are now routinely used in fibre lasers, and have been demonstrated in many rare earth doped fibres including erbium fibres [153,154].

Figure 2.24: A simple configuration of a fibre laser with two fibre grating reflectors.

A simple fibre laser configuration is shown in Figure 2.24. The active meduim is pumped in most cases by a laser diode at an appropriate wavelength lower than the lasing wavelength of the active medium. There is usually an isolator after the second Bragg reflector in order to remove the pump wavelength from the laser output. In many cases the amount of available power has been limited by the amount of single mode pump power available from diode lasers. To overcome this problem, cladding pumping has been introduced in special fibres, which have a special cladding for guiding the multimode pump[155].

Another laser application of in-fibre gratings is in the frequency stabilisation of laser diodes[156] where the grating is often fabricated directly in the fibre pigtail of the laser. There are many of the configurations of lasers employing fibre Bragg gratings, many of which are mentioned in reference [152].

2.7.4 Add/Drop Filters

In WDM systems, add/drop nodes are required to select the individual channels, or to insert a signal onto a particular channel. There have been many different configurations presented including gratings written in Mach-Zehnder intereferometers [157], and in fused couplers [158], shown in Figure 2.25.

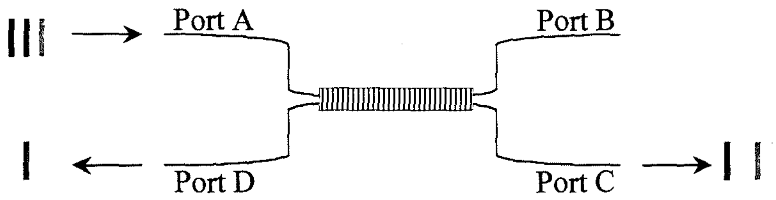

Figure 2.25 : An OADM based on a Bragg grating in a 100% fused coupler

The quality of gratings required for WDM applications is very high and the uniform period gratings required for the channel filters, can themselves cause dispersion penalties [159,160].

3 GRATING FABRICATION USING QUADRUPLED ND:YAG

3.1 Introduction

There are now many examples of grating fabrication using different wavelengths. Common choices include KrF Excimer lasers (248-249nm, pulsed [161]) and frequency doubled Argon Ion lasers (244nm, cw) [162]. However, there are also examples of gratings fabricated using both near UV (333-364nm [163]) and far UV (193nm [164]) lasers. Though there are many different wavelengths suitable for grating fabrication, the lasers can be divided into two types: low spatial and temporal coherence, and high coherence. Low coherence sources, such as the KrF Excimer laser (248nm), are suitable only for grating fabrication by contact printing with a phasemask. Low coherence sources have poor spatial beam quality and so spatial filtering of the beam is often required in order to fabricate good quality gratings. In addition, the properties of the beam can vary significantly between pulses, meaning that averaging spatial irregularities over a large number of pulses is often required to obtain good quality gratings. Argon ion lasers operating at a variety of UV wavelengths (244nm, 257nm, 302nm, either at the fundamental wavelength or frequency doubled) provide excellent coherence and are therefore ideally suited to grating fabrication and are frequently employed in research laboratories.

The requirement for most industrial grating fabrication utilities is for the mass production of high quality gratings, at as low a cost as possible. Frequency quadrupled Nd:YAG lasers provide a high power, low cost, UV source. Using phasemasks, they have the potential to provide the UV source for many gratings fabrication utilities simultaneously, for a much lower initial outlay and year-on-year maintenance cost when compared to an Argon-ion laser, and they do not require the supply of gases needed by Excimer lasers. For these reasons, it was decided to invest in a frequency quadrupled Nd:YAG laser, along with Nortel Technologies research laboratories.

The aim of this chapter is to identify and illustrate the advantages and disadvantages of using a frequency quadrupled Nd:YAG for the fabrication of in-fibre Bragg gratings. Various standard characterisation techniques are introduced that were used to identify areas in which the fabrication utility could be improved, and to understand a little more about the grating writing process. The later sections in the chapter concentrate on improving the repeatability of grating fabrication, and identifying aspects of the optical alignment of the set-up required to reduce imperfections in the grating profiles.

3.1.1 Why Choose a Quadrupled Nd:YAG?

As mentioned previously, at the time that the Nd:YAG laser was acquired, industry was looking to use high power pulsed sources rather than frequency doubled argon ion lasers for grating fabrication. Reported fabrication of gratings by a single excimer pulse [165], and subsequently gratings written during fibre drawing, was the likely cause of this interest in high power pulsed sources. Many research institutions chose to use KrF excimer lasers at 248nm. However, in conjunction with Nortel research labs, it was decided to follow investigation of an alternative laser source for grating fabrication – the quadrupled Nd:YAG. Frequency quadrupled Nd:YAG lasers are an unusual choice. The advantages include the very high output power and that they are relatively cheap compared to other lasers. They also have very high peak pulse powers (>>10MW) enabling them to be used to make type II (damage) gratings.

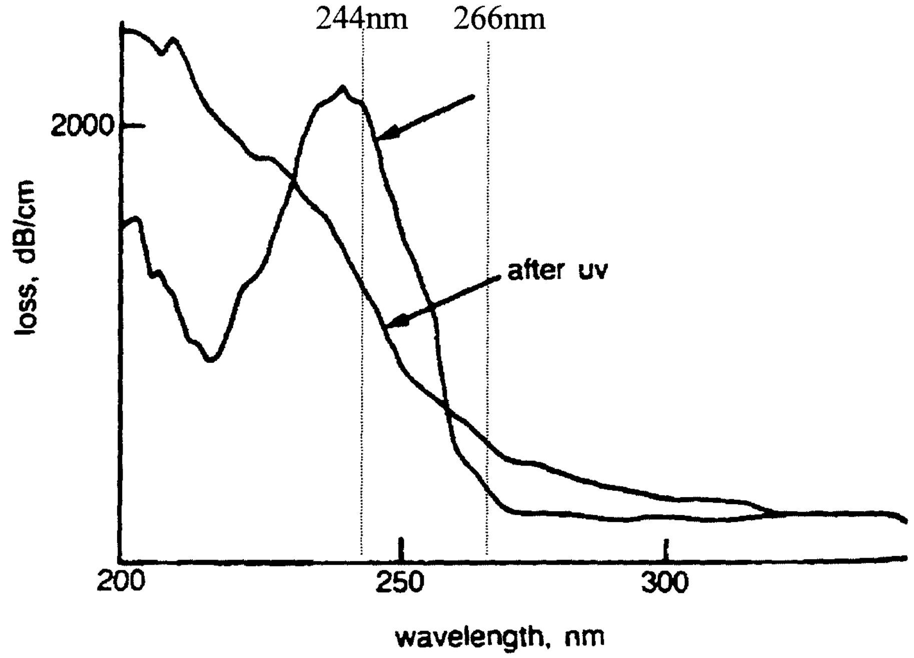

Figure 3.1: The transmission spectrum of a 15mm thick preform before and after irradiation with 244nm light [166].

Figure 3.1 shows the absorption spectrum for a germanosilicate preform, before and after exposure with 244nm light (wavelength of the frequency doubled argon ion laser – FreD). It can be seen that before exposure, the transmission loss for 244nm is ~ 2000dB/cm greater than that for 266nm light, indicating that the absorption at 266nm is far less than that at 244nm. However, despite very low absorption properties of the fibre at 266nm, it is still possible to fabricate type I gratings at this wavelength.

LASER	FreD	Quad Nd:YAG
Max. UV Power (Peak)	100mW (100mW)	>1W (>>10MW)
Wavelength	244nm	266nm
Coherence	High	Poor (coherence length ~10mm)
Repitition Rate	Cw	30Hz
Pulse Duration		9ns
Beam Size	~3mm	>1cm
Suited Applications	Holographic fabrication, high quality gratings	Type II gratings, mass production?

Table 3.1: Comparison of properties of Argon Ion (FreD) and Nd:YAG lasers

Some of the work in this thesis has been carried out using the FreD laser at 244nm. The argon laser is more suited to the production of single type I gratings than the quadrupled Nd:YAG; whose advantage is the capability of running many fabrication utilities using one laser, due to the very high power output. Table 3.1 shows a comparison of the properties of the two lasers used for grating fabrication in this thesis. The maximum average UV output power of the Nd:YAG is 10 times that of the FreD. In addition, due to the pulsed nature of the source, the maximum average UV power which can be used to fabricate gratings is ~25mW (average fluence ~2.5×10^{7}Jcm^{-2}). Above this power level, when the beam is focussed into the fibre core during fabrication, the fibre breaks, especially if the beam is not scanned during grating fabrication. The spatial intensity profile of the Nd:YAG UV beam is of poor quality, and therefore only suitable for fabricating gratings by scanning the phasemask and fibre [167] in order to average out irregularities in the beam profile.

3.2 Grating Fabrication

3.2.1 Fabrication Set-up

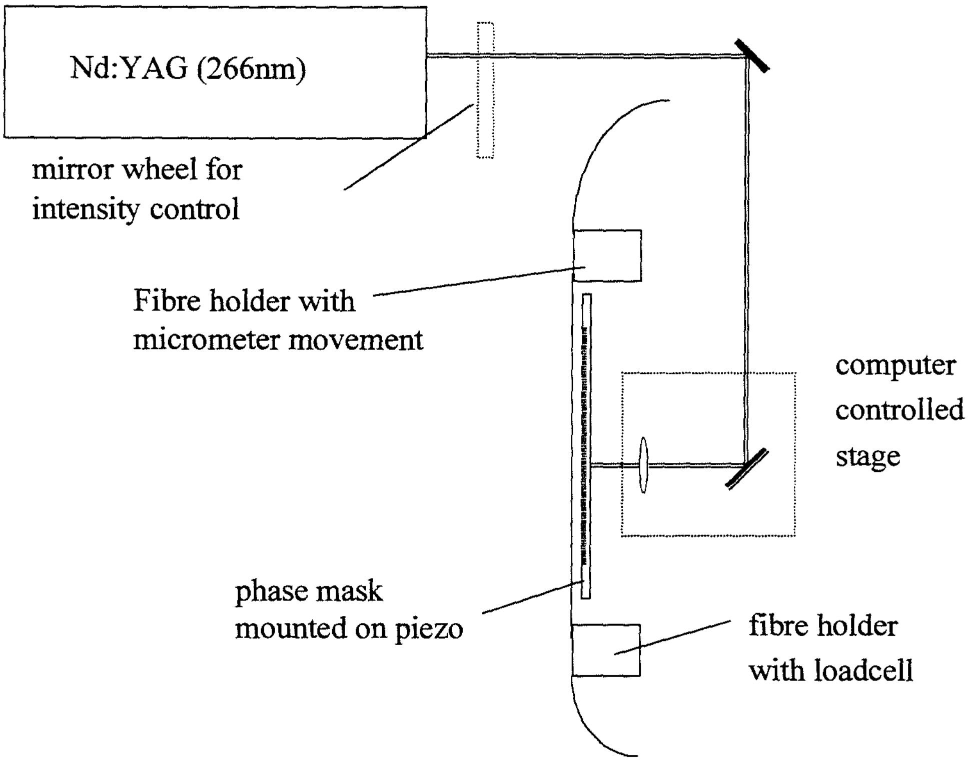

Figure 3.2: Grating fabrication set-up for Nd:YAG laser

Figure 3.2 shows the grating fabrication set-up of the Nd:YAG laser. One of the biggest challenges involved in fabricating gratings with this laser has been the control of the laser beam. The lack of availability of high power UV optics (e.g. neutral density filters and apertures etc.), particularly at 266nm, resulted in perhaps unconventional methods for reducing the laser power at the fibre. For maximum stability, the laser must be run continuously at full power (UV output ~ 1.3W). The laser power drops by ~4% over 6 hours, but this can be compensated for. If the laser is not run at full power, the beam quality deteriorates and tuning stability suffers. The Nd:YAG laser contains a seed laser which controls the timing of the pulses and ensures good temporal properties of the laser pulses, but the spatial properties of the laser beam suffer as a result. Therefore, if the seeder is turned off then the spatial quality of the beam increases, however, the beam positioning stability of the beam is then no longer acceptable.

The UV power reaching the fibre is controlled by the use of a mirror wheel, which dumps the unwanted portion of the laser power into a beam dump. The mirror wheel contains a 99% reflector, used for alignment of the fibre and fabrication set-up, and a 70% reflector used for grating fabrication. The beam pointing is not changed significantly when alternating between the 70% and 99% reflectors. The periscope reduces the beam height from 200mm to 125mm and contains a 70% reflector and a 4° wedged silica flat (giving 4% reflection). The wedge separates the beams reflected from the front and back faces of the flat, leaving the transmitted beam clean.

For laser safety, the high power laser beam is encased in black tubing wherever possible. In addition, the mirror wheel is positioned before the periscope, so that the laser power is reduced to safer levels as rapidly as possible. The periscope is encased in a black box in order to reduce scatter from the green light (532nm) present in the laser beam.

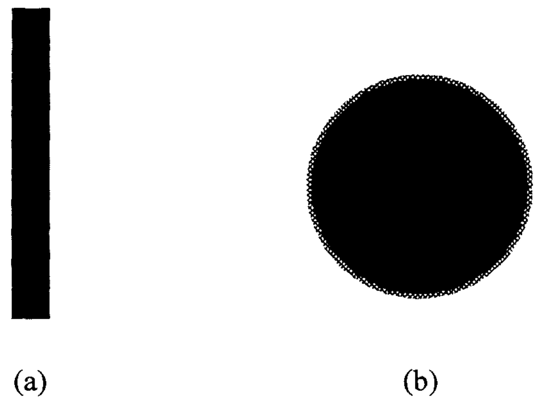
(a) (b)

Figure 3.3: Apertures used for filtering the UV beam

The UV output beam from the YAG has dimensions ~1.0cm×1.0cm. As was mentioned previously, the spatial intensity profile of the beam is very uneven. The laser beam diverges very little, and therefore it was possible to filter out a good quality part of the beam simply using an aperture, with no need for a telescope and spatial filtering arrangement, which would have proved very costly. To begin with, an aperture, shown in Figure 3.3(a), was simply placed in front of the cylindrical lens used to focus the beam into the fibre core. Whilst this aperture allowed selection of a region of the beam with more uniform spatial intensity, the position so near to the fibre and phasemask limited the ability to use back-reflections from the fibre and phasemask in order to align the set-up. In addition, the slot shape of the aperture meant that it was critical that the aperture was positioned absolutely vertically, or the width of the focussed beam in the fibre would be greater than that of the aperture. The other approach tried involved a circular aperture fixed to the shutter housing, shown in Figure 3.3(b). This was an improvement in two respects: the circular aperture shape meant that there were no problems with the focussing of the beam in the fibre and any changes in the pointing of the beam as the laser warmed up affected the whole grating equally. In the case where the aperture was fixed to the cylindrical lens, the intensity of light passing through the aperture and to the fibre could change as the beam scanned, due to the spatially uneven intensity profile. The aperture placed on the shutter housing also had fuzzy edges in an effort to eliminate any strange diffraction effects which may be caused by an aperture with very sharp edges.

3.2.2 Fabrication of Apodised Gratings

The first apodisation method to be implemented as part of this thesis involved oscillating the fibre along its axis during fabrication, a method which was presented by Cole *et al* [168]. The magnitude of the oscillations was largest at either end of the grating and zero in the centre.

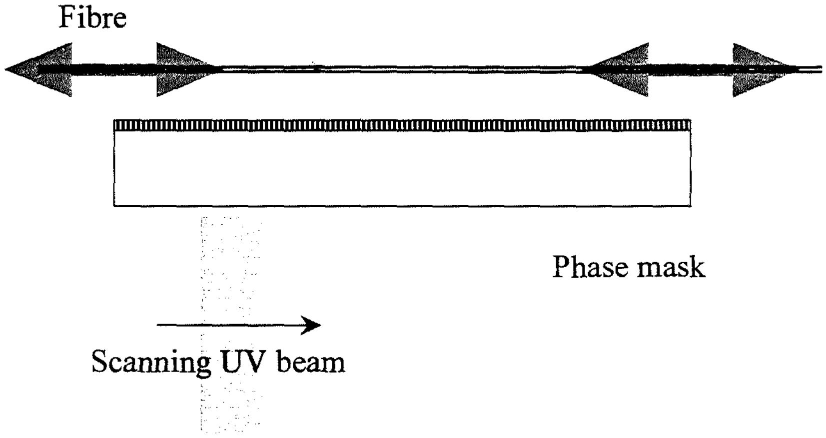

Figure 3.4: Setup for apodisation by dithering the fibre as the beam scans across

The fibre was clamped onto piezoelectric micrometers, which were mounted onto the standard fibre holding blocks, shown in Figure 3.2. The two piezos were controlled by the same voltage, and could be driven at a frequency up to ~5Hz. The details of calculating the appropriate scan speeds and other technical information can be found in chapter 4. A grating apodised using this technique is shown in Figure 3.5, compared with an unapodised grating. The setup was designed so that one of the piezos could be turned around, meaning that the fibre would be alternately stretched and released when an oscillating voltage was applied. This alternative arrangement of the piezos meant that they could be used to stretch the fibre symmetrically about the centre of the grating (only in the case where the grating was fabricated in the centre of the fibre) for fabricating moiré gratings.

The technique adopted for the apodisation study in chapter 4 was to dither the phasemask instead of the fibre, meaning that only one piezo was required. The technique was more suitable for use with the argon laser. The scan speeds for making gratings with the argon laser are much faster than for the YAG, therefore a piezo specially designed for dynamic operation was required. Full details on this apodisation technique can be found in chapter 4.

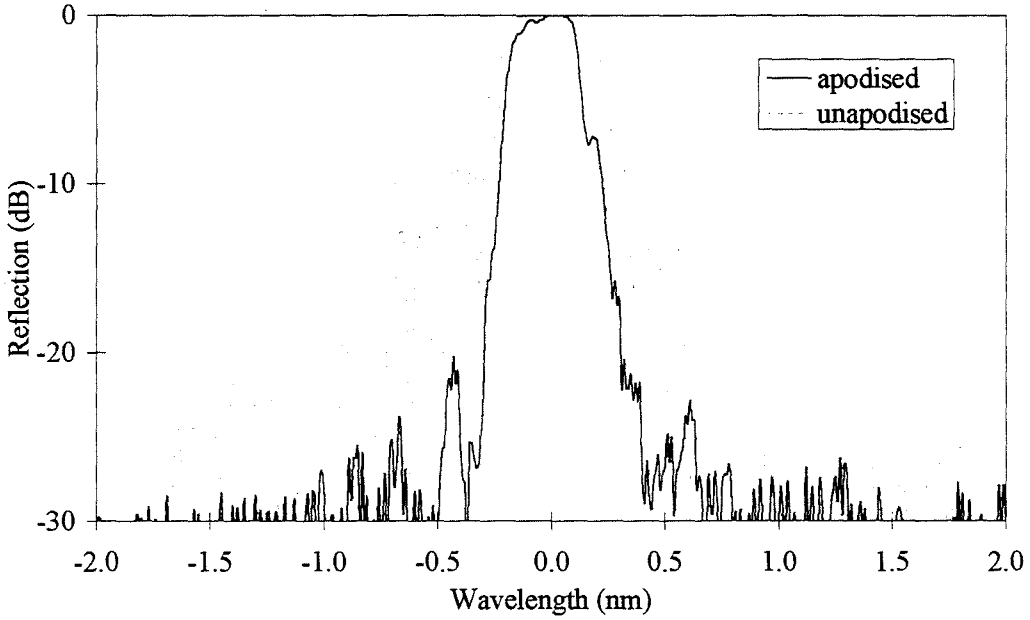

Figure 3.5: Comparison between the spectra of apodised and unapodised gratings. The grating was apodised by dithering the fibre.

3.2.3 Addition of Camera for Monitoring Phasemask-Fibre Alignment

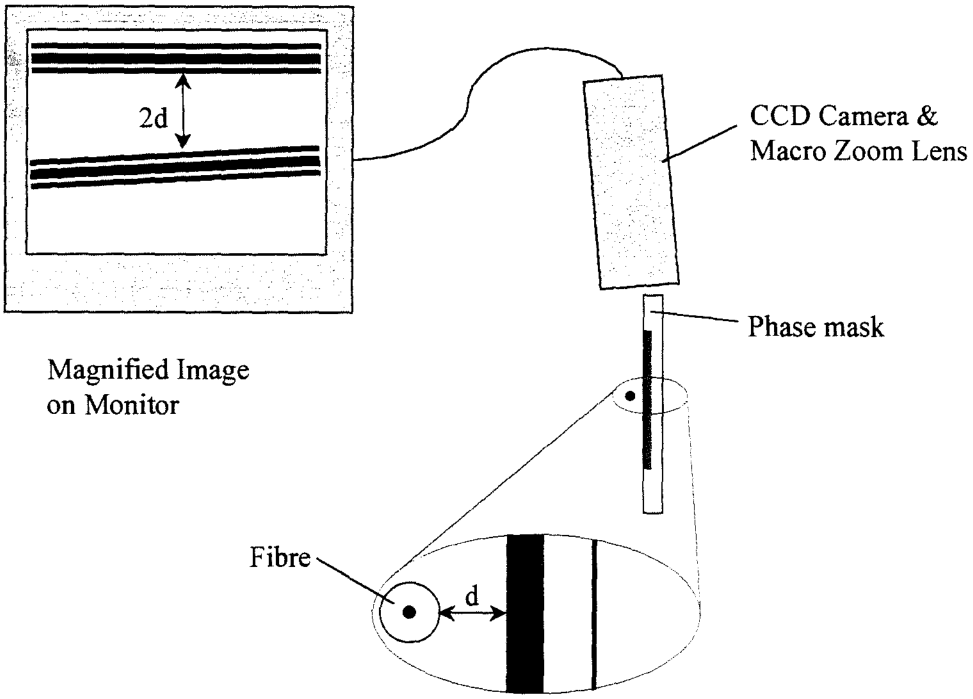

Figure 3.6: Arrangement using a CCD camera for aligning the phasemask and fibre (the shaded area of the phase mask merely indicates the area of the mask in which there are corrugations).

The introduction of phasemasks for grating fabrication increased the repeatability significantly. However, with gratings requiring apodisation for many applications, the tolerances on the quality of grating profiles have decreased significantly. At Aston, many problems with the repeatability and predictability of the grating fabrication process were put down to problems with alignment. In order to investigate the effect of variations in alignment with the fabrication set-up used in this thesis, a CCD camera with macro zoom lens was set up in order to give a magnification of approximately 200 times.

The arrangement of the camera with respect the grating fabrication set-up is shown in Figure 3.6. The camera was mounted in such a way that it could be focussed at a certain magnification using a vertical micrometer movement. The camera could also be translated along the fibre to view the phasemask-fibre separation at various positions along the fibre, to check that the fibre was parallel to the phasemask. The camera was mounted at a slight angle to the vertical, so that the camera viewed both the reflection of the fibre in the phasemask and the fibre itself. The distance between the two fibres on the screen is therefore twice the distance of the fibre from the phasemask.

3.3 Grating Characterisation

3.3.1 Grating Spectrum Characterisation

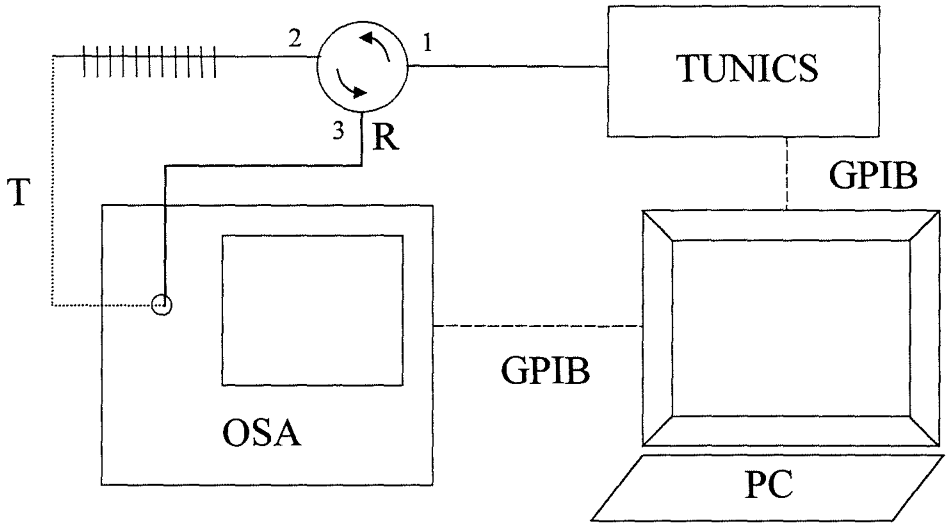

Figure 3.7: Experimental set-up for high dynamic range and high wavelength resolution characterisation of the grating spectra

The equipment required to measure the spectral response of gratings is shown in Figure 3.7. The grating is fusion spliced onto port 2 of a 3 port, 2 stage circulator in order to minimise the return loss and therefore maximise the dynamic range available when measuring a grating in reflection. A Photonetics Tunics tuneable laser (P=0.5mW) with picometer resolution is the input to port 1 of the circulator. For transmission loss measurements, a patch cord is attached between the end of the grating and the HP Optical Spectrum Analyser - OSA (wavelength resolution 0.1nm and sensitivity –80dBm). For reflection spectra measurements, port 3 of the circulator is attached to the OSA. In order to temperature stabilise the gratings, they are sandwiched between two pieces of polystyrene during characterisation, to minimise the effects on the grating spectrum of the fluctuating lab temperature and any air currents.

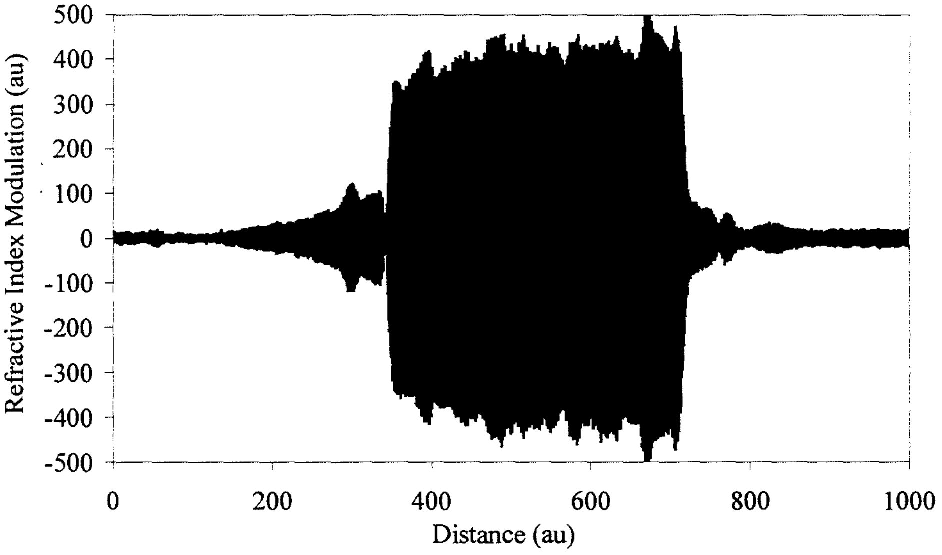

(a)

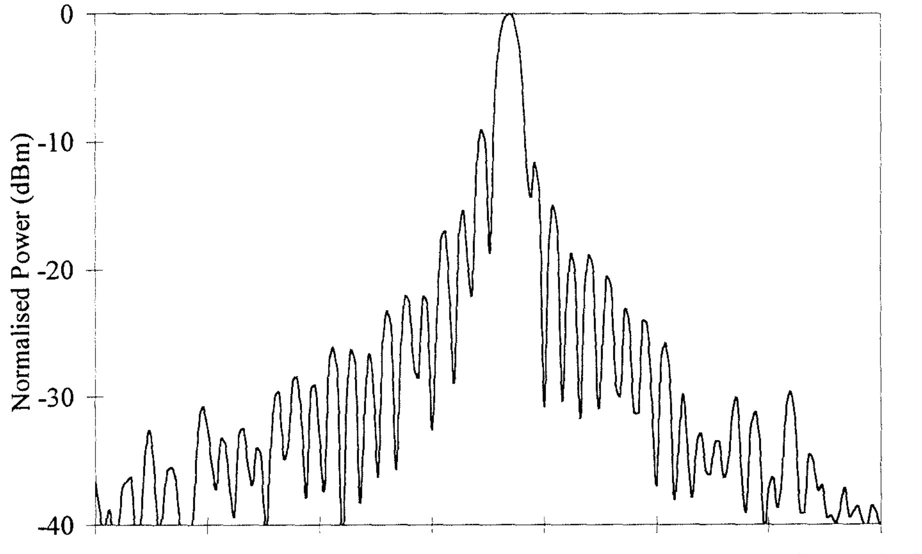

(b)

Figure 3.8: (a) The refractive index profile of an unapodised grating measured using DFTS and (b) the grating reflection profile

Results from another method of characterising gratings are shown in Figure 3.8[4]. The map of the refractive index modulation, as shown in the figure, can be used to calculate the grating spectrum using a fast Fourier transform. The technique is only suitable for weak gratings at present, as the Fourier transform approximation for measurement of the grating spectrum only applies for weak gratings (R<90%). The results shown in Figure 3.8(a) show that the refractive index modulation gradually increases along the length of the grating. This change in refractive index modulation is most likely to be due to a variation in alignment of the fibre with respect to the focus of the scanning laser beam and the phasemask during fabrication. There is quite a lot of noise on the profile, which is most likely to be due to the temporal variation in the power of the laser beam. The asymmetry in the refractive index profile is echoed in the reflectivity profile, shown in Figure 3.8(b), where the sidelobes are not symmetrical about the grating peak.

---

[4] The grating refractive index was measured using discrete Fourier transform spectroscopy by Gordon Flockhart of Heriot-Watt University.

3.3.2 Grating Growth

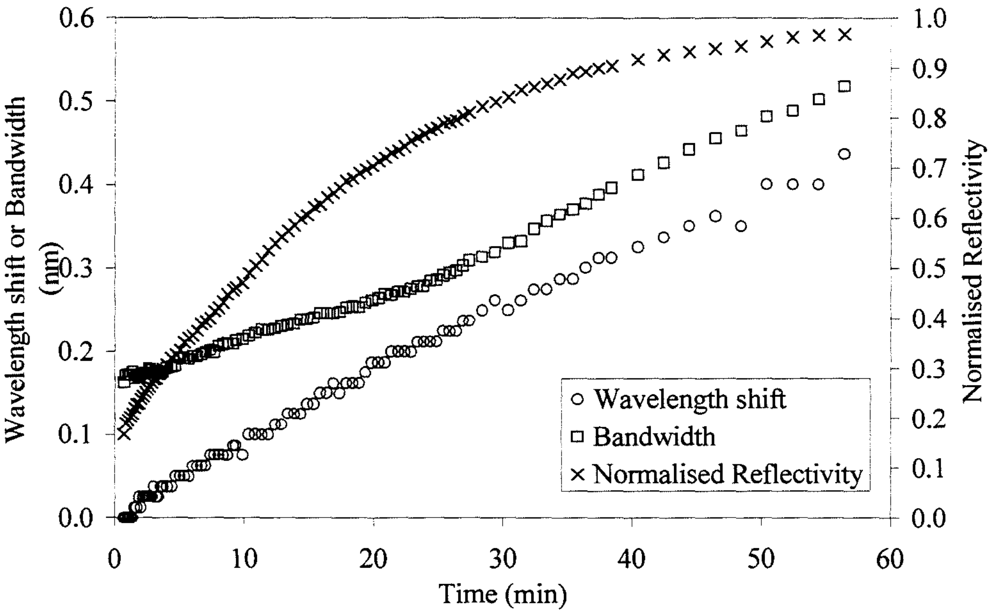

Figure 3.9: Evolution of various grating properties during grating fabrication using a static beam.

Figure 3.9 shows the growth of a grating fabricated using a phasemask and static beam (width ~ 1cm) in hydrogen loaded boron-germania co-doped fibre. The grating spectrum was monitored during fabrication using a broadband Erbium fluorescence source and optical spectrum analyser. The early bandwidth measurements are probably limited by the resolution of the OSA (0.1nm) and would be expected to be narrower than the recorded values. The wavelength and bandwidth of the grating increase as the transmission loss of the grating increases with UV exposure.

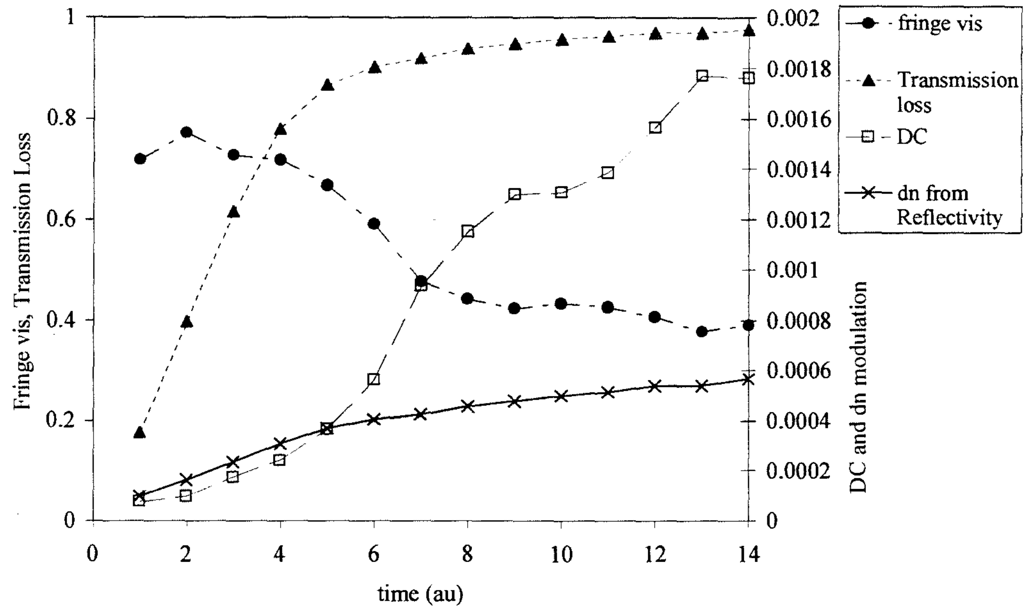

Figure 3.10: The change in various grating properties with exposure time. The distance between the phasemask and the fibre is 13μm.

The change in refractive index and fringe visibility during grating fabrication is shown in Figure 3.10. The grating was fabricated using a static beam of length 2mm. The total refractive index change of the core was calculated from the wavelength shift of the grating during fabrication and the amplitude of the refractive index modulation was calculated from the grating reflectivity. The fringe visibility

$$V = \frac{\Delta n}{n_{UV}},$$

Equation 3-1

where Δn is the amplitude of the refractive index modulation, and n_{UV} is the average UV induced refractive index. The fringe visibility rapidly decreases once the grating transmission begins to saturate. The DC refractive index contribution rapidly increases, meaning that there is not very efficient use of the available photosensitive refractive index when producing the grating. Some of the observed effect could be caused by the inability of the OSA to resolve the bottom of the grating transmission dip. However, this is unlikely to account for much of the observed effect. Physically, this effect could be caused by a stability problem, so that in time the fringes of the grating become less distinct. If this is the case then this factor is less of a concern for the scanning beam technique, as the beam does not stay in one position for very long. The eventual refractive index modulation is only 5.5×10^{-4}, whereas the average UV induced refractive index is 1.75×10^{-3}.

Phasemasks allow a small amount of UV through in the zero diffracted order, as is shown in Figure 3.11. This zero order results in a DC offset for the UV induced refractive index modulation in the fibre core. However, the intensity of light in the zero order of this phasemask, shown in Figure 3.12, which has been specially designed for use with UV at 266nm, is not enough to cause such a large DC offset as observed in Figure 3.10.

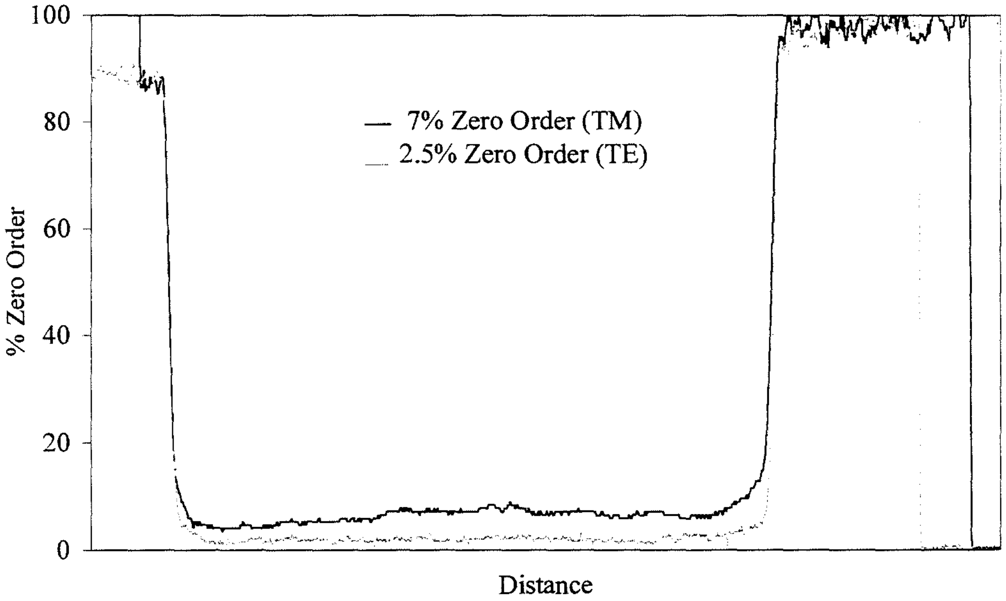

Figure 3.11: Variation of % of intensity in zero order beam for holographic phasemask optimised for use with YAG laser

Figure 3.11 shows how the percentage of light in the zero order of a phasemask varies as the phasemask is scanned between the phasemask and a UV detector. This phasemask was designed for use with a 266nm laser, and was fabricated using holographic lithography techniques. The suppression of the zero diffraction order is better for TE polarised light, than for TM polarised light. The polarisation vectors for the electric field of the incident UV are parallel for TE polarisation, whilst for

TM polarisation the vectors are no longer parallel. The percentage of zero order is taken as a fraction of the total UV transmitted by the phasemask.

Figure 3.12 shows the zero order suppression for a phasemask made for use with 266nm light using electron beam lithographic techniques. The zero order suppression for this mask is not uniform along the length. Factors such as the etch depth of the quartz substrate, and the mark-space ratio of the grating corrugations can affect the amount of zero order which is transmitted by the mask.

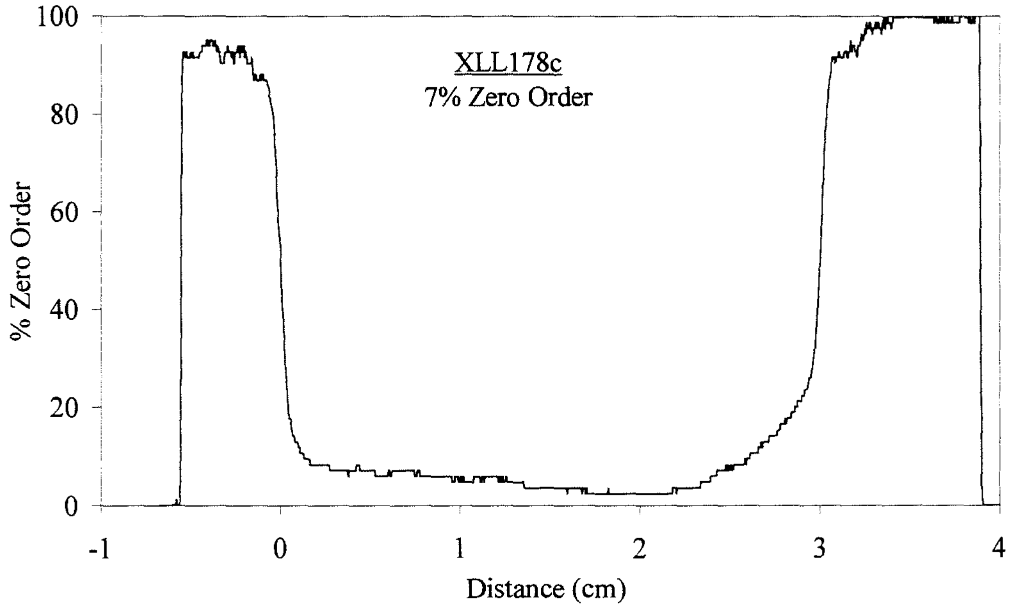

Figure 3.12: Zero order measurement (TE) for an e-beam mask with poor zero order suppression at one end

3.3.3 Type II Gratings

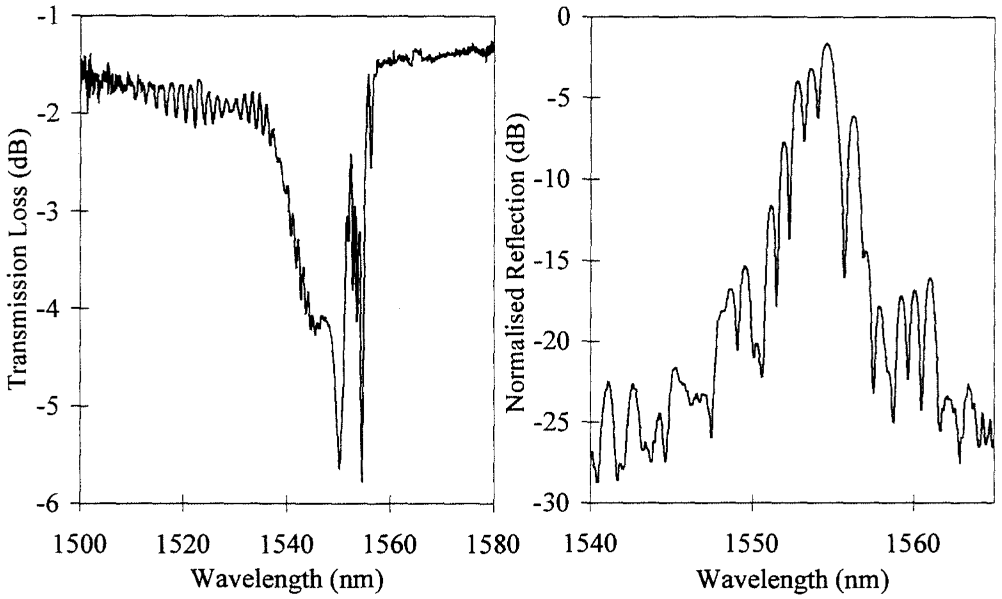

Figure 3.13: The transmission and reflection spectra of a type II grating fabricated using the quadrupled Nd:YAG laser

One of the advantages of the Nd:YAG laser is the high UV power, meaning that it is possible to fabricate type II gratings. Figure 3.13 and Figure 3.14 show spectra of type II gratings. The transmission spectrum displays surprisingly low loss, this is probably due to an effect reported by Malo [169], that in the case of type II gratings fabricated using normal incidence of a phasemask, the period of the grating in the fibre is the same as that of the phasemask. This suggests that the gratings are in fact second order gratings, with the first order gratings at 3000nm. This would explain the relatively low transmission loss, but characteristic spectrum of a type II grating displayed by these gratings.

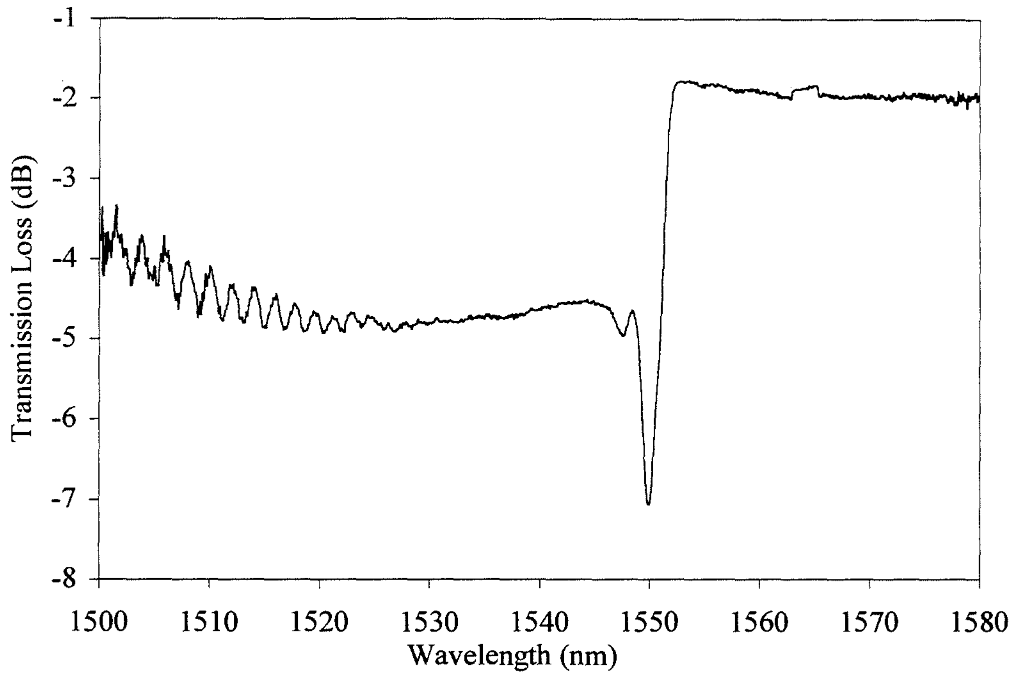

Figure 3.14: Second order Type II grating fabricated using a 100ms exposure.

At the time that the Nd:YAG laser was acquired, there was much interest in the fabrication of type II gratings, with the prospect of writing gratings as the fibre came off the fibre drawing tower. The high power produced by this laser makes it ideal for the production of damage gratings, though the fluence required to fabricate damage gratings using this laser is greater than for many other reports, due to the low absorption of the fibre at 266nm.

3.3.4 Type IIA Gratings

Type IIA gratings have yet to be reported in hydrogen-loaded fibres. However, the growth of gratings was investigated in order to investigate the production of negative index gratings in hydrogen loaded fibre using the quadrupled Nd:YAG laser. Figure 3.15 shows the evolution of a grating in hydrogen-loaded B/Ge co-doped fibre over 30 minutes. The grating length was determined by the beam width, which was 2mm. Figure 3.15 shows the growth and decay of one grating, followed by the subsequent growth of another grating at a lower wavelength than the first. The grating exposure was stopped when there had been no noticeable change in the grating profile for a few minutes.

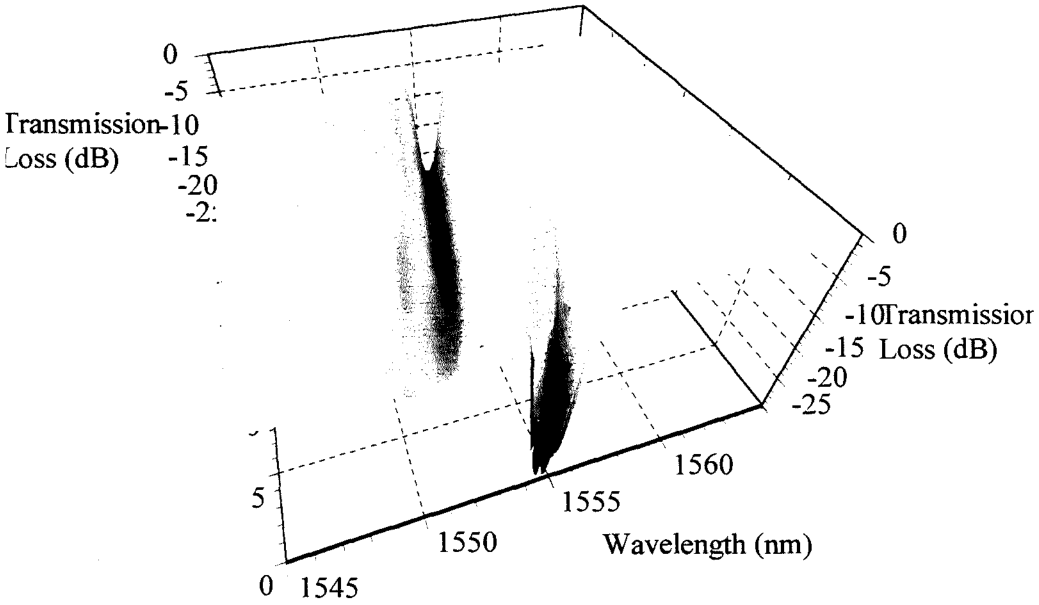

Figure 3.15: Evolution of a Bragg grating over ~30 minutes using a quadrupled Nd:YAG laser.

The reasons for the behaviour of the grating in Figure 3.15 are still not clear, and researchers have yet to agree on the exact mechanisms involved with this type of grating growth. The growth of a second grating at a lower wavelength from the first suggests a 'negative refractive index' or type IIA grating, however, as this grating grows the wavelength shifts to higher wavelengths, so the lower wavelength of the second grating is probably misleading. In 1997, Hübner presented a paper explaining this observed grating growth in terms of fringe visibility [170]. They investigated the effect of the grating source on grating growth. It is unclear whether the grating growth observed here is due to the growth of type IIa gratings or could be explained by Hübner's theory. Further investigation would enable this to be determined.

3.3.5 Effect of Beam Width and Fibre-Phasemask Distance

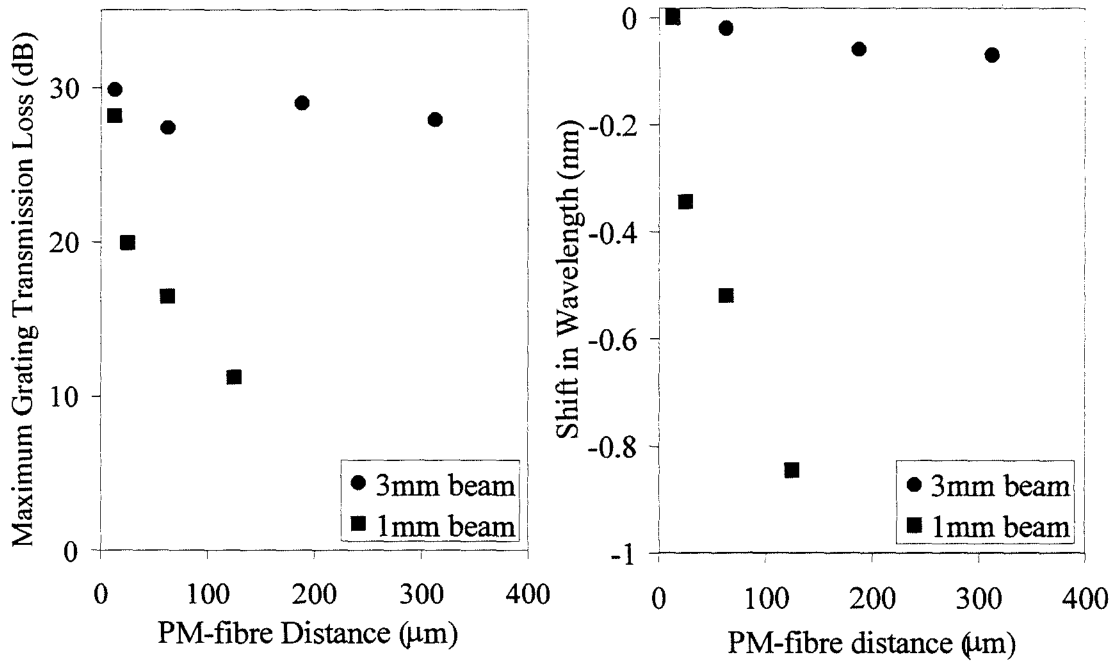

Figure 3.16: The effect of varying the separation of the phasemask and fibre for different beam widths

The dependence of the grating strength on the separation of the phasemask and fibre was investigated for two different beam widths for grating lengths of 5mm. The gratings were fabricated using the scanning phasemask technique described earlier in this chapter. The phasemask was moved in order to adjust the distance from the fibre during the experiments, so that the focussing of the beam with respect to the fibre remained constant throughout all exposures. The results are shown in Figure 3.16 and show that the grating strength is reduced quite significantly as the fibre is positioned further from the fibre for the 1mm beam, but the variation is significantly less for the 3mm beam.

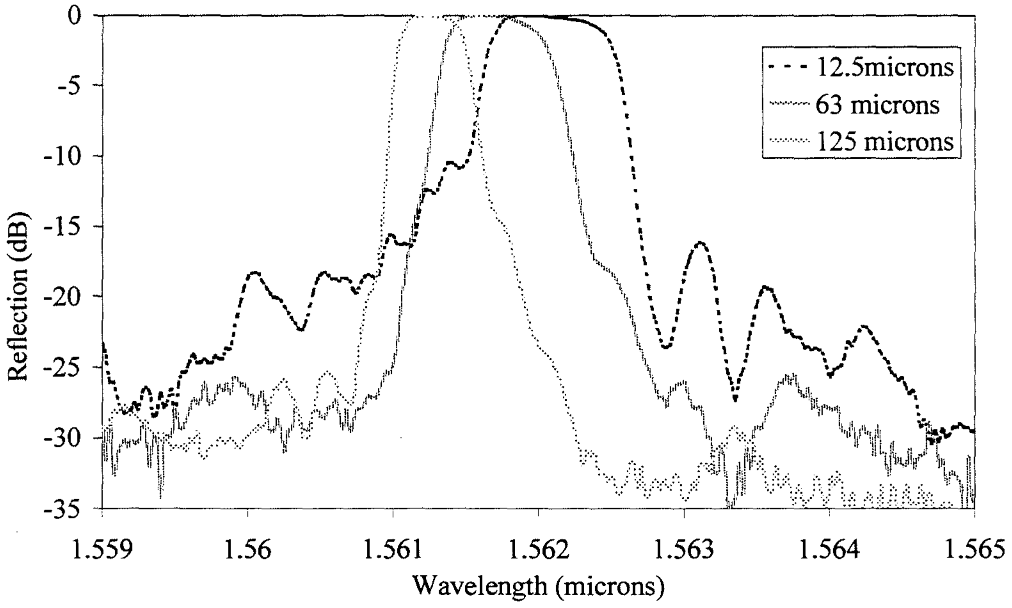

Figure 3.17: Spectra for gratings fabricated with the phasemask at different distances from the fibre

Figure 3.17 shows both the shift to longer wavelengths and the increased bandwidth observed with decreasing separation of the phasemask and fibre during grating fabrication. The gratings were fabricated with a beam width of 1mm, and grating length of 1cm in hydrogen loaded boron-germania co-doped fibre. The increased bandwidth is due to the increase in the refractive index modulation, which is observed for gratings fabricated with smaller phasemask-fibre separation. The shift to longer wavelengths of gratings (also shown in Figure 3.16) irradiated with the fibre close to the phasemask is caused by a higher average refractive index of the fibre core than when the fibre is further from the phasemask.

The reason for the different rates of decrease in the grating transmission loss with fibre-phasemask separation can be explained in part by Figure 3.18. For a smaller beam width the region in which the first diffracted orders overlap extends a shorter distance behind the phasemask than is the case for a larger beam, as is shown in Figure 3.18. For a given beam width, as the distance behind the fibre increases, the width of the overlap region decreases and the DC contribution from the part of the first orders that are not in the overlapping region increases.

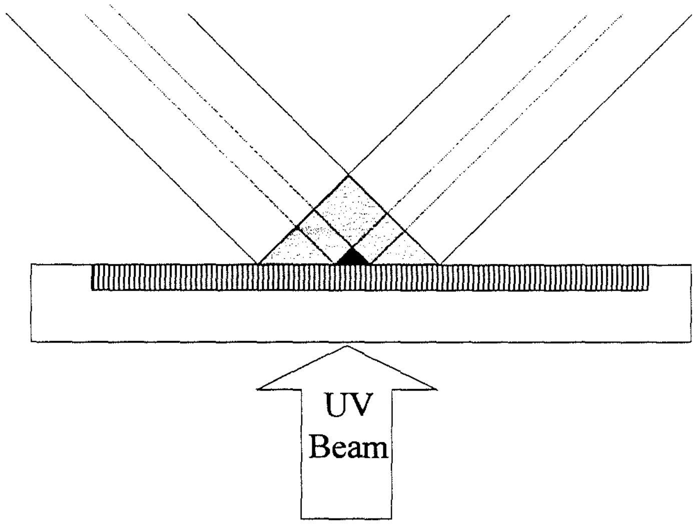

Figure 3.18: A smaller beam width leads to a reduction in the distance behind the phasemask where the interference pattern is formed

Another problem highlighted by the use of the camera to monitor the fibre and phasemask, is that when the fibre is placed very close to the phasemask (<30μm), the fibre bends, as is illustrated in Figure 3.19. The fibre actually sticks to the phasemask if the fibre is not under sufficient tension. The most likely reason for this is static between the phasemask and the fibre. This is quite a serious issue, since if the fibre touches the phasemask during the fabrication of apodised gratings by dithering either the fibre or the phasemask, then the phasemask will be damaged. The solutions seem to be to put sufficient strain on the fibre, and also to make sure that the fibre and phasemask are not too close.

Figure 3.19: Placing the fibre very close to the phasemask can result in a bend in the fibre.

3.3.6 Effect of Phasemask-Fibre Angle

It is not only the distance between the fibre and the phasemask, which can make a difference to the repeatability of the gratings. Both Painchaud *et al*[171] and Othonos and Lee [172] have shown that varying the angle between the phasemask and fibre can be used to vary the Bragg wavelength of the grating. Orthonos and Lee presented a simple expression for the Bragg wavelength,

$$\lambda_B = \lambda_0\sqrt{1+(\tan(\alpha))^2}\,,$$

Equation 3-2

where $\lambda_0 = 2np$, p is the period of the grating in the fibre, and n is the refractive index of the fibre core. This expression is designed to predict the wavelength shift for the case of normal incidence on the phasemask, which is the case here.

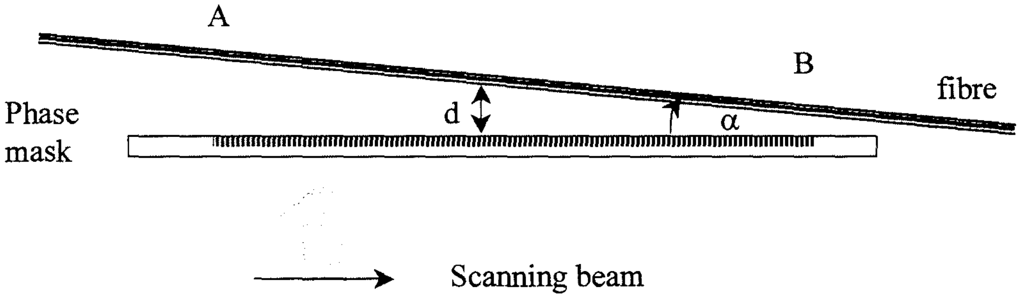

Figure 3.20 : The setup for investigating the effect of fibre angle on grating properties

The fibre at the centre of the grating was maintained at a distance of 200μm from the phasemask for all exposures, in order to try to reduce any effects from varying the distance of the fibre from the phasemask, as discussed earlier on page 78. The gratings were fabricated by the scanning the phasemask with a 3mm beam, the scan length was 5mm. The 3mm beam-width was chosen to try and reduce the sensitivity of the grating strength to the distance of the fibre behind the phasemask. The phasemask angle was controlled by mounting the phasemask on a rotating stage. The angle was calculated by measuring the distance between the phasemask and the fibre at either end of the phasemask, the angle was then derived using trigonometry.

The angle of the beam was adjusted to be at normal incidence to the phasemask. A simple diagram of the fabrication set up for the investigation is shown in Figure 3.20.

Fibre Angle (degrees)	Max. Transmission Loss (dB)	Measured 3dB Bandwidth (nm)	Wavelength (nm)	Predicted Centre Wavelength (nm)
0.00	49.19	0.19	1567.17	1567.17
0.14	48.42	0.21	1567.19	1567.18
0.29	51.10	0.20	1567.20	1567.19
0.46	49.10	0.26	1567.22	1567.22

Table 3.2: Properties of gratings fabricated with different angles between the fibre and phase mask.

The results in Table 3.2 show the wavelength predicted by Equation 3-2, and the agreement between the obtained wavelengths and those predicted is good. Another trend is shown by the data in Table 3.2. As the angle between the phasemask and fibre is increased, so is the bandwidth of the grating peak. The transmission loss of the gratings varies only by ~2dB, and this variation is random, so this cannot be said to be the cause of the broadened bandwidth of the grating peaks. The most likely reason is variation of the average refractive index of the fibre core along the grating. The spectra of 2 gratings fabricated at different fibre angles are shown in Figure 3.21, showing the increased bandwidth.

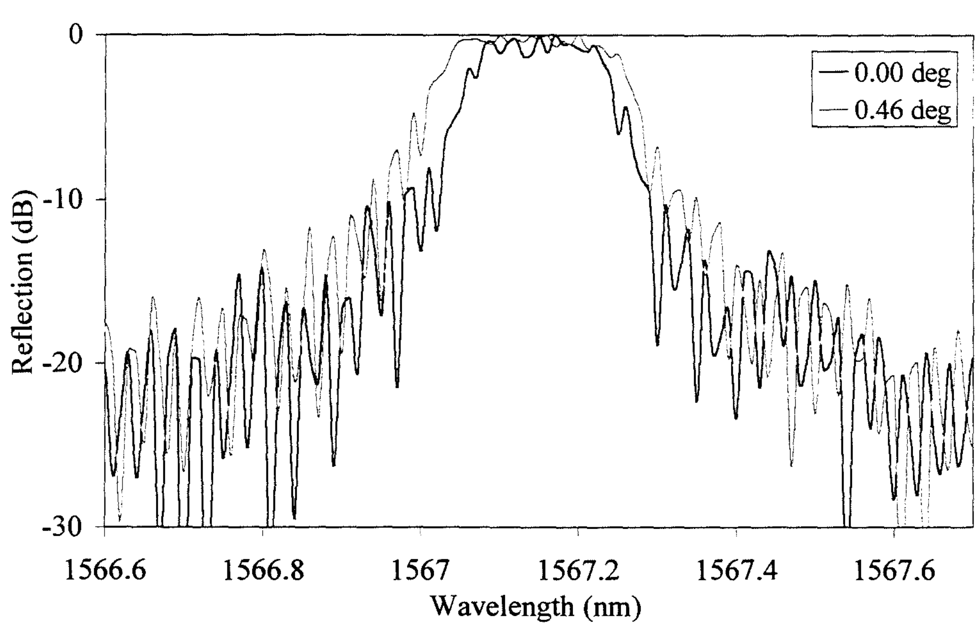

Figure 3.21: Gratings fabricated with the phase mask at different angles to the fibre, showing the resulting chirping of the grating spectrum.

The gratings shown in Figure 3.21 have ripples on the top of the grating peak, which are probably due to the laser power being very unstable at the time of fabrication, and the very strong refractive index modulation of the grating. The gratings were fabricated using a uniform period phasemask and were not apodised.

3.4 Chapter Summary and Discussion

As part of the investigation of the quadrupled Nd:YAG laser, a fabrication utility has been set-up to fabricate type I gratings. Various studies have been made in order to improve the repeatability of gratings and minimise sources of error. Monitoring a grating fabricated using a static beam revealed a low fringe visibility of the grating refractive index modulation. At the beginning of the grating fabrication, the fringe visibility was ~0.78. This fringe visibility decreased with increasing exposure, to 0.4. This result suggests a stability problem for gratings fabricated using a static beam. However, the set-up was designed primarily to fabricate gratings by scanning a phasemask, so the beam does not stay in one position on the fibre for long enough for this to be a significant problem.

Measurements of the zero order in phasemasks used with this fabrication utility have been made for a mask specially designed for use with 266nm exposure. The light intensity of the zero diffracted order of the phasemask was found to vary according whether the light was TE or TM polarised. TE polarisation was found to give a better zero order suppression (97.5%) than TM polarised light (93%). However, the stability and quality of the laser when the frequency doubling crystals are set for TM polarisation is better than for TE polarisation.

A CCD camera with a macro-zoom lens was introduced to monitor the alignment of the fibre and phasemask. Using the camera, the effect of varying the fibre-phasemask distance has been investigated for 1 and 3mm beam widths. The transmission loss of the gratings was found to decrease with increasing separation of the fibre and phasemask. The decrease in transmission loss was much more pronounced for the 1mm beam than for the 3mm beam. This decrease has been attributed to the decrease in the overlap of the first diffraction orders of the phasemask with increasing distance behind the phasemask. However, a wavelength shift to higher wavelengths was observed, for both beam widths, with decreasing fibre-phasemask separation. This wavelength shift suggests that the average refractive index along the grating length is not independent of fibre-phasemask separation, this could be because the photosensitive mechanisms are more efficient at higher fluence. Variation in the angle between the fibre and phasemask was also studied. It was found that when the fibre and phasemask were not parallel, an increase in the Bragg wavelength of the grating was observed, as reported previously by Othonos and Lee [172]. However, this was not the only effect observed. The grating bandwidth was also found to increase with increasing angle between the phasemask and fibre. An angle of 0.46° between the fibre and phasemask resulted in an increase in the Bragg wavelength of 0.5nm and an increase in bandwidth of 0.07nm. The results showing the variation in transmission loss with fibre-phasemask distance suggest that the most likely cause for the increase in the grating bandwidth is a non-uniform average refractive index along the grating length.

There are many other parameters and effects not mentioned so far in this chapter, which may influence grating profiles. Very slight defects in any parameter may cause an increase in the sidelobe levels of a grating (the effect is far more pronounced and undesirable in the case of apodised gratings). Some of the issues of concern include the method employed to strip the acrylate coating from the fibre. Mechanical stripping can introduce cracks in the fibre. The use of chemical stripping techniques improves the quality of the resulting bare fibre, but care must be taken to remove all traces of the coating before exposure to UV, or this may affect the profile. Alignment issues such as changes in the focussing of the laser beam in the fibre core along the grating length will introduce effects such as chirp, caused by an non-uniform average refractive index in the fibre core. Defects in the phase mask, caused by stitch errors in e-beam generated masks, dust, scratches and chemical deposits all degrade the quality of the phase mask and therefore the grating. In addition, properties of the laser may have undesirable effects. The beam divergence may cause a change in focus in the fibre core. The beam intensity profile may cause problems, as without the use of apertures to define the length of apodised gratings using the scanning technique, irregularities in the beam profile may result in non-uniform average refractive index at the edge of the grating (this effect is particularly pronounced in short gratings).

Table 3.3 summarises the advantages and disadvantages of the frequency quadrupled Nd:YAG laser as a source for fabricating fibre Bragg gratings. The use of a quadrupled Nd:YAG laser for the fabrication of Bragg gratings in germanosilicate fibres is limited due to the poor absorption of the fibre at 266nm. Highly photosensitive fibres have to be used in order to fabricate gratings. Fabrication times for good quality Bragg gratings using a quadrupled Nd:YAG are long and therefore this detracts from the ability to run many fabrication utilities using a single laser. The fibres may also require extra pre-fabrication processing (e.g. High pressure hydrogen loading) compared to those required to fabricate the same gratings using an argon (244nm) or excimer laser (248nm). If a quadrupled Nd:YAG is used to run a single fabrication utility it is extremely inefficient, requiring many optics to reduce the power to appropriate levels for grating fabrication. In addition, the high peak pulse powers can lead to damage mechanisms occurring in the fibres, reducing the quality of the gratings. The power stability of the laser can be a problem, unless the flash lamps are relatively new, and there are considerable laser safety issues with a high power frequency quadrupled system.

ADVANTAGES	
High average power (>1W UV)	Many grating fabrication set-ups can be run from one laser
High peak powers (>10MW)	Fabrication of type II (damage) gratings possible
Low cost	Low initial outlay and maintenance costs
DISADVANTAGES	
High peak powers	High power weakens the fibre, and may cause it to break during fabrication.
High Wavelength (266nm)	The grating fabrication process is very inefficient, due to the low absorption of the fibre at 266nm
Poor beam quality	Poor temporal and spatial beam stability results in a noisy spectral profile of gratings

Table 3.3: Advantages and disadvantages of using a frequency quadrupled Nd:YAG laser for grating fabrication

At the time that the quadrupled Nd:YAG was acquired, it was hoped that it might provide a source for the mass-production of fibre Bragg gratings. However, given the time taken to fabricate one grating, and the need for special fibres and the decrease in mechanical strength of gratings fabricated using a pulsed laser source, the quadrupled Nd:YAG laser is not an ideal source for general fabrication of Bragg gratings in fibres. Having said this, it may be a suitable source for applications where the fabrication parameters are not so critical, such as the fabrication of long period gratings. Also, as new fibre coatings are presented which are transparent to UV at ~266nm, the laser may be suitable for grating fabrication through the fibre coating due to the high peak pulse powers.

4 GRATING APODISATION STUDY

4.1 Introduction

Advances in fibre grating technology in recent years have meant that gratings are increasingly being considered as viable alternatives to existing device technologies; this is particularly true in the fast moving field of telecommunications. Research into WDM networks has lead to a heightened interest in the use of fibre Bragg gratings as filters.

The reflection spectrum of a standard uniform period Bragg grating exhibits sidelobes either side of the grating peak. These sidelobes are highly undesirable in many applications, as they result in crosstalk between different channels and an increase in the general noise level in a system. Apodisation minimises these sidelobes by reducing the refractive index modulation at the ends of the grating. A large proportion of the grating exposure length is taken up in apodising the grating, meaning that the effective length of the grating is a fraction of the total exposure length. It is fairly straightforward to fabricate apodised gratings with the desired spectral characteristics for a particular application when there is no maximum length constraint imposed on the grating exposure. However, in practise there are often packaging restrictions imposed on the grating length, meaning that the grating design is not trivial.

To date, most of the work published on apodisation has been on fabrication methods, or presentation of a chosen design for a particular device [173,174,175,176,177,178]. A theoretical comparison of apodisation profiles for chirped dispersion compensating gratings has been published [176], but as yet none have compared the effects of apodisation functions for uniform period gratings. Many in industry seem to have settled recently on a Gaussian apodisation function. However, the results in this chapter indicate that this is not always the most appropriate function, particularly when a maximum grating length is imposed.

This chapter represents the first in-depth experimental and theoretical comparison of apodisation functions for uniform period gratings. In addition, a new flexible method of apodising gratings is presented. The gratings in this study are subject to a length limitation, which is the case in many industrial applications, where there is a maximum length imposed on the grating due to packaging restrictions. Using the new versatile fabrication method, the spectral characteristics are investigated for 3 different apodisation functions for gratings of fabrication length 5mm. The functions are 3 very different shapes, chosen to provide an insight into the effect of different characteristics of the profile shape on the grating properties. The function width or roll-off factor of each function was varied as appropriate. Two applications of apodised gratings are presented at the end of the chapter. An application to TDM to WDM switching is demonstrated, and a fast tuneable filter for use in WDM systems.

The aim of the chapter is to make the reader aware that there are many trade-offs involved in the design of length limited gratings, to highlight the advantages and disadvantages of each of the apodisation functions, and demonstrate two applications of apodised gratings in WDM devices.

4.2 Background

As mentioned in the introduction to this chapter, the practical limitations confronted by this study are derived from packaging constraints. Telecommunications is not the only application requiring optimised gratings of short length. Fibre grating sensing systems often require very short gratings in order to make quasi-point strain measurements. At the same time, a high dynamic range is required, meaning that the spectral quality of the grating must be high, with as narrow as possible grating bandwidth and significantly reduced sidelobes. This requires that the grating is apodised.

4.2.1 Apodisation Methods

REF:	METHOD:	PROFILE:	ADVANTAGES:	LIMITATIONS:
[179]	Using profile of static beam	Gaussian (depends on profile of beam)	Simple	Fabry-Perot resonances at short λ in grating peak
[180]	Dual scan refractive index profiling	Any profile	Uses any phasemask, no dithering required	Fairly involved, have to remove phasemask before second compensating scan
[181]	Moving fibre/phasemask technique	Any profile	Flexible	Repeatability??
[182], [183]	Apodised (variable diffraction efficiency) phasemask	Any profile	Repeatable	Only one profile per mask – special mask required
[184]	Moiré phasemask	Raised cosine	Repeatable	Only raised cosine profile
[185]	Continuous stretching and releasing of fibre	Raised cosine (or truncated)	Fairly simple	Only one profile, need to make sure exposure is in middle of length of fibre
[186], [187], [188], [189]	Others presented			

Table 4.1: Summary of reported apodisation techniques

Many apodisation methods have been presented, and they are summarised in Table 4.1 chronologically. Originally, gratings were intrinsically apodised by the intensity profile of a static UV beam [179]. However, this results in a non-uniform average refractive index along the grating length, meaning that while the refractive index modulation decreases at the grating edges, the grating edges reflect light at a shorter wavelength from that of the centre of the grating due to the different refractive index. The low wavelength at both ends of the grating means that a resonator is formed, resulting in Fabry-Perot resonances on the short wavelength side of the grating peak. As phasemask scanning was introduced for making gratings, refractive index profiling was developed [180]. The technique involved controlling the UV dose along the length of the grating by varying the scan speed of the beam across the phasemask. In order to overcome the Fabry-Perot fringes, a second scan without the phasemask was required to ensure that the average refractive index remained constant along the grating length. This method proved flexible, but has largely been superseded by simpler techniques. Cole *et al* presented a novel technique providing excellent flexibility [181]. The method demonstrated in Cole's paper involved the dithering of the fibre in order to vary the refractive index modulation along the grating. Since the scan speed for this method is constant along the grating length, the refractive index remains constant. Methods aimed at mass-production of gratings have also been presented by several groups, all using apodised phasemasks [182,183,184]. Only one apodisation profile is possible with an apodised mask, but mass production is simple. However, for commercial situations, the emphasis now seems to be on flexibility and fabrication that does not require specialist phasemasks. Other methods presented include the continuous stretching and releasing of the fibre to create a Moiré grating effect [185], and using carefully profiled apertures in order to control the UV doses with and without a phasemask [189].

4.3 Theoretical Modelling of Apodised Gratings

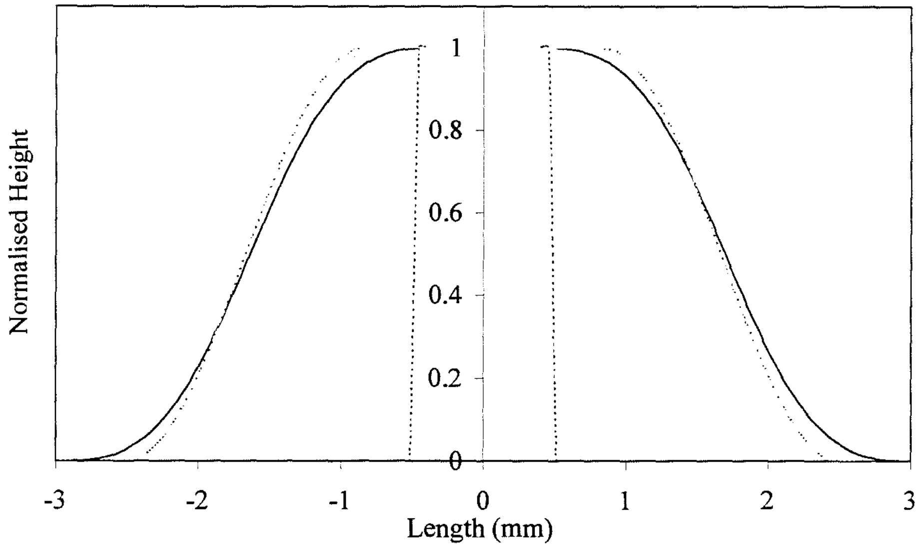

Figure 4.1: The effect of 1mm beam width on the apodisation profile of 5mm grating: --- beam profile, programmed apodisation profile, —— resulting apodisation profile for grating.

The theoretical spectral response for each of the gratings was calculated using integration of the Ricatti equation [13]. The function describing the variation of the coupling constant, κ, along the grating length was calculated by convolving the function generated due to the dithering of the phasemask with the beam profile so that

$$\kappa(z) = \kappa(A(z) * B(z)),$$

Equation 4-1

where κ is the maximum coupling constant (maximum at the centre of the grating), $A(z)$ is the apodisation function, and $B(z)$ describes the beam profile. Figure 4.1 shows a modelled raised cosine envelope (α=0.4). The finite beam width has the effect of increasing the width of the apodisation profile (and the length of the grating) and decreasing the width of the central flat region of the profile, which is shown in Figure 4.1. For this reason, in order to obtain an apodisation function as close as possible to that described by *A(z)*, the beam width needs to be as small as possible.

The effect of the beam width on the grating spectrum is shown in Figure 4.2. The comparisons are shown for a 5mm long grating with Gaussian apodisation (FWHM 3.3mm).

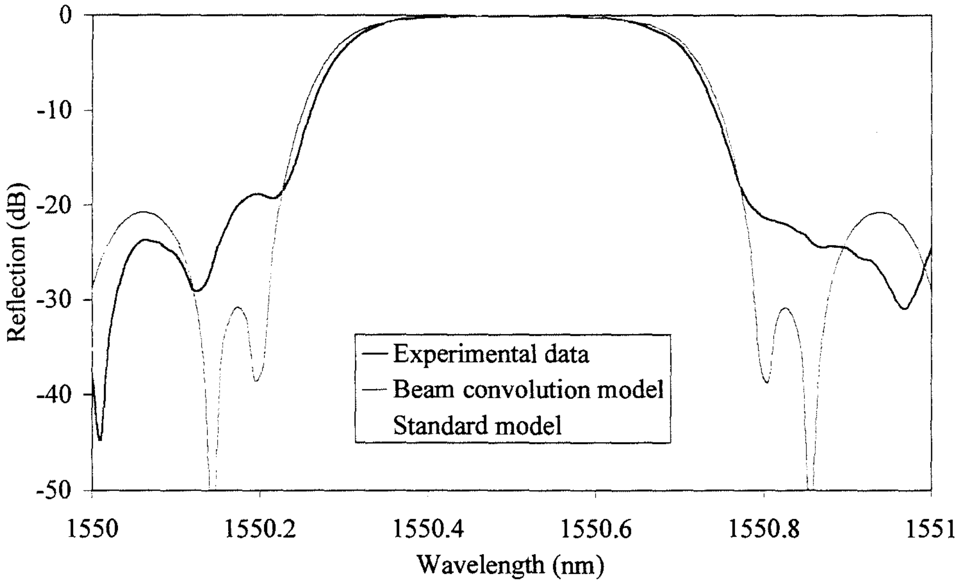

Figure 4.2: The effect of the beam convolution model on the modelled grating spectrum

4.3.1 Apodisation Profiles

Three different profiles were investigated in this study: raised cosine, truncated cosine and Gaussian. Each profile was normalised to give unity height and width (centred on the origin).

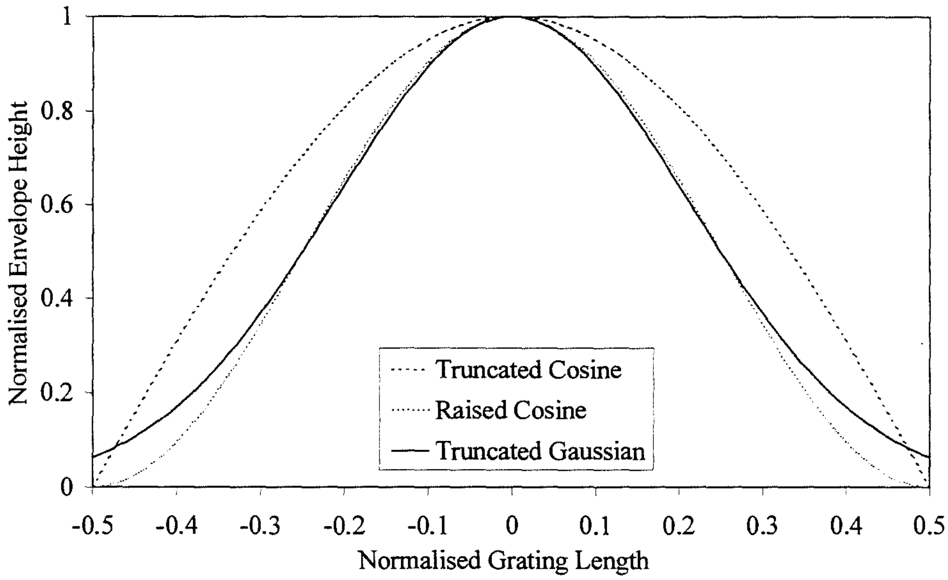

Figure 4.3: Comparison between the 3 profiles considered: Raised Cosine (a=1), Gaussian (FWHM 2.5mm), Truncated Cosine (FW 5mm)

The basic shapes of the three different profiles considered in this study are compared in Figure 4.3. Each profile has a different characteristic shape. Both the raised cosine and truncated Gaussian profiles fall off fairly rapidly from the centre of the grating. However, whilst the raised cosine decreases to zero at the grating edges, the Gaussian profile flattens off due to the infinite wings of a Gaussian function. The truncated cosine profile reduces to zero at the edges, but rises rapidly towards the centre of the grating in a more domed or circular shape than the other 2 functions considered. Therefore when this function is truncated, the envelope height at the edges rises rapidly with increasing function width.

The investigation compares the spectra of gratings apodised with these 3 different profile shapes. The effects of the function shape and width on the sidelobe suppression, peak shape, bandwidth and interchannel crosstalk are considered.

Truncated Gaussian Profile

$$y = \exp\left\{-\left(2x\sqrt{\ln(2)}\right)^2\right\}$$

Equation 4-2

The Gaussian function used in this investigation is shown in Equation 4-2, which yields a function with unity FWHM and height. The absolute width of a Gaussian function is infinite and so this function is always truncated when used to apodise gratings. The width of this function is defined in this study as the FWHM.

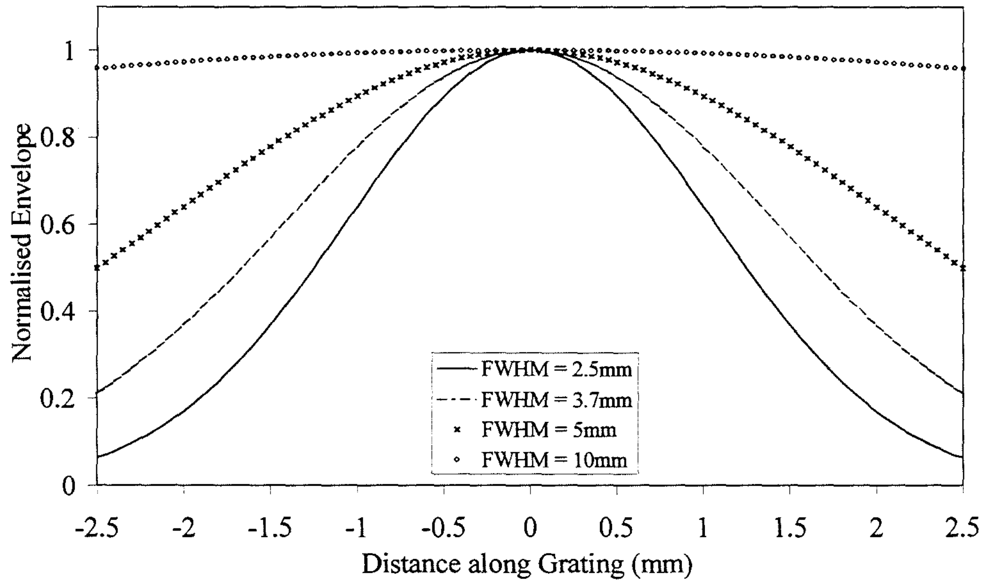

Figure 4.4: Normalised Gaussian apodisation profiles with varying function widths between 2.5 and 10mm.

Figure 4.4 shows the theoretical refractive index profile of Gaussian apodised gratings of length 5mm, with FWHM widths of between 2.5mm and 10mm, the range under investigation. The narrowest function shown here falls off steeply from the grating centre and flattens towards the edges, giving a shorter effective grating length than for wider functions. The widest function yields an almost flat profile, with very little decrease in height at the grating edge. As the function width decreases, so does the effective grating length.

Truncated Cosine Profile

$$y = \cos\{\pi |x|\} \qquad |x| < 0.5$$

$$y = 0 \qquad |x| \geq 0.5$$

Equation 4-3

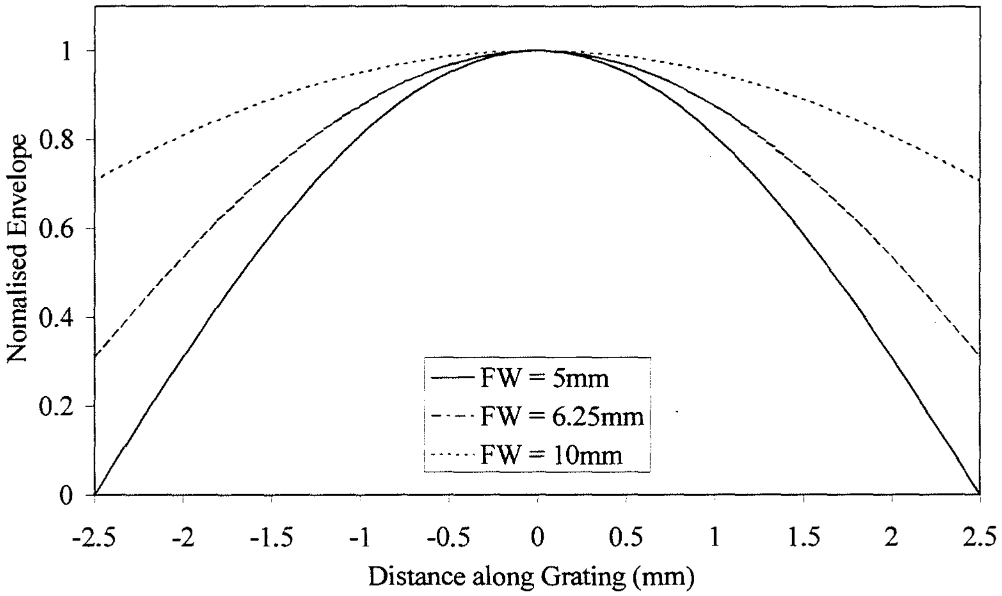

Figure 4.5: Normalised truncated cosine apodisation profiles

The truncated cosine profile is described by Equation 4-3. The function has a domed shape, as is shown in Figure 4.5, and in this case the function width is described by the full width where the function decreases to zero. The broadest function considered here decreases more at the edges of the grating than in the case of the Gaussian profile.

Raised Cosine Profile

$$y = 0.5\left[1 - \sin\left\{\frac{\pi|x|(1+\alpha)}{-\alpha}\right\}\right] \qquad \frac{1-\alpha}{2(1+\alpha)} \le |x| < 0.5$$

$$y=1 \qquad |x| < \frac{1-\alpha}{2(1+\alpha)}$$

$$y=0 \qquad |x| \ge 0.5$$

Equation 4-4

The raised cosine profile is different from the other two profiles considered previously. Equation 4-4 describes the function.

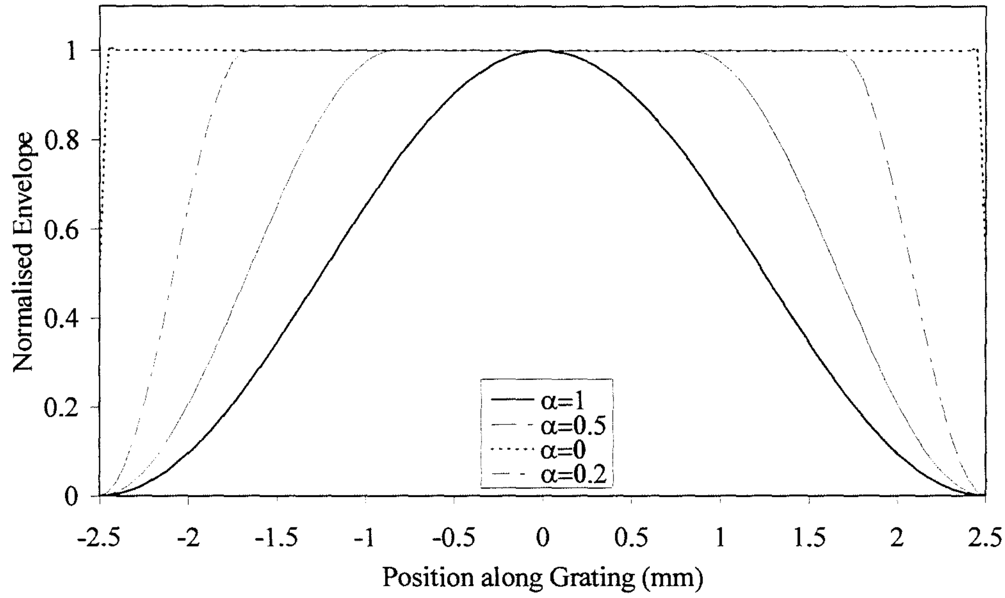

Figure 4.6: Normalised raised cosine apodisation profiles with varying roll-off factors, α.

The first line of the equation describes the roll-off at the edges of the function. Figure 4.6 illustrates the variation of function shape with roll of factor, α. The width of the flat section at the grating centre decreases as the roll of factor,α, decreases from 1 to 0. A roll off factor of 0 results in a top hat function whilst a value of 1 yields a pure raised cosine envelope. This profile has not been truncated in the study, and therefore always decreases to zero at the grating edges.

4.4 Fabrication of Apodised Gratings

Apodisation Technique

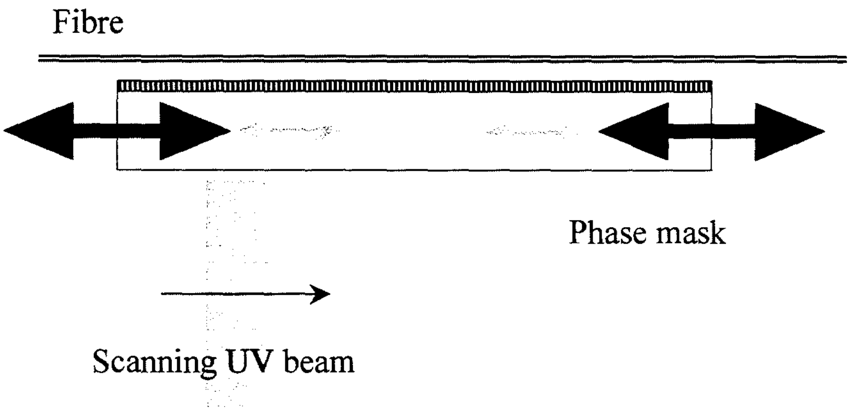

Figure 4.7: The gratings are apodised by dithering the phasemask. The dither is large at the grating edges, decreasing to zero at the centre

A schematic of the technique adopted for apodising the gratings is shown in Figure 4.7; it is simple yet flexible. The phasemask is dithered as the beam is scanned across the phasemask, with the amplitude of the dither being zero at the centre of the grating and maximum at the grating edges. The phasemask is mounted on a piezo translator and is dithered from side to side as the beam scans across, allowing apodisation of gratings being written in pre-assembled devices, such as Mach-Zehnder interferometers. The phasemask is dithered using a triangle wave generated by a function generator. The peak to peak amplitude of the triangle wave piezo translation is controlled by computer and is equal to half the phasemask period at the grating edges decreasing to zero at the centre of the grating.

The refractive index profile of the grating can be represented by:

$$A(z)F(z) = \frac{\Lambda}{\pi}\left[\cos\left(\frac{2\pi z}{\Lambda}\right)\cos\left(\frac{2\pi a(z)}{\Lambda}\right)\right]$$

Equation 4-5

where *A(z)* is the apodisation envelope, *F(z)* describes the UV fringes, Λ is the grating period, *z* is the distance along the fibre axis and *a(z)* is the piezo oscillation amplitude (i.e. the distance that each fringe has be dithered from side to side).

$$F(z) = \cos\left(\frac{2\pi z}{\Lambda}\right)$$

Equation 4-6

describes the fringes generated by the phasemask, and so the piezo amplitude as a function of distance along the phasemask may be calculated for each required profile as:

$$a(z) = \frac{\Lambda}{2\pi}\cos^{-1}\left(\frac{\pi}{\Lambda}A(z)\right).$$

Equation 4-7

4.4.1 Experimental Procedure

Throughout this study, type I Bragg gratings were fabricated with a length of 5mm. The gratings were fabricated in boron-germania codoped fibre which had been hydrogen loaded for at least 2 weeks prior to exposure at room temperature and a pressure of 150 Bar. The laser used was a frequency doubled argon ion laser, wavelength 244nm. A telescope arrangement was used in order to produce a well collimated beam of width ~0.8mm. The gratings were fabricated by scanning the beam along the fibre and the phasemask. As far as possible the experimental arrangements were kept the same for each grating exposure. The same portion of the phasemask was used in order to keep the stitch errors present in the gratings as consistent as possible. In order to maintain a grating reflectivity of ~12dB for all the gratings, the grating coupling constant, κ, had to be increased for gratings with shorter effective lengths, which meant decreasing the scan speed. A well apodised grating requires a slower scan speed than an unapodised grating, as the peak value of the coupling coefficient has to be higher for a given grating reflectivity. The range of reflectivities obtained for the fabricated gratings was quite large (±2dB), as this grating fabrication utility did not include a camera for monitoring the distance between the phasemask and fibre.

4.4.2 Grating Characterisation

Spectral Characterisation

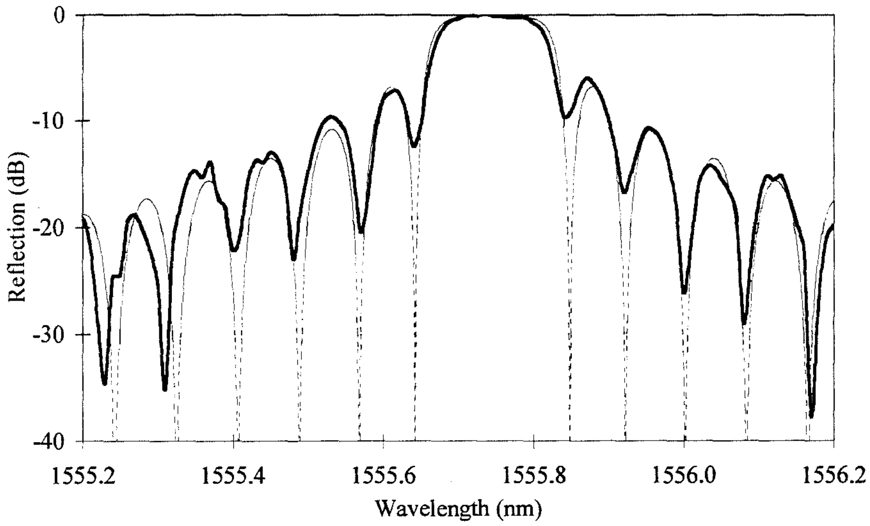

Figure 4.8: An unapodised grating viewed in reflection. The grating sidelobes are far more visible when the reflected power is measured in decibels

Following exposure, the gratings were heated in an oven for ~18 hours in order to remove the hydrogen from the fibre. The gratings were then measured using the technique described in Chapter 3. The most crucial measurements for this investigation were the reflection spectra of the gratings, as the grating sidelobes are most visible in reflection. This is illustrated in Figure 4.8, which shows the experimental and modelled spectra of an unapodised grating. The laser was stepped through wavelengths at a resolution of 0.01nm or less for the reflection measurements. The power level of the laser peak was recorded for each laser wavelength.

Refractive Index Characterisation

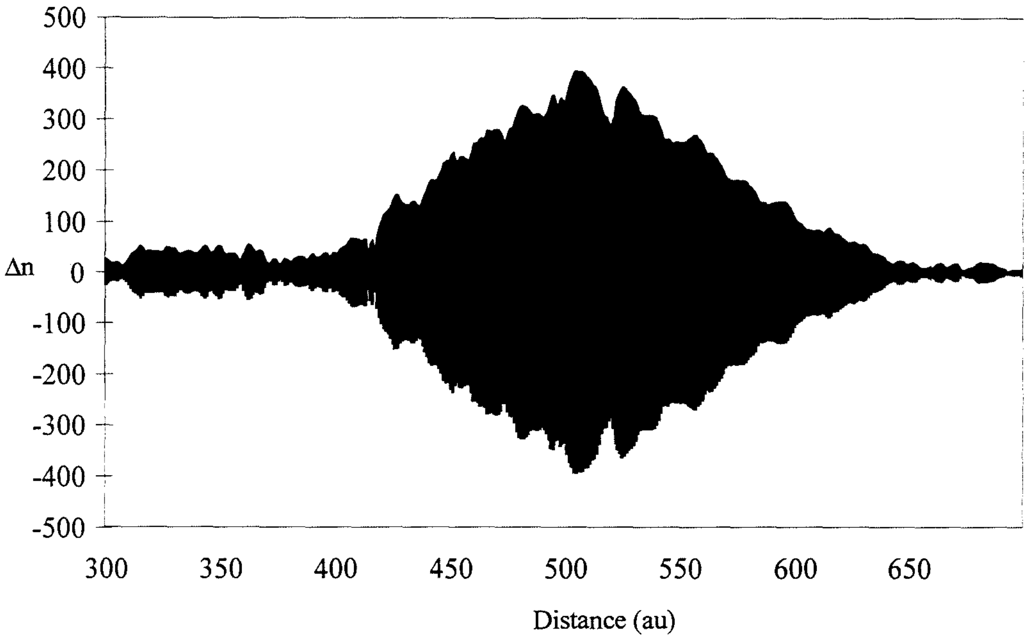

Figure 4.9: The refractive index profile of a Raised Cosine apodised grating measured using discrete Fourier transform spectroscopy

Gratings may also be characterised by examining the grating structure itself. The refractive index profile of an apodised grating is shown in Figure 4.9. The measurements were performed using dispersive Fourier transform spectroscopy (DFTS)[5]. This grating was fabricated using the quadrupled Nd:YAG laser and shows quite significant profile noise, which leads to increased sidelobe levels and an imperfect grating spectral response [190]. The most likely cause of this noise is the temporal power instability of the laser beam. The asymmetry of the profile is probably caused by misalignment of the fibre and phasemask during fabrication. It

---

[5] Measurements performed by Gordon Flockhart of Heriot-Watt University. For more information on DFTS see Appendix 8.1

was not possible to characterise all the gratings in this study using this method. However, it illustrates the refractive index modulation of the grating structure well.

4.5 Experimental Results

Truncated Gaussian

Figure 4.10 shows the spectra of 2 gratings apodised with truncated Gaussian profiles. The profile widths (FWHM) are 10mm and 3.3mm respectively. The theoretical profiles were calculated as described on page 92. The broader of the 2 apodisation functions used in Figure 4.10 leads to more pronounced sidelobes than the 3.3mm width profile. The height of the Gaussian function at the grating edge for the broader function width is 0.2. The deviation of the sidelobe shape from that predicted by modelling is most likely to be due to phasemask stitching errors, or other phase mask related effects.

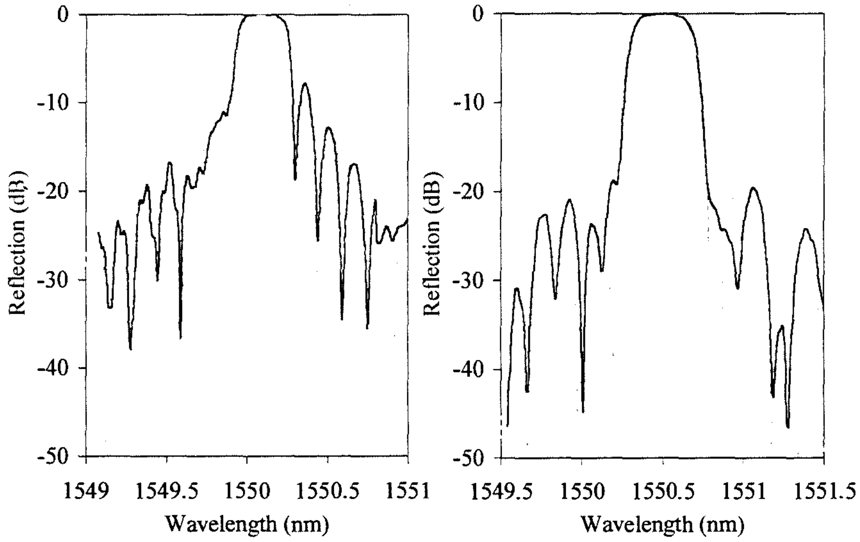

Figure 4.10: Experimental (solid line) and theoretical profiles(dotted line) of Gaussian apodised gratings, length 5mm. Left: Gaussian FWHM 10mm. Right: Gaussian FWHM 3.3mm

Gratings were fabricated with a variety of function widths, varying from 2.5mm to 10mm. Figure 4.11 shows the variation of sidelobe suppression with grating bandwidth as the function width changes. The sidelobe suppression was calculated by measuring the separation in dBs of the highest sidelobe from the maximum of the grating peak. The theoretical values were calculated by modelling the spectra of gratings with varying apodisation function widths, with a grating reflectivity of 14.11dB, which is the average value for the fabricated gratings. The agreement between the experimental and theoretical values is fair. The error bars show the deviations in bandwidth and sidelobe suppression caused by the average variation in reflectivity from the mean value. The theoretical bandwidths and sidelobe suppression are generally lower than the experimental values. This is not unexpected, as any deviations from a 'perfect' grating tend to broaden the bandwidth and decrease the sidelobe suppression. The experimental sidelobe suppression is limited by the stitching errors on the phasemask and other sources of errors, such as dirt on the phasemask, irregularities in the fibre properties and a spatially uneven beam profile.

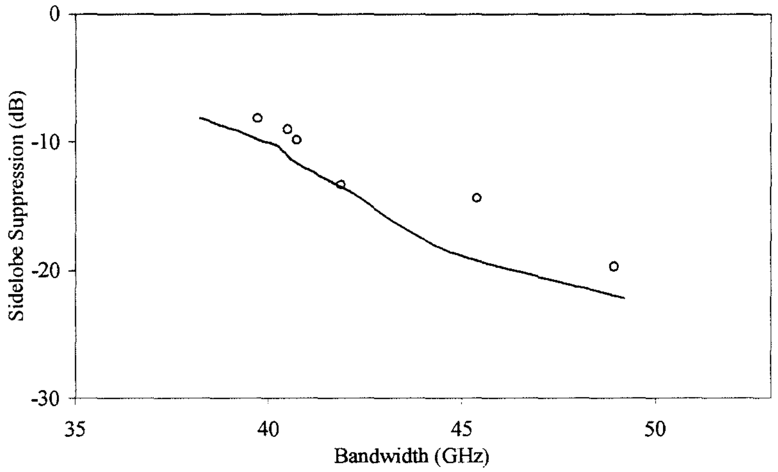

Figure 4.11: Comparison between theoretical (line) and experimental (o) variation of sidelobe suppression with grating bandwidth for truncated Gaussian apodisation functions.

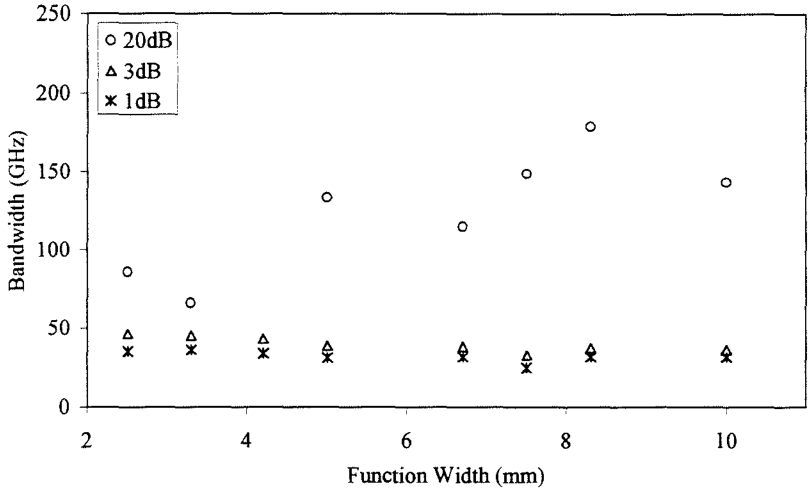

Figure 4.12: Variation of 20, 3, and 1dB grating bandwidths with function width for truncated gaussian apodisation function

For WDM applications, the ideal peak shape would be one with equal 1, 3 and 20dB bandwidths, meaning that the peak was square and had a very flat top. Figure 4.12 shows the variation in these 3 bandwidth figures with truncated Gaussian apodisation function width. The 20dB bandwidth is much wider than the 1 and 3dB values because for most values of the function width, the sidelobe suppression is less than 20dB with respect to the grating peak. The widest function width here can be seen to have the narrowest bandwidth and a very square peak top. As the function width decreases and the sidelobe suppression increases, the 20dB bandwidth decreases and converges on the values for the 1 and 3dB bandwidths. However, as the 20dB bandwidth decreases, the separation of the 1 and 3dB bandwidths increases, indicating that the peak shape is becoming less square and the sides of the peak are not as steep as for less apodised gratings.

Truncated Cosine

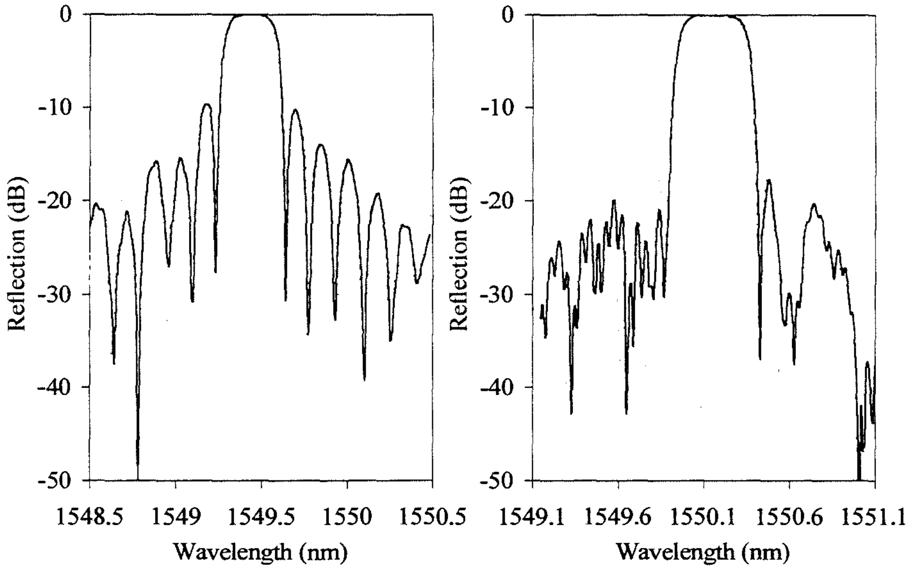

Figure 4.13: Experimental (solid line) and theoretical profiles (dotted line) of truncated cosine apodised gratings, length 5mm. Left: Truncated cosine FW 10mm. Right: Truncated cosine FW 5.6mm

Figure 4.13 shows 2 gratings apodised with a truncated cosine profile with function widths of 10 and 5.6mm respectively. The broadening of the grating peak caused by a narrower apodisation function is well illustrated, as is the fine structure below –20dB caused by stitching errors and other imperfections.

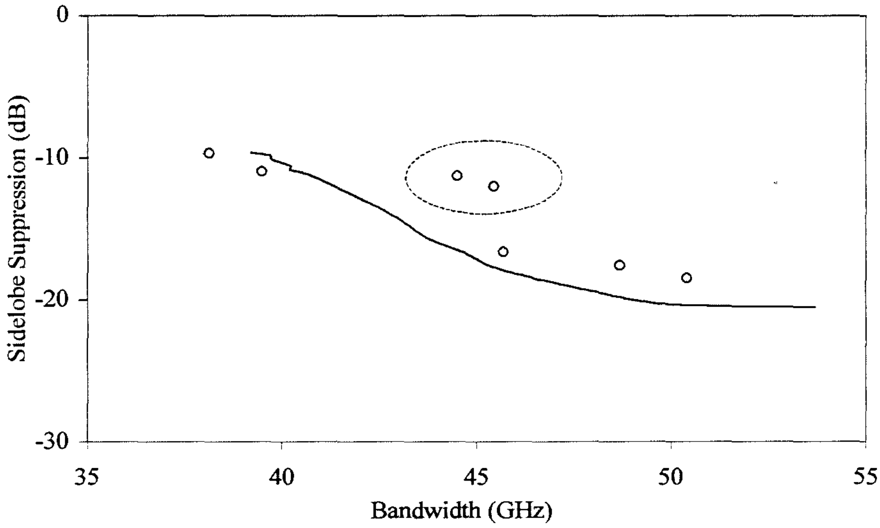

Figure 4.14: Comparison between theoretical (line) and experimental (o) variation of sidelobe suppression with grating bandwidth for truncated cosine apodisation functions.

Figure 4.14 compares the experimental and theoretical results for the truncated cosine profile as the function width is varied from 5mm to 10mm. Again, the error bars illustrate the variations caused by the range of grating reflectivities. The two points which are ringed are both gratings at >15dB reflectivity, stronger than the average value of 13.98 for this data set. This explains the increased bandwidth and reduced sidelobe suppression when compared with the theoretical values. The trend here is similar to that for the Gaussian profile, though both the experimental and theoretical sidelobe suppression levels off at a minimum value of –20dB due to the steep sides of the profile at the grating edges.

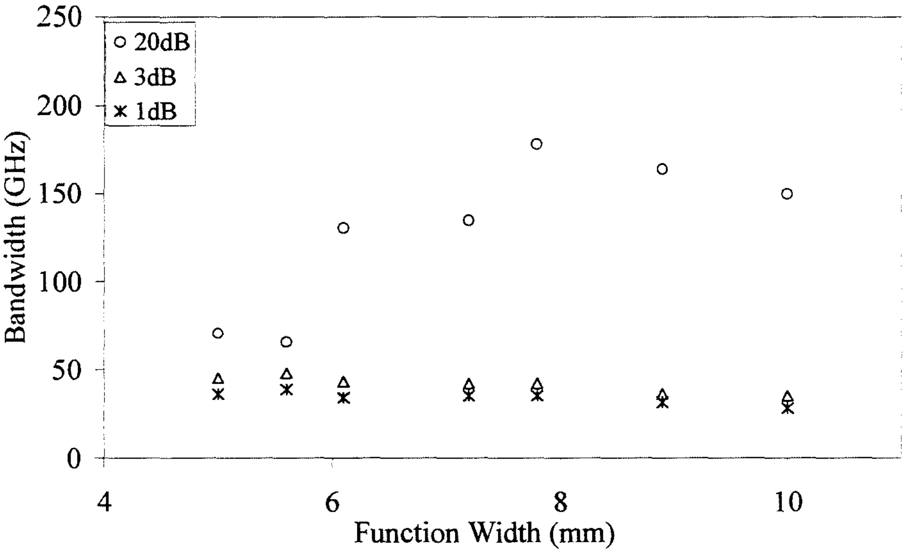

Figure 4.15: Variation of 20, 3, and 1dB grating bandwidths with function width for truncated cosine apodisation function

Figure 4.15 shows that the effect of the truncated cosine profile on the peak shape is very similar to that of the Gaussian profile, with the top of the peak becoming more square as the 20dB bandwidth decreases.

Raised Cosine

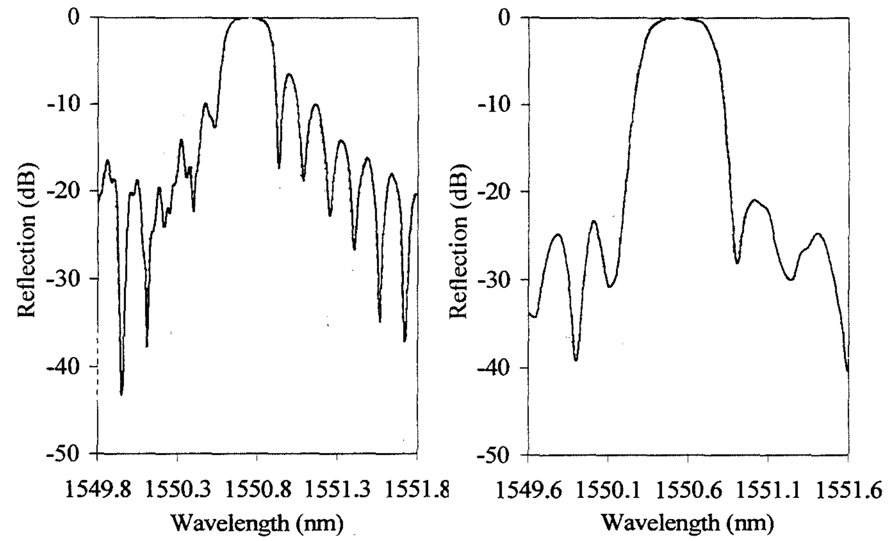

Figure 4.16: Experimental (solid line) and theoretical profiles (dotted line) of raised cosine apodised gratings, length 5mm. Left: Raised cosine $\alpha=0$ *Right: Raised cosine* $\alpha=0.8$.

The left hand spectrum shown in Figure 4.16 shows an unapodised grating with a roll-off factor, $\alpha=0$. The spectrum of the grating with a roll off factor of 0.8 displays a much faster decrease in sidelobe levels than for the 2 truncated profiles, though the level of the first sidelobes is similar. However, the peak shape is not as square as for the truncated profiles.

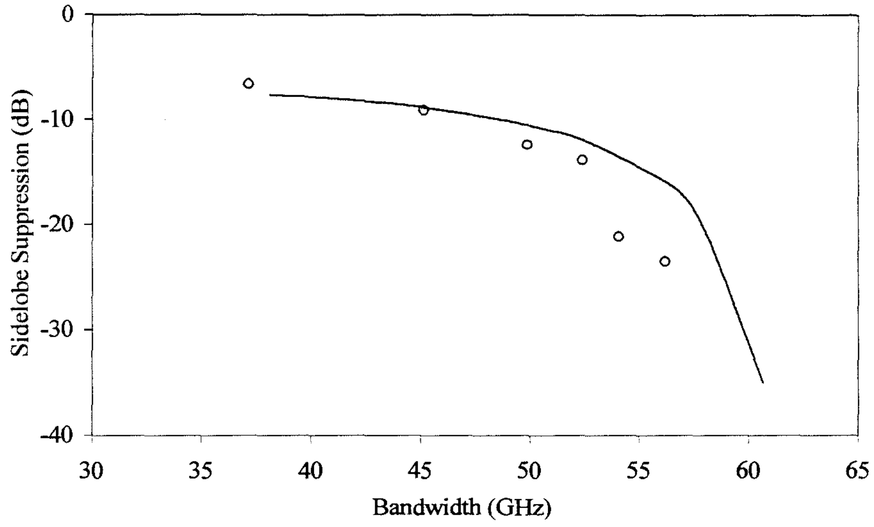

Figure 4.17: Comparison between theoretical (line) and experimental (o) variation of sidelobe suppression with grating bandwidth for raised cosine apodisation functions.

Figure 4.17 shows the variation of sidelobe suppression with grating bandwidth for gratings apodised using a raised cosine profile with α varying between 0 and 1. The variation of the sidelobe suppression with bandwidth for the raised cosine profile displays a sharp drop off in sidelobe suppression for grating bandwidths above ~50GHz. The experimental results are severely limited by the noise level of the grating spectra. The sharp drop off in sidelobe levels is due to the overall shape of the function, which always decreases to zero at the grating edges.

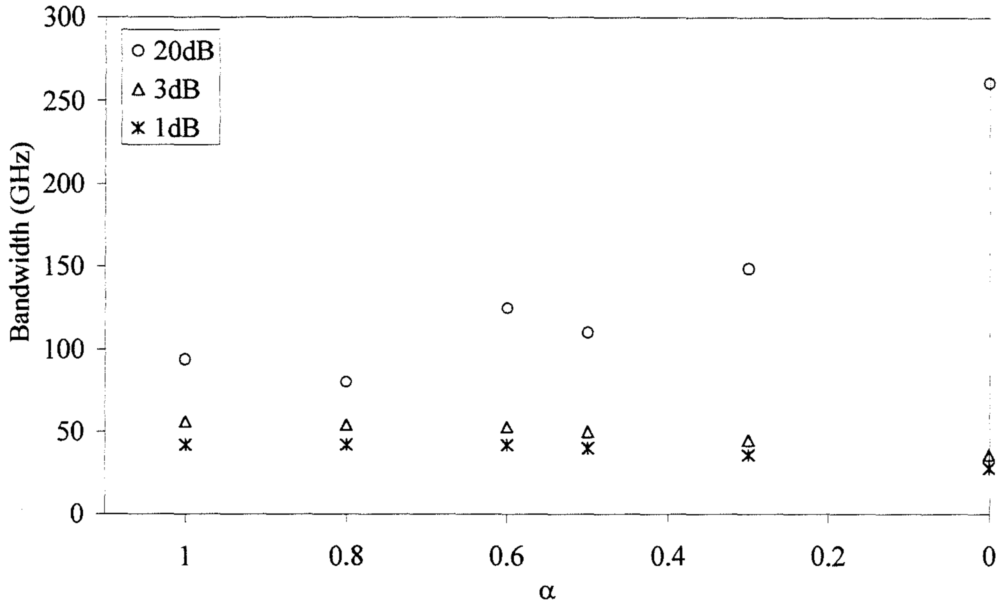

Figure 4.18: Variation of 20, 3, and 1dB grating bandwidths with roll off factor, α for raised cosine apodisation function.

Figure 4.18 shows that as the roll off factor of the raised cosine envelope increases from 0 to 1, there is a much more marked increase in the 1 and 3dB bandwidths than for the other profiles. The very high 20dB bandwidth for α=0 is to be expected as this grating is essentially unapodised (a top hat profile). The difference between the 1 and 3dB bandwidth is also consistently greater than for the other 2 profiles. Though the 20dB bandwidth converges on the 1 and 3dB values more quickly than for the other profiles there is a penalty to pay in the increased 3dB bandwidth compared to the previous two functions. This increase in the required coupling constant may increase the effect of the stitch errors on the profile, which in turn increases the 20dB bandwidth.

4.6 Discussion

The study of the three apodisation profiles investigated here has shown that the spectral properties of a uniform period grating are highly dependent upon the shape of the envelope of the grating refractive index modulation. A theoretical comparison of the variation in sidelobe suppression with 3dB bandwidth is shown in Figure 4.19 for each of the apodisation functions studied here. The figure shows the wide range of values for sidelobe suppression possible for a given grating bandwidth and fabrication length.

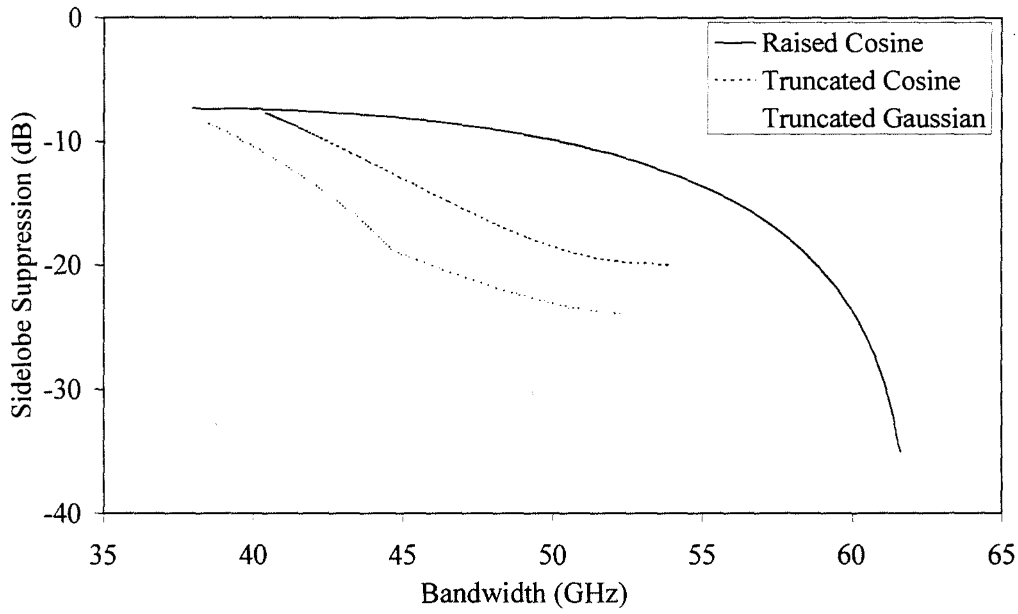

Figure 4.19: Theoretical comparison in the variation of sidelobe suppression with grating bandwidth as the function width or roll off factor is varied for each of the apodisation profiles

It is important to remember at this point that the gratings in the study were all of the same UV exposure length. For some of the gratings, a large proportion of the UV exposure length will have been taken up with apodising the grating. This is particularly the case for the raised cosine apodised gratings. The figure shows that for any given sidelobe suppression, the bandwidth of gratings apodised with a raised cosine profile is always the greatest. The raised cosine profile is the only profile considered here which always decreases to zero at the grating edges, and the effective grating length is shorter than for the other functions, resulting in a broader grating bandwidth. Despite this apparent potential drawback of the raised cosine function, it also results in the gratings with the best sidelobe suppression, for all the functions considered here.

In contrast to the raised cosine profile, the truncated profiles investigated result in the best sidelobe suppression for a given grating bandwidth. This similar behaviour may seem surprising given the very different shapes of the profiles. However, this behaviour shows the effect of a non-zero refractive index modulation at the edge of the grating. The behaviour of the gratings apodised by the different profiles becomes more similar as the apodisation decreases in each case.

PROFILE	1dB BW (GHz)	3dB BW (GHz)	20dB BW (GHz)	SIDELOBE SUPPRESSION (dB)
Raised Cosine α=0.3	36.7	45.1	148.5	-9.1
Truncated Cosine FW= 7.2mm	35.2	45.4	134.6	-12.0
Truncated Gaussian FWHM=3.3mm	34.0	45.4	291.9	-14.4

Table 4.2: Comparison of experimental parameters of apodised gratings with 3dB bandwidth ~45GHz.

Table 4.2 illustrates the wide variation in spectral properties of the gratings fabricated with each of the apodisation profiles, for a 3dB bandwidth of ~45GHz. Whilst the Gaussian function results in the best sidelobe suppression, it has the narrowest 1 dB bandwidth, so the grating peak shape is not as square as for the raised cosine apodised grating, which in this instance results in a sidelobe suppression of ~9dB but a 1dB bandwidth of 39.7dB. Therefore, there is not only a trade-off between bandwidth and sidelobe suppression, but also between sidelobe suppression and how square the peak is (which indicates the variation in loss over the 3dB bandwidth of the grating peak). A square peak shape can be obtained by increasing the transmission loss of the grating – however, this in turn raises the sidelobe level and increases the bandwidth of the grating peak. The effect of stitch errors and other imperfections are also exaggerated by higher grating coupling constants. In general, throughout this study, the squarest peak shapes were obtained using the truncated cosine and truncated Gaussian profiles.

4.6.1 Crosstalk

Another important factor when fabricating gratings for use in WDM networks is interchannel crosstalk. Whilst there is a requirement for a square peak shape with low sidelobes it is also necessary to minimise the level of the grating sidelobes at the position of the adjacent channel. This maximises the isolation between the channels.

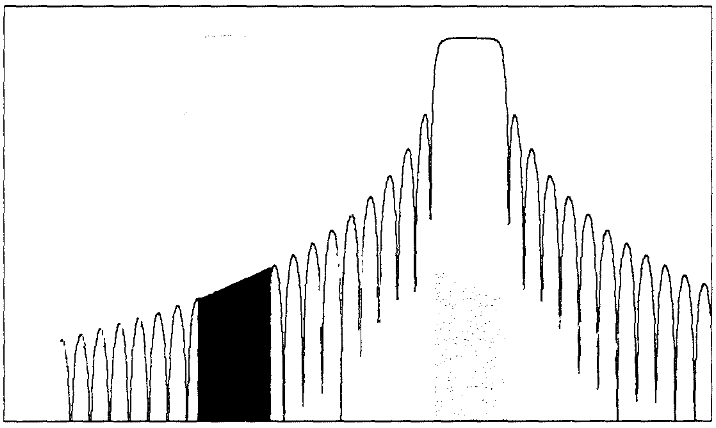

Figure 4.20: Interchannel crosstalk caused by grating sidelobes

Figure 4.20 shows what is meant by crosstalk in this study. For any grating, the crosstalk with the next channel can be calculated as

$$crosstalk = \frac{P_{SL}}{P_p}$$

Equation 4-8

Where P_{SL} is the sum of the power in the grating sidelobes in the adjacent channel over the channel 3dB bandwidth and P_p is the power in the grating peak integrated over the channel 3dB bandwidth.

The variation of interchannel crosstalk with grating bandwidth for the three apodisation profiles is shown in Figure 4.21. The widths of the 2 truncated functions and the roll off factor of the raised cosine were varied in order to effect the change in bandwidth. The crosstalk of the raised cosine apodised grating decreases rapidly as the roll off factor, α increases from 0 to 1. The crosstalk of the gratings apodised using the truncated profiles decreases much more slowly. For any given grating bandwidth, the raised cosine gives the best reduction in crosstalk and the truncated Gaussian yields the greatest values for crosstalk between one channel and the next. This may seem surprising given the results in Figure 4.19 which show that the best suppression of the highest sidelobe for any given bandwidth is given by the truncated Gaussian profile and the least sidelobe suppression is given by the raised cosine profile.

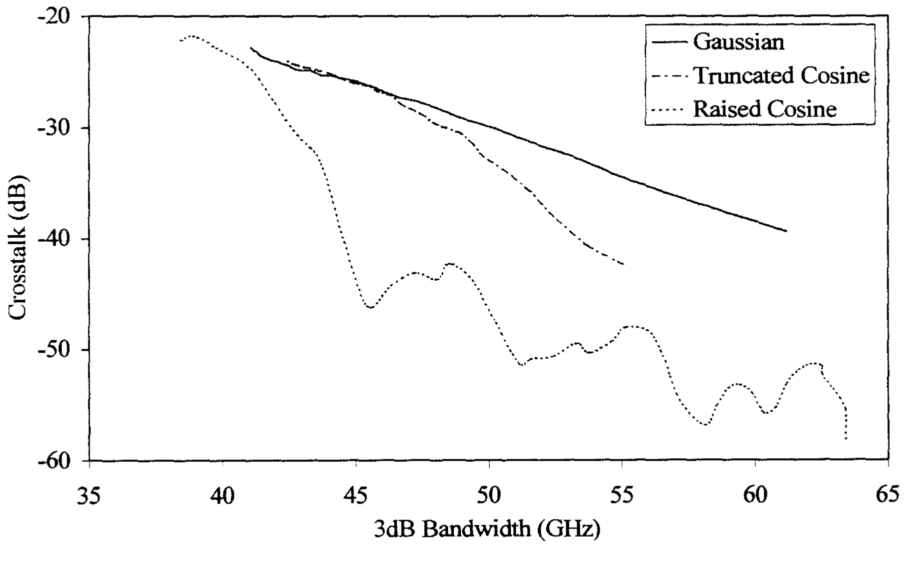

Figure 4.21: Modelled variation in crosstalk with grating bandwidth as the properties of apodisation profiles are varied for gratings of 12dB reflectivity, with a channel spacing of 200GHz

The reason for this apparent contradiction is illustrated in Figure 4.22. Here, comparison is made between the modelled spectra of a raised cosine apodised grating (roll off factor 0.3) and a Gaussian apodised grating (function width 3.3mm). Both gratings have the same 3dB bandwidth of 47GHz and reflectivity of 12dB.

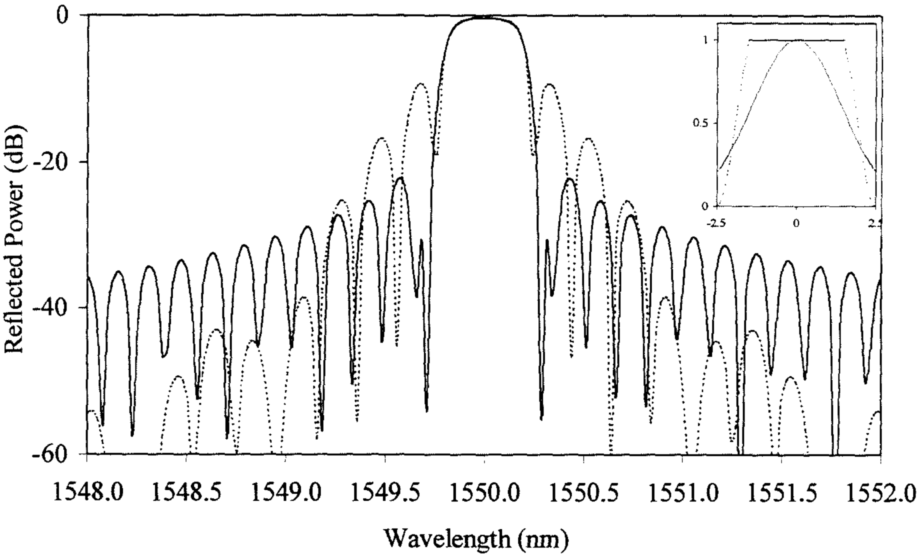

Figure 4.22: Comparison between the sidelobe roll off rates for gratings fabricated using Gaussian (w=3.3mm, solid line) and raised cosine profiles (a=0.3, dotted line). Insert shows the apodisation profiles.

The height of the highest sidelobe for the raised cosine profile is 9.4dB below the grating peak and for the Gaussian profile the sidelobe is 22.3dB below the peak. The sidelobe levels are approximately equal at 0.8nm from the wavelength of the grating peak. 1.6nm from the grating peak the sidelobe suppression of the raised cosine apodised grating is ~50dB below the peak and for the Gaussian grating is ~34dB below the peak. The rate of sidelobe roll off for the raised cosine grating is far greater than that of the Gaussian apodised grating, despite the superior suppression of the sidelobes immediately next to the grating peak for the Gaussian apodisation. Thus there is yet another variable to consider when designing gratings for WDM applications. The 2 apodisation profiles used to fabricate the gratings shown in Figure 4.22 have very different shapes, as shown in the insert. The raised cosine profile used has a flat top and then rapidly decreases to zero at the edges of the grating, giving rise to a sharp sidelobe drop off away from the grating peak whilst leaving a few relatively high sidelobes near to the grating peak. The Gaussian profile decreases gradually but the envelope only decreases to ~0.2 at the grating edge, so the grating is not fully apodised, leading to the persistent sidelobes away from the grating peak. The optimised design for WDM channels of 200GHz separation may not be appropriate for use in WDM systems with a channel spacing of 100GHz.

4.7 Applications

4.7.1 Spectral Slicing

One elegant application of apodised fibre gratings is spectral slicing of broadband laser sources in order to effect WDM channel sources, negating the requirement for separate different wavelength sources. An experiment to demonstrate an application of this technique to a TDM to WDM optical interface was performed, using gratings fabricated using the techniques described in this chapter[6].

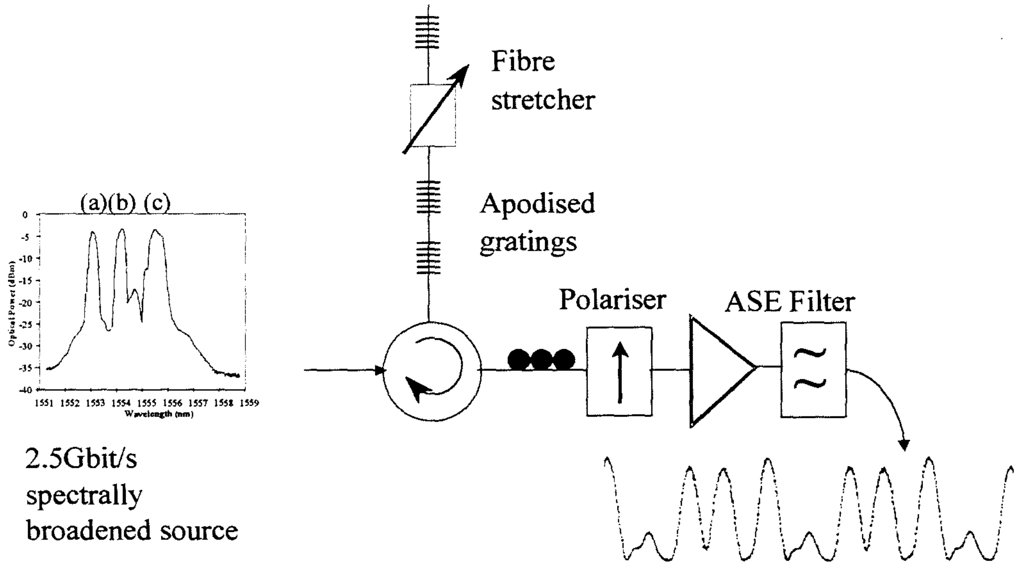

Figure 4.23: Experimental configuration for spectral slicing of a broadband source for OTDM to WDM conversion using apodised Bragg gratings

The broadened pulse source was produced by compressing pulses from a gain switched DFB laser (λ=1556nm) to 5ps FWHM. The compressed pulses were then propagated through 8km of dispersion shifted fibre (λ_0=1574nm). These 2.5GHz

---

[6] Experiment performed by Des Ryan and Steve Alleston, Photonics Research Group, Aston University.

pulses formed the input to the spectral slicing unit shown in Figure 4.23. The gratings (a, b and c) reflect the signal at three different wavelengths. The gratings were separated by fibre stretchers in order to introduce a time delay between the reflection of the pulses at each particular wavelength, essentially producing a delay line. The spatial separation of the gratings was adjusted using the fibre stretchers so that the output from the spectral slicing unit was at 10GHz, with 4 different wavelength channels each at 2.5GHz (though in this case one was missing), as shown in Figure 4.23.

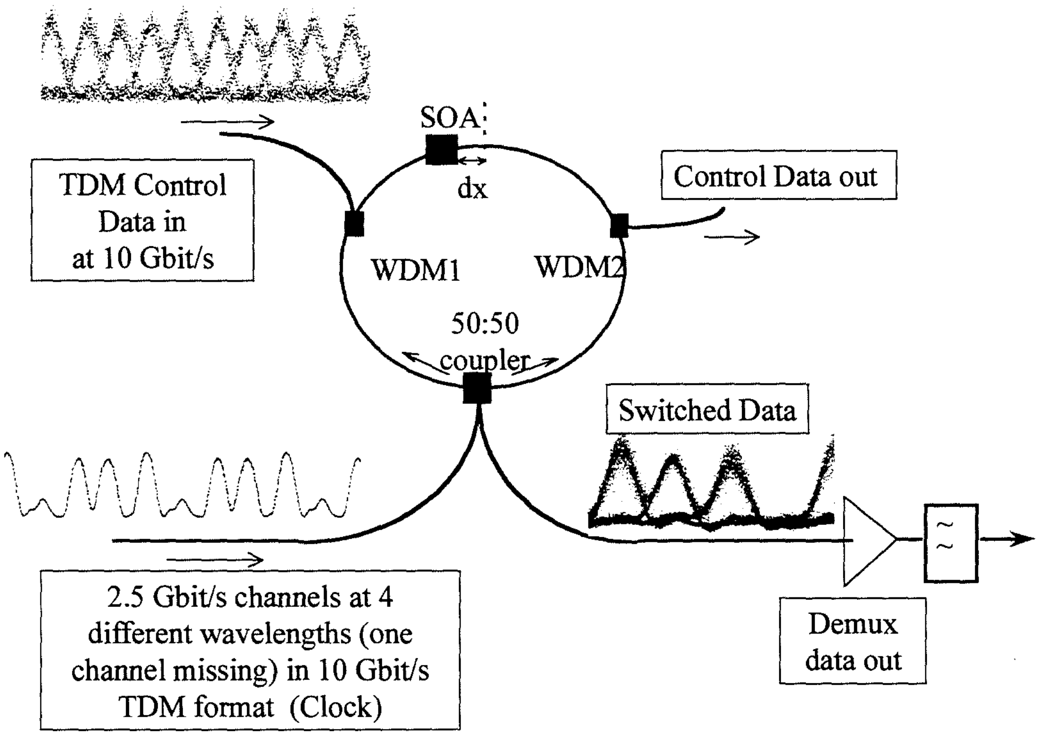

Figure 4.24: Set-up for 10 Gbit/s OTDM to 4x2.5 Gbit/s WDM conversion using an SOA-NOLM [191].

The switching set-up used was a nonlinear loop mirror with a semiconductor optical amplifier as the nonlinear element (SOA-NOLM), shown in Figure 4.24. The switching, or control data is a 4×2.5Gbit/s TDM format PRBS signal at 1534nm. The clock pulses are obtained from the spectral slicing unit and input as shown in the figure. Each TDM data channel switches a different wavelength clock channel, resulting in a 3 channel WDM PRBS output.

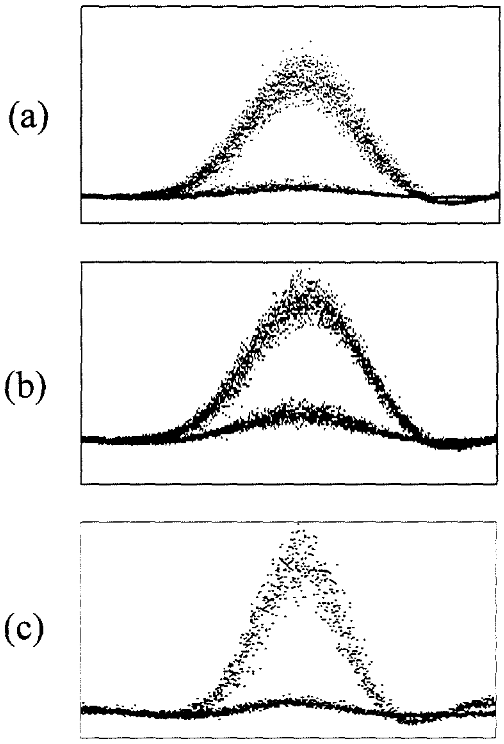

Figure 4.25: Eye diagrams for the 3 channels tested (shortest wavelength channel at the top)

The eye diagrams for the 3 WDM channels are shown in Figure 4.25. All three channels show good eye opening, however channel (c) is somewhat noisier than the others and channel (b) displays a small pulse even when there is no data in the channel. The origin of this noise is crosstalk between channels (b) and (c). This can be understood with reference to the spectral diagram inset in Figure 4.23. The two longer wavelength channels show strong spectral overlap, whilst the short wavelength channel does not. The spectral overlap is caused by large stitch error peaks in the spectrum of channel (c), caused by a poor quality phasemask fabricated using e-beam technology. The origin of the observed channel noise indicates that the spectral profile of the gratings is critical for this type of application , and poor quality severely limits the distance over which error free transmission is possible.

4.7.2 Fast Tuneable Filter

The wavelength of a Bragg grating can be shifted either by changing the grating period by straining or compressing the fibre. The change in grating period can be induced either thermally or mechanically. However, the thermal expansion coefficient of fibre is very small (10-11pm/°C) at 1550nm and silica exhibits excellent behaviour under stress, making tension or compression of the fibre the obvious choice for obtaining a wide tuning range of the Bragg wavelength. Grating compression has previously been used to implement a tuneable fibre laser with 36nm tuning range [192], and a tuneable filter with 15nm tuning range and a settling time in the order of milliseconds [193].

The shift of the Bragg wavelength of the grating, $\Delta\lambda$, is related to the change in the effective refractive index of the fibre core, Δn, and the change in the grating period, $\Delta\Lambda$ by the following relationship:

$$\frac{\Delta\lambda}{\lambda} = \frac{\Delta\Lambda}{\Lambda} + \frac{\Delta n}{n}.$$

Equation 4-9

This wavelength shift can also be expressed as:

$$\frac{\Delta\lambda}{\lambda} = (1 - p_e)\varepsilon,$$

Equation 4-10

where p_e is the photoelastic coefficient which has a value of 0.21 [194]. The resulting wavelength shift is negative for compressive strains and positive for tensile strains.

The tuneable filter presented here is designed for use in WDM telecommunication systems, for wavelength multiplexing and routing or as a wavelength selective filter. The filter uses a 2.5mm long apodised grating as the spectral element[7].

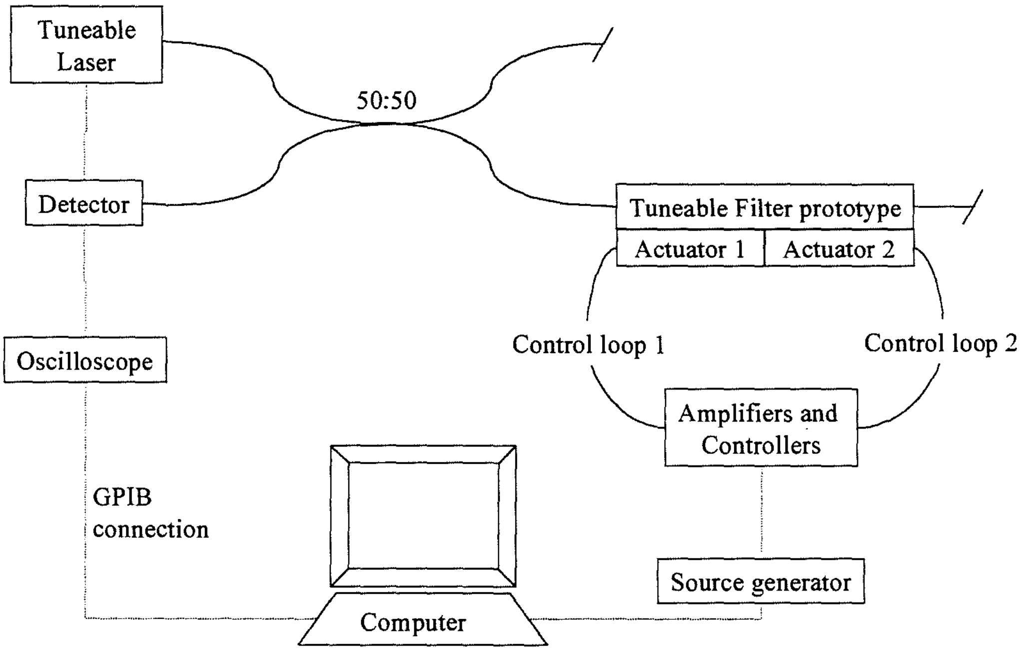

Figure 4.26: Schematic diagram of tuneable filter system.

Figure 4.26 shows the system used to characterise the tuneable filter. Piezoelectric stack actuators are used to axially stress the fibre. The maximum displacement of the actuators is 120μm and they have movement accuracy better than 2% of the nominal displacement. The position of each of the actuators is controlled using a control loop, which are based on a strain gauge, and the whole system is controlled using a computer.

The grating is protected by a guiding system, which uses several special shaped ceramic ferrules and is compressed using steel moveable plates, directly connected to the piezoelectric actuators. The system is designed to work either with both

---

[7] The filter was implemented at the Swiss Federal Institute of Technology by Alessandro Iocco as part of the European ACTS-PHOTOS project. The grating was designed and fabricated at Aston with Lorna Everall.

actuators in compression, or one in compression whilst the other is in extension. The ferrules are designed to minimise the bending of the fibre during compression. The positioning of the grating in the ferrules is critical, and OLCR was used to locate and position the grating in the ferrules [195].

Results

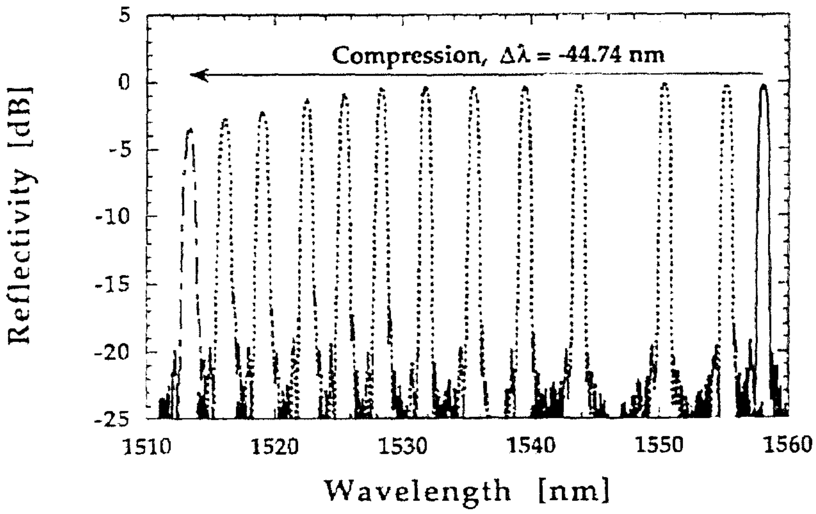

Figure 4.27: Reflection spectra of a 2.5mm apodised Bragg grating under compression.___ Unstrained Grating, ---- compressed grating (measurement accuracy 10pm).

Figure 4.27 shows the reflection spectra of the compressed grating. The grating in this case was 2.5mm long and apodised using a raised cosine profile, to yield the best possible sidelobe suppression and fastest sidelobe roll-off. The unstressed Bragg wavelength was 1558nm, the 3dB bandwidth 0.7nm, and the spectral rejection 20dB. The maximum wavelength shift of –44.74nm was obtained with a combined compression of 240μm (using both actuators), which is the highest tuning range using a Bragg grating to date. For 30nm tuning range, the spectral shape of the filter remained almost unchanged. However, for the highest values of compression, the grating began to buckle resulting in a reduction in the reflected power of 3.4dB.

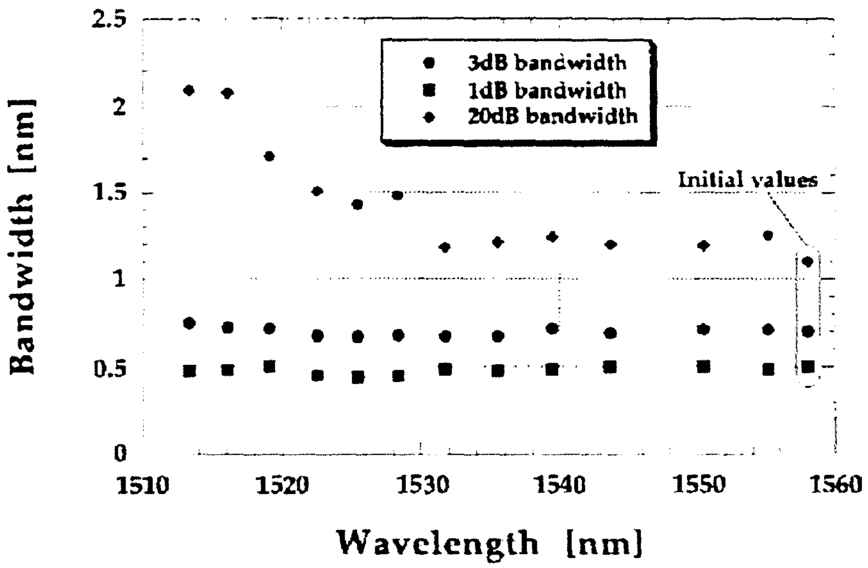

Figure 4.28: Bandwidth evolution during compression of the grating

The change in the grating bandwidth as the grating is compressed is shown in Figure 4.28. Again, only very slight fluctuations are observed for the first 30nm of the tuning range. Over the first 30nm the 1dB bandwidth decreased by 0.05nm, whilst the 3dB bandwidth exhibited fluctuations of the order of ±0.05nm and the 20dB bandwidth increased by 0.15nm. For wavelength shifts greater than 30nm, the variation in the 1 and 3dB bandwidths did not change. However, the 20dB bandwidth doubled to 0.99nm, which correlates with the increase in peak loss shown in Figure 4.27.

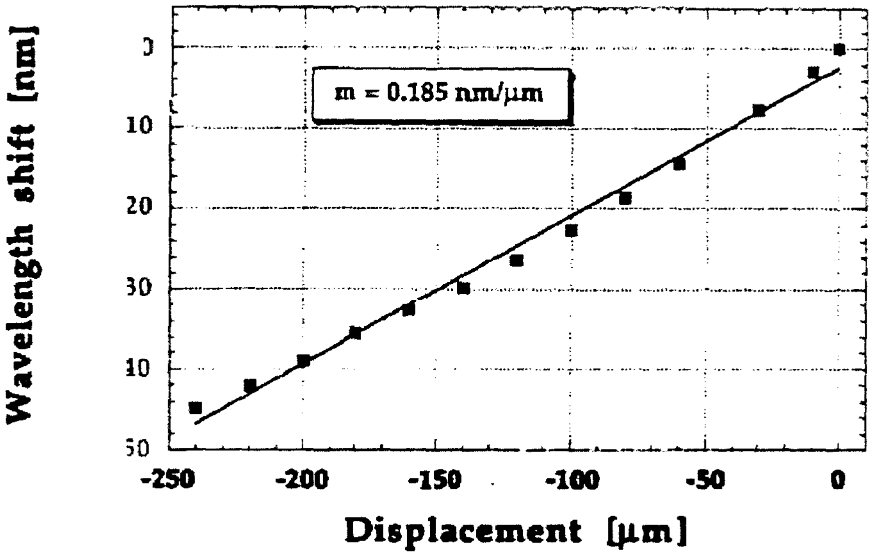

Figure 4.29: Bragg grating wavelength shift versus piezoelectric actuator displacement

The wavelength shift of the grating for different actuator displacements is shown in Figure 4.29. The wavelength shift is linear with a slope of 0.185nm/μm. The strain induced in the fibre due to the compression was calculated from the wavelength shift and using Equation 4-10 was found to be 3.7%. The deviation of the experimental results from the straight line fit is due to fibre buckling during compression.

The settling time of the filter was also characterised by measuring the delay between an external square wave signal used to drive the piezoelectric actuators and the signal of the tuneable laser, reflected off the tuning grating. The decrease in settling time for a given wavelength for increased actuator tensions was expected. The settling time of the filter was limited to a minimum of 0.2ms by the resonant frequency of the piezoelectric actuator.

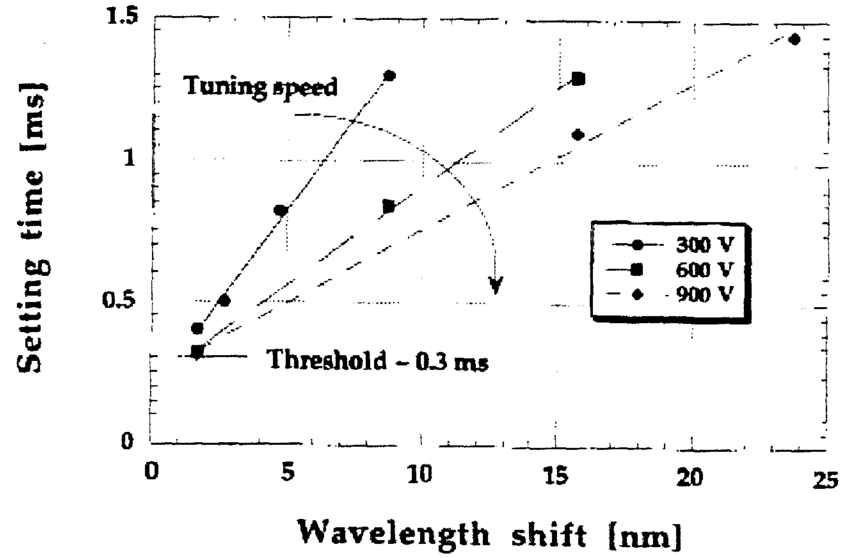

Figure 4.30: Setting time for different wavelength shifts and actuator tensions

4.8 Chapter Conclusions

A simple method for apodising fibre Bragg gratings has been demonstrated and used to study the spectral response of gratings constrained in length to 5mm, fabricated with a range of apodisation functions. This new fabrication method is more simple and flexible than that which involves dithering of the fibre [180], as it can be used to apodise gratings in different pre-assembled fibre devices. Engineers at Alcatel have recently adopted the technique in order to fabricate apodised gratings in Mach-Zehnder add-drop filters.

Three different types of apodisation profiles have been investigated for the apodisation of uniform period gratings. In the case of the truncated Gaussian and truncated cosine profiles, the function width was varied; in the case of raised cosine profile, the roll-off factor was varied. The study has shown that no apodisation function can be said to be ‘best’ overall, especially when considering gratings fabricated subject to stringent length constraints. Many factors have to be taken into consideration during the grating design process, and the most appropriate apodisation function will depend on the spectral priorities for a given application. However, for a given 3dB bandwidth of the grating peak, the truncated Gaussian profile has been shown to give the best suppression of the first sidelobe, while the raised cosine always results in the worst sidelobe suppression. This effect is due to the different shapes of the 2 functions; more of the grating exposure length is taken up with apodisation for raised cosine profiles, than for the truncated profiles. Therefore, the effective length of raised cosine apodised gratings is shorter, resulting in a broader bandwidth grating. The peak shape (difference between 1dB and 3dB bandwidths) is also affected by the apodisation function, with the truncated profiles resulting in the squarest peak shapes. A theoretical comparison of the grating spectra has shown that the rate at which the sidelobes reduce away from the grating peak also varies according to the apodisation function. For a given 3dB bandwidth, the raised cosine function was found to result in the worst sidelobe suppression, yet yielded the lowest crosstalk values for grating arrays with a frequency separation of the arrays of 200GHz.

The use of apodised gratings has been demonstrated in order to effect a TDM to WDM signal converter. The gratings were used to spectrally slice a broadened 2.5Gbit/s DFB laser source. A semiconductor optical amplifier-nonlinear optical loop mirror (SOA-NOLM) was used to transfer the TDM data to the WDM channels. The eye diagrams of the wavelength channels indicate that good quality gratings should be able to be used as a TDM/WDM switch in transmission systems. However, the poor spectral quality of the long wavelength channel grating lead to noise on the pulse and crosstalk between the long wavelength channel and middle wavelength channel.

A grating based fast tuneable filter has been demonstrated, which is suitable for WDM applications. The filter employed an apodised grating of length 2mm, which was tuned by compression. A maximum settling time of 1.5ms, and a tuning range of 44.74nm were achieved.

5 SPECIAL GRATINGS FOR SENSING DEVICES

5.1 Introduction

Fibre Bragg gratings are now widely used in smart structures for strain sensing [196] and their versatility means that they also find application in sensing a wide range of measurands, such as temperature [137] and pressure [136]. Interest has particularly increased in recent years in the use of FBGs as distributed sensors, and the ability to measure arbitrary strain profiles. Techniques are largely based on optical low coherence reflectometry [197], interferometry and Fourier transform techniques [198]. Both uniform period and chirped gratings have been used for intragrating sensing [199,200] and arrays of individual gratings have also been used as quasi-distributed sensors [201,202]. From the outset, the challenge has been to produce a sensor with the capability to measure arbitrary strain profiles with high strain and spatial resolution.

To date, the techniques presented, resulting in the highest spatial resolution of $300\mu m$ [197], have involved optically probing the grating structure itself. However, LeBlanc *et al* reported a technique, which involved measurement of the grating spectrum, using Fourier techniques to infer the grating structure and therefore the strain distribution within the grating structure [207]. The spatial resolution obtained using this technique was 0.8mm.

In this chapter, two methods of quasi-distributed strain sensing are presented and discussed. The first comprises arrays of very short apodised gratings (2mm in length). The results in this chapter show an improvement in the fabrication of grating arrays designed for distributed sensing over distances of the order of millimetres. The main advance presented in this chapter involves the novel use of chirped Moiré gratings as distributed sensors. The distinct phase shifts and amplitude nulls in chirped Moiré gratings make them ideal for taking discrete measurements in a very short distance. The work on Moiré sensors represents a significant improvement on the spatial resolution for sensors where the reflection spectrum is measured.

In addition to the work on quasi-distributed strain sensing, the final section of this chapter details the design, fabrication and testing of a novel grating sensor designed to imitate the behaviour of an interferometer.

5.2 Background

The theory of fibre Bragg grating sensors is now well known. The change in strain or temperature of a fibre can be easily determined from the shift in the Bragg wavelength of a grating $\Delta\lambda_B$, caused largely by stretching or thermal expansion of the fibre.

The change in strain in the fibre

$$\Delta\varepsilon = \frac{\Delta\lambda_B}{\lambda_B \xi},$$

Equation 5-1

Where $\Delta\lambda_B$ is the difference between the strained and unstrained Bragg wavelengths of the grating, and λ_B is the unstrained Bragg wavelength of the grating. ξ is the strain optic coefficient, which describes how the refractive index of the fibre changes with strain. ξ has a typical value of $0.78\times10^{-6}\ \mu\varepsilon^{-1}$[203].

The change in temperature of the fibre

$$\Delta T = \frac{\Delta\lambda_B}{\lambda_B \kappa},$$

Equation 5-2

where κ is the combined thermo-optic coefficient for the fibre which has a value of $6.67\times10^{-6}\text{K}^{-1}$for germanosilicate fibre[137].

Using Equation 5-1 and Equation 5-2, it is straightforward to calculate the strain or temperature of a grating; though ξ and κ vary with material composition of the fibre. However, it is difficult to distinguish between strain and temperature information when both are retrieved by monitoring the shift in Bragg wavelength. Extra calibrating gratings that are either isolated from strain or thermally compensated are required in sensing systems.

5.3 Arrays

Arrays of gratings, where the gratings are separated spatially along the fibre, have previously been used to measure strain and temperature gradients, though the gratings are typically separated by a few centimetres. However, it is possible to perform distributed strain and temperature measurements with significantly higher resolution than a few centimetres. The work contained within this next section illustrates the effectiveness of grating arrays for performing quasi-distributed measurements with a spatial resolution of a few millimetres.

5.3.1 Introduction

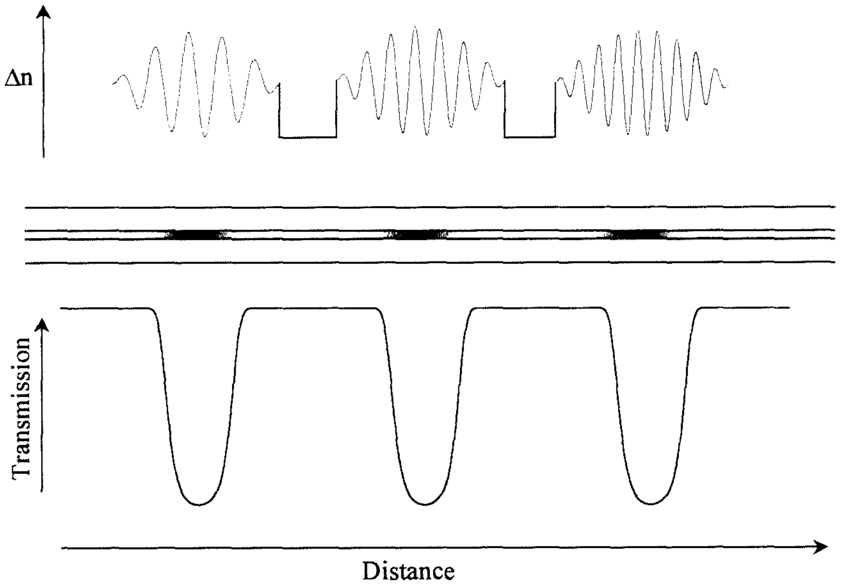

Figure 5.1: The theoretical refractive index profile and associated transmission spectrum of an apodised grating array

A basic diagram of an apodised-grating array is shown in Figure 5.1. The requirements, in order to provide a high spatial resolution, are that the individual gratings are very short in length and the separation of the gratings is as short as possible.

5.3.2 Fabrication of Sensing Arrays

Grating arrays were fabricated using the scanning phasemask method, using the setup shown in Figure 5.2.

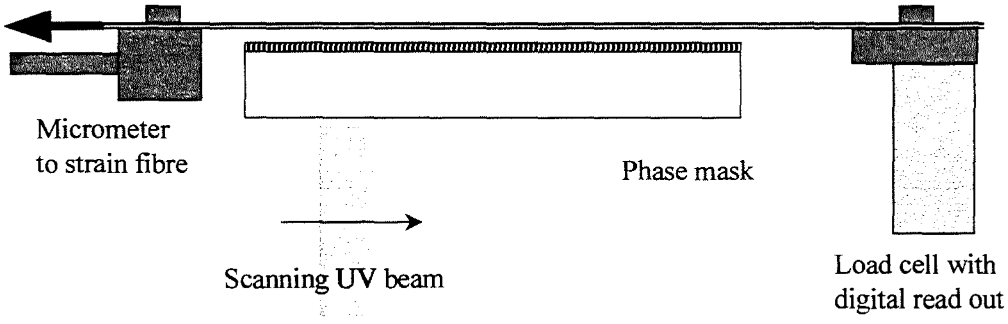

Figure 5.2: The set-up for fabricating grating arrays by straining the fibre between exposures

The first grating was fabricated and then the fibre was strained by controlled amounts before exposures of subsequent gratings. Stretching the fibre during grating exposure resulted in a grating at a shorter wavelength when the fibre was eventually released [204]. The higher the strain, the shorter the wavelength of the resultant grating. The spatial separation of the gratings in the arrays was typically only ~0.5mm. The fibre alignment was adjusted before the fabrication of each grating in the array to minimise any variations in UV dose of each grating, which results in a variation in the maximum transmission loss of the gratings. Hydrogen loaded boron germania co-doped fibre was used to provide maximum photosensitivity. The high photosensitivity of the fibre resulted in the high UV induced refractive index modulation required to achieve a transmission loss of ~10dB in very short apodised gratings.

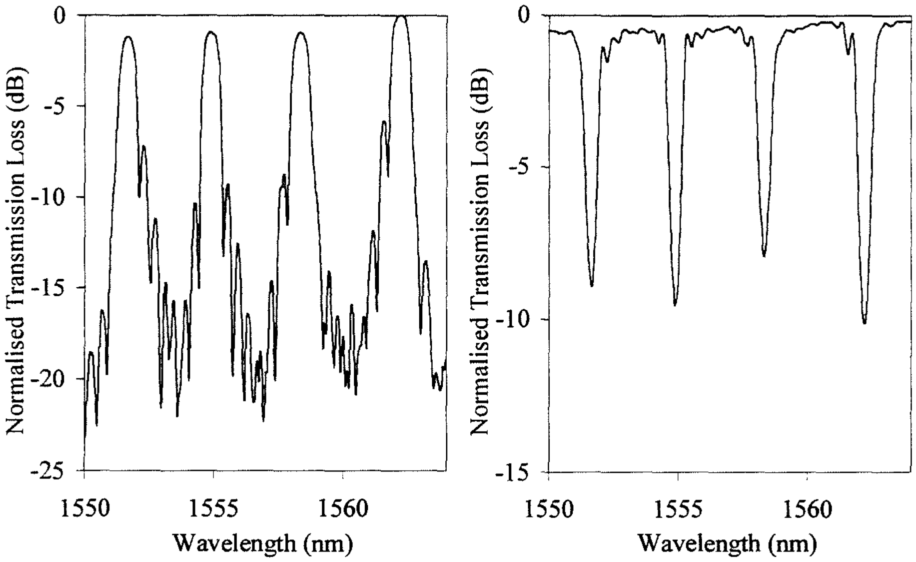

Figure 5.3: An unapodised grating array, the individual grating length is 2mm.

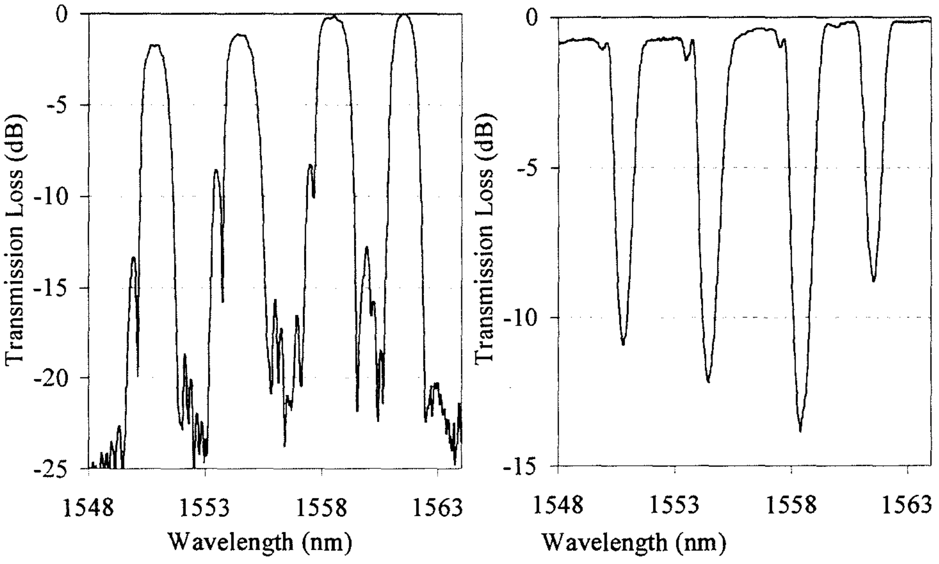

Figure 5.4: An apodised grating array, the individual grating length is 2mm, and the gratings were apodised using a raised cosine function, α=0.7.

The spectrum of an unapodised grating array, with the length of the individual gratings being 2mm, is shown in Figure 5.3. The array was fabricated using the quadrupled Nd:YAG laser with a beam size of ~0.5mm. The level of the highest sidelobe is only ~7dB below the grating peak, and this can cause problems detecting the grating peaks in reflection. For sensing applications, gratings are usually viewed in reflection, and so need to have a good dynamic range for easy peak detection. In order to increase the dynamic range of the arrays in reflection, it was necessary to apodise the gratings in order to reduce the sidelobe level.

Figure 5.4 shows the spectrum of an apodised grating array, where the individual grating length is only 2mm. The gratings were apodised using a raised cosine function with a roll-off factor of 0.7. The sidelobe level has been reduced as a result of the apodisation, but the bandwidth of the grating peak is broader than for the apodised grating array. The peak broadening has been caused mainly by the apodisation, though some is due to the fact that the transmission loss of the gratings in the apodised array is greater than for the unapodised array. The highest wavelength grating in the apodised array is of similar transmission loss to the gratings in the unapodised array and has a narrower bandwidth than the stronger gratings. There is a definite improvement in the reflection profile of the array due to apodisation, but noise still remains on the grating peaks. Very short apodised gratings such as are shown here have very high coupling coefficients, and due to this, effects of defects on the phasemask are exaggerated compared to longer apodised gratings displaying the same transmission loss. In addition, the scan speeds for such short gratings fabricated with the YAG laser are very small (~50μms^{-1}) and the translation stage used to scan the beam along the phasemask and fibre does not run smoothly at such slow speeds, resulting in profile noise on the gratings.

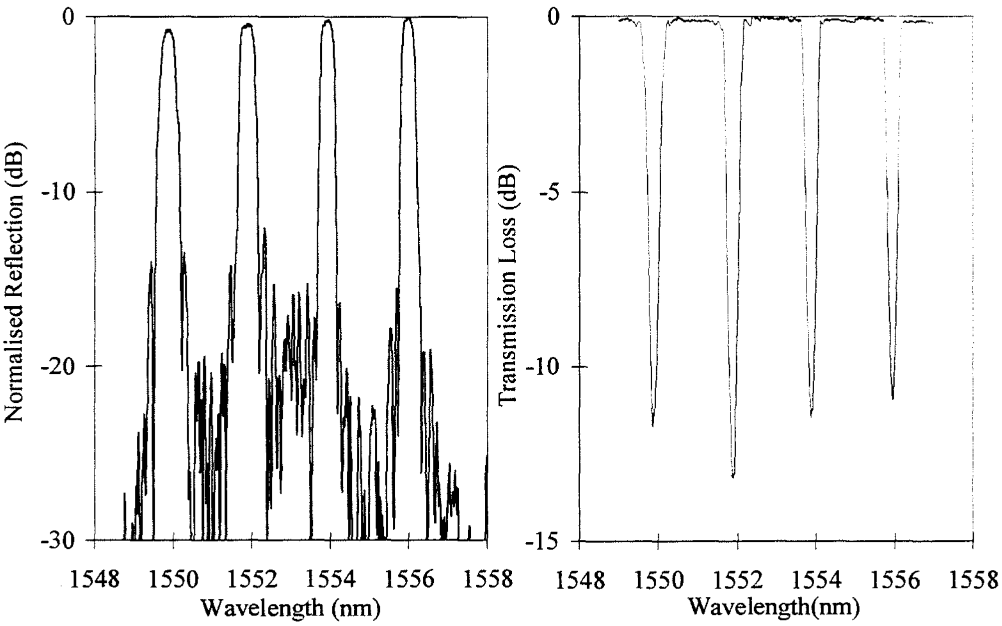

Figure 5.5: An apodised grating array, individual grating length 5mm. The gratings were apodised using a Gaussian function, FWHM 5mm.

An apodised grating array with individual grating lengths of 5mm is shown in Figure 5.5. The separation of the gratings is 0.5mm, and the gratings were apodised with a Gaussian function, FWHM 5mm. The noise on the grating peaks of this array is much less than for the array of 2mm gratings, largely because of the reduced coupling coefficient.

5.3.3 Strain Sensing

To my knowledge, grating arrays have not previously been used to measure varying strain profiles with such high spatial resolution as offered by the structure of these arrays. In order to test the response of the arrays to a varying strain profile, they were subjected to a linear strain gradient.

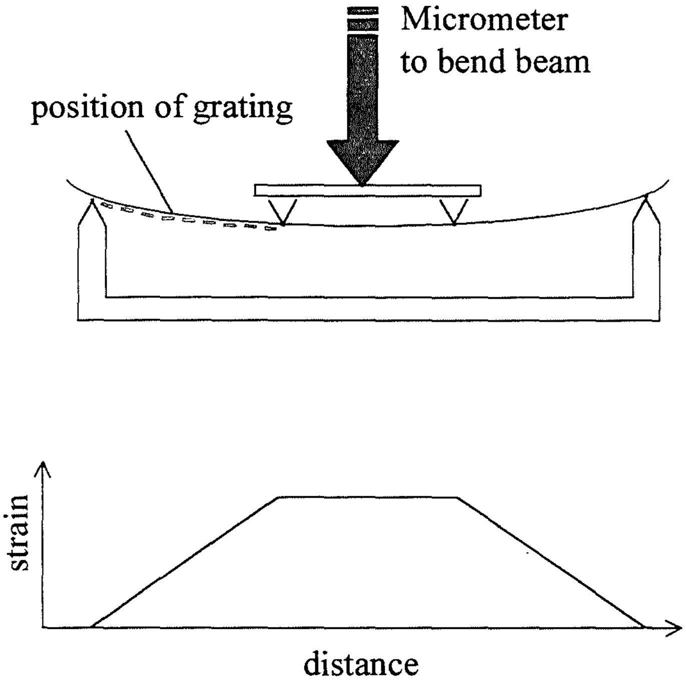

Figure 5.6: 4-point bending rig for engineering a linear strain gradient

In order to realise a linear strain gradient, the gratings were bonded into grooves on a piece of spring steel using an acrylate based super glue. The steel was bent using a 4-point bending rig, shown in Figure 5.6. The steel rested on two outer knife-edges, whose position was fixed. The steel was bent by bringing the two inner knife-edges down onto the steel using a micrometer. The micrometer acted against a spring so that the inner knife-edges would rise away from the steel when the micrometer was released. Between the middle two knife-edges of a four point bending rig, the strain distribution in the steel is uniform. The strain decreases linearly with distance along the steel to zero at the outer knife-edges [205].

Strain Gradient Testing of Grating Arrays

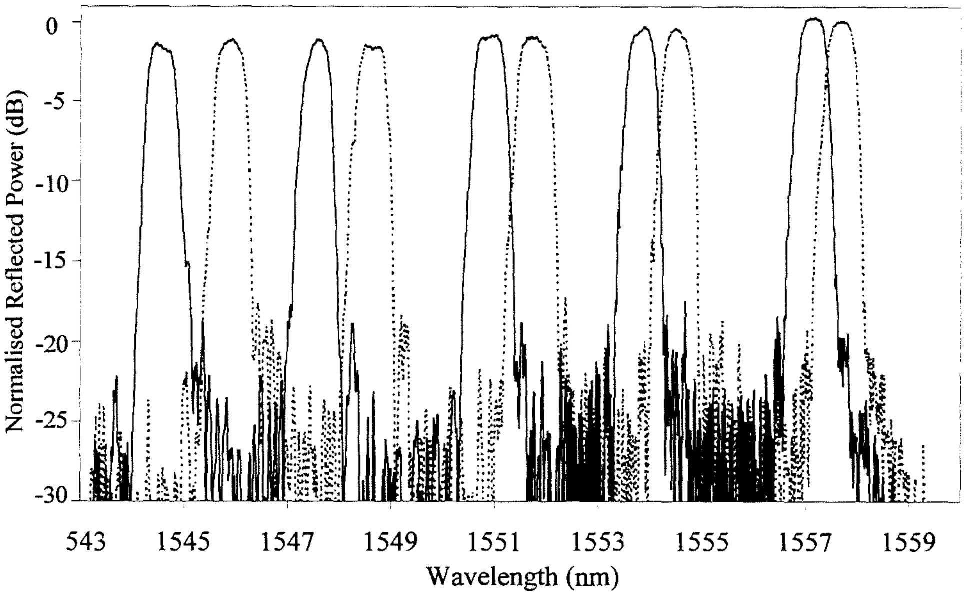

Figure 5.7: Spectra of a 5x5mm apodised grating array, —— unstrained, ·········· subjected to a linear strain gradient of -29με/mm (highest strain at short wavelengths)

The spectrum of a grating array before and after being subjected to a linear strain gradient of -29με/mm is shown in Figure 5.7. The apodised grating array was fabricated using a special phasemask with 5 adjacent patches each of length 5mm and different periods[8].

Spectral Broadening of Grating Peaks

The grating peaks of the strained grating in Figure 5.7 are not the same shape as those of the unstrained grating. This is caused by the fact that the individual gratings are not point sensors, and have a finite length, over which the strain exerted on the fibre changes. The strain gradient across each of the gratings causes them to become slightly chirped, and results in some broadening of the reflection peaks. Structure

---

[8] Grating made by Lorna Everall, Aston University.

becomes evident on the grating peaks because of this chirping effect. The broadening of the grating peaks for different arrays used to measure the linear strain gradient is detailed in Table 5.1. Chang *et al* have recently observed this effect and reported a special bonding technique for overcoming the problem for individual gratings [206]. However, this method would be hard to implement for grating arrays. This broadening of the peaks could cause errors in the detection of the wavelength of the grating peak and therefore the induced strain, particularly if the broadened peak has noise at the top.

Grating No.	5x5mm Array $\Delta\lambda$(nm)	5x5mm Array $\Delta\lambda$ increase (nm)	4x2mm Array $\Delta\lambda$ (nm)	4x2mm Array $\Delta\lambda$ increase (nm)
1	0.61	0.06	0.97	0.00
2	0.57	0.07	1.10	0.00
3	0.64	0.03	1.15	0.00
4	0.57	0.03	0.97	0.00
5	0.60	0.04		

Table 5.1 : Spectral Broadening of Grating peaks due to linear strain gradient of 50με/mm (bandwdith increase accuracy ±0.03nm).

The results in Table 5.1 show the broadening of the grating peaks due to the linear strain gradient across the gratings. The results show that the peak broadening is more significant for the 5mm gratings than for the 2mm gratings, which would be expected due to the increased grating length and therefore induced chirp. Whilst the results for the 2mm gratings suggest that there is no broadening, this is probably due to the limited resolution of the OSA used to measure the bandwidth of the peaks. Slight variations in the results for the 5mm gratings are most likely to be due to the resolution problems and also imperfections in the bonding of the grating to the spring steel. A simple calculation using Equation 5-1 for a strain gradient of 50με/mm, and effective grating length of 4mm (due to apodisation of the 5mm grating), yields a bandwidth increase of 0.07nm. Therefore the results in Table 5.1 are of the expected magnitude. A grating of length ~1mm subjected to such a strain gradient would only experience broadening of the order of 0.017nm, which as expected is smaller than the accuracy of the measurements.

Strain Measurements Using Arrays

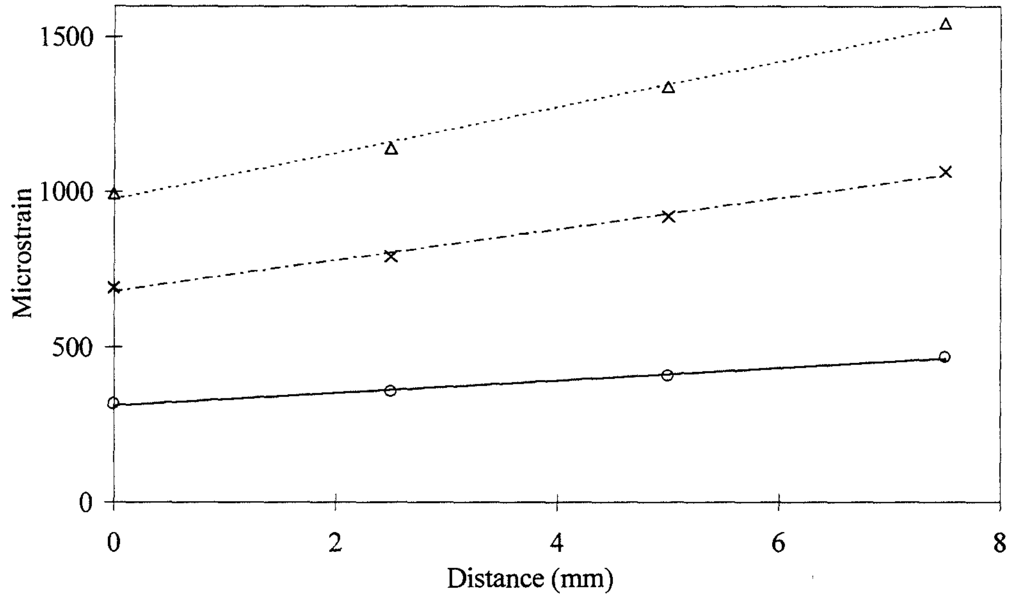

Figure 5.8: Measurements of linear strain gradients using a 4x2mm grating array. △ *74με/mm,* × *50με/mm,* o *20με/mm. (The straight lines are linear fits).*

Figure 5.8 shows the response of a 4x2mm grating array (shown in Figure 5.4) to linear strain gradients. The symbols are the experimental readings from the gratings and the lines are straight-line fits. The strain was calculated from the shift in wavelength of the grating peaks, relative to the wavelengths of the peaks in the unstrained state. Equation 5-1 gives the strain for a given wavelength shift. The spatial resolution of this sensor was 2.5mm, determined by the length and separation of the gratings. The grating array was monitored using a broadband source and optical spectrum analyser (spectral resolution 0.1nm). The peak wavelengths were determined using LabVIEW, and the strain resolution of 13με was determined by the spectral resolution of the OSA. The experimental points agree well with the theoretical fits and within the errors stated. Variations may be caused by the simple gluing technique used, leading to slight non-linearities in the strain gradient across the gratings. This effect may result in the average strain in the grating not being representative of the strain at the centre point of the grating length.

Discussion on Arrays as Distributed Sensing Devices

The results in the previous sections have shown both that it is possible to fabricate grating arrays and that they can be used successfully to measure non-uniform strain profiles. However, there are two main issues that limit the use of such grating arrays for quasi-distributed sensing.

The number of gratings/unit length in the array limits the length of the individual gratings. For long arrays with a relatively small number of gratings the size of individual gratings is not particularly constrained. Gratings with lengths in the order of 1cm tend to be used because this gives a small reflection bandwidth where the peak is easily identified. For short arrays the grating-grating separation becomes comparable to the grating length and increasing the number of gratings over a given length in the array means that the grating size must decrease. This rapidly increases the grating bandwidth and decreases spectral resolution of the devices.

The physical length of each grating means that it cannot be treated as a point sensor. Changes in the measurand along the grating length ideally result in an average value being recorded as a result of the shift in wavelength of the grating peak. However, non-linear changes in the measurand over the grating length may result in spurious measurements, caused by distortion to the spectral shape of the grating peak (e.g. splitting of the grating peak).

5.4 Moiré Grating Sensors

The previous section of this chapter alluded to shortcomings in the use of grating arrays for distributed sensing. Most of the techniques presented thus far for distributed sensing involve interrogation of the grating structure itself, with many requiring the use of interferometers. However, LeBlanc *et al* have demonstrated a technique that enables the strain profile to be deduced from the Fourier transform of the reflection spectrum of a grating [207].

The following section presents the first reported work on the use of chirped Moiré gratings as sensors. Chirped Moiré gratings provide a simple and effective solution to many of the problems associated with grating array sensors, yielding high spatial and spectral resolution simultaneously.

5.4.1 Chirped Moiré Grating Sensor Concept

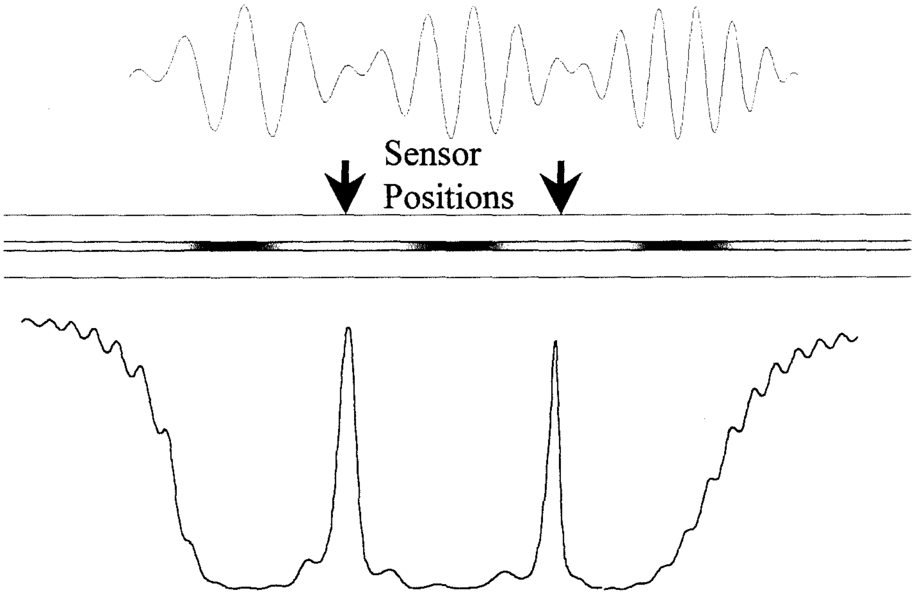

Figure 5.9: Schematic of a Moiré sensor: The amplitude nulls and phase shifts in the refractive index profile lead to passbands in the chirped Moiré grating spectrum.

Chirped Moiré gratings are usually formed by the inscription of two gratings at the same position in the fibre. One grating has a slightly different period or chirp-rate to the other. The amplitudes of the superimposed gratings are added together producing a beating effect between the two grating refractive index profiles, as shown in Figure 5.9. The resulting amplitude envelope of the refractive index modulation leads to the formation of bandpass peaks within the grating spectrum, also shown in Figure 5.9. At the points in the fibre where nulls in the amplitude envelope and phase shifts occur, passbands are formed. It is these phase shifts in the grating structure and their associated passbands, which form the basis of the chirped Moiré grating sensor.

Theoretical Description of Chirped Moiré Gratings:

The refractive index profile of a Moiré grating is given by

$$\Delta n(z) = \Delta n\left(2 + 2\cos\frac{2\pi z}{\Lambda_c}\cos\frac{2\pi z}{\Lambda_s}\right),$$

Equation 5-3

where

$$\Lambda_S = \frac{2\Lambda_1\Lambda_2}{(\Lambda_1 + \Lambda_2)}, \Lambda_C = \frac{2\Lambda_1\Lambda_2}{(\Lambda_1 - \Lambda_2)}.$$

Equation 5-4

Λ_1 and Λ_2 are the periods of the gratings and are functions of z for chirped gratings. The spatial separation of the sensors is given by Λ_C . Therefore the number of passbands in a chirped Moiré grating is given by

$$N_{PB} = \frac{L}{\Lambda_C},$$

Equation 5-5

where L is the length of the grating.

5.4.2 Fabrication of Moiré Sensors

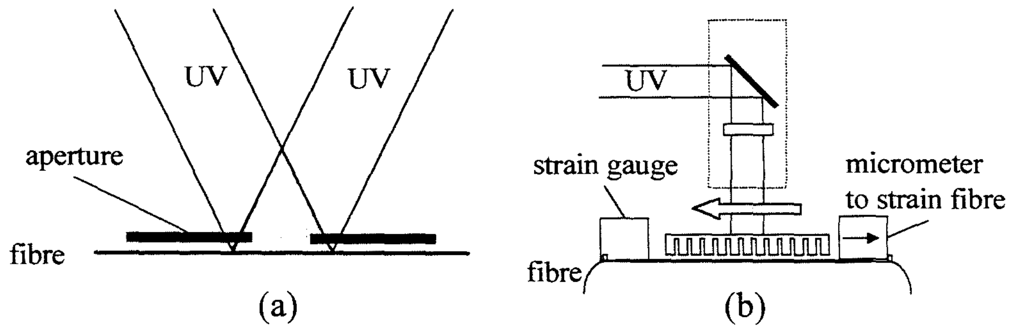

Figure 5.10: (a) Holographic method and (b) phasemask method for making chirped Moiré grating sensors.

The Moiré gratings can be fabricated using a number of different methods [208,209,210]. The gratings used in the first of the Moiré grating sensing experiments were fabricated using the two-beam interference holographic method [208], shown in Figure 5.10(a). The gratings were made with a frequency doubled Argon Ion laser (244nm) in hydrogen loaded germanium doped fibre (Ge ~ 20mol%)[9]. One chirped grating was fabricated (maximum transmission loss ~70%), then the fibre was translated along the fibre axis before the inscription of a second grating. The number of passbands in the Moiré gratings was dependent upon the magnitude of the sideways translation of the fibre (typically <1mm). An aperture of length 5mm was placed in front of the fibre during UV exposure. The aperture was translated sideways along with the fibre, so that exactly the same length of fibre was exposed during the second UV exposure, in order to avoid any unwanted effects at the edge of the grating due to the gratings not fully overlapping. Ultimately, the length of the gratings was limited by the width of the beam in the holographic fabrication setup (~7mm). However, despite this limitation this method is very flexible, allowing the fabrication of gratings with centre wavelengths in the range 600-1600nm, and with chirps up to ~60nm.

---

[9] The quadrupled Nd:YAG laser was not suitable for making these gratings, because of the poor spatial beam quaility and also because of the high coupling coefficient required for these gratings.

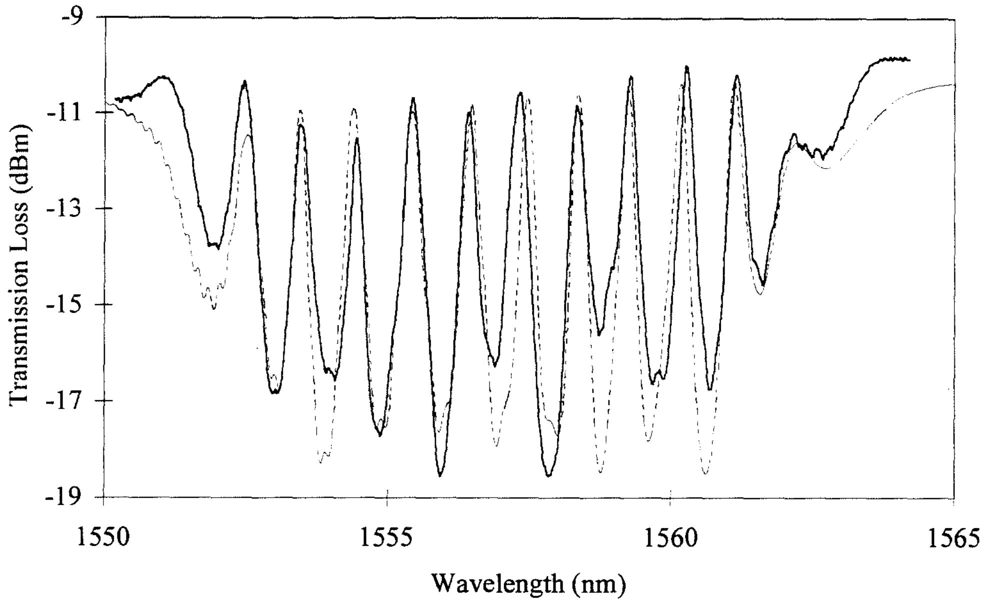

Figure 5.11: ——Spectrum of a 5mm long Moiré fabricated using the holographic technique. ········ Modelled response of the Moiré grating

The grating shown in Figure 5.11 was fabricated using the technique described above. The total bandwidth is 12.6nm, average bandwidth of the passband peaks is 0.39nm and the finesse is ~2.5. The finesse of a resonator,

f = passband spacing/passband bandwidth.

Equation 5-6

The variation in transmission loss of the grating minima is largely due to the spatial profile of the irradiating UV beam. (The modelled spectrum shown in Figure 5.11 was calculated using a Gaussian spatial variation in the beam intensity.) Hydrogen loaded germania doped fibre was used to provide the high photosensitivity required because of the fairly large chirp rate of the grating(~2nm/mm). This fibre was used in preference to boron-germania co-doped fibre, because of the reduced short wavelength loss exhibited by gratings in this fibre. The passbands at short wavelengths in the transmission spectrum of the Moiré grating can exhibit increased loss due to short wavelength loss originating from the long wavelengths of the Moiré grating. The increased core-cladding refractive index difference of high germania doped fibre reduces the coupling between core and cladding modes and therefore the loss at short wavelengths in Moiré gratings.

Figure 5.12 shows the modelled refractive index profile of the grating in Figure 5.11. The average refractive index along the grating length is determined by the spatial profile of the irradiating UV beam.

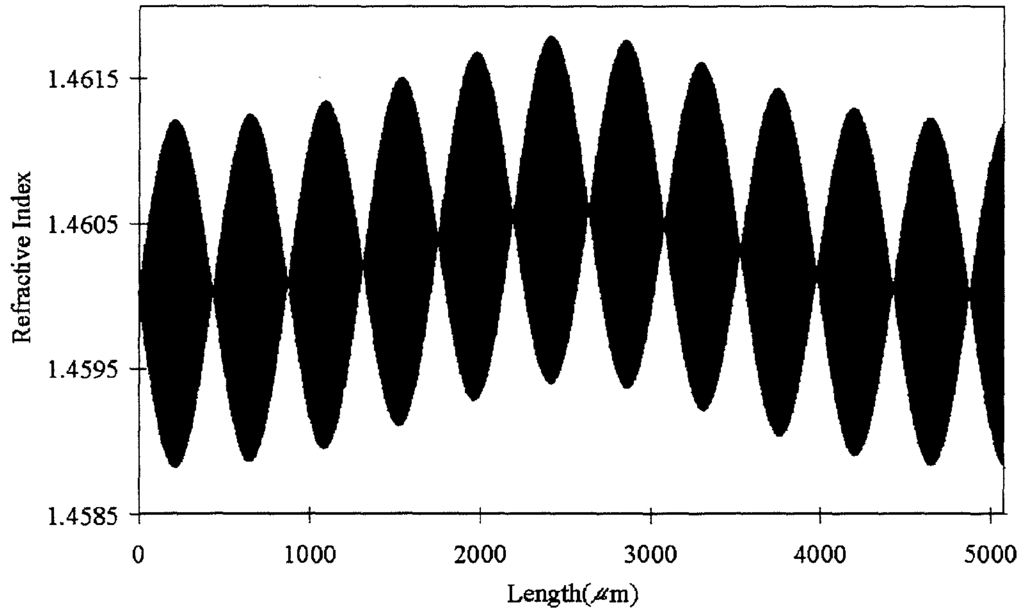

Figure 5.12: Modelled refractive index profile of the Moiré in Figure 5.11.

Another method of fabricating Moiré gratings uses a dual-scan-phasemask technique, shown in Figure 5.10(b)[210]. The first chirped grating is fabricated, then the fibre is stretched by a controlled amount before the second exposure of the phasemask. Straining the fibre results in the fabrication of a grating at a lower wavelength than that dictated by the phasemask. Figure 5.13 shows a grating fabricated using this method. The grating is 5cm in length, and the total spectral chirp is 5nm. The grating has 22 passbands, which exhibit low loss (<0.5dB). The bandwidth of the passbands is 0.08nm, and the finesse is ~2.8.

It is possible to fabricate longer devices using the phasemask method, than using the holographic technique. However, the chirp rate of the grating is determined by that of the phasemask, and the maximum possible grating length is limited by the phasemask length (at present up to 10cm). In addition, it was not possible to achieve such high refractive index modulation using the phasemask method, as for the holographic method. There was a large amount of light transmitted through chirped phasemask in the zero order rather than the first orders, which form the interference pattern in the fibre core. Therefore there was a poorer fringe visibility of the refractive index modulation for the chirped phasemask gratings, than for those fabricated holographically.

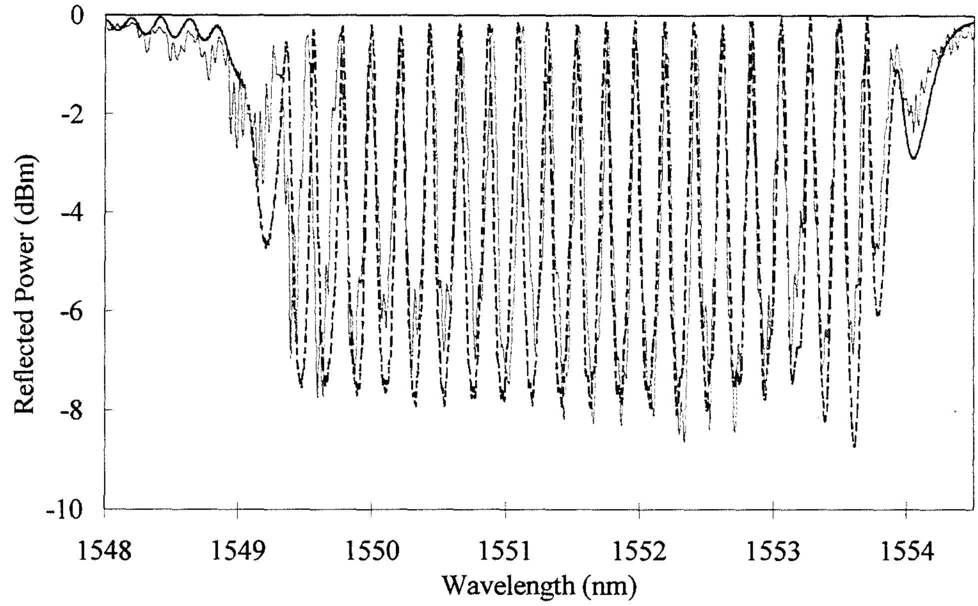

Figure 5.13: Experimental (—) and modelled (····) spectra of a 5cm Moiré fabricated by dual scan of a 5nm chirped phasemask.

5.4.3 Moiré Gratings As Distributed Sensors

Strain Sensing

The behaviour of the Moiré gratings as strain sensors was investigated using the same 4 point bending rig as for the grating arrays (see page 134). The gratings were again bonded into the grooves in the spring steel strip. Data was taken at a variety of strain gradient values with the 10-peak Moiré shown in Figure 5.11. The grating spectrum was measured in each case using a tuneable laser and OSA giving a resolution of 10pm. The strain was calculated by comparing the strained and unstrained wavelengths of the grating peaks and using Equation 5-1.

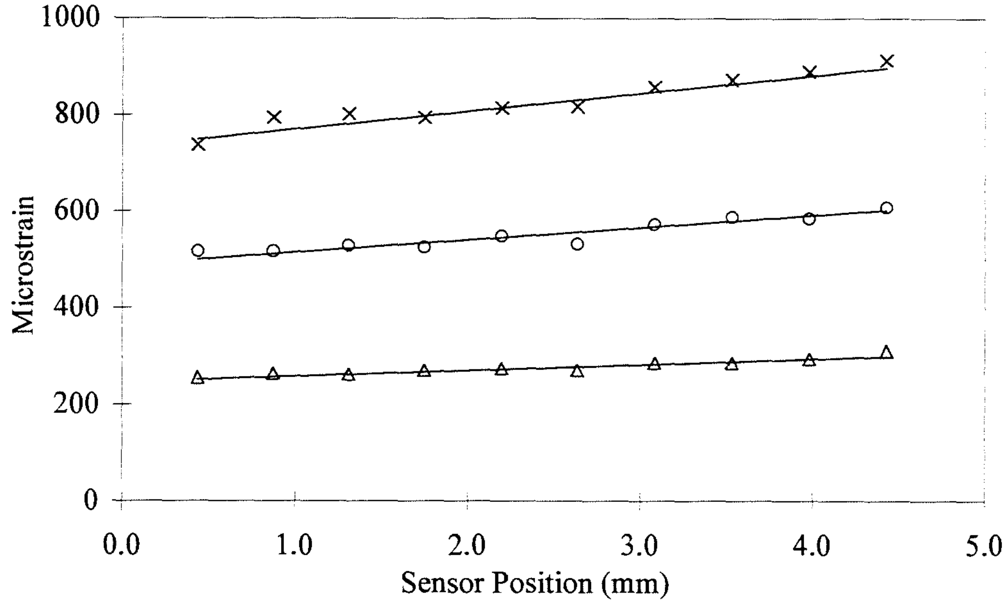

Figure 5.14: Experimental results from using a 10 peak Moiré grating to measure a variety of linear strain gradients.

The results obtained for three different strain gradients are shown in Figure 5.14. The positions of the sensors (phase shifts) were calculated by modelling the grating spectrum and refractive index profile, as shown previously in Figure 5.12. In this case IFO_Gratings was used to model the grating properties. The strain gradient measurements taken using this Moiré grating have a strain resolution of 13$\mu\varepsilon$ and a spatial resolution of ~450µm. It is difficult to determine the actual sensor length. The minimum value of the sensor size is given by the length of the phase shift in the grating structure, leading to a value of ~0.25µm. However, a rough maximum value can be obtained by knowing the chirp rate of the grating. Translating the FWHM of the grating passbands into equivalent grating length gives an approximate sensor size of <200µm. In contrast, a 200µm long uniform period Bragg grating with a transmission loss of 7dB, would have a FWHM of >5nm. In addition, the bandwidth of this grating would only increase with greater transmission loss. An increase in transmission loss for the Moiré would result in an increase in the finesse and thus a decrease in the bandwidth of the passbands.

The work on Moiré sensors continues to be developed in conjunction with Oxford Fiber Optic Tools Ltd. In order to develop a prototype sensor system, a LabVIEW program was written by Yu Liu of the Photonics Research Group, to take data from an OSA and derive the strain or temperature at points along the grating from that data. Figure 5.15 shows the 22-peak Moiré as viewed on the OSA, with a resolution of 0.08nm. The peaks are not resolved, but the basic structure of the Moiré can still be seen.

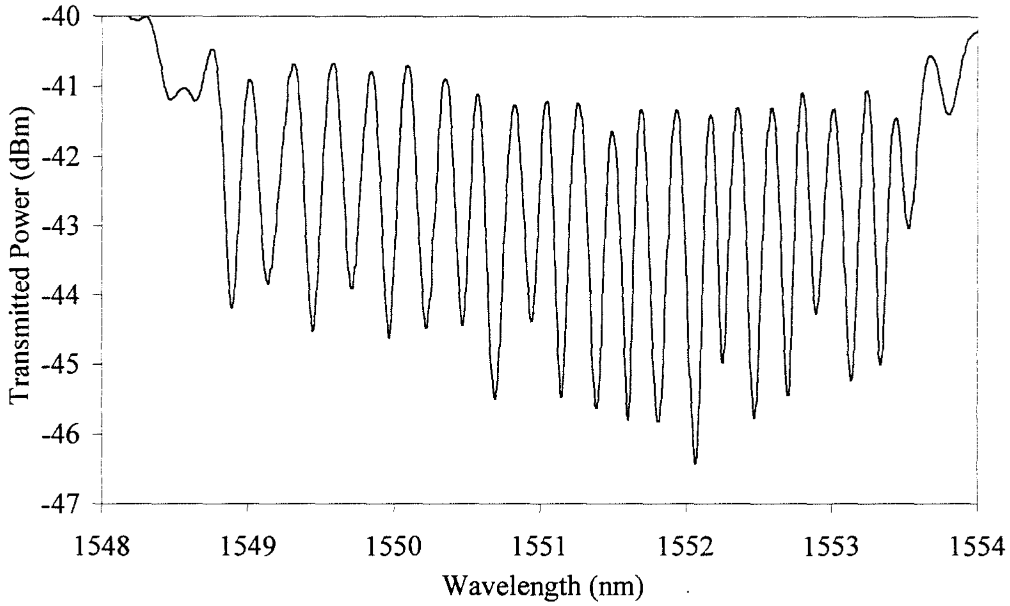

Figure 5.15: 22-peak Moiré grating fabricated using a 5nm, 5cm chirped phasemask, viewed on an OSA.

Figure 5.16 shows results from the 22 peak Moiré used for measuring the strain on the spring steel in the 4-point bending rig. The LabVIEW program only detected the central 20 peaks of the Moiré, due to the reference levels set for measuring the peaks. The grating was actually measured in reflection, and the program was used to detect the valleys instead of peaks, however, this method worked just as well. The strain was plotted against peak number, giving a fairly straight line due to the constant separation of the sensors. The strain profile flattens off after peak 18, this is due to the grating extending onto the region of the spring steel which is in between the central 2 knife edges of the 4 point bending rig. In this central portion of the bending rig, the strain is constant. A glitch in the strain is expected at the position of the knife edge, which can be seen from the results. At present, the resolution of the results is limited by the resolution of the OSA, however, it should be possible to improve on this in time.

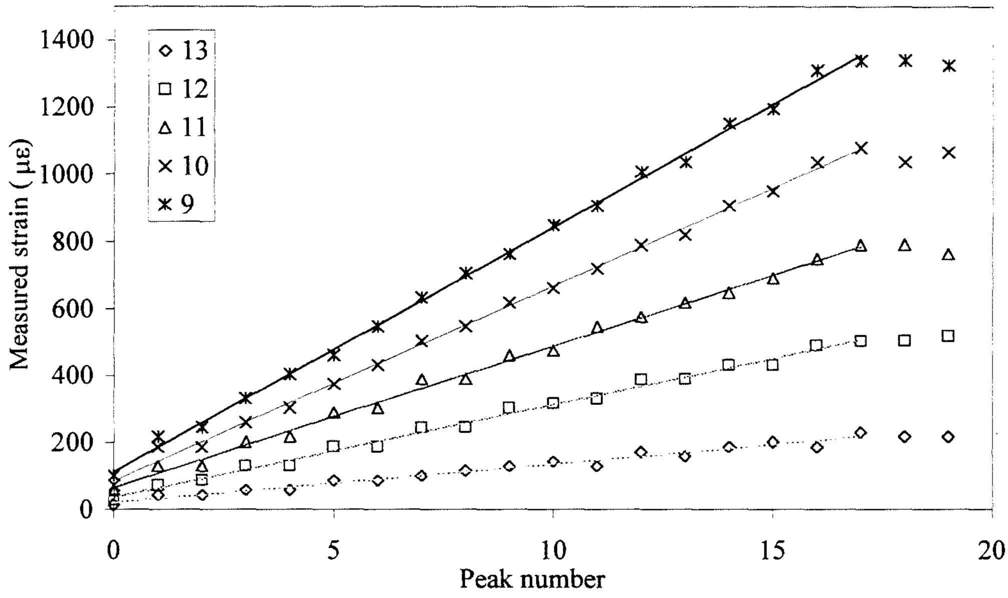

Figure 5.16: Results from measuring the strain of the steel in the 4-point bending rig using a 5cm Moiré sensor and the LabVIEW program.

Temperature sensing

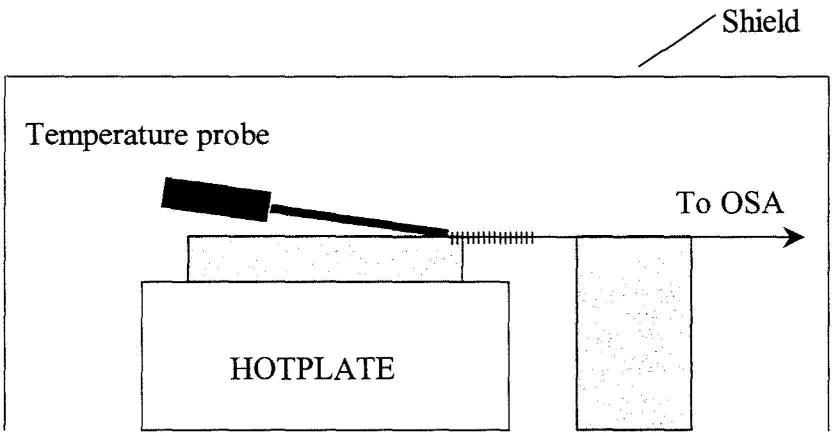

Figure 5.17: Set-up for non-linear temperature profile sensing

Moiré gratings also have the potential to be used as temperature gradient sensors. Two simple experiments were performed in order to demonstrate the principle. The first experiment involved using the fibre itself as a non-insulated bar, and using the Moiré grating to measure the temperature along the fibre. One end of the grating was placed on the edge of a hotplate, the other was supported on a metal block, as is shown in Figure 5.17. Care was taken in order to insure that the fibre was not sagging, but was not significantly strained either. The temperature of the hotplate was measured as close to the grating as possible, using a temperature probe. The set-up was shielded to eliminate the effect of air currents on the grating profile.

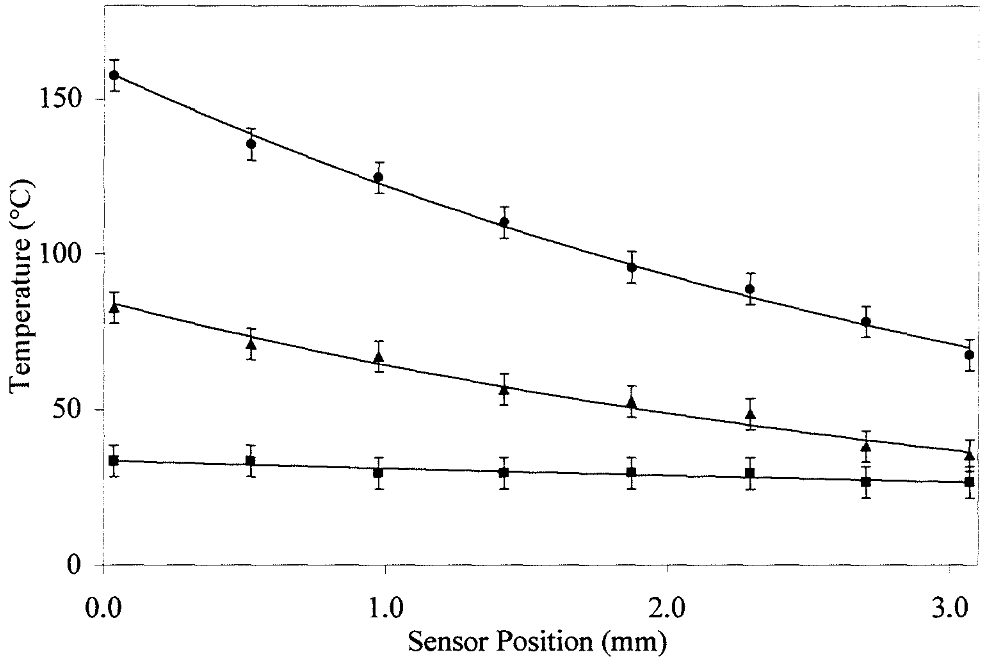

Figure 5.18 : Results from a Moiré grating subjected to an exponetial temperature profile. The experimental results are shown by symbols, the lines are theoretical fits.

The Moiré grating used for this measurement had 8 peaks, a total bandwidth of 8.5nm and a finesse of 2.5. The results from the hotplate experiment are shown in Figure 5.18. The error bars shown on the graph represent the uncertainty in the temperature measurements resulting from the resolution of the OSA. Traces were recorded on the OSA for various temperatures of the hotplate, once the grating profile had stabilised. As for the strain measurements, the temperature was derived by noting the wavelength shifts of the grating peaks. The temperature shift was then calculated using Equation 5-2.

The heat distribution inside the fibre can be modelled by considering the fibre as a bar. The temperature at a distance x from the hotplate which is at temperature θ_0,

$$\theta = \theta_0 \exp\left[-x\sqrt{\frac{c\varepsilon}{\kappa A}}\right],$$

Equation 5-7

where c is the circumference of the fibre, ε is the emissivity of the surface, κ is the thermal conductivity of fused silica and A is the cross sectional area of the fibre.

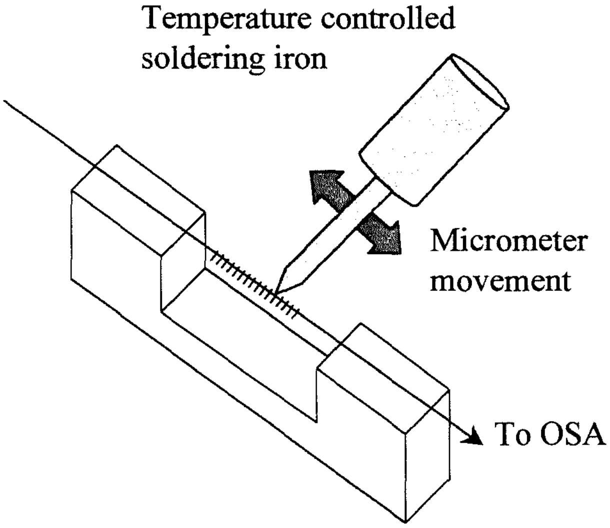

Figure 5.19: Experimental setup for soldering iron experiment

In order to evaluate the suitability of the Moiré grating for measuring arbitrary profiles, a temperature controllable soldering iron was used to provide a quasi-point heat source. The apparatus was set up as shown in Figure 5.19. The soldering iron was mounted on a translation stage with a micrometer movement, so that it could be translated along the grating. The distance between the soldering iron and the fibre was ~0.3mm. The soldering iron was set at a temperature of 200°C. The shift in wavelength of the peaks was measured using an OSA as before, and thus the temperature was calculated for each sensor point. Sets of data were taken for different positions of the soldering iron with respect to the grating.

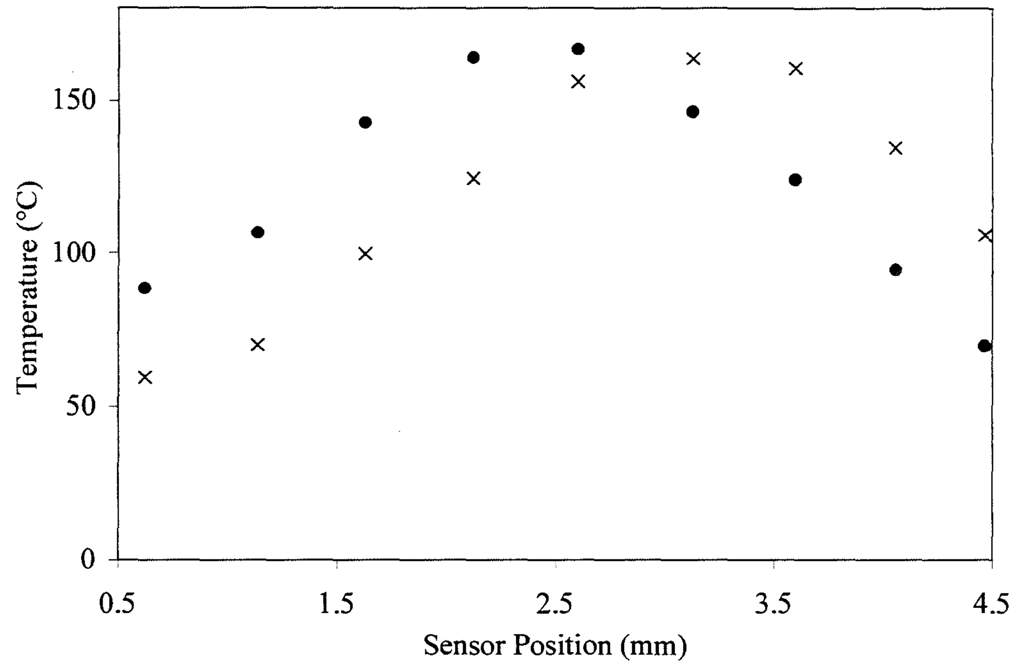

Figure 5.20: Measurements of the temperature profile ~0.3mm from a soldering iron tip, taken using a Moiré grating. The different symbols represent data sets taken at two positions of the iron tip along the grating, separated by 0.5mm.

The results for the experiment are shown in Figure 5.20. The two different symbols represent two different positions of the soldering iron along the grating. The temperature profile measured by the Moiré grating is shifted along the grating length with the soldering iron, as expected. There is a slight drop in the measured peak temperature of the profile for the data set (x) compared to that marked by a •. This change in the measured temperature is probably due to the soldering iron being slightly further from the fibre in this data set, a trend which is evident when studying all the data sets taken.

The temperature at the fibre due to thermal radiation from the soldering iron tip can be calculated approximately by considering that the heat flow per second between two surfaces

$$Q = \sigma T_s^4 = \frac{K}{r}\left(T_s - T_f\right)$$

Equation 5-8

Where σ is Boltzman's constant, T_s is the temperature of the soldering iron, T_f is the temperature of the fibre, K is the thermal conductivity of air, and r is the distance between the soldering iron and the fibre. For a soldering iron temperature of 200°C, the calculated temperature at the fibre is 164.5°C. This value agrees with that measured using the Moiré grating.

5.4.4 Application - Detecting Breakages in Packaged Fibres

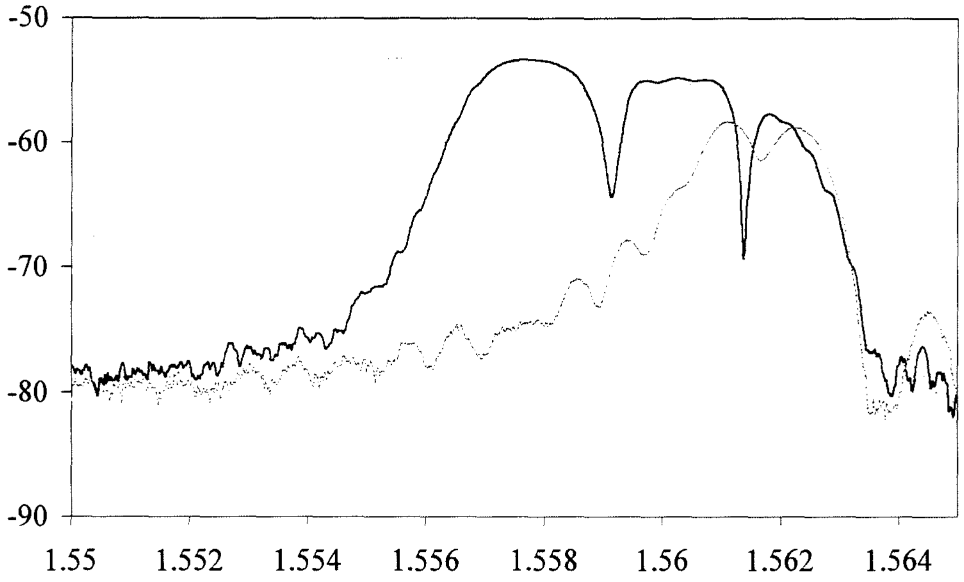

Figure 5.21: Preliminary results showing the effect of breakage at various points along a Moiré grating

Optical fibres are now used for a wide variety of applications, in different environments – many of which are harsh. Packaging requirements are becoming more stringent as fibres are required to stand up to more extreme working conditions, for example extremes of temperature or exertion to large forces. The fibres frequently have to be embedded, or glued into place using resins. Many fibres get broken during packaging, significantly increasing the unit cost of each fibre device. One particular example is of laser diodes which have fibre pigtails. The fibres are embedded in epoxy, and the percentage of devices fit for sale is frequently low. In order to improve the percentage of devices that are fit for sale, a method is required for detecting the position in the fibre where the breakage occurs. The Moiré gratings provide a potential method of locating the point at which the fibre is broken and also monitoring the strains exerted on the fibre as the epoxy cures.

In order to assess the possibilities of detecting breakages in fibres using Moiré gratings, a Moiré grating was broken at various positions along the grating length. The results are shown in Figure 5.21. Whilst the break cannot be located exactly, the grating spectrum provides important information as to the approximate location of the break. The passbands provide 'markers' along the length of the chirped grating, so that even if the grating is strained, it is still possible to tell where the grating is broken. However, if the grating is not chirped enough, then the passbands can overlap and it is not possible to gain much useful information from the spectra.

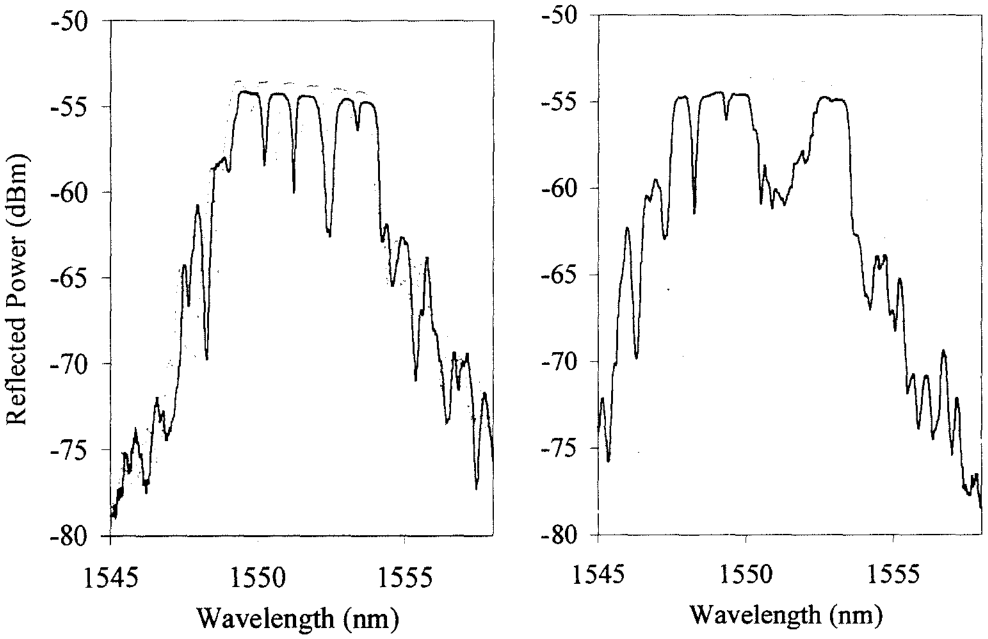

Figure 5.22: A Moiré grating embedded in epoxy, showing a break as the glue hardens

Figure 5.22 shows the evolution of the spectrum of a Moiré grating as the epoxy it is embedded in cures. The grey spectra in each figure are the original spectra of the grating, before it was embedded. The right hand figure shows that the short wavelength end of the grating has become compressed as the epoxy has cured. The passbands have become indistinct, this is probably due to the relatively narrow bandwidth of the grating. The grating used for this demonstration was a 5cm, 5nm

Moiré fabricated by dual scan of a phasemask. A 20nm phasemask would probably afford better resolution of the passbands throughout curing of the epoxy.

5.4.5 Moiré Gratings Discussion

	ARRAYS	MOIRÉS
Sensor Length	>500μm	<200μm
Minimum Spatial Resolution	Sensor Length	<450μm
Strain Resolution	Both at present limited by measuring system.	
Fabrication	Apodised individual gratings, uniform period phasemask	2 scans of a chirped phasemask
Dynamic Range in Reflection	>15dB (apodised gratings)	~10dB
Dynamic Range in Transmission	Decreases with grating length	Decreases with grating length and increasing chirp

Table 5.2: Comparison of the properties of grating arrays and Moirés considered in this study.

The main aim of the preliminary work on Moiré sensors has been to prove the principle of operation. The results illustrate the versatility of Moiré gratings and also the ability to tailor the grating profile to the specific needs of the application. The Moiré sensors offer the potential for the highest spatial resolution for distributed sensing and it should be possible to improve the strain and temperature resolution with more sophisticated signal processing methods.

Table 5.2 compares the properties of arrays and Moirés relevant to sensing applications. The main advantage of the Moiré sensors over grating arrays is the potential for increased spatial resolution. The spatial resolution of grating array sensors is severely limited by the grating length. The gratings can be apodised using the technique described in the apodisation chapter down to lengths of 1mm, however, there is a penalty to be paid in increased spectral bandwidth. It is possible to make gratings as short as 500µm which are unapodised, and have a reduced bandwidth penalty. The Moiré gratings, in contrast, effectively have point sensors (depending on how the physical size of the sensor is defined). It could be argued that the sensor size in a Moiré grating is actually as small as 0.5µm, due to the fact that the passband in the grating is caused by the phase shift in the refractive index modulation. In addition, the bandwidth of the passbands in the Moiré spectrum is determined by the maximum transmission loss of the grating. The spatial resolution of the arrays is limited by the length of the gratings themselves, whilst for the Moirés it should be possible to have a spatial resolution <100µm. The real limitation on the spatial separation of the sensors in the Moiré is the spectral spacing required between the passbands and therefore the chirp rate required. The transmission loss of the Moiré is limited for gratings with very rapid chirp rates due to the photosensitive refractive index available. The dynamic range between the peaks and troughs in the system is important for signal processing, the extra peaks in unapodised gratings viewed in reflection cause problems for systems which detect peaks, as they can be detected as main peaks and give spurious readings. The Moiré gratings have limited dynamic range, but the peaks are cleaner than those in the arrays and so should cause less problems. The real limitation on the dynamic range in both cases is the available refractive index, mentioned earlier. However, in the case of arrays, the maximum possible dynamic range is most affected by the limited refractive index in transmission. In reflection the dynamic range (in dBs) is less affected, and in some cases is better for weak gratings, though for weak gratings there is significant loss of power in reflection.

5.5 Novel Grating Based Sensor

The work in the following section was carried out in collaboration with Tom Allsop of Plymouth University, who provided the specifications for a sensor. The aim of the sensor was to imitate the response of an interferometer, using a fibre Bragg grating.

5.5.1 Concept

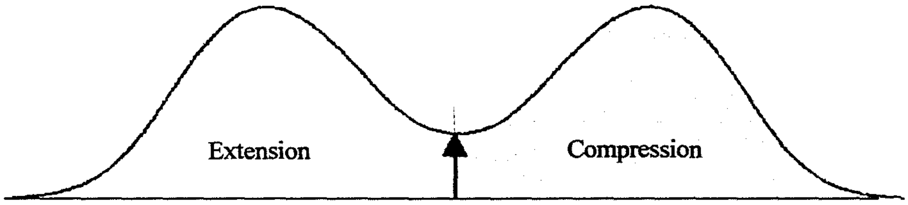

(a) Sensor Operation Regimes

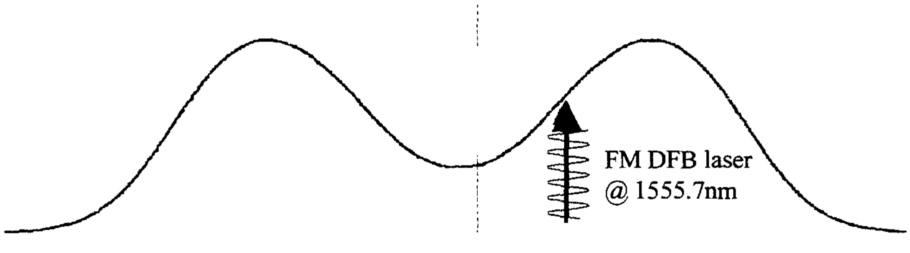

(b) Compressed Grating

Figure 5.23: How the sensor grating works and is interrogated (a) shows the regions of the grating which measure the grating under strain and compression respectively, and the position of the DFB at zero strain (b) shows the interrogation of the grating in a compressed state.

The sensor system was designed at Plymouth University. The idea was to measure the change in gradient of the novel grating reflection spectrum at a given wavelength and thus deduce the induced strain. The reflection profile of the sensing grating was designed so that the response of the system would mimic that of an interferometer. The grating was interrogated in reflection by a frequency modulated DFB laser with an operating wavelength of 1555.7nm (the specified central wavelength of the grating). As the grating was subject to extension, the grating profile shifted to higher wavelengths. In compression the profile shifted to shorter wavelengths. The position in the grating profile which was interrogated by the DFB changed accordingly, as shown in Figure 5.23(b). Figure 5.23(a) shows the regions of the grating profile used for the 2 regimes. The system measured the amplitude of the first and second harmonics of the resultant signal from the grating and FM DFB.

Theory

The first and second harmonics in the photodetector signal are generated by the interrogation of the grating profile by a modulated DFB laser, whose signal phase may be written as:

$$\phi_{dfb} = \phi_d + \phi_s \sin(\omega_s t),$$

Equation 5-9

where ϕ_d is the phase contribution from noise sources, and ϕ_s from the signal. The photocurrent of the detector then can be written as

$$I_D = I_{OD}\left[1 + V\cos(\phi_d + \phi_s \sin(\omega_s t))\right].$$

Equation 5-10

The resultant frequency spectrum of the signal received by the photodetector is, [211]

$$\begin{aligned}\cos(\phi_d + \phi_s \sin(\omega_s t)) = \cos\phi_d &\left\{J_0(\phi_s) + 2\sum_{i=1}^{\infty} J_{2i}(\phi_s)\cos(2i\omega_s t)\right\} \\ -\sin\phi_d &\left\{2\sum_{1=0}^{\infty} J_{2i+1}(\phi_s)\sin[(2i+1)\omega_s t]\right\}.\end{aligned}$$

Equation 5-11

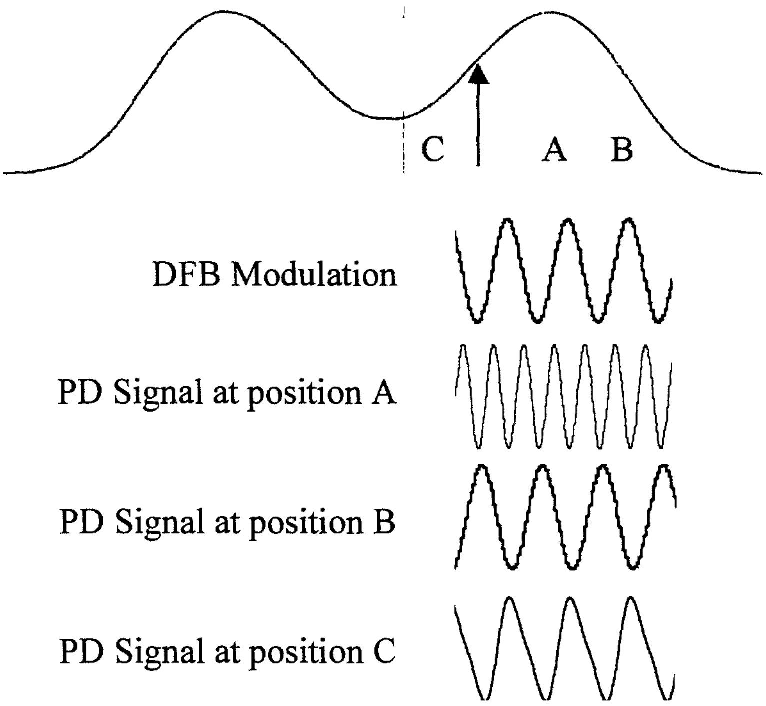

Figure 5.24: How the second harmonic amplitude modulation is generated at different points (A,B,C) on the grating spectrum.

Figure 5.24 can be used to explain how the second harmonic is generated as a result of interrogation of the grating profile by a FM DFB. At position A, the maximum amplitude occurs in the middle of the frequency range of the modulated DFB. At the maximum and minimum frequencies of the DFB, the amplitude is lower than at the mid-frequency, resulting in an amplitude response which is double the frequency of the laser modulation. At position B, the response of the grating profile is approximately linear, and so the gradient does not change over the frequency range of the DFB. The resultant amplitude response at this position is a direct replica of the modulation imposed on the DFB. At position C, the response is some combination of higher order harmonics resulting in an amplitude response similar to that shown in the figure.

System

The system used to interrogate the sensor is shown in Figure 5.25. The laser is modulated at a frequency ω_0. The reflection of the DFB signal off the sensing grating is detected via 2 lock in amplifiers, one tuned to ω_0, and the other to $2\omega_0$. By plotting the signals recorded from each of these lock-in amplifiers against each other, the gradient of the grating profile at the wavelength of the DFB can be obtained. The expected lissajous plot shape should be a colloid shape.

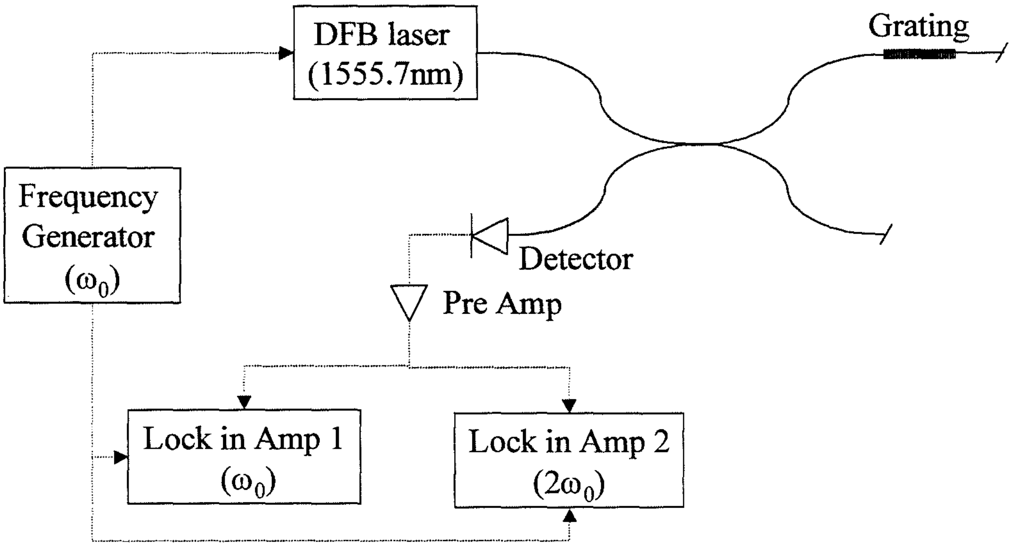

Figure 5.25: The system used for interrogating the sensor

5.5.2 Grating Specifications

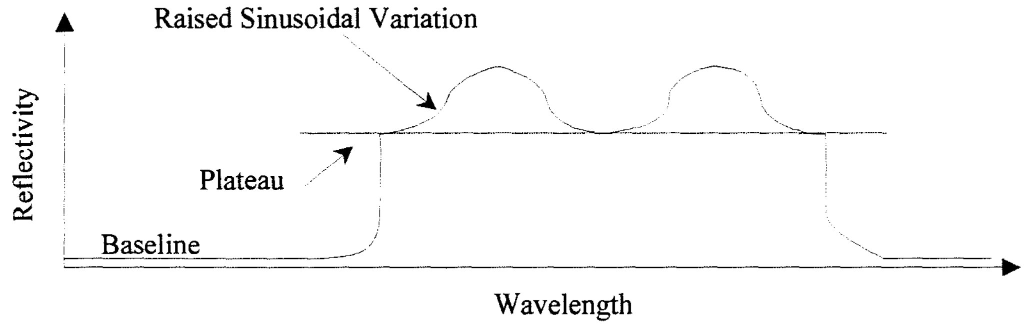

Figure 5.26: The specification for the spectral response of the sensor

Table 5.3 details the specifications for the sensor. The grating was to be used as a point sensor, and so had to be as short as possible.

Bandwidth	1.5nm
Central Wavelength	1555.7nm
Grating Length	As short as possible
Spectral Profile	See Figure 5.26

Table 5.3 : Plymouth sensor specifications

5.5.3 Grating Design

The simplest design option was to control the variation of grating transmission with wavelength by adjusting the grating refractive index modulation amplitude along the length of a chirped grating. This approach was modelled using IFO_Gratings and the results are shown in Figure 5.27. Figure 5.27 shows modelled grating responses for 1cm long gratings, with various maximum refractive index modulations. The following normalised apodisation function was used to vary the coupling constant along the length of the grating:

$$a(z) = \left[0.5 + \cos\left\{ \pi - \left(\frac{2\pi x}{l} \right) \right\} + \left[0.5 + 2\cos\left\{ \pi - \left(\frac{4\pi x}{l} \right) \right\} \right] \right] \Big/ 2.5 .$$

Equation 5-12

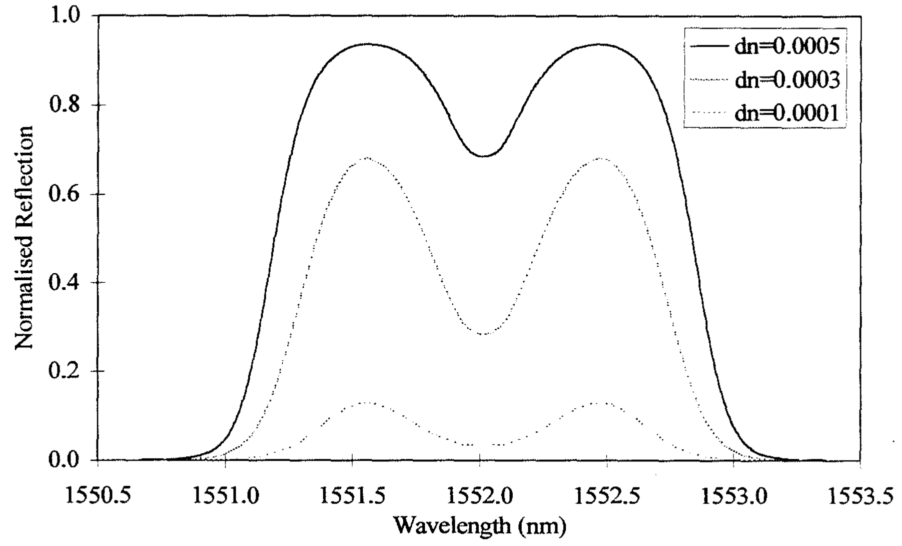

Figure 5.27: The modelled effect of varying the grating refractive index on the spectral response of the filter

In Figure 5.27 the dependence of the grating shape on refractive index modulation is shown. If the refractive index modulation is too strong then the grating shape becomes distorted from the ideal sine wave shape. Equally, if the refractive index modulation is too low, the dip in the centre of the profile is not raised up above zero sufficiently. It is necessary to have a compromise between achieving the desired spectral shape and the loss associated with a reduced refractive index modulation. The maximum possible grating transmission is ~70% before the shape begins to distort.

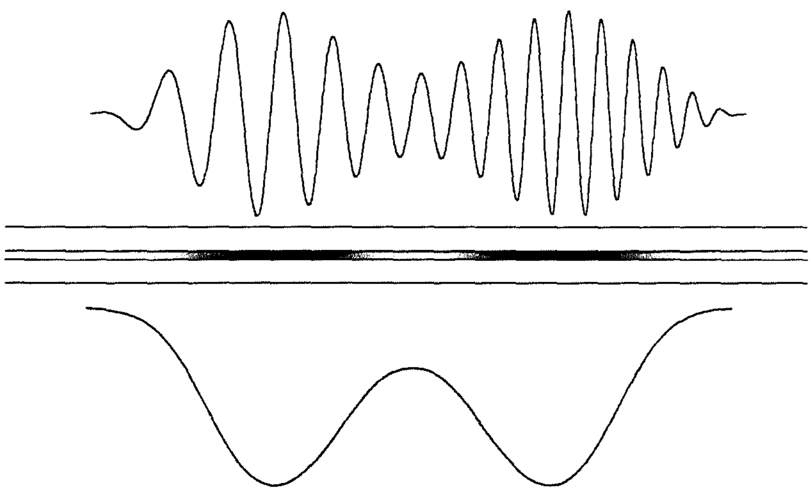

Figure 5.28: The refractive index profile and transmission spectrum of the grating novel grating sensor.

A simple representation of the special grating designed for the sensor is shown in Figure 5.28. It is important that the average refractive index remains constant along the grating length in order to insure that the chirp remains linear and is not distorted by increasing or decreasing refractive index.

5.5.4 Grating Fabrication and System Results

The gratings were fabricated using the scanning phasemask technique with the apodisation performed, as described previously, by dithering the phasemask during exposure. (Due to the required grating profile, it was only possible to fabricate the grating using phasemask techniques). The minimum possible fabrication length of the grating was determined by the choice of phasemasks available. A 2nm chirped e-beam fabricated phasemask was used, the grating length was 1cm. In order to achieve the required central wavelength high germania doped fibre was used, which gave a grating centre wavelength ~7.5nm higher than a similar grating fabricated using the same phasemask in boron germania co-doped fibre. The fibre was then strained slightly during exposure in order to lower the grating wavelength slightly to that specified.

Figure 5.29 shows the measured spectrum and model of a sensor that provided good strain measurements. There is however, a slight asymmetry in the profile, probably caused by misalignment of the fibre during fabrication. There is also quite a lot of noise on the spectrum, which may reduce the accuracy of the sensor. However, the general shape of the sensor is that required and the experimental spectrum agrees well with theory.

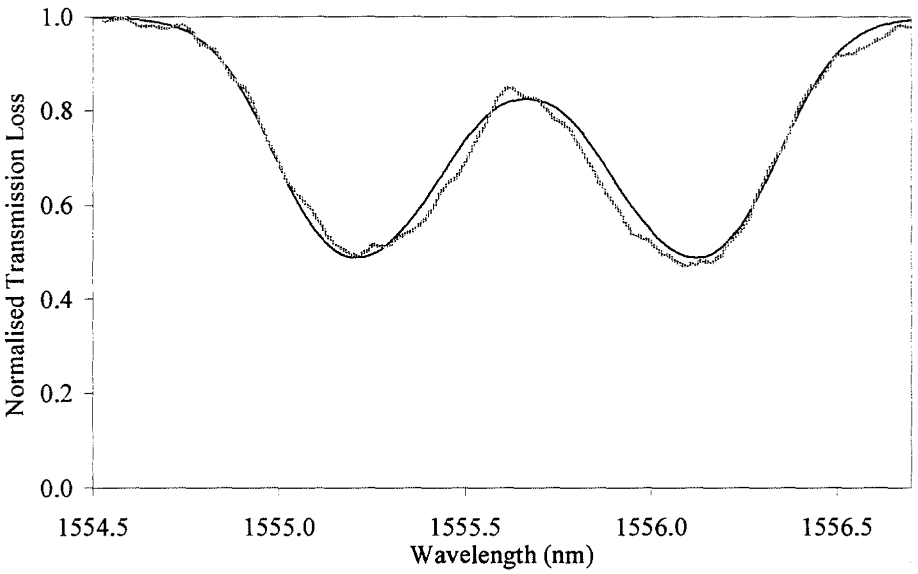

Figure 5.29: The measured and modelled spectra of a grating, which provided good results.

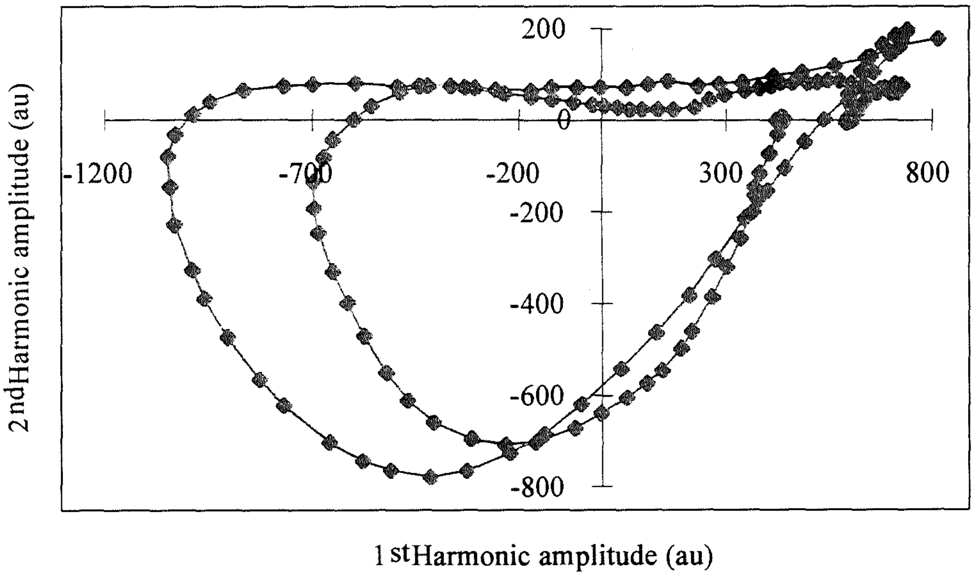

Figure 5.30: Results from the working sensor (spectrum shown in Figure 5.29) showing the characteristic shape expected. The 2 curves shown are for compression and extension of the sensor.

The results from a working sensor are shown in Figure 5.30. The two lines are for the full range of compression and tensile strains, which can be detected by the sensor. The shape is not a true colloid because of the grating shape at the edges of the profile – the gradient does not decrease to zero as it would if the sine wave were continuous. The tension and compression profiles are different shapes too, which is caused by asymmetry in the grating spectrum.

Fabrication Issues

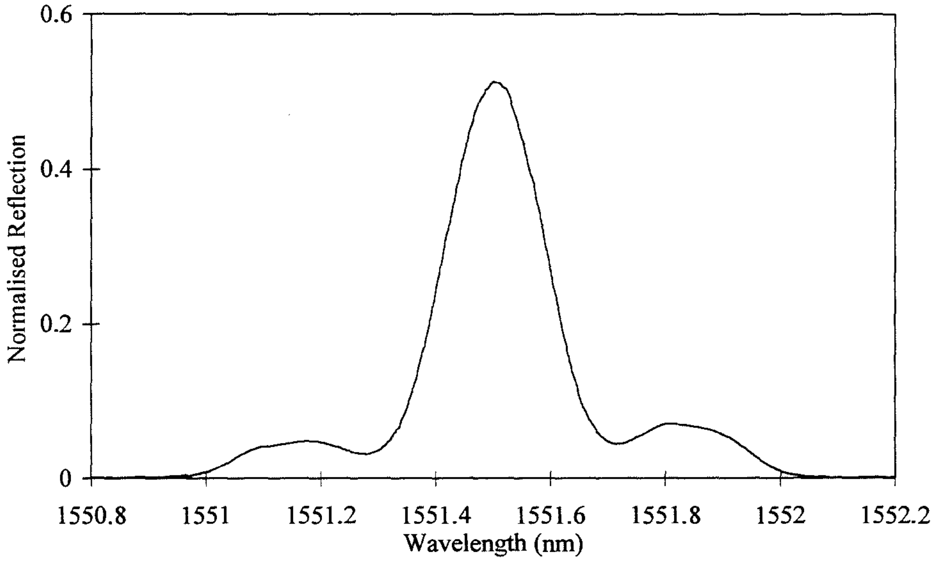

Figure 5.31: A 1cm grating with only 1nm chirp, displaying the central peak which appears between the two peaks in the grating design, due to the chirp on the grating being too small.

There were several problems encountered when fabricating the gratings, which are worth mentioning here. Figure 5.31 shows the grating profile obtained for a 1cm long grating with insufficient chirp. As the chirp of the grating is decreased, an inflexion develops in between the two peaks of the grating, and the height of this peak relative to the two peaks in the grating design gradually increases with decreasing chirp. The problem can also occur because the width of the incident UV beam is not infinitely small (width ~500μm). Increasing the width of the exposing beam has the effect of drawing the two peaks in the apodisation function closer together, giving rise to the inflexion problem, as the two peaks are then not spaced far enough apart in wavelength.

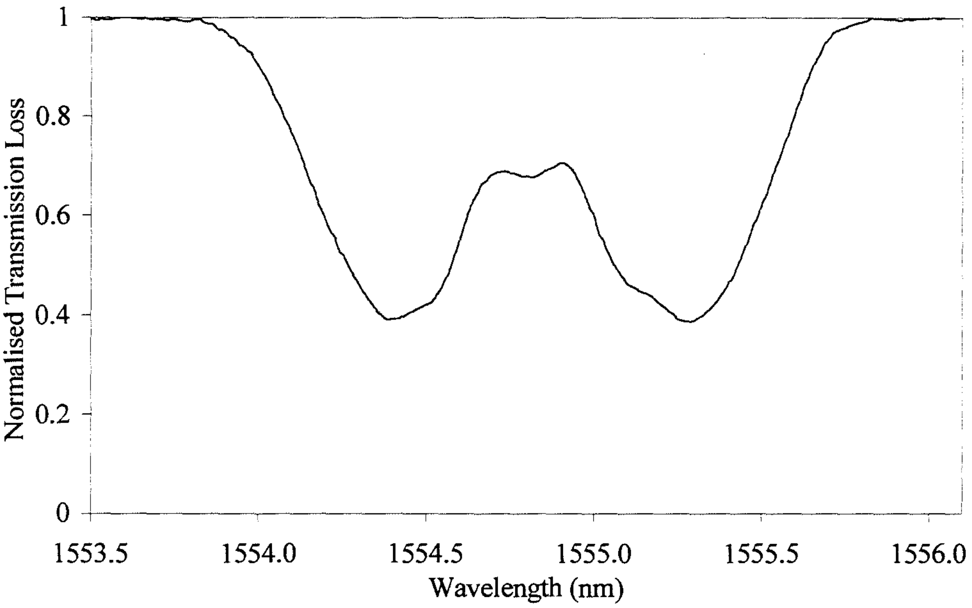

Figure 5.32: A grating with the refractive index modulation too high, causing the inflexion problem.

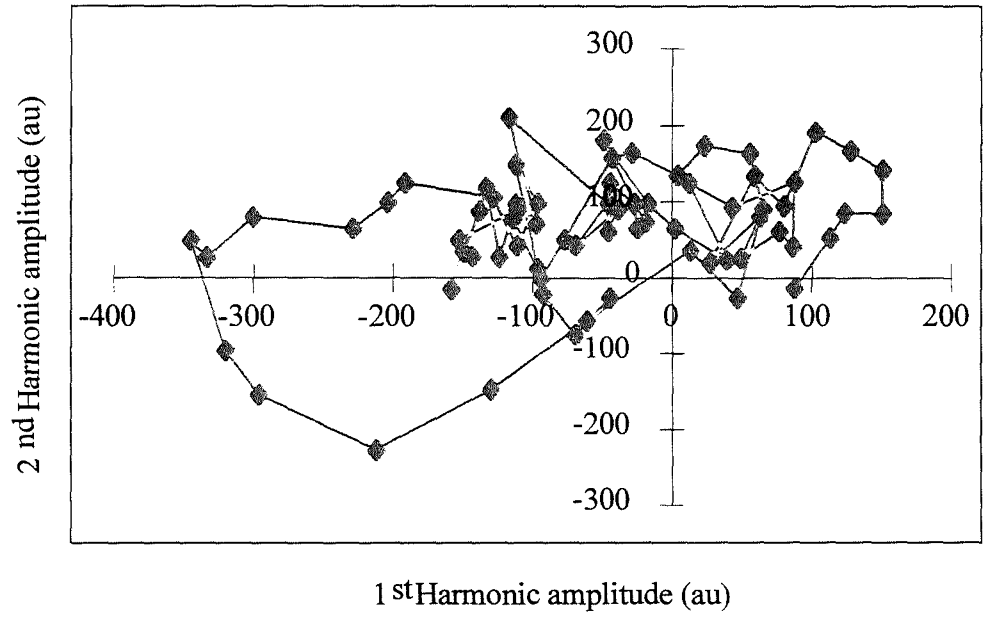

Figure 5.33: Results for the sensor with inflexion problem

Another grating exhibiting the inflexion problem is shown in Figure 5.32. The most likely cause of the inflexion in this grating is that the maximum grating transmission loss is too high. Not only is there an inflexion, but the shape of the peaks is distorted also. The system results from this grating are shown in Figure 5.33. The results can be used to give no information about the strain on the sensor, this is caused by the inflexion problem discussed on page 163. Though the achieved spectrum of the grating does not appear to be that different from the specification, the problem is caused by the gradient of the grating spectrum changing far more frequently than that of the specified spectrum.

5.6 Chapter Summary

Two different methods of performing distributed sensing measurements using fibre Bragg gratings have been demonstrated. The design of grating arrays for use as quasi-distributed sensors has been discussed, with particular emphasis on the required apodisation of the individual gratings. The arrays of very short gratings (2mm) have been used to measure strain and were shown to be effective strain sensors, capable of measuring changing strain profiles over a few millimetres. The highest spatial resolution achieved using this technique was 2.5mm, with 4 adjacent apodised uniform period gratings. The spatial resolution was limited by the necessary length and separation of the apodised gratings. Apodising the individual gratings increased the dynamic range required for locating the grating peaks in reflection to >15dB. However, apodisation of such short gratings resulted in a grating peak bandwidth of typically 0.5nm, resulting in a low spectral and strain resolution.

Chirped Moiré gratings have been presented as a solution to many of the shortcomings associated with the use of grating arrays as distributed sensors. In this chapter, CMGs have been used as distributed sensors for the first time to my knowledge. The chirped Moiré grating provides a superior solution to distributed sensing problems when compared to the grating arrays. Phase shifts along the grating length behave as quasi-point sensors, which correspond to narrow passbands with well defined peaks in the grating transmission spectrum. The phase shifts mean that the Moiré gratings can be used to achieve high spectral and spatial resolution simultaneously, whereas an increase in spatial resolution for the arrays resulted in a decrease in the spectral resolution and vice versa. The CMGs have been successfully used to measure a number of different strain and temperature profiles with a spatial resolution of 450μm.

Finally, a novel grating sensor has been designed and implemented.

6 THERMAL DECAY OF BRAGG GRATINGS

6.1 Introduction

The commercial viability of fibre Bragg gratings is dependent upon the ability to predict their long term behaviour in terms of wavelength response and reflectivity [212]. Many applications require extremely high stability of the optical properties of gratings over long time scales. It has been shown that annealing gratings at temperatures higher than the operating temperature significantly increases the stability, providing realistic operational performance over 50 years [213]. Grating lifetimes in various fibre types have been investigated [213,214,215,216,217], and hydrogen-loaded fibres [218,219,220,221,222,223] have also been studied.

To date, experiments have focused on decay of the grating refractive index modulation, but have not addressed the additional material decay of the fibre itself and how this affects the device lifetimes. Douay *et al* have reported the observed negative wavelength shift due to annealing gratings in purely Ge doped fibres [224]. However, to my knowledge the results in this chapter are the first to be presented showing how the centre wavelength shift of gratings as a result of annealing is affected by the addition of boron to the fibre. The combination of the changing optical properties of the B/Ge co-doped fibre and the decay of refractive index modulation of the gratings results in some positive wavelength shifts being observed. The findings presented in this chapter have been published [225] and highlight the importance of considering the changing fibre properties in addition to those of the grating itself when predicting device lifetimes.

The first part of this chapter investigates the general decay of the gratings themselves and the different rates of decay in 3 types of silica fibres: standard telecommunication fibre (typically 3-5 mol% Ge), high germania doped (~20 mol% Ge), and boron-germania codoped fibres (>20 mol% Ge). The second part concentrates on the wavelength shifts due to annealing gratings in boron-germania codoped silica fibres and particularly the affect of the boron present in the fibre on these wavelength shifts.

6.2 Grating Refractive Index Decay

6.2.1 Background

Atkins and Mizrahi have shown that thermal erasure of Bragg gratings in Ge doped fibres involves the significant reversal of changes to the fibre absorption spectrum which are induced by UV exposure[226]. Erdogan *et al* have presented a simple picture of the photosensitive process represented by a continuum of trapped states and an empirical model describing the decay of the UV induced index modulation [213] in Al/Ge/Er doped fibres[10]. This decay of induced refractive index modulation results in a decrease in the average refractive index of the fibre core, producing a negative Bragg wavelength shift. Erdogan investigated gratings fabricated in Al/Ge/Er doped fibres and showed that the decay of the UV induced index modulation can be represented by the normalised integrated coupling constant (ICC),

$$\eta = \frac{1}{1 + A\left(t/t_1\right)^{\alpha}},$$

Equation 6-1

where $A = A_0 exp(aT)$ and $\alpha = T/T_0$. This theory has since been verified experimentally by Williams *et al* for the decay of gratings in boron-germania co-doped fibres [217], although gratings made in this fibre decay more rapidly than those made in other types of fibres.

---

[10] See section 2.6.2

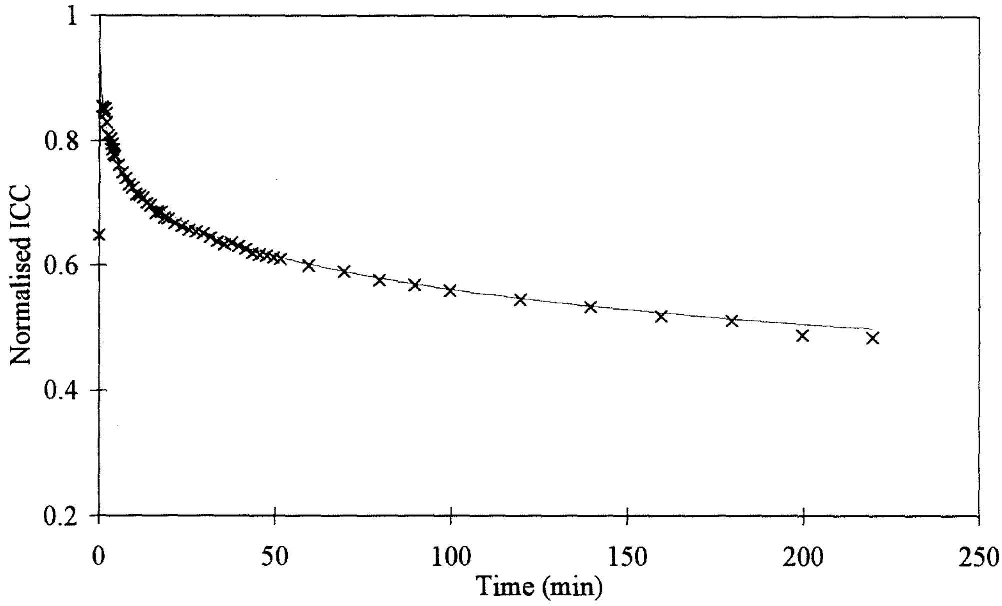

Figure 6.1: Decay of grating annealed at 350°C in B/Ge fibre (R~70%).

Figure 6.1 shows the decay of the ICC of a 70% reflectivity uniform period grating at 350°C (length 9mm), fabricated in the B/Ge fibre used in this investigation. The normalised ICC is proportional to the UV induced refractive index modulation of the grating and is calculated from the measured transmission data using the following relation:

$$\eta = \tanh^{-1}\sqrt{1-T_{trans}}$$

Equation 6-2

where η is the ICC, and T_{trans} is the grating transmission minimum. The theoretical fit was obtained using Equation 6-1 with the values for the constants $A_0=(3\pm 1)\times10^{-6}$, $\alpha=(1.88 \pm 0.02)\times10^{-2}$ K^{-1} and $T_0=(2000 \pm 50)$ K following the same general trend reported by Williams *et al* for B/Ge fibre. The initial value of refractive index modulation was calculated from the grating reflectivity and bandwidth using coupled mode theory[11] [227]. Following an initial rapid decay in the grating strength, the rate of change in the refractive index modulation decreases, and the grating becomes

---

[11] See section 2.2.1

more and more stable. Erdogan also showed that this decay process could be accelerated by annealing the gratings at elevated temperatures for a reduced length of time. This pushes the ICC to a point along the decay curve where the decay over 25 years (for example) is negligible. If the grating in Figure 6.1 were annealed for 6 hours at 350°C, the equivalent decay time at an operating temperature of 80°C would be 4×10^{12} years. The relation giving this equivalent decay was derived by Erdogan from Equation 6-1 as:

$$t_2 = \exp\left[aT_0\left(\frac{T_1}{T_2} - 1\right)\right] t_1^{(T_1/T_2)},$$

Equation 6-3

where t_2 is the equivalent time for which a grating has to be annealed at temperature T_2 in order to yield an equivalent decay to that obtained for heating at T_1 for a time t_1.

6.3 Effect of Annealing on Gratings in B/Ge Fibres

It is known that the type of fibre used in the fabrication of FBGs can greatly affect the stability of gratings at high temperatures. Williams *et al* showed that the decay of gratings fabricated in B/Ge fibres is more rapid than in the Al/Ge/Er fibre used by Erdogan. The grating decay properties vary greatly with fibre composition and so it is necessary to characterise the behaviour of gratings in each fibre independently.

Boron/germania co-doped fibre is highly photosensitive, leading to higher refractive index modulations for lower UV powers and shorter exposure times [228]. The introduction of boron is used to counteract the increasing refractive index of the core due to the increased concentration of germania. This allows the photosensitivity of the fibre to be increased whilst maintaining the numerical aperture at the required value. However, the addition of boron makes the core softer and, consequently, less easy to draw into a circular core. Still, boron fibre is especially useful in situations where standard fibre will not suffice. For instance, when making gratings with the quadrupled Nd:YAG laser, where the irradiating wavelength is in the tail of the absorption band of the fibre, or when a large refractive index modulation ($\Delta n>10^{-3}$) is required. A drawback though, is that gratings fabricated in B/Ge codoped fibres exhibit far lower thermal stability than those fabricated in other Ge codoped fibres[216]. At the time that the work contained in this chapter was carried out, there was little published data on the behaviour of gratings in B/Ge fibre. In particular, there was no information on the expected wavelength shift of gratings in B/Ge fibres during annealing, or during the grating lifetime. This chapter aims to address this omission.

Experimental Procedure

The gratings under investigation were fabricated in 3 types of fibre: boron-germania codoped, standard telecommunications and hi-germania doped silica fibres, all of which are single mode at 1550nm. Uniform period gratings were fabricated holographically [229] using a cw argon ion laser (244nm wavelength). Type I gratings were fabricated with a length of 6mm and a range of refractive index modulations in both hydrogen-loaded and non-hydrogen-loaded fibre, producing a range of UV induced index modulations. The gratings were intrinsically apodised by the Gaussian profile of the laser beam. The fibres were hydrogen-loaded at 150 atmospheres at room temperature for at least 2 weeks prior to grating inscription and then stored for 2 weeks at room temperature following inscription to allow out-diffusion of the hydrogen [230], thereby ensuring that subsequent measurements were not influenced by this out-diffusion process. Each grating was spliced onto longer pigtails to facilitate monitoring of the grating spectrum during the annealing process.

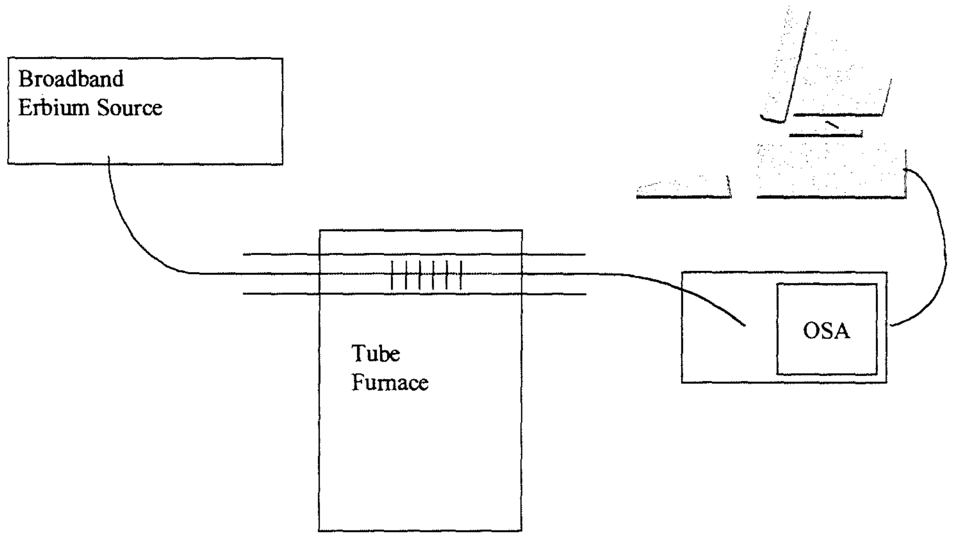

Figure 6.2: Experimental set-up for monitoring gratings during annealing

The experimental arrangement for monitoring the gratings during annealing is shown in Figure 6.2. Each of the gratings was annealed isothermally in a temperature controlled tube furnace for 6 hours at a constant temperature in the range 150°C to 475°C; care was taken not to strain the fibre in the tube. The grating transmission spectra were monitored during the annealing process using an optical spectrum analyser (OSA) and broadband erbium fluorescence light source. The grating spectra were recorded during the annealing process, at set time intervals the central wavelength and transmission loss of the grating were calculated and recorded. In addition to this monitoring, the grating spectra were also measured at room temperature before and after annealing.

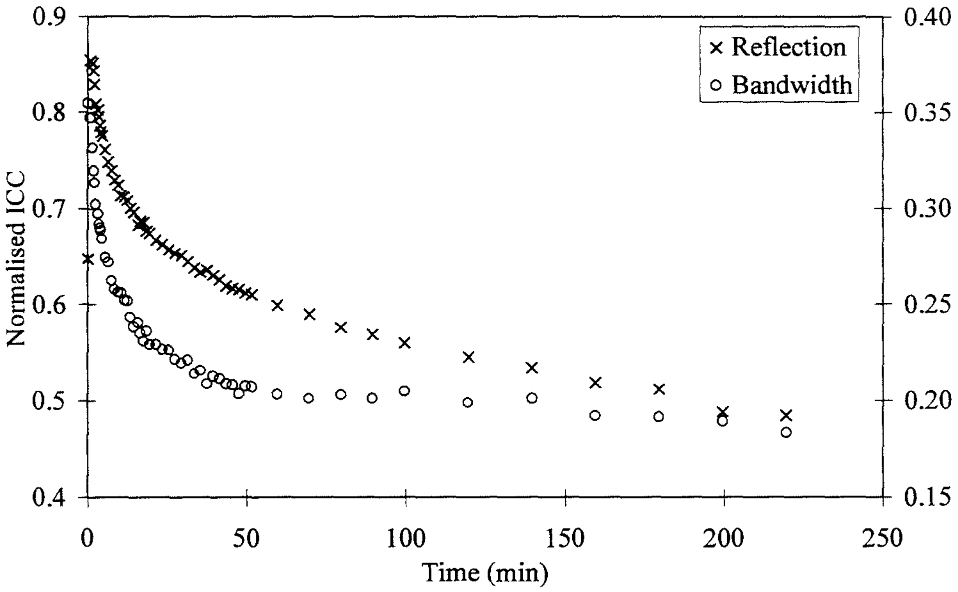

Figure 6.3: Change in bandwidth and coupling constant for a grating in B/Ge fibre at 350 ℃.

Figure 6.3 shows the evolution of the bandwidth during annealing of the grating shown in Figure 6.1, the decay of the ICC is also shown for comparison. The bandwidth of the grating decreases as the grating decays, which is to be expected as the bandwidth is dependent upon the UV induced refractive index modulation.

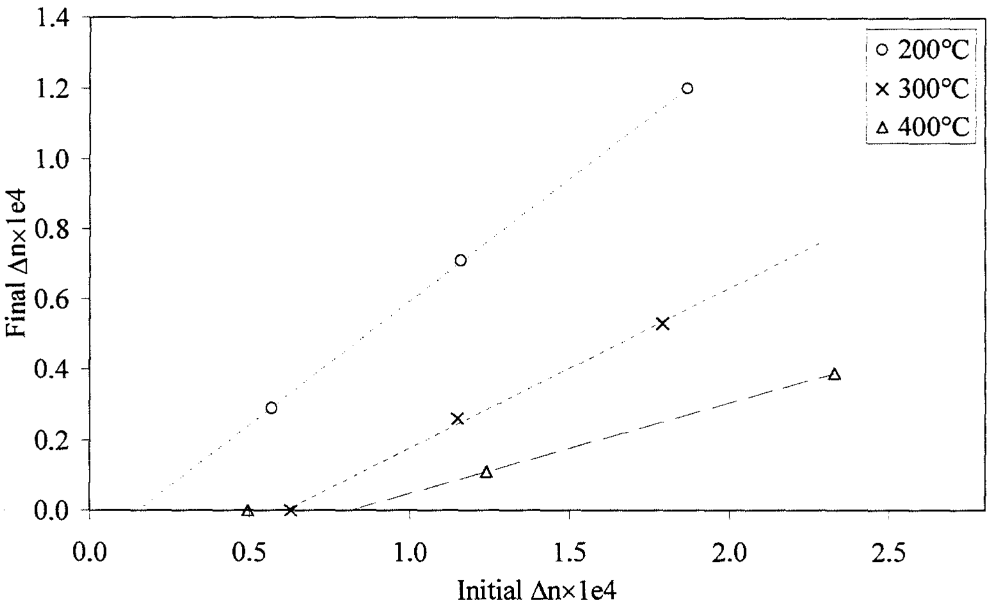

Figure 6.4: Change in refractive index with temperature for gratings annealed for 6 hours in B/Ge fibre.

As can be seen in Equation 6-1, the amount of Δn decay experienced by a grating is dependent upon the annealing temperature. Figure 6.6 compares the refractive index modulations of gratings with initial transmission losses of 50, 70 and 90% and of length 6mm before and after 6 hours annealing at 200, 300 and 400°C, in the non-hydrogen-loaded B/Ge fibre. There is an increase in the fractional decay of Δn with annealing temperature, indicating a higher decay rate at higher temperatures. The weakest gratings at both 300 and 400°C have disappeared, confirming that gratings fabricated in B/Ge codoped fibres have poor high temperature stability.

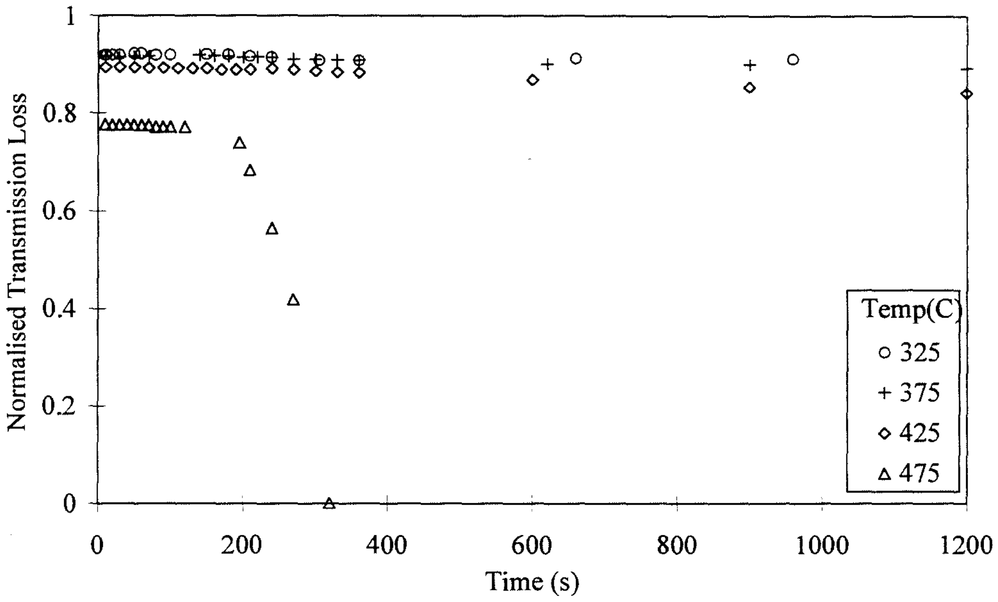

Figure 6.5: Changes in Reflectivity during isochronal annealing of a grating in B/Ge codoped fibre.

In Figure 6.5, a grating fabricated in hydrogen loaded B/Ge codoped fibre was annealed initially at 325°C and then the temperature was increased in increments of 50°C. The grating was held at each temperature for 20 minutes. The rate of decay of the grating increased slowly with each temperature increment until the rapid decrease in reflectivity and 'death' of the grating at the relatively low temperature of 475°C. Other authors give examples of good grating stability up to and above 700°C for other Ge codoped fibres, with codopants Pr,Al,Er and Sn for example [216,214]. This experiment again illustrates the poor temperature stability of gratings fabricated in B/Ge doped fibres.

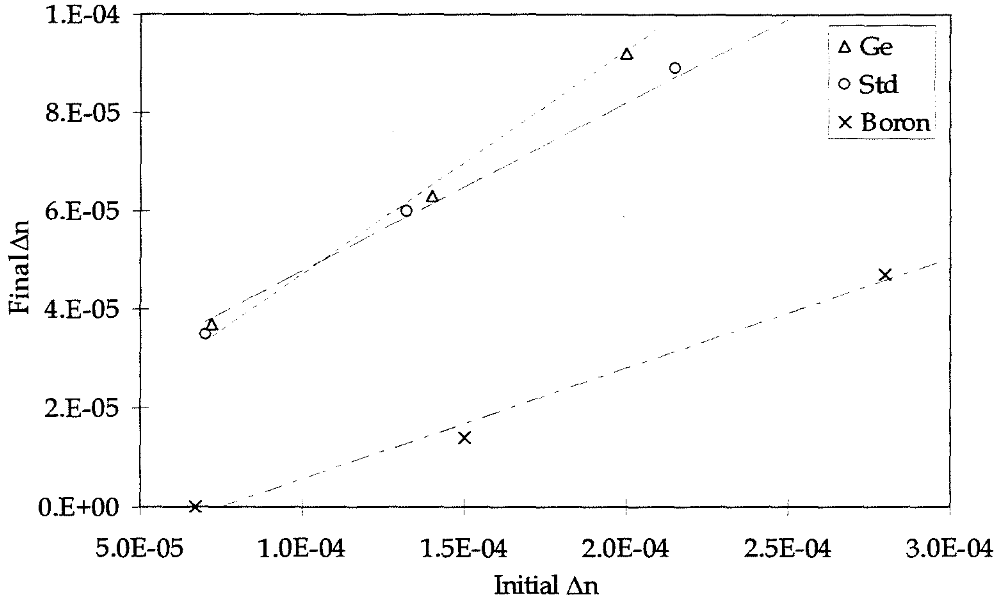

Figure 6.6: The variation in decay of gratings made in different fibres, annealed for 6 hours at 400°C.

The poor temperature stability of gratings in B/Ge fibre is compared to that of gratings in standard and highly Ge doped fibres in Figure 6.6. The remaining Δn of gratings in the B/Ge codoped fibres is less than half that of gratings fabricated in the other two fibres when annealed for 6 hours at 400°C. This high temperature behaviour of gratings in B/Ge fibres severely limits their use in harsh conditions.

6.4 Study of Annealing Wavelength Shifts in B/Ge Co-doped Fibres

This section of the chapter investigates the effect that the addition of boron to fibre core has on the shift in Bragg wavelength as a result of the decay of gratings in B/Ge codoped fibres.

6.4.1 Introduction

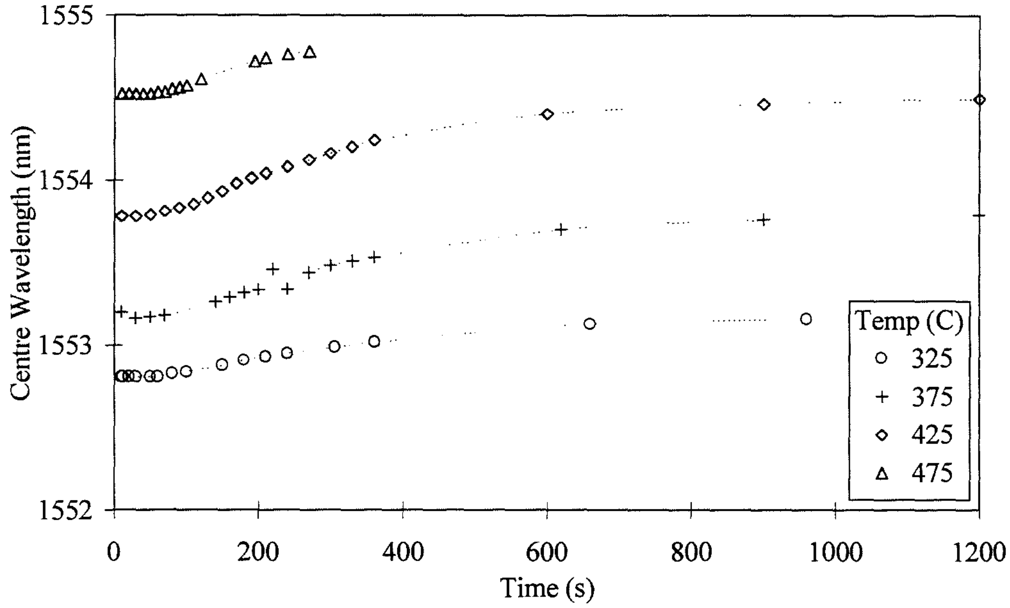

Figure 6.7: Changes in the Bragg wavelength of gratings in B/Ge fibre during isochronal annealing.

Whilst the introduction of boron to the fibre core increases the fibre photosensitivity, it brings with it complications involving the spectral response of the gratings with ageing. As discussed earlier, the stability of these gratings at elevated temperatures is poor. However, whilst annealing gratings in B/Ge fibre another effect was observed, illustrated in Figure 6.7. As the gratings were annealed, the Bragg wavelength *increased* rather than decreasing as would be expected if the only mechanism affecting the Bragg wavelength was that of the decay of the UV induced refractive index modulation. This wavelength increase became greater as the temperature was increased, until 475°C, where the rapid decrease in UV induced refractive index became the dominant effect and the grating disappeared.

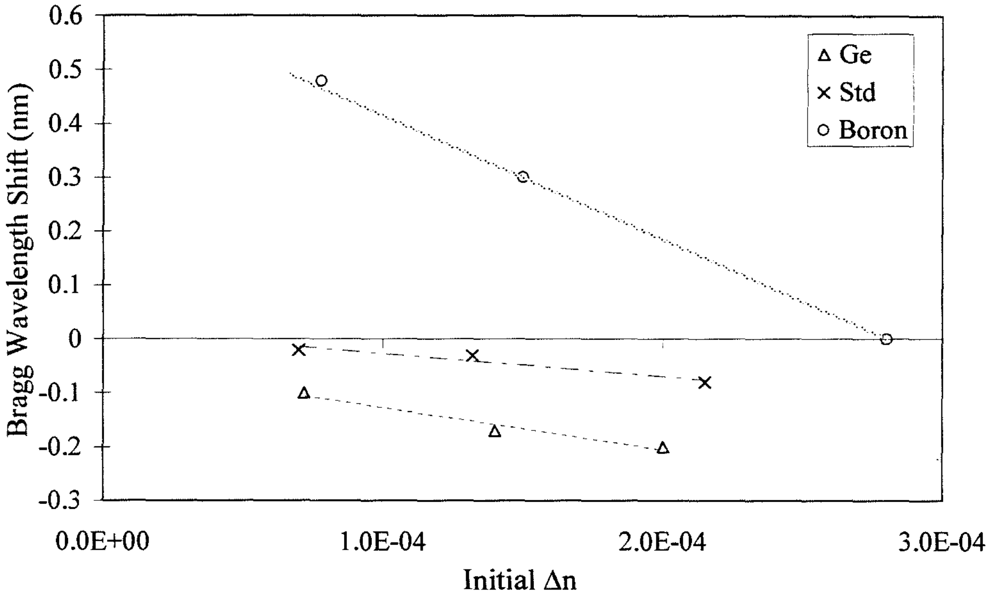

Figure 6.8: Wavelength shifts of gratings annealed for 6 hours at 400℃ in 3 types of fibres.

The magnitude of the wavelength shift can be seen in Figure 6.8, which shows wavelength shifts experienced by gratings fabricated in 3 different types of fibres annealed for 6 hours at 400°C. From this graph it can be seen that for gratings fabricated in pure germanosilicate fibres, stronger gratings experience a greater negative wavelength shift than weaker gratings associated with a greater decrease in refractive index due to the initial grating strength. However, for gratings fabricated in boron-germania codoped fibres, a shift to longer wavelengths is observed. In addition, the largest red wavelength shifts are observed for the weakest gratings. The remainder of this chapter explains this phenomenon in terms of combining existing theories in order to predict the wavelength shifts experienced by gratings in B/Ge fibres.

6.4.2 Theory

Two different mechanisms are responsible for the shift in Bragg wavelength of gratings in boron-germania co-doped fibres. The first is the decay of the UV induced refractive index, which results in a decrease in the average core refractive index (as described previously in this chapter). This mechanism explains the observed *negative* wavelength shift. However, it is evident from Figure 6.8, that this is not the only mechanism present in the annealing of gratings in B/Ge co-doped fibres which contributes to a change in the Bragg wavelength. Camlibel *et al.* showed in 1975 that the refractive index of borosilicate fibre cladding increases as the fibre anneals[231]. They showed that, as the fibre ages, the refractive index of the borosilicate cladding changes as follows

$$\Delta n_{boron}(t,T) = \Delta n_0 \{1 - \exp[-t/(\tau_0 \exp(F/k_B T))]\},$$

Equation 6-4

where F is the activation energy, k_B is Boltzmann's constant, and Δn_o is the difference in refractive index between fully annealed and fully quenched borosilicate glass. The temperature at which the borosilicate fibre is fully annealed is dependent upon the annealing time. This is illustrated in Figure 6.9; the values used to calculate the curves, F=0.91eV, $\tau_o=(1.3\pm0.2)\times10^{-6}s^{-1}$, $\Delta n_o=(4.5\pm0.5)\times10^{-4}$ were obtained from fitting this theory to our experimental data shown in Figure 6.11 later in the chapter. The graph shows that significant changes in refractive index can occur at below 100°C during device lifetimes, and also under the conditions required to anneal gratings after inscription.

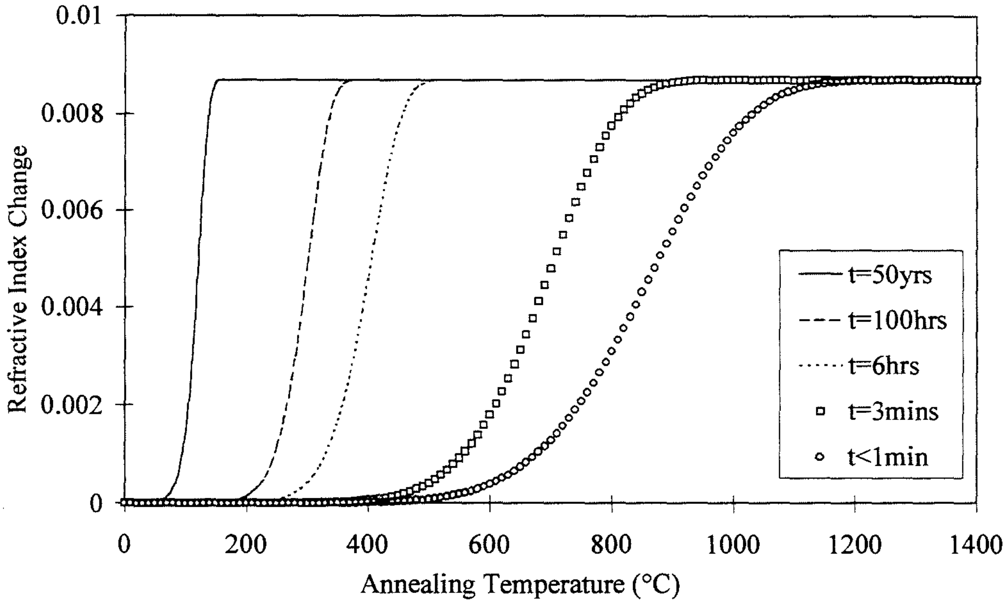

Figure 6.9: Refractive index changes of borosilica with temperature over various time scales.

In order to predict the wavelength shift experienced by gratings written in this fibre, both effects must be taken into account. The wavelength shift caused by annealing gratings in B/Ge fibres may be determined by

$$
\begin{aligned}
\Delta\lambda_{TOTAL} = {} & \textit{shift due to decay of } \Delta n \\
& + \textit{shift due to annealing of borosilica} \\
& + \textit{shift due to decay of UV induced DC contribution}
\end{aligned}
$$

$$\Delta\lambda_{TOTAL} = \lambda_{gr}\left\{\left(0.5\Delta n_{initial}(1-\eta)\right) + \Delta n_{boron} + \mathrm{N}\right\},$$

Equation 6-5

where

$$\Delta n_{final} = \eta\Delta n_{initial},$$

Equation 6-6

and λ_{gr} is the wavelength of the grating, $\Delta n_{initial}$ is the calculated initial index modulation, η is the final normalised ICC, and N accounts for any background UV induced refractive index change caused by non-unity fringe visibility.

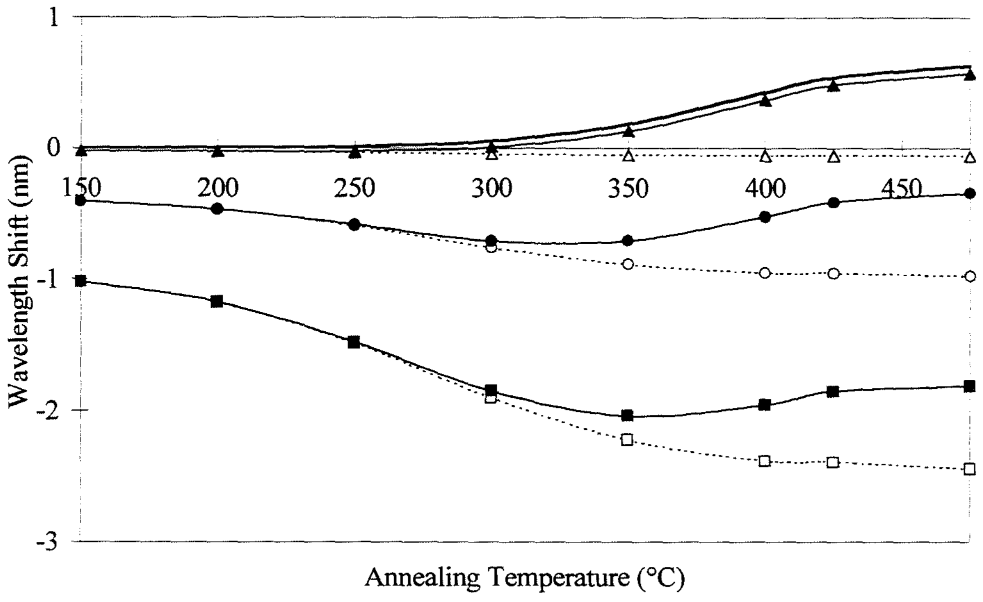

Figure 6.10: Predicted wavelength shifts for gratings of varying strengths fabricated in boron/germania co-doped fibre annealed for 6 hours.(——— Shift due to boron annealing, ▲ ($\Delta n=5\times10^{-5}$), ■ ($\Delta n=8\times10^{-4}$), ● ($\Delta n=2\times10^{-3}$). In each case the hollow symbols and dotted lines show the shift due to grating decay, and the solid line and symbol shows the total shift of the grating).

Using this simple empirical model it is possible to predict the wavelength shift experienced by a grating in B/Ge codoped fibre during annealing. Figure 6.10 shows the predicted wavelength shifts when annealing gratings with a variety of initial refractive index modulations (Δn=0.00005, 0.0008, 0.002). The solid lines with symbols represent the overall shift for a grating in this fibre. The heavy solid line at the top of the graph shows the refractive index change of the core due to annealing of the borosilica, and the dotted lines are the wavelength shift due to the grating refractive index decay. The wavelength shift experienced by the grating is dependent upon the initial strength of the UV induced refractive index modulation of the grating. For weaker gratings, the effect of the boron dominates, but for stronger gratings there is still a strong shift to shorter wavelengths. It can also be seen that over these timescales the boron is not significantly annealed until temperatures of ~400°C are reached.

6.4.3 Experimental Results

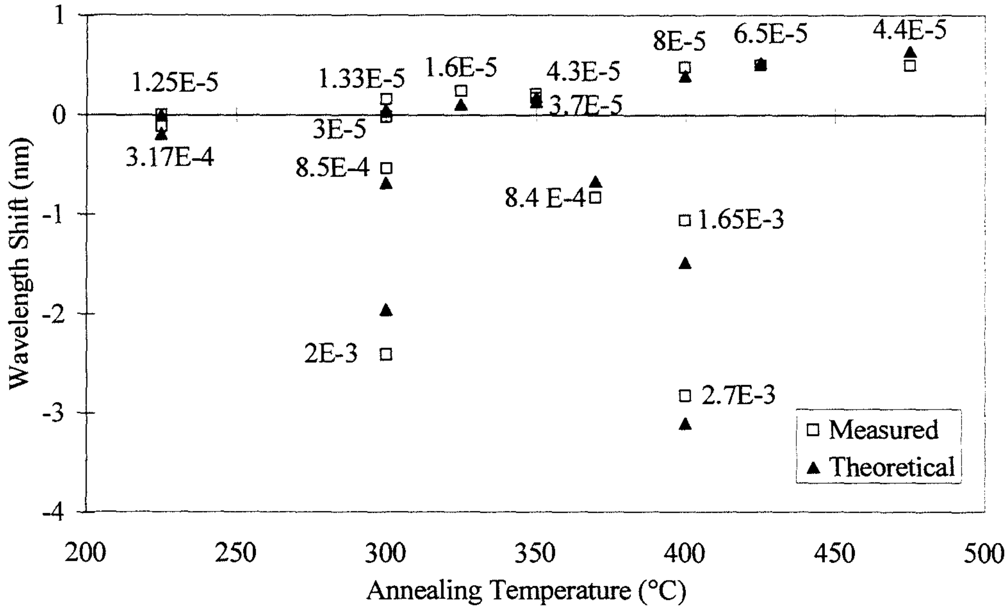

Figure 6.11: Experimental and predicted values of annealing wavelength shifts for gratings of varying initial refractive index modulations (values beside data points) annealed for 6 hours.

To verify the model, a number of type I gratings [6] were fabricated in hydrogen-loaded B/Ge fibre, using a uniform period phasemask [232] and a pulsed frequency quadrupled Nd:YAG laser (266nm wavelength). The gratings were of varying length and reflectivity, producing a range of UV induced index modulations.

Figure 6.11 shows the wavelength shifts experienced by gratings annealed for 6 hours at several temperatures. The initial UV induced refractive index modulation of each of the gratings is given alongside the corresponding data point and was calculated using coupled mode theory [11]. The theory in Equation 6-5 has been fitted and is shown as ▲ on the graph. Fitting the data yielded values of F=0.91eV, $\tau_0=(1.3\pm0.2)\times10^{-6}s^{-1}$, $\Delta n_o=(4.5\pm0.5)\times10^{-4}$. Shifts to longer wavelengths as large as 0.75nm were observed for gratings with an initial refractive index modulation of $<1\times10^{-4}$. This occurs where the positive change in refractive index of the fibre core due to annealing of the boron is far greater than the negative average change in refractive index due to decay of the UV induced refractive index modulation. In contrast, negative wavelength shifts of up to 2.83nm have been observed for gratings in B/Ge fibre with initial $\Delta n = 2.7\times10^{-3}$. Such large negative shifts are due to the rapid decay of the grating structure in B/Ge fibres resulting in a reduction in reflectivity from 100% to 33%. Matching experimental and theoretical data shows agreement of wavelength shift of ± 0.05nm. This accuracy decreases for stronger gratings to ±0.3nm due to the difficulty in determining the initial refractive index for strong gratings.

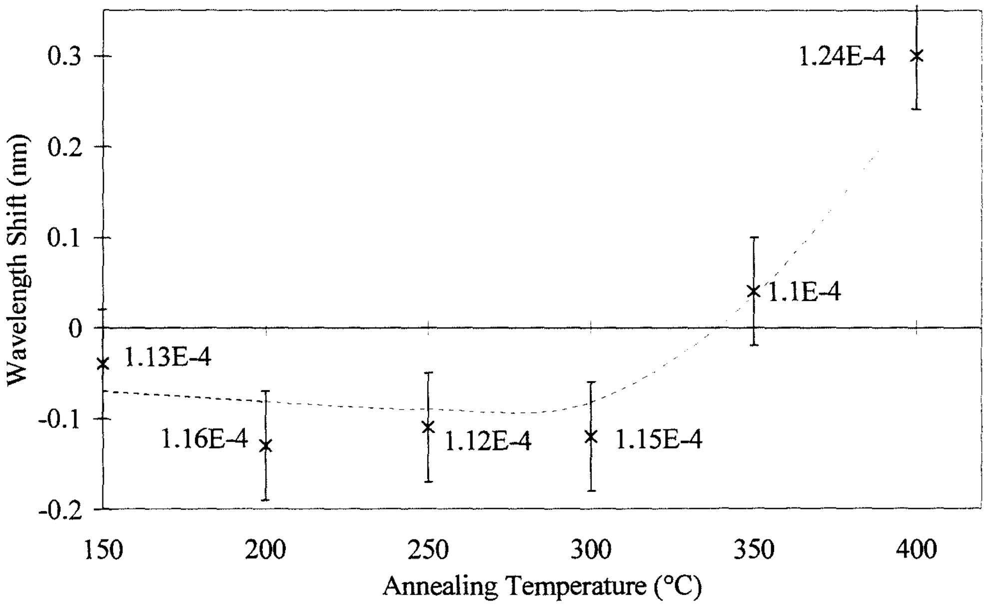

Figure 6.12: Experimental (points) and predicted values (line) of annealing wavelength shifts for gratings with initial reflectivity of ~70% annealed for 6 hours.

Figure 6.12 shows the wavelength shifts experienced by gratings with initial $\Delta n \sim 1.1\times10^{-4}$ annealed for 6 hours at different temperatures: these gratings were fabricated in non-hydrogen loaded B/Ge-doped fibres using the argon ion laser and side exposure holographic technique. As the temperature is increased to 275°C, an increasing downward shift the wavelength is observed. However, when 275°C is reached, the boron annealing begins to affect the wavelength shift and becomes more dominant than the negative shift caused by the decay of the grating itself.

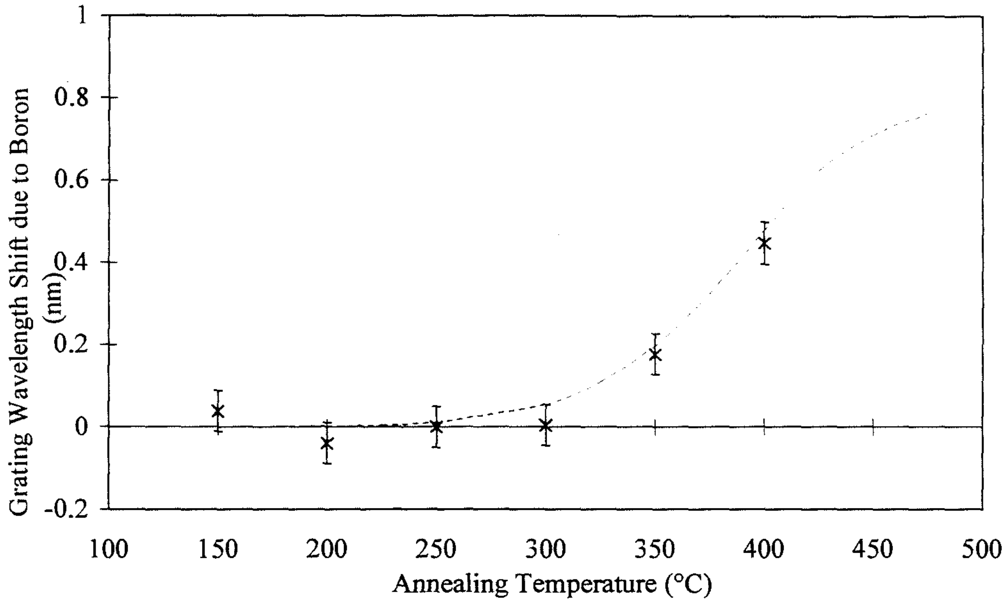

Figure 6.13: Experimental (points) and predicted values (line) of annealing wavelength shifts due to boron annealing for 6 hours.

Figure 6.13 shows the grating wavelength shifts, observed and predicted, due to annealing of boron alone. The data for Figure 6.13 was calculated from the experimental data in Figure 6.12 using Equation 6-5. The wavelength shift due to grating decay, calculated from the measured decay in reflectivity, was subtracted from the measured grating wavelength shift. Though this effect is pronounced, it is easily overlooked when annealing strong gratings, as can be seen in the modelled predictions in Figure 6.10.

6.5 Discussion

The decay of gratings fabricated in B/Ge fibres is markedly different from those in pure germanosilicate fibres. The decay of the grating structure in B/Ge fibres is more rapid than for those in germanosilicate fibres, with gratings not surviving for temperatures above ~450°C. The wavelength shifts exhibited by gratings in boron fibres are not only as much as 6 times larger than in germanosilicate fibres, but the wavelength shift is positive, not negative as is the case for germanium doped fibres. Both of these characteristics mean that the use of boron-germania doped fibres must be carefully considered when fabricating gratings for use in devices requiring long lifetimes, and robust behaviour.

Even at the highest temperatures at which gratings in B/Ge can be annealed before they are completely destroyed, the boron in the fibre is not completely annealed, meaning that the wavelength of annealed gratings could still increase during the grating lifetime. A grating made in this type of B/Ge fibre at ~1550nm can be expected to exhibit a wavelength shift up to 0.8nm due to annealing of the boron. For jacketed fibre one possible solution may be to pre-anneal the fibre before fabrication. An elevated temperature <200°C for at least one week would be required. However, temperatures this high have detrimental effects on fibre coatings and tend to make the glass brittle. These results have important implications for the implementation of grating devices in B/Ge fibres. Gratings fabricated in the fibre studied display complex properties on annealing. To ensure grating stability, the boron in the fibre must be completely annealed and thus care should be taken when predicting the lifetimes of gratings. In addition, as the borosilica anneals, the refractive index of the fibre core increases, meaning that the boron may no longer do the job of reducing the refractive index. This work may also have implications for gratings made in suppressed cladding mode fibres (which have boron added to the cladding to lower the refractive index)[233]. Annealing effects will have to be considered carefully, as the refractive index of the cladding will rise if the gratings are annealed in the conventional manner. This may reverse the mode suppression effect that the boron was introduced for.

	Non-hydrogen loaded B/Ge fibre	Hydrogen loaded B/Ge fibre
A_0	4×10^{-6}	3×10^{-6}
a	$1.9\times10^{-2}K^{-1}$	$1.88\times10^{-2}K^{-1}$
T_0	2000K	2000K

Table 6.1: Comparison between decay coefficients for gratings in non-hydrogen loaded and hydrogen loaded B/Ge codoped fibre.

Over the years, there have been varying reports on the effect of hydrogen loading on the annealing of Bragg gratings. In this study, no significant effects were observed; that is, the effect observed here, of the shift in Bragg wavelength due to annealing of the borosilica, is more dominant than any effect of hydrogen loading on the wavelength shift of gratings made in B/Ge fibres. However, the coefficients describing the decay of gratings for the cases of hydrogen loaded and non-hydrogen loaded gratings used in the study are shown in Table 6.1. The variation in values shown here is consistent with the error values previously quoted for the values in section 6.2.1. The results in this chapter show that under the conditions considered here, the effect of the hydrogen on the decay process does not seem to be significant.

6.6 Conclusions

Decay of FBGs in non-hydrogen loaded and hydrogen loaded B/Ge codoped fibre has been found to agree with the theoretical model presented by Erdogan over timescales of 6 hours, with values of $A_0=(3\pm 1)\times10^{-6}$, $a=(1.88\pm 0.02)\times10^{-2}\ K^{-1}$ and $T_0=(2000\pm 50)$ K for the decay constants. Grating bandwidth has been shown to decrease more rapidly than the ICC and stabilise more rapidly. As expected, higher annealing temperatures give rise to a greater decay of the grating refractive index modulation. The reported poor high temperature stability of gratings fabricated in B/Ge codoped fibre has also been confirmed with gratings becoming extinguished at temperatures below 500°C. The decay of gratings fabricated in 3 different types of fibre has been studied: standard telecommunications, high germania doped, and boron-germania-co-doped fibres. The gratings that show the least change in their properties during annealing are those fabricated in standard telecommunications fibres.

In particular, the thermal decay experienced by fibre Bragg gratings fabricated in boron/germania co-doped fibre has been studied. A shift of the Bragg wavelength during annealing of gratings in B/Ge codoped fibres has been observed. Two processes must be considered when modelling the effect of annealing: the thermal decay of the UV induced refractive index change of the grating and the thermal annealing of the boron related refractive index of the fibre. Grating wavelengths can shift to higher or lower wavelengths on heating depending on the initial refractive index modulation of the grating. For weak gratings (initial Δn $<2\times10^{-4}$) positive wavelength shifts of up to 0.5nm have been observed when heated at 425°C compared with a shift of -2.83nm for a strong grating (initial $\Delta n = 2.7\times10^{-3}$) heated at 400°C for 6 hours. Thus the combination of the change in optical properties of the fibre during annealing due to the added boron and the decay of the grating refractive index modulation has a significant effect on both the magnitude and direction of the central wavelength shift exhibited during annealing. By combining the theory on both processes, annealing wavelength shifts and long term behaviour of gratings in B/Ge fibre can be accurately predicted (±0.3nm). The theory has been shown to be in good agreement with the experimentally obtained data. There was no noticeable effect due hydrogenation of the fibres under the annealing conditions considered here.

7 THESIS CONCLUSIONS

The work contained in this thesis has been concerned with the fabrication and application of short and novel structure in-fibre Bragg gratings. The majority of the gratings were fabricated using the scanning phasemask technique. In particular, a fabrication utility based on a frequency quadrupled Nd:YAG laser (266nm) was developed, requiring methods for removing most of the power of the laser beam. A camera was installed to monitor the alignment of the fibre relative to the phasemask, enabling the investigation of various alignment parameters. The distance between the phasemask and the fibre, and the width of the UV beam both affect the grating transmission loss for a given exposure time. The addition of the camera for monitoring alignment dramatically increased the reproducibility of grating fabrication. The camera enabled the detection of undesirable effects such as static between the fibre and the phasemask causing the fibre to bend if the fibre is placed too close to the phasemask. Damage gratings were fabricated using the quadrupled Nd:YAG laser, and attempts were made to fabricate type IIA (negative index) gratings though with mixed success.

A new method for apodising gratings has been demonstrated, and shown to be simple yet flexible. The apodisation method was used in the fabrication of gratings for an in depth study of the apodisation of gratings restricted in exposure length to 5mm. Three families of apodisation profiles were investigated, each having a different characteristic shape. There was good agreement between the experimental and modelled grating spectra. However, the effect of stitch errors and other imperfections in the grating structure could be clearly seen in the spectra of these short gratings. The study showed that no apodisation function could be said to be best overall, but that each family of functions had different advantages depending on the priorities of the application. For any given 3dB bandwidth of the grating peak in reflection, the raised cosine function always resulted in the poorest sidelobe suppression but yet yielded the fastest roll-off of the sidelobes from the grating peak. The function yielding the best sidelobe suppression for any given grating bandwidth was the Gaussian. The peak shape was also studied, with the truncated cosine and

Gaussian profiles resulting in the squarest peak shapes. The use of apodised gratings in 2 telecommunications applications was demonstrated. Apodised gratings were used in the implementation of a novel TDM to WDM optical interface and also in a tuneable grating filter producing the widest tuning range (44.74nm) of a grating filter presented so far.

Two different methods of performing distributed measurements of strain and temperature have been presented. The first method employed grating arrays comprising very short apodised gratings (individual grating exposure length 2mm). The arrays of very short gratings have been shown to be very effective in measuring strain profiles with a spatial resolution of 2.5mm. However, the short apodised gratings had a 3dB bandwidth of 0.5nm in reflection, which will restrict the strain resolution of the sensor. In addition, chirped Moiré gratings have been demonstrated as an elegant solution to many of the problems associated with distributed sensing of arbitrary profiles using fibre Bragg gratings. Chirped Moiré gratings yield both quasi-point sensors and very narrow passbands providing the possibility of achieving high spatial and spectral resolution simultaneously. A spatial resolution of $450\mu m$ has been achieved by monitoring the grating spectrum, which is the best reported to date for distributed grating sensing performed by measuring the grating spectrum. However, results indicate that this is by no means the limit of the resolution possible using Moiré gratings.

The technique presented for apodisation of Bragg gratings enabled the fabrication of a novel fibre Bragg grating sensing element, designed to imitate the behaviour of an interferometer. The amplitude of the refractive index modulation of a chirped grating was varied along the grating length, resulting in a spectrum with a sinusoidal variation in transmission loss with wavelength. The strain resolution achieved using this sensor was $20\mu\varepsilon$.

The behaviour of fibre Bragg gratings fabricated in Boron-Germania-co-doped fibres has been studied. Gratings in these fibres have been found to behave in a different manner to those fabricated in germania-doped fibres. A positive shift of the Bragg wavelength during annealing of some gratings in B/Ge codoped fibres has been observed. Two processes must be considered when modelling the effect of annealing: the thermal decay of the UV induced refractive index change of the grating and the thermal annealing of the boron related refractive index of the fibre. Grating wavelengths can shift to higher or lower wavelengths on heating depending on the initial refractive index modulation of the grating. For weak gratings (initial Δn $<2\times10^{-4}$) positive wavelength shifts of up to 0.5nm have been observed when heated at 425°C compared with a shift of -2.83nm for a strong grating (initial $\Delta n = 2.7\times10^{-3}$) heated at 400°C for 6 hours. By combining the theory on both processes, annealing wavelength shifts and long term behaviour of gratings in B/Ge fibre can be accurately predicted (±0.3nm).

7.1 Future Work

Whilst the work in this thesis has provided the answers to many questions, it has highlighted several areas which require further investigation. There are many areas of general grating fabrication which could be improved, particularly concerning the fabrication of gratings using the Nd:YAG laser. An unusual growth of gratings using the Nd:YAG laser has been highlighted. This observed growth could be explained in terms of fringe visibility, or perhaps in terms of growth of negative index (type IIa) gratings. The exact mechanism and the effect of other parameters on this observed growth such as laser power, and strain on the fibre, need to be determined.

The apodisation chapter is a self-contained study but opens up the possibilities for similar studies to be carried out on other apodised gratings, such as sinc apodised gratings. Another interesting investigation, would be to see if type IIA apodised gratings could be fabricated using this method, as they are reputed to have a higher temperature stability than type I gratings.

The work presented in this thesis on quasi-distributed sensing using grating arrays and Moiré gratings provides many avenues for further research. Longer grating arrays could be used for quasi-distributed sensing over longer distances (a few centimetres) whilst the concept of Moiré gratings as sensors should be improved to increase the spatial resolution to the order of 100μm. A method of experimentally determining the exact position of the phase shifts in the Moiré refractive index profile would be invaluable for this application. Both these distributed sensors are suitable for trial in various applications, such as monitoring bond-lines on aircraft structures, and in the fibre packaging industry.

Finally, the long-term stability of gratings is an on-going issue. The work on the thermal decay of gratings in B/Ge fibres has highlighted several areas which require further investigation. The work in this thesis highlighted the need to study the thermal evolution of grating spectra in depressed cladding fibres, as the annealing of the borosilica cladding may cause the reappearance of the cladding mode losses. In addition, preannealing B/Ge fibres may help to minimise the wavelength drift of gratings due to annealing of the boron.

7.2 Final Thoughts

This thesis has been concerned with many of the aspects that are being considered as fibre Bragg gratings continue to make the transition from the research laboratory to the commercial world. The need for cost effective mass production facilities, capable of producing a variety of different gratings to meet customer needs is becoming increasingly evident. Fabrication techniques, such as that presented in this thesis for apodising gratings, capable of producing almost any profile in any device, are required to meet the increasing demand for tailor made gratings. The need for automated fabrication of gratings is required if they are to be able to provide a cost-effective solution.

Research in fibre Bragg gratings is increasingly moving towards their application to industrial problems. In many instances, Bragg gratings provide the ideal device solution. However, if they are to be fully exploited research into simple solutions, such as that presented here in the chirped Moiré grating sensor, is imperative. The work on the thermal decay of gratings in Boron-Germania co-doped fibres has highlighted the importance of full characterisation of fibres for grating fabrication, as gratings are now being implemented in devices designed to last 25 years or more. Gratings embedded inside composite structures are expected to last the lifetime of the structure itself. Whilst much work has been done on the spectral and material lifetime of gratings, the is undoubtedly still much research remaining.

Finally, Bragg gratings provide a simple, fibre-compatible solution to a seemingly never-ending array of applications and look to have a very bright future.

8 APPENDICES

8.1 Dispersive Fourier Transform Spectroscopy (DFTS)

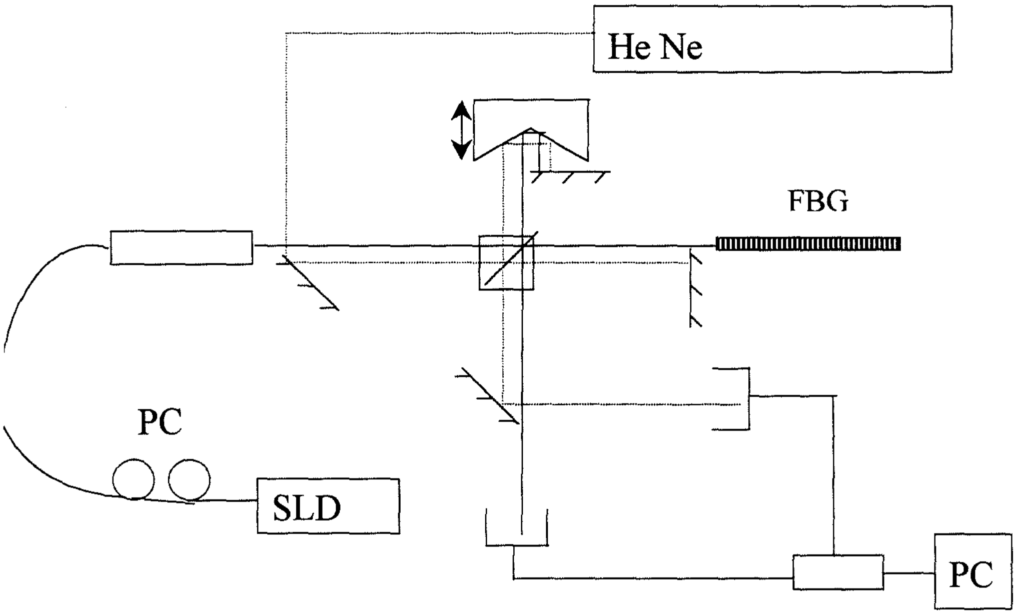

Figure 8.1: Dispersive Fourier Transform Spectroscopy (DFTS) set-up

Figure 8.1 shows the set-up used by Heriot-Watt University to interrogate fibre Bragg gratings [234,235]. DFTS allows the measurement of both amplitude and phase. The set-up is based on a scanning Michelson interferometer. The fibre Bragg grating under interrogation acts as a mirror and the He Ne laser is used to calibrate the optical path difference during the scan. Differences in path length and dispersion between the two arms of the interferometer will produce a phase difference between the two recombining beams. The interferogram received by the detector monitoring the signal from the grating is a direct representation of the refractive index modulation of the grating. The grating spectrum can be obtained by performing a Fourier transform of the interferogram [14].

8.2 Transfer Matrix Method for Modelling Gratings

The transfer matrix (T-matrix) method is widely used for modelling the spectrum of long and complex-structure Bragg gratings [236,237]. The grating structure is split into segments, and the coupled mode equations are used to calculate the response of each grating segment. The principle of the T-matrix method is illustrated in Figure 8.2.

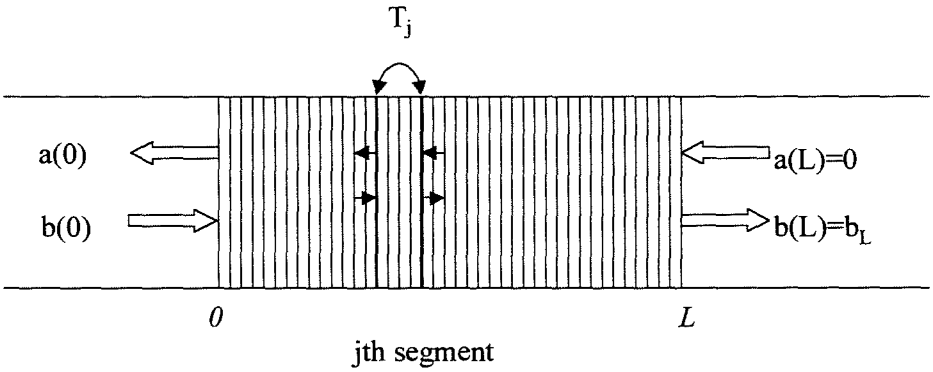

Figure 8.2: T-matrix model

The propagation of the forwards (b) and backwards (a) modes through a grating segment of length l, can be described by Equation 8-1:

$$\begin{bmatrix} a(0) \\ b(0) \end{bmatrix} = \begin{bmatrix} T_{11} & T_{12} \\ T_{21} & T_{22} \end{bmatrix} \begin{bmatrix} a(l) \\ b(l) \end{bmatrix}$$

Equation 8-1

where

$$T_{11} = T_{22}^* = \frac{\Delta\beta \sinh(Sl) + iS\cosh(Sl)}{iS} \exp(-i\beta_0 l),$$

Equation 8-2

$$T_{12} = T_{21}^* = \frac{\kappa \sinh(Sl)}{iS} \exp(i\beta_0 l),$$

Equation 8-3

and $S = \sqrt{\kappa^2 - (\Delta\beta)^2}$.

This method is ideally suited to calculating a the response of a cascade of gratings, or a non-uniform grating structure made up of lots of different segments (e.g. a chirped or apodised grating). For a non-uniform grating:

$$\begin{bmatrix} a(0) \\ b(0) \end{bmatrix} = [T_M][T_{M-1}]....[T_j]....[T_1]\begin{bmatrix} a(L) \\ b(L) \end{bmatrix}$$

Equation 8-4

This method of grating spectrum modelling is used by the commercial package *IFO_Gratings,* which is used to model some of the gratings in this thesis.

9 PUBLICATIONS

1. K E Chisholm, K Sugden and I Bennion, “Novel high spatial resolution strain and temperature sensor using chirped Moiré fibre gratings”, *OSA Topical Meeting: Bragg Gratings, Photosensitivity and Poling in Glass Waveguides* (BGPP’99), Stuart, Florida, FC3 (Sept 1999)

2. H.G.Limberger, A.Iocco, R.P.Salathe, L.A.Everall, K.E.Chisholm, and I.Bennion, “Wideband tuneable fibre Bragg grating filters”, *Proceedings of the 25th European Conference on Optical Communications (ECOC'99)*, Nice, France, TuD1 (Sept 1999)

3. A.Iocco, H.G.Limberger, R.P.Salathe, L.A.Everall, K.E.Chisholm, J.A.R.Williams, and I.Bennion, “Bragg grating fast tunable filter for wavelength division multiplexing”, *J.Lightwave.Technol.* 17 (7), pp. 1217-1221 (July 1999)

4. G M H Flockhart, R McBride, J D C Jones, K E Chisholm, L Zhang, I Bennion, and P Foote, “Reflectivity spectrum and group delay measurement on in-fibre Bragg gratings by dispersive Fourier transform spectroscopy”, *Institute of Physics Meeting on In-Fibre Bragg Gratings and Special Fibres*, London (May 1999)

5. K.Sugden, K.E.Chisholm., and L.Zhang, “fiber sensor”, Patent Application

6. A Iocco, H G Limberger, R P Salathe, L Everall, K. Chisholm, and I Bennion, "Fast and widely tunable Bragg grating reflection filter", *Conference on Optical Fibre Communications (OFC'99), Techn Digest,* San Diego, California, ThJ1 (Feb 1999)

7. K E Chisholm, L A Everall, J A R Williams, L Zhang, and I Bennion, "Apodised fibre Bragg grating arrays for quasi-distributed strain sensing", *11th IEEE Lasers and Electro-Optics Society Annual Meeting*, Orlando, Florida, WEE2 (Dec 1998)

8. K E Chisholm, L A Everall, J A R Williams, I Bennion, X Liu, R M De La Rue, and J S Aitchison, "Apodised fibre Bragg grating design subject to length

constraints", *Proceedings of the 24th European Conference on Optical Communications* (ECOC'98), Madrid, Spain, pp. 385-386 (Sep 1998)

9. K E Chisholm, L A Everall, J A R Williams, and I Bennion, "Comparison of theoretical and experimental performance of uniform period fibre grating apodisation functions", *Summer School on Photosensitivity in Optical Waveguides and Glasses, Lake Lucerne, Switzerland* (Jul 1998)

10. K E Chisholm, L A Everall, J A R Williams, and I Bennion, "Comparison of the performance of uniform period fibre Bragg gratings with different apodisation functions", *Institute of Physics Meeting on In-Fibre Bragg Gratings and Special Fibres*, London (May 1998)

11. K E Chisholm, K Sugden, and I Bennion, "Effects of thermal annealing on Bragg fibre gratings in boron/germania co-doped fibre", *J. Phys. D* 31, pp. 61-64 (1998)

12. K Sugden, L Zhang, J A R Williams, R W Fallon, L A Everall, K E Chisholm, and I Bennion, "Fabrication and characterisation of bandpass filters based on concatenated chirped fibre gratings", *J. Lightwave Technol.* 15 (8), pp. 1424-1432 (Aug 1997)

13. K E Chisholm, K Sugden, and I Bennion, "Thermal behaviour of gratings fabricated in boron/germania co-doped fibres", *Institute of Physics Meeting on In-Fibre Bragg Gratings and Special Fibres*, London (May 1997)

10 REFERENCES

1 G.Meltz, W.W.Morey, and W.H.Glenn, "Formation of Bragg gratings in optical fibers by a transverse holographic method", *Opt. Lett.*, **14**, 823-825 (1989)

2 K.C.Kao, and T.W.Davies, "Spectrophotometric studies of ultra low loss optical glasses 1: single beam method", *J.Sci.Instr.*, **2-1**, 1063-1068 (1968)

3 F.P.Kapron, D.B.Keck, and R.D.Maurer, "Radiation losses in glass optical waveguides", *Appl.Phys.Lett.*, **17**, 423-425 (1970)

4 T.Miya, Y.Terunuma, T.Hosaka, and T.Miyashita, "Ultimate low-loss single-mode fibre at 1.55μm", *Electron.Lett.*, **15**, 106-108 (1979)

5 R.J.Mears, L.Reekie, L.M.Jauncey, and D.N.Payne, "Low-noise Erbium-doped fibre amplifier operating at 1.54μm", *Electron.Lett.*, **23**, 1026-1028 (1987)

6 K.O.Hill, Y.Fujii, D.C.Johnson, and B.S.Kawasaki, "Photosensitivity in optical fiber waveguides: Application to reflection filter fabrication", *Appl. Phys. Lett.*, **32**, 647-649 (1978)

7 B.Malo, K.O.Hill, F.Bilodeau, D.C.Johnson, and J.Albert, "point-by-point fabrication of micro-Bragg gratings in photosensitive fibre using single excimer pulse refractive index modification techniques", *Electron.Lett.*, **29**, 1668-1669 (1993)

8 K.O.Hill, B.Malo, F.Bilodeau, D.C.Johnson, and J.Albert, "Bragg gratings fabricated in a monomode photosensitive optical fiber by UV exposure through a phase mask", *Appl.Phys.Lett.*, **62**, 1035-1037 (1993)

9 D.Z.Anderson, V.Mizrahi, T.Erdogan, and A.E.White, "Production of in-fibre gratings using a diffractive optical element", *Electron.Lett.*, **29**, 566-568 (1993)

10 H.Kogelnik, "Coupled wave theory for thick hologram gratings", *Bell.Syst.Techn.J.*, **48**, 2909-2947 (1969)

11 A.Yariv, "Coupled-mode theory for guided-wave optics", *IEEE J.Quantum.Electron.*, **QE-9**, 919-933 (1973)

12 T.Erdogan, "Fiber grating spectra", *J.Lightwave.Technol.*, **15**, 1277-1294 (1997)

13 H.Kogelnik, "Filter response of nonuniform almost-periodic structures", *Bell.Syst.Techn.J.*, **55**, 109-126 (1976)

14 K.O.Hill, "Aperiodic distributed-parameter waveguides for integrated optics", *Appl.Opt.*, 13, 1853-1856 (1974)

15 D.K.W.Lam, and B.K.Garside, “Characterization of single-mode optical fiber filters”, *Opt. Lett.*, **20**, 440-445 (1981)

16 E.M.Dianov, K.M.Golant, R.R.Khrapko, A.S.Kurkov, B.Leconte, M.Douay, P.Bernage and P.Niay, “Grating formation in a germanium free silicon oxynitride fibre”, *Electron. Lett.*, **33**, 236-238 (1997)

17 P. St J Russell, D.P.Hand, and Y.T.Chow, “Optically induced creation, transformation and organisation of defects and colour-centres in optical fibres” *SPIE 1516 International Workshop on Photo-induced Self-Organisation effects in Optical Fibres* 47-54 (1992)

18 T.Erdogan, V.Mizrahi, P.J.Lemaire, and D.Monroe, “Decay of ultraviolet-induced fiber Bragg gratings”, *J.Appl.Phys*, **76**, 73-80 (1994)

19 D.P.Hand, and P.St.J.Russell, “Photoinduced refractive-index changes in germanosilicate fibers”, *Opt. Lett.*, **15**, 102-104 (1990)

20 R.M.Atkins and V.Mizrahi, “Observations of changes in UV absorption bands of singlemode germanosilicate core optical fibres on writing and thermally erasing refractive index gratings”, *Electron. Lett.*, **28,** 1743-1744 (1992)

21 V.Mizrahi, S.LaRochelle, G.I.Stegeman and J.E.Sipe, “Physics of photosensitive-grating formation in optical fibres”, *Phys. Rev. A.*, **43**, 433-438 (1991)

22 K.S.Chiang, M.G.Sceats, and D.Wong, “Ultraviolet photolytic-induced changes in optical fibers: the thermal expansion coefficient”, *Opt. Lett.*, **18,** 965-967 (1993)

23 P.Y.Fonjallaz, H.G.limberger, R.P.Salathé, F.Cochet, and B.Leuenberger, “Correlation of index changes with stress changes in fibers containing UV-written Bragg gratings”, *in 20th European Conference on Optical Communications, September 25-29, Florence, Italy*, 1005-1008 (1994)

24 P.Cordier, S.Dupont, M.Douay, G.Martinelli, P.Bernage, P.Niay, J.F.Bayon, and L.Dong, “Evidence by transmission electron microscopy of densification associated to Bragg grating photoimprinting in germanosilicate optical fibers”, *Appl.Phys.Lett.*, **70**, 1204-1206 (1997)

25 B.Poumellec, P.Niay, M.Douay, and J.F.Bayon, “The UV-induced refractive index grating in Ge:SiO_2 preforms: additional CW experiments and the macroscopic origin of the change in index”, *J.Phys.D: Appl. Phys.*, **29**, 1842-1856 (1996)

26 T-E.Tsai, G.M.Williams and E.J.Friebele, “Index structure of fiber Bragg gratings in Ge-SiO_2 fibers”, *Opt. Lett.*, **22**, 224-226 (1997)

27 M.Douay, W.X.Xie, T.Taunay, P.Bernage, P.Cordier, B.Poumellec, L.Dong, J.F.Bayon, H.Poignant, and E.Develaque, “Densification involved in the UV-based

photosensitivity of silica glasses and optical fibers", *IEEE J.Lightwave.Technol.*, **LT-15**, 1329-1342 (1997)

28 W.X.Xie, P.Niay, P.Bernage, M.Douay, J.F.Bayon, T.Georges, M.Monerie and B.Poumellec, "Experimental evidence of two types of photorefractive effects occurring during photoinscriptions of Bragg gratings within germanosilicate fibres", *Optics Comm.*, **104**, 185-195 (1993)

29 L.Dong, W.F.Liu, and L.Reekie, "Negative-index gratings formed by a 193-nm excimer laser", *Opt. Lett.,* **21**, 2032-2034 (1997)

30 P.E.Dyer, R.J.Farley, R.Giedl, K.C.Byron and D.Reid, "High reflectivity fibre gratings produced by incubated damage using a 193nm laser", *Electron. Lett.*, **30**, 860-862 (1994)

31 J-L Archambault, L.Reekie, and P.St.J.Russell, "High reflectivity and narrow bandwidth fibre gratings written by single excimer pulse", *Electron.Lett.*, **29**, 1577-1578 (1993)

32 B.Malo, D.C.Johnson, F.Bilodeau, J.Albert, and K.O.Hill, "Single-excimer-pulse writing of fiber gratings by use of a zero-order nulled phase mask: grating spectral response and visualisation of index perturbations", *Opt.Lett.*, **18**, 1277-1279 (1993)

33 J-L.Archambault, L.Reekie, and P.St.J.Russell, "100% reflectivity Bragg reflectors produced in optical fibres by single excimer pulses", *Electron.Lett.*, **29**, 453-454 (1993)

34 S.J.Mihailov, and M.C.Gower, "Periodic cladding surface structures induced when recording fiber Bragg reflectors with a single pulse from a KrF excimer laser", *Appl.Phys.Lett.*, **65**, 2639-2641 (1994)

35 P.C.Hill, G.R.Atkins, J.Canning, G.C.Cox, and M.G.Sceats, "Writing and visualization of low-theshold type II Bragg gratings in stressed optical fibers", *Appl.Opt.*, **33**, 7689-7694 (1995)

36 P.E.Dyer, R.J.Farley, R.Geidl, K.C.Byron, and D.Reid, "High reflectivity fibre gratings produced by incubated damage using a 193nm ArF laser", *Electron.Lett.*, **30**, 860-862 (1994)

37 P.J.Lemaire, R.M.atkins, V.Mizrahi, and W.A.Reed, "High pressure H_2 loading as a technique for achieving ultrahigh UV photosensitivity and thermal sensitivity in GeO_2 doped optical fibres", *Electron. Lett.*, **29**,1191-1193 (1993)

38 R.M.Atkins, P.J.Lemaire, T.Erdogan, and V.Mizrahi, "Mechnaisms of enhanced UV photosensitivity via hydrogen loading in germanosilicate glasses", *Electron. Lett.*, **29**,1234-1235 (1993)

39 P.J.Lemaire, "Enhanced UV photosensitivity in fibers and waveguides by high-pressure hydrogen loading", in *Optical Fiber Communications Conference, vol.8, 1995, OSA Technical Digest Series (Optical Society of America, Washington, DC, 1995),* 162-163

40 I.Riant, S.Borne, and P.Sansonetti, "Dependence of fiber Bragg grating thermal stability on grating fabrication process", in *Optical Fiber Communications Conference, vol.9, 1996, OSA Technical Digest Series (Optical Society of America, Washington, DC, 1996).*86-87

41 C.L.Liou, L.A.Wang, M.C.Shih, and T.J.Chuang, "Characteristics of hydrogenated fiber Bragg gratings", *Appl. Phys. A*, 1 **64**, 191-197 (1997)

42 F.Bilodeau, B.Malo, J.Albert, D.C.johnson, K.O.Hill, Y.Hibino, M.Abe, and M. Kawachi, "Photosensitization of optical fibre and silica-on-silicon/silica waveguides", *Opt. Lett.*, **18**, 953-955 (1993)

43 D.L.Williams, B.J.Ainslie, J.R.Armitage, R.Kashyap, and R.Campbell, "Enhanced UV photosensitivity in boron codoped germanosilicate fibres", *Electron. Lett.*, **29**, 45-47 (1993)

44 L.Dong, J.L.Cruz, L.Reekie, M.G.Xu and D.N.Payne, "Enhanced photosensitivity in tin-codoped germanosilicate fibers", *IEEE Photon.Tech.Lett.*, 7, 1048-1050 (1995)

45 L.Dong, P.J.Wells, D.P.Hand, and D.N.Payne, "UV-induced refractive index change in Ce^{3+}-doped fibres*", in Conference on Lasers and Electro-Optics, 1991 (Optical Society of America, Washington, DC, 1991)* 68-71

46 L.Dong, J.-L.Archambault, E.Taylor, M.P.Roe, L.Reekie, and P.St.J.Russell, "Photosensitivity in tantalum doped silica optical fibres", *JOSA B*, **12**, 1747-1750 (1995)

47 E.M.Dianov, K.M.Golant, R.R.Khrapko, and A.L.Tomashuk, "Nitrogen doped silica core fibres : A new type of radiation resisitent fibre", *Electron. Lett.*, **31**, 1490-1491 (1995)

48 J.Albert, B.Malo, F.Bilodeau, D.C.Johnson, K.O.Hill, Y.Hibino, and M.Kawachi, "Photosensitivity in Ge-doped silica optical wave-guides and fibers with 193nm light from an ArF Excimer laser", *Opt.Lett.*, **19**, 387-389 (1994)

49 K.C.Byron, K.Sugden, T.Bricheno, and I.Bennion, "Fabrication of chirped Bragg gratings in photosensitive fibre", *Electron. Lett.*, **29**, 1659-1660 (1993)

50 R.M.Atkins, V.Mizrahi, and T.Erdogan, "248nm induced vacuum spectral changes in optical-fiber preform cores – support for a colour center model of photosensitivity", *Electron. Lett.*, **29**, 385-387 (1993)

51 L.Zhang, Y.Liu, I.Bennion, D.Coutts, and C.Webb, "High refelectivity single- and mulitple-grating fabrication of Bragg and long-period structures using 255nm UV light from a frequency-doubled copper vapour laser", in Bragg Gratings, Photosensitivity, and Poling in Glass Fibers and Waveguides: Applications and Fundamentals, *vol.17, 1999, OSA Technical Digest Series (Optical Society of America, Washington, DC, 1999)* 66-68

52 S.E.Kanellopoulos, V.A.Handerek, and A.J.Rogers, "Photoinduced polarization couplers in elliptic core optical fibers written using 532 and 266nm sources" *Electron. Lett.*, **28**, 1558-1560 (1992)

53 R.M.Atkins, and R.P.Espindola, "Photosensitivity and grating writing in hydrogen loaded germaosilicate core optical fibers at 325 and 351nm", *Appl.Phys.Lett.*, **9**, 1068-1069 (1997)

54 E.M.Dianov, D.S.Starodubov, S.A.Vasilev, A.A.frolov, and O.I.Medvedkov, "Refractive-index gratings written by near-ultraviolet radiation", *Opt. Lett.*, **22**, 221-223 (1997)

55 M.J.Yuen, "Ultraviolet-absorption stutdies of germanium silicate-glasses", *Appl. Opt.*, **21**, 136-140 (1982)

56 D.D.Davis, T.K.gaylord, E.N.Glytsis, S.G.Kosinski, S.C.Mettler, and A.M.Vengsarkar, "Long-period fibre grating fabrication with focused CO laser pulses", *Electron. Lett.*, **34**, 302-303 (1998)

57 K.O.Hill, B.Malo, F.Bilodeau, D.C.Johnson, and J.Albert, "Bragg gratings fabricated in monomode photosensitive optical fiber by UV exposure through a phase mask", *Appl.Phys.Lett.*, **62**, 1035-1037 (1993)

58 D.Z.Anderson, V.Mizrahi, T.Erdogan, and A.E.White, "Production of in-fibre gratings using a diffractive optical element", *Electron. Lett.*, **29**, 566-567 (1993)

59 J.D.Prohaska, E.Snitzer, S.Rishton, and V.Boegli, "Magnification of mask fabricated fibreBragg gratings", *Electron. Lett.*, **29**, 1614-1615 (1993)

60 Q. Zhang, D.A.Brown, L.Reinhart, T.F.Morse, J.Q.Wang, and G.Xiao, "Tuning Bragg wavelength by writing gratings on pre-strained fibers", *IEEE Photon.Technol.Lett.*, **6**, 839-841 (1994)

61 J.Martin, and F.Ouellette, "Novel writing technique of long and highly relfective in-fibre gratings", *Electron.Lett.*, **30**, 811-812 (1994)

62 H.N.Rourke, S.R.Baker, K.C.Byron, K.C.Byron, R.S.Baulcomb, S.M.Ojha, and S.Clements, "Fabrication and characterisation of long, narrowband fibre gratings by phase msak scanning", *Electron.Lett.*, **30**, 1341-1342 (1994)

63 R.Kashyap, H-G.Froelich, A.Swanton, and D.J.Armes, "1.3m long super-step-chirped fibre Bragg grating with a continuous delay of 13.5ns and bandwidth 10nm for broadband dispersion compensation", *Electron.Lett.*, **32**, 1807-1809 (1996)

64 A.Asseh, H.Storøy, B.E.Sahlgren, S.Sandgren, and R.A.H.Stubbe, "A writing technique for long fiber Bragg gratings with complex reflectivity profiles", *IEEE J.Lightwave Technol.*, **LT-15**, 1419-1423 (1997)

65 A.Orthonos, and X.Lee, "Novel and improved methods of writing Bragg gratings with phase masks", *IEEE Photon.Technol.Lett.*, 7, 1183-1185 (1995)

66 T.Komukai, and M.Nakzawa, "Fabrication of high-quality long-fiber Bragg grating by monitoring 3.1eV radiation (400nm) from GeO defects", *IEEE Photon.Technol.Lett.*, **8**, 1495-1497 (1996)

67 B.J.Eggleton, P.A.Krug, L.Poladian, and F.Ouellette, "Long periodic superstructure Bragg gratings in optical fibres", *Electron.Lett.*, **30**, 1620-1621 (1994)

68 J.Albert, S.Theriault, F.Bilodeau, D.C.Johnson, K.O.Hill, P.Sixt, and M.J.Rooks, "Minimization of phase errors in long fiber Bragg grating phase masks made using electron beam lithography", *IEEE Photon.Technol.Lett.*, **8**, 1334-1336 (1996)

69 J.Albert, S.Théiault, F.Bilodeau, D.C.johnson, K.O.Hill, P.Sixt, and M.J.Rooks, "Minimization of phase errors in long fiber Bragg grating phase masks made using electron beam lithography", *IEEE Photon.Technol.Lett.*, **8**, 1334-1336 (1996)

70 W.H.Loh, M.J.Cole, M.N.Zervas, an R.I.Laming, "Compensation of imperfect phase mask with moving fibre-scanning beam technique for production of fibre gratings", *Electron. Lett.*, **31**, 1483-1485 (1995)

71 J.Albert, K.O.Hill, B.Malo, S.Thèriault, F.Bilodeau, D.C.Johnson, and L.E.Erickson, "Apodisation of the spectral response of fibre Bragg gratings using aphase maskwith variable diffraction efficiency", *Electron. Lett.*, **31**, 222-223 (1995)

72 R.Kashyap, A.Swanton, and D.J.Armes, "Simple technique for apodising chirped and unchirped fibre Bragg gratings", *Electron. Lett.*, **32**, 1226-1228 (1996)

73 P-Y.Cortès, F.Ouelette, and S.LaRochelle, "Intrinsic apodisation of Bragg gratings written using UV-pulse interferometry", *Electron. Lett.*, **34**, 396-397 (1998)

74 K.Sugden, I.Bennion, A.Molony, and N.J.Copner, "Chirped gratings produced in photosensitive fibres by fibre deformation during exposure", *Electron.Lett.*, **30**, 440-442 (1994)

75 M.C.Farries, K.Sugden, D.C.J.Reid, I.Bennion, A.Molony, and M.J.Goodwin, "Very broad reflection bandwidth 44nm) chirped fibre gratings and narrow bandpass filters produced by the use of an amplitude mask", *Electron.Lett.*, **31**, 891-892 (1994)

76 M.C.Farries, K.Sugden, D.C.J.Reid, I.Bennion, A.Molony, and M.J.Goodwin, "Very broad reflection badnwidth (44nm) chirped fibre gratings and narrow bandpass filters produced by the use of an amplitude mask", *Electron.Lett.*, **31**, 891-892 (1994)

77 R.Kashyap, P.F.McKee, R.J.Campbell, and D.L.Williams, "Novel method of producingall fibre photoinduced chirped gratings", *Electron.Lett.*, **30**, 996-998 (1994)

78 K.O.Hill, F.Bilodeau, B.Malo, T.Kitagawa, S.Thériault, D.C.Johnson, J.Albert, and K.Taliguchi, "Chirped in-fiber Bragg gratings for compensation of optical-fiber dispersion" *Opt.Lett.*, **19**, 1314-1316 (1994)

79 K.C.Byron, and H.N.Rourke, "Fabrication of chirped fibre gratings by novel stretch and write technique", *Electron.Lett.*, **31**, 60-61 (1995)

80 Y.Painchaud, Achandonnet, and J.Lauzon, "Chirped fibre gratings produced by tilting the fibre", *Electron.Lett.*, **31**, 171-172 (1995)

81 R.Kashyap, H-G.Froelich, A.Swanton, and D.J.Armes, "Super-step-chirped fibre Bragg gratings", *Electron.Lett.*, **32**, 1394-1396 (1996)

82 M.J.Cole, R.I.Laming, M.N.Zervas, M.K.Durkin, and M.Ibsen, "Continuous, arbittrary profile fibre Bragg grating fabrication technique", *IEE Colloqium on Optical Fibre Gratings, London* (1997)

83 V.Mizrahi, T.Erdogan, D.J.DiGiovanni, P.J.Lemaire, W.M.MacDonald, S.G.Kosinski, S.Cabot and J.E.Sipe, "Four channel fibre grating demaultiplexer", *Electron.Lett.*, **30**, 780-781 (1994)

84 K.Sugden, L.Zhang, J.A.R.Williams, R.W.Fallon, L.A.Everall, K.E.Chisholm, and I.Bennion, "Fabriction and characterisation of bandpass filters based on concatenated chirped fiber gratings", *IEEE J.Lightwave Technol.*, **LT-15**, 1424-1432 (1997)

85 J.Canning and M.G.Sceats, "π-phase-shifted periodic distributed structures in optical fibres by UV post-processing", *Electron. Lett.*, **30**, 1344-1345 (1994)

86 L.Zhang, K.Sugden, J.A.R.Williams, I.Bennion, D.C.J.Reid, and C.M.Ragdale "In-fiber transmission filters with broad stopbands using chirped Bragg gratings", *Topical Meeting on Photosensitivity and Quadratic Nonlinearity in Glass Waveguides: Fundamentals and Applications, 1995, OSA Technical Digest Series (Optical Society of America, Washington, DC, 1995) pp. 132-135*

87 M.Janos and J.Canning, "Permanent and transient resonances thermally induced in optical fibre Bragg gratings", *Electron.Lett.*, **31**, 1007-1009 (1995)

88 R.Kashyap, P.F.McKee, and D.Armes, "UV Written reflecction grating structures in photosensitive optical fibres using phase-shifted phase masks", *Electron.Lett.*, **31**, 1977-1978 (1994)

89 F.Bakhti, and P.Sansonetti, "Wide bandwidth, low loss and highly rejective doubly phase-shifted UV-written fibre bandpass filter", *Electron.Lett.*, **32**, 581-582 (1996)

90 F.Bakhti and P.Sansonetti, "Design and realization of multiple quarter-wave phase-shifts UV written bandpass filters in optical fibers", *J.Lightwave Technol.*, **LT-15**, 1433-1437 (1997)

91 J.A.R.Williams, X.Liu, L.A.Everall, I.Bennion, J.S.Aitchison, S.Thoms, and R.M.DeLaRue, "Effects of phase steps in E-beam written phase-masks used for fibre grating fabrication by near-field holography", *in Proc. European Conference on Optical Communications 1997, (IEE Conference Publication No.488, 1997) pp 187-189*

92 D.C.J.Reid, C.M.Ragdale, I.Bennion, D.R.Robbins, J.Buus, and W.J.Stewart, "Phase-shifted Moiré grating fibre resonators", *Electron.Lett.*, **26**, 10-12 (1990)

93 S.Legoubin, E.Fertein, M.Douay, P.Bernage, P.Niay, F.Bayon, and T.Georges, "Formation of Moiré grating in core of germanosilicate fibre by transverse holographic method", *Electron.Lett.*, **27**, 1945-1947 (1991)

94 L.Zhang, K.Sugden, I.Bennion, and A.Molony, "Wide-stopband chirped fibre Moiré grating transmission filters", *Electron.Lett.*, **31**, 477-479 (1995)

95 K.Sugden, L.A.Everall, J.A.R.Williams, and I.Bennion, "Single and multi-passband broadband Moiré filters from dual exposure of uniform-period and chirped phase masks", *Proc SPIE,* **2998**, 29-34 (1997)

96 L.A.Everall, K.Sugden, J.A.R.Williams, I.Bennion, X.Liu, J.S.Aitchison, S.Thoms, and R.M.De La Rue, "Fabrication of multipassband Moiré resonators in fibers by the dual-phase-mask exposure method", *Opt.Lett.*, **22**, 1473-1475 (1997)

97 L.R.Chen, D.J.F.Cooper, and P.W.E.Smith, "Transmission filters with multiple flattened passbands based on chirped Moiré gratings", *IEEE Photon.Technol.Lett.*, **10,** 1283-1285 (1998)

98 A.Orthonos, X.Lee, and R.M.Measures, "Superimposed multiple Bragg gratings", *Electron.Lett.*, **30**, 1972-1974 (1994)

99 L.A.Everall, "Advances in UV-written fibre Bragg gratings",PhD Thesis, Aston University (1999)

100 B.J.Eggleton, P.A.Krug, L.Poladian, and F.Ouellette, "Long periodic superstructure Bragg gratings in optical fibres", *Electron.Lett.*, **31**, 1620-1621 (1994)

101 M.Ibsen, M.K.Durkin, M.J.Cole, and R.I.Laming, "Sinc-sampled fiber Bragg gratings for identical multiple wavelength operation", *IEEE Photon.Technol.Lett.*, **10**, 842-844 (1998)

102 V.Mizrahi and J.E.Sipe, "Optical properties of photosensitive fiber phase gratings", *J.Lightwave.Technol.*, **LT-11**, 1513-1517 (1993)

103 X.Clivaz, F.Marquis-Weible, and R.P.Salathé, "Optical low coherence relfectometry with 1.9μm spatial resolution", *Electron.Lett.*, **28**, 1553-1554 (1992)

104 M Volanthen, H.Geiger, M.J.Cole, R.I.Laming, and J.P.Dakin, "Low coherence technique to characterise relfectivity and time delay as a function of wavelength within a long fibre grating", *Electron. Lett.*, **32**, 757-758 (1996)

105 D.Yu. Stephanov, J.Canning, and Z.Brodzeli, "High-resolution measurements of fibre Bragg grating transmission spectra", *in 24th European Conference on Optical Communications, September 20-24, Madrid, Spain*, 407-408 (1998)

106 I.Petermann, B.Sahlgren, J.Skaar, P-Y.Fonjallaz, and R.Stubbe, "Phase distribution measurement of fibre Bragg gratings with white light interferometry", *in 24th European Conference on Optical Communications, September 20-24, Madrid, Spain*, 399-400 (1998)

107 G.M.H.Flockhart, R.McBride, J.D.C.Jones, K.E.Chisholm, L.Zhang, I.Bennion, and P.Foote, "Reflectivity spectrum and group delay measurement on in-fibre Bragg gratings by dispersive Fourier transform spectroscopy", *Institute of Physics Meeting on In-Fibre Bragg Gratings and Special Fibres*, London (May 1999)

108 T.Erdogan, "Cladding-mode resonances in short- and long- period fiber grating filters", *J.opt.Soc.Am.A,* **14**, 1760-1773 (1997)

109 L.Dong, L.Reekie, J.L.Cruz, J.E.Caplen, J.P.de Snadro, and D.N.Payne, "Optical fibers with depressed claddings for suppression of coupling into cladding modes in fibre Bragg gratings", *IEEE Photon.Technol.Lett.*, **9**, 64-66 (1997)

110 C.W.Haggans, H.Singh, W.F.Varner, and J-S Wang, "Narrow-depressed cladding fiber design for minimization of cladding mode losses in azimuthally asymmetric fiber Bragg gratings", *J.Lightwave.Technol.*, **LT-16**, 902-908 (1998)

111 W.W.Morey, G.Meltz, J.D.Love, and S.J.Hewlett, "Mode-coupling characteristics of UV-written Bragg gratings in depressed-cladding fibre", *Electron.Lett.*, **30**, 730-732 (1994)

112 S.J.Hewlett, J.D.Love, G.Meltz, T.J.Bailey, and W.W.Morey, "Cladding-mode coupling characteristics of Bragg gratings in depressed-cladding fibre", *Electron.Lett.*, **31**, 820-822 (1995)

113 P.A.Krug, R.Stolte, and R.Ulrich, "Measurement of index modulation along an optical fiber Bragg grating", *Opt.Lett.*, **20**, 1767-1769 (1995)

114 M.Schiano, and G.Zaffiro, "Polarisation mode dispersion in chirped fibre gratings", *in 24th European Conference on Optical Communications, September 20-24, Madrid, Spain*, 403-404 (1998)

115 T.Erdogan, and V.Mizrahi, "Characterization of UV-induced birefringence in photosensitive Ge-doped silica optical fibers", *J.Opt.Soc.Am.B*, **11**, 2100-2105 (1994)

116 S.R.Baker, R.E.Epworth, "Bragg reflective grating creation in optical fibres", *UK Patent No. GB2298287*

117 R.Feced, M.P.Roe-Edwards, S.E.Kanellopoulos, N.H.Taylor, and V.A.Handerek, "Mechanical strength degradation of UV exposed optical fibres", *Electron.Lett.*, **33**, 157-159 (1997)

118 D.Varelas, H.G.Limberger, and R.P.Salathé, "Enhanced mechanical performance of singlemode optical fibres irradiated by a CW UV laser", *Electron.Lett.*, **33**, 704-705 (1997)

119 "Reliability of Optical Fibres and Components", *Final Report of COST 246, Springer-Verlag, London, 1999*, Eds: T.Volotinen, W.Griffioen, M.Gadonna, and H.Limberger

120 R.P.Espindola, R.M.Atkins, N.P.Wang, D.A.Simoff, M.A.Paczkowski, R.S.Windeler, D.L.Brownlow, D.S.Shenk, P.A.Glodis, T.A.Strasser, J.J.DeMarco, and P.J.Chandonnet , "40dB fiber Bragg grating written through the fiber coating at 257nm", in *Bragg Gratings, Photosensitivity and Poling in Glass Waveguides: Applications and Fundamentals, Vol 17, OSA Technical Digest Series, (Optical Society of America, Washington, DC, 1997)* **PD2**

121 K.Imamura, T.Nakai, K.Moriura, Y.Sudo, and Y.Imada, "Mechanical strength characteristics of tin-codoped germanosilicate fibre Bragg gratings by writing through UV-transparent coating", *Electron.Lett.*, **34**, 1016-1017 (1998)

122 M.Douay, E.Fertein, W.X.Xie, P.Bernage, P.Niay, J.F.Bayon, and T.Georges, "Thermal hysteresis of Bragg wavelengths of intra-core fiber gratings", *IEEE Photon.Tech.Lett.*, **5**, 1331-1334 (1993)

123 K.E.Chisholm, K.Sugden and I.Bennion, "Effects of thermal annealing on Bragg fibre gratings in boron/germania co-doped fibre", *J.Phys.D.*, **31**, 61-64 (1998)

124 H.Patrick, S.L.Gilbert, A.Lidgard, and M.D.Gallagher, "Annealing of Bragg gratings in hydrogen-loaded optical fiber", *J.Appl.Phys.*, **78**, 2940-2945 (1995)

125 R.J.Egan, H.G.Inglis, P.Hill, P.A.Krug, and F.Ouellette, "Effects of hydrogen loading and grating strength on the thermal stability of fiber Bragg gratings", *Optical Fiber Communications Conference, vol.9, 1996, OSA Technical Digest Series (Optical Society of America, Washington, DC, 1996),* 83-84

126 D.L.Williams, and R.P.Smith, "Accelerated lifetime tests on UV written intra-core gratings in boron germania codoped silica fibre", *Electron. Lett.*, **31**, 2120-2121 (1995)

127 P.Niay, P.Bernage, S.Legoubin, M.Douay, W.X.Xie, J.F.Bayon, T.Georges, M.Monerie, and B.Poumellec, "Behaviour of spectral transmissions of Bragg gratings written in germania-doped fibres: writing and erasing experiments using pulsed or cw UV exposure", *Optics Comm.*, **113**, 176-192 (1994)

128 E.J.Friebele, C.G.Askins, M.A.Putnam, A.A.Fosha, Jr., J.Florio, Jr., R.P.Donti, and R.G.Blosser, "Distributed strain sensing with fibre Bragg grating arrays embedded in CTRM composites", *Electron.Lett.*, **30**, 1783-1785 (1994)

129 A.D.Kersey, T.A.Berkoff, and W.W.Morey, "Multiplexed fiber Bragg grating strain-sensor system with a fiber Fabry-Perot wavelength filter",*Opt.Lett.*, **18**, 1370-1372 (1993)

130 S.H.Yun, and B.Y.Kim, "Fiber grating sensor array demodulation using wavelength-swept fiber laser", *Optical Fiber Sensors Conference, vol.10, 1997, OSA Technical Digest Series (Optical Society of America, Washington, DC, 1997),* PD2

131 M.A.Davis, and A.D.Kersey, "Matched-filter interrogation technique for fibre Bragg grating arrays", *Electron.Lett.*, **31**, 822-823 (1995)

132 T.A.Berkoff, and A.D.Kersey, "Experimental demonstration of a fiber Bragg grating accelerometer", *IEEE Photon.Technol.Lett.*, **8**, 1677-1679 (1996)

133 J.D.Prohaska, and R.A.Lieberman, "A tunable matched fiber gratings filter for chemical detection", *Optical Fiber Sensors Conference, vol.10, 1997, OSA Technical Digest Series (Optical Society of America, Washington, DC, 1997),* PD1

134 Y.J.Rao, D.A.Jackson, D.J.Webb, L.Zhang, and I.Bennion, "In-fibre Bragg grating flow-directed thermodilution catheter for cardiac monitoring", *Optical Fiber Sensors Conference, vol.10, 1997, OSA Technical Digest Series (Optical Society of America, Washington, DC, 1997),* 354-357

135 P.M.Cavaleiro, F.M.Araujo, and A.B.Lobo Ribeiro, "Metal-coated fibre Bragg grating sensor for electric current metering", *Electron.Lett.*, **34**, 1133-1135 (1998)

136 M.G.Xu, L.Reekie, Y.T.Chow, and J.P.Dakin, "Optical in-fibre grating high pressure sensor", *Electron.Lett.*, **29**, 398-399 (1993)

137 W.W.Morey , G.Meltz, and W.H.Glenn, "Bragg-grating temperature and strain sensors", *Springer Proc. Phys. (Optical Fiber Sensors)*, **44**, 526-531 (1989)

138 N.E.Fisher, D.J.Webb, C.N.Pannell, D.A.Jackson, L.R.Gavrilov, J.W.Hand, L.Zhang, and I.Bennion, "Ultraonic field and temperature sensor based on short in-fibre Bragg gratings", *Electron.Lett.*, **34**, 1139-1140 (1998)

139 A.M.Vengsarkar, J.A.Greene, B.R.Fogg, and K.A.Murphy, "Spatially weighted, grating-based, two-mode, elliptical-core optical fiber vibration sensors", *Opt.Lett.*, **16**, 1707-1709 (1991)

140 F.Zhao, K.Sayano, H.E.miller, and N.Karvolac, "Subpicometer accuracy laser wavelength sensor using multiplexed Bragg gratings", *IEEE Photon.Technol.Lett.*, **9**, 1493-1495 (1997)

141 S.E.Kanellopoulos, V.A.Handerek, and A.J.Rogers, "Simultaneous strain and temperature sensing with photogenerated in-fiber gratings", *Opt.Lett.*, **20**, 333-335 (1995)

142 M.G.Xu, J-L.Archambault, L.Reekie, and J.P.Dakin, "Discrimination between strain and temperature effects using dual-wavelength fibre grating sensors", *Electron.Lett.*, **30**, 1085-1087 (1994)

143 F.M.Haran, J.K.Rew, and P.D.Foote, "A strain-isolated fibre Bragg grating sensor for temperature compensation of fibre Bragg grating strain sensors", *Meas.Sci.Technol.*, **9**, 1163-1166 (1998)

144 M.G.Xu, L.Dong, L.Reekie, J.A.Tucknott, and J.L.Cruz, "Temperature-independent strain sensor using a chirped Bragg grating in a tapered optical fibre", *Electron.Lett.*, **31**, 823-825 (1995)

145 F.Ouelette, "All-fiber filter for efficient dispersion compensation", *Opt.Lett.*, **16**, 303-305 (1991)

146 J.A.R.Williams, I.Bennion, K.Sugden, and N.J.Doran, "Fibre dispersion compensation using a chirped in-fibre Bragg grating", *Electron.Lett.*, **30**, 985-986 (1994)

147 K.O.Hill, F.Bilodeau, B.Malo, T.Kitagawa, S.Theriault, D.C.Johnson, and J.Albert, "Chirpedin-fiber Bragg gratings for compensation of optical fiber dispersion", *Opt.Lett.*, **19**, 1314-1316 (1994)

148 J.A.R.Williams, I.Bennion, and L.Zhang, "The compression of optical pulses using self-phase-modulation and linearly chirped Bragg gratings in fibers", *IEEE Photon.Technol.Lett.*, **7**, 491-493 (1995)

---

149 B.J.Eggelton, T.Stephens, P.A.Krug, G.Dhosi, Z.Brodzeli, and F.Ouelette, "Dispersion compensation using a fibre grating in transmission", *Electron.Lett.*, **32**, 1610-1611 (1996)

150 D.Pastor, J.Capmany, D.Ortega, V.Tatay, and J.Marti, "Design of apodized linearly chirped fiber gratings for disperison compensation", *J.Lightwave.Technol.*,**LT-14**, 2581-2588 (1996)

151 M.Durkin, M.Ibsen, M.J.Cole, and R.I.Laming, "1m long continuously-written fibre Bragg gratings for combined second- and third-order dispersion compensation", *Electron.Lett.*, **33**, 1891-1893 (1997)

152 J-L Archambault and S.G.Grubb, "Fiber gratings in lasers and amplifiers", *J.Lightwave.Technol.*, **LT-15**, 1378-1390 (1997)

153 R.Kashyap, I.R.Armitage, R.Wyatt, S.T.Davey, and D.L.Williams, "All-fibre narrow-bandwidth relefection gratings ar 1500nm", *Electron.Lett.*, **26**, 730-732 (1990)

154 S.V.Chernikov, R.Kashyap, P.F.McKee, and J.R.Taylor, "Dual frequency all fibre grating laser source", *Electron.Lett.*, **29**, 1089-1091 (1993)

155 H.Po, J.D.Cao, B.M.Laliberte, R.A.Minns, R.F.Robinson, B.H.Rockney, R.R.Triccca, and Y.H.Zhang, "High power neodymium-doped single transverse mode fiber laser", *Electron.Lett.*, **29**, 1500-1501 (1993)

156 D.M.Bird, J.R.Armitage, R.Kashyap, R.M.A.Fatah, and K.H.Caneron, "Narrow line semiconductor laser using fibre grating", *Electron.Lett.*, **27**, 1115-1116 (1991)

157 T.J.Cullen, H.N.Rourke, C.P.Chew, S.R.Baker, T.Bricheno, K.C.Byron, and A.Fielding, "Compact all-fibre wavelength drop and insert filter", *Electron.Lett.*, **31**, 2160-2162 (1994)

158 F.Bakhti, P.Sansonetti, C.Sinet, L.Gasca, L.Martineau, S.Lacroix, X.Daxhelet, and F.Gonthier, "Optical add/drop multiplexer based on UV-written Bragg grating in a fused 100% coupler", *Electron.Lett.*, **33**, 803-804 (1997)

159 H.Geiger, and M.Ibsen, "Complexity limitations of optical netweorks from out-of-band dispersion of grating filters", *in 24th European Conference on Optical Communications, September 20-24, Madrid, Spain*, 405-406

160 G.Nykolak, B.J.Eggleton, G.Lenz, and T.A.Strasser, "Dispersion penalty measurements of narrow fiber Bragg gratings at 10Gb/s", *IEEE Photon.Technol.Lett.*, **10**, 1319-1321 (1998)

161 K.O.Hill, B.Malo, F.Bilodeau, D.C.Johnson, and J.Albert, "Bragg gratings fabricated in monomode photosensitive optical fiber by UV exposure through a phase mask", *Appl.Phys.Lett.*, **10**, 1035-1037 (1993)

162 H.Patrick, and S.L.Gilbert, "Growth of Bragg gratings produced by continuous-wave ultraviolet light in optical fiber", *Opt. Lett.*, **18**, 1484-1486 (1993)

163 E.M.Dianov, D.S.Stardubov, S.A.Vasiliev, A.A.Frolov, and O.I.Medvedkov, "Refractive-index gratings written by near-ultraviolet radiation", *Opt.Lett.*, **22**, 221-226 (1997)

164 B.Malo, J.Albert, K.O.Hill, F.Bilodeau, D.C.Johnson, and S.Thériault, "Enhanced photosensitivity in lightly doped standard telecommunication fibre exposed to high fluence ArF excimer laser light", *Electron.Lett.*, **31**, 879-880 (1995)

165 J-L.Archambault, L.Reekie, and P.St.J.Russell, "High reflectivity and narrow bandwidth fibre gratings written by single excimer pulse", *Electron.Lett.*, **29**, 28-29 (1993)

166 R.Kashyap, J.R.Armitage, R.J.Campbell, D.L.Williams, G.D.Maxwell, B.J.Ainslie, and C.A.Millar, "Light-sensitive optical fibres and planar waveguides", *BT. Technol.J.*, **11**, 150-160 (1993)

167 H.N.Rourke, S.R.Baker, K.C.Byron, R.S.Baulcomb, S.M.Ojha, and S.Clements, "Fabrication and characterisation of long, narrowband fibre gratings by phase mask scanning", *Electron.Lett.*, **30**, 1341-1342

168 M.J.Cole, W.H.Loh, R.I.Laming, M.N.Zervas, and S.Barcelos, "Moving fibre/phase mask-scanning beam technique for enhanced flexibility in producing fibre gratings with uniform phase mask", *Electron. Lett.*, **31**, 1488-1489 (1995)

169 B.Malo, D.C.Johnson, F.Bilodeau, J.Albert, K.O.Hill, "Single-excimer pulse writing of fiber gratings by use of a zero-order nulled phase mask: grating spectral response and visualization of index perturbation", *Opt.Lett.*, **18**, 1277-1279 (1993)

170 J.Hubner, M.Svalgaard, L.Nielsen, and M.Kristensen, "Phenomenolgical model of UV-induced Bragg grating growth in Germanosilicate fibers", *SPIE*, **2998**, 11-21 (1997)

171 Y.Painchaud, A.Chandonnet, and J.Lauzon, "Chirped fibre gratings produced by tilting the fibre", *Electron.Lett.*, **31**, 171-172 (1995)

172 A.Othonos and X.Lee, "Novel and Improved Methods of Writing Bragg Gratings with phase masks", *IEEE Photon.Technol.Lett.*, 7, 1183-1185 (1995)

173 M.Matsuhara, and K.O.Hill, "Optical-waveguide band-rejection filters: design", *Appl. Opt.*, **13**, 2886-2888 (1974)

174 B.E.Little, C.Wu, and W-P. Huang, "Synthesis of ideal window filter response in grating-assisted couplers", *Opt. Lett.*, **21**, 725-727 (1996)

175 B.E.Little, and C.Wu, "Window functions for ideal response in distributed feedback reflection filters", *IEEE Photon. Technol. Lett.*, **9**, 76-78 (1997)

176 D.Pastor, J.Capmany, D.Ortega, V.Tatay, and J. Marti, "Design of apodized linearly chirped fiber gratings for dispersion compensation", *J. Lightwave. Technol.*, **LT-14**, 2581-2588 (1996)

177 H.Storoy, H.E.Engan, B.Shlgren, and R.Stubbe, "Position weighting of fiber Bragg gratings for bandpass filtering", *Opt. Lett.*, **22**, 784-786 (1997)

178 M.Ibsen, M.K.Durkin, M.J.Cole, and R.I.Laming, "Optimised square passband fibre Bragg grating filter with in-band flat group delay response", *Electron. Lett.*, **34**, 800-802 (1998)

179 G.Meltz, W.Morey, and W.H.Glenn, "Formation of Bragg gratings in optical fibres by a transverse holographic method", *Opt. Lett.*, **14**, 823-825 (1989)

180 K.O.Hill, S.Theirault, B.Malo, F.Bilodeau, T.Kitagawa, D.C.Johnson, J.Albert, K.Takiguchi, T.Kataoka, and K. Hagimoto., "Chirped in-fibre Bragg grating dispersion compensators: Linearisation of dispersion characteristic and demonstration of dispersion compensation in 100km, 10Gbit/s optical fibre link", *Electron. Lett.*, **30**, 1755-1756 (1994)

181 M.J.Cole, W.H.Loh, R.I.Laming, M.N.Zervas, and S.Barcelos, "Moving fibre/phase mask-scanning beam technique for enhanced flexibility in producing fibre gratings with uniform phase mask", *Electron. Lett.*, **31**, 1488-1489 (1995)

182 J.Albert, K.O.Hill, B.Malo, S.Thierault, F.Bilodeau, D.C.Johnson, and L.E.Erickson, "Apodisation of the spectral response of fibre Bragg gratings using a phase mask with variable diffraction efficiency", *Electron. Lett.*, **31**, 222-223 (1995)

183 B.Malo, S.Theirault, D.C.Johnson, F.Bilodeau, J.Albert, and K.O.Hill, "Apodised in-fibre Bragg grating reflectors photoimprinted using a phase mask", *Electron. Lett.*, **31**, 223-225 (1995)

184 J.Albert, K.O.Hill, D.C.Johnson, F.Bilodeau and M.J.Rooks, "Moire phase masks for automatic pure apodisation of fibre Bragg gratings", *Electron. Lett.*, **32**, 2260-2261 (1996)

185 R.Kashyap, A.Swanton, and D.J.Armes, "Simple technique for apodising chirped and unchirped fibre Bragg gratings", *Electron. Lett.*, **32**, 1226-1228 (1996)

186 K E Chisholm, L A Everall, J A R Williams, I Bennion, X Liu, R M De La Rue, and J S Aitchison, "Apodised fibre Bragg grating design subject to length constraints", *in 24th European Conference on Optical Communications, September 20-24, Madrid, Spain*, 403-404 (1998). 385-386

187 P-Y. Cortes, F.Ouellette, and S.LaRochelle, "Intrinsic apodisation of Bragg gratings written using UV-pulse interferometry", *Electron. Lett.*, **34**, 396-397 (1998)

188 H-G.Frölich, and R.Kashyap, "Two methods of apodisation of fibre-Bragg gratings", *Optics Comm.*, **157**, 273-281 (1998)

189 K.C.Byron, "Forming Bragg gratings in photosensitive optical waveguides", *UK Patent Application* GB 2302599 A

190 F.Ouellette, "The effect of Profile noise on the spectral response of fiber gratings", *in Bragg Gratings, Photosensitivity and Poling in Glass Waveguides: Applications and Fundamentals, Vol 17, OSA Technical Digest Series, (Optical Society of America, Washington, DC, 1997)* 222-224

191 D.M.Ryan, S.B.Alleston, and N.J.Doran, "10 Gbit/s OTDM to 4x2.5 Gbit/s WDM conversion using an SOA-NOLM*", Nonlinear Guided Waves, Vol 19, OSA Technical Digest Series, (Optical Society of America, Washington, DC, 1999)*

192 G.A.Ball and W.W.Morey, "Compression-tuned single frequency Bragg grating fibre laser", *Opt.Lett.*, **19**, 1979-1981 (1994)

193 A.Iocco, H.G.Limberger, and R.P.Salathe, "Bragg grating fast tuneable filter", *Electron. Lett.*, **32**, 2000-2001 (1996)

194 S.M.Melle, K.Liu, and R.M.Measures, "Practical fiber-optic Bragg grating strain gauge system", *Appl.Opt*, **32**, 3601-3609 (1993)

195 P.Lambelet, P.Y.Fonjallaz, H.G.Limberger, R.P.Salathe, Ch.Zimmer, and H.H.Gilgen, "Bragg grating characterisation by optical low-coherence reflectometry", *IEEE Photon.Technol.Lett.*, **5**, 511-567 (1993)

196 Y-J.Rao, "In-fibre Bragg grating sensors", *Meas.Sci.Technol.*, **8**, 355-375 (1997)

197 M.Volanthen, H.Geiger, and J.P.Dakin, "Distributed Grating Sensors Using Low-coherence Reflectometry", *J.Lightwave Technol.*, **LT-15**, 2076-2082 (1997)

198 M.M.Ohn, S.Y.Huang, R.M.Measures, and J.Chwang, "Arbitrary strain profile measurement within fibre gratings using interferometric Fourier transform technique", *Electron.Lett.*, **33**, 1242-1243 (1997)

199 S,Huang, M.LeBlanc, M.M.Ohn, and R.M.Measures, "Bragg intragrating structural sensing", *Appl.Opt.*, **34**, 5003-5009 (1995)

200 M.Volanthen, H.Geiger, M.J.Cole, and J.P.Dakin, "Measurement of arbirary strain profiles within fibre gratings", *Electron.Lett.*, **32**, 1028-1029 (1996)

201 R.T.Jones, D.G.Bellemore, T.A.Berkoff, J.S.Sirkis, M.A.Davis, M.A.Putnam, E.J.Friebele, and A.D.Kersey, "Determination of cantilever plate shapes using

wavelength division multiplexed fiber Bragg grating sensors and a least-squares strain-fitting algorithm", *Smart Mater. Struct.* 7, 178-188 (1998)

202 M.Froggatt and J.Moore, "Distributed measurement of static strain in an optical fiber with multiple Bragg gratings at nominally equal wavelengths", *Appl.Opt.*, **37**, 1741-1746 (1998)

203 S.M. Melle, A.T. Alavie, S. Karr, T. Coroy, K. Liu and R.M. Measures, "Strain sensing using a fibre optic Bragg grating", *SPIE Fiber Optic SMART Structures and Skins IV*, 1588, 1991, pp 255-263.

204 Q.Zhang, D.A.Brown, L.Rienhart, T.F.Morse, J.Q.Wang, and G.Xiao, "Tuning Bragg wavelength by writing gratings on prestrained fibers", *IEEE Photon.Technol.Lett*, **6**, 839-841 (1994)

205 J.M.Gere, and S.P.Timoshenko, "Mechanics of Materials", 4th Edition, 1984, International Thomson Publishing, Boston, MA.

206 C-C.Chang, and S.T.Vohra, "Spectral broadening due to non-uniform strain fields in fibre Bragg grating based transducers", *Electron.Lett.*, **34**, 1778-1779 (1998)

207 M.LeBlanc, S.Y.Huang, M.Ohn, R.M.Measures, A.Guemes, and A.Orthonos, "Distributed strain measurement based on a fiber Bragg grating and its reflection spectrum analysis", *Opt.Lett.*, **21**, 1405-1407 (1996)

208 S.Legoubin, E.Fertein, M.Douay, P.Bernage, P.Niay, F.Bayon, and T.Georges, "Formation of Moiré grating in core of germanosilicate fibre by transverse holographic double exposure method", *Electron.Lett.*, **27**, 1945-1947 (1991)

209 L.Zhang, K.Sugden, I.Bennion, and A.Molony, "Wide-stopband chirped fibre Moiré grating transmission filters", *Electron.Lett.*, **31**, 477-479 (1995)

210 L.A.Everall, K.Sugden, J.A.R.Williams, I.Bennion, X.Liu, J.S.Aitchison, S.Thoms, and R.M.De La Rue, "Fabrication of multipassband Moiré resonators in fibres by the dual-phase-mask exposure method", *Opt. Lett.*, **22**, 1473-1475 (1997)

211 B.Culshaw and J.Dakin (Eds), "Optical Fiber Sensors: Systems and Applications", Artech House Inc., Norwood, MA, 348-349 (1989)

212 S.Kannan, J.Z.Y.Guo, and P.J.Lemaire,"Thermal stability analysis of UV-induced fiber Bragg gratings", *J.Lightwave.Technol.*, **LT-15**,1478-1483 (1997)

213 T.Erdogan, V.Mizrahi, P.J.Lemaire, and D.Monroe, "Decay of ultraviolet-induced fiber Bragg gratings" *J.Appl. Phys.*, **76**, pp.73-80 (1994)

214 L.Dong, J.L.Cruz, L.Reekie, M.G.Xu, and D.N.Payne, "Enhanced photosensitivity in tin-codoped germanosilicate optical fibers", *IEEE Photon. Tech. Lett.*, **7**, 1048-1050 (1995)

---

215 E.M.Dianov, K.M.Golant, R.R.Khrapko, A.S.Kurkov, B.Leconte, M.Douay, P.Bernage and P.Niay, "Grating formation in a germanium free silicaon oxynitride fibre", *Electron. Lett.*, **33**, 236-238 (1997)

216 P.Niay, P.Bernage, S.Legoubin, M.Douay, W.X.Xie, J.F.Bayon, T.Georges, M.Monerie, and B.Poumellec, "Behaviour of spectraal transmissions of Bragg gratings written in germania-doped fibres: writing and erasing experiments using pulsed or cw uv exposure" *Optics Comm.*, **113**, 176-192 (1994)

217 D.L.Williams, and R.P.Smith, "Accelerated lifetime tests on UV written intra-core gratings in boron germania codoped silica fiber" *Electron. Lett.*, **31**, 2120-2121 (1995)

218 H.Patrick, S.L.Gilbert, A.Lidgard, and M.D.Gallagher, "Annealing of Bragg gratings in hydrogen-loaded optical fiber", *J. Appl. Phys.*, **78**, 2940-2945 (1995)

219 P.J.Lemaire and T.Erdogan, "Hydrogen-enhanced UV photosensitivity of optical fibers: Mechanism and reliability", *in Tech.Dig.Conf.Photosensitivity and Quadratic Nonlinearity in Glass Waveguides*, Portland, OR, **22**, 78-81 (Sept. 1995)

220 R.J.Egan, H.G.Inglis, P.Hill, P.A.Krug, and F.Ouelette, "Effects of hydrogen loading and grating strength on the thermal stability of fiber Bragg gratings", *Optical Fiber Communications Conference, vol.9, 1996, OSA Technical Digest Series (Optical Society of America, Washington, DC, 1996),* 83-84

221 S.Kannan, and P.J.Lemaire, "Thermal reliability of strong Bragg gratings written in hydrogen sensitized fibers" *Optical Fiber Communications Conference, vol.9, 1996, OSA Technical Digest Series (Optical Society of America, Washington, DC, 1996),* 84-85

222 C.L.Liou, L.A.Wang, M.C.Shih, and T.J.Chuang, "Characteristics of hydrogenated fiber Bragg gratings", *Appl, Phys, A.*, **64**, 191-197 (1997)

223 I.Riant, and B.Poumellec, "Thermal decay of gratings written in hydrogen-loaded germanosilicate fibers", *Electron. Lett.*, **34**, 1603-1604 (1998)

224 M.Douay, E.Fertein, W.X.Xie, P.Bernage, P.Niay, J.F.Bayon, and T.Georges, "Thermal hysteresis of Bragg wavelengths of intra-core fiber gratings", *IEEE Photon.Technol.Lett.*, **5**, 1331-1334 (1993)

225 K.E.Chisholm, K.Sugden, and I.Bennion, "Effects of thermal annealing on Bragg fibre gratings in boron/germania co-doped fibre", *J.Phys. D*, **31**, 61-64 (1998)

226 R.M.Atkins, and V.Mizrahi, "Observations of changes in UV absorption bands of singlemode germanosilicate core optical fibres on writing and thermally erasing refractive index gratings" *Electron.Lett.*, **28**, 1743-1744 (1992)

227 H.Kogelnik, "Filter response of nonuniform almost-periodic structures" *Bell Syst. Tech. J.*, **55**, 109-126 (1976)

228 D.L.Williams, B.J.Ainslie, J.R.Armitage, R.Kashyap, and R.Campbell, "Enhanced UV photosensitivity of boron codoped germanosilicate fibers" *Electron. Lett.*, **29**, 45-47 (1993)

229 G.Meltz, W.W.Morey, and W.H.Glenn, "Formation of Bragg gratings in optical fibers by a transverse holographic method", *Opt.Lett.*, **14**, 823-825 (1989)

230 B.Malo, J.Albert, K.O.Hill, F.Bilodeau, and D.C.Johnson, "Effective index drift from molecular hydrogen diffusion in hydrogen-loaded optical fiber and its effect on Bragg grating fabrication", *Electron. Lett.*, **30**, 442-444 (1994)

231 I.Camlibel, D.A.Pinnow, and F.W.Dabby, "Optical aging characteristics of borosilicate clad fused silica core fiber optical waveguides" *Appl. Phys. Lett.*, **26**, 185-187 (1975)

232 D.Z.Anderson, V.Mizrahi, T.Erdogan, and A.E.White, "Production of in-fibre gratings using a diffractive optical element" *Electron. Lett.*, **29**, 566-568 (1993)

233 L.Dong, L.Reekie, J.L.Cruz, J.E.Caplen, J.P.de Sandro, and D.N.Payne, "Optical fibers with depressed claddings for suppression of coupling into cladding modes in fiber Bragg gratings" *IEEE Photon. Tech. Lett.*, **9**, 64-66 (1997)

234 D.A.Flavin, R.McBride, and J.D.C.Jones, "Short optical path scan interferometric interrogation of a fibre Bragg grating embedded in a composite", *Electron.Lett.*, **33**, 319-321 (1997)

235 D.A.Flavin, R.McBride, J.D.C.Jones, J.G.Burnett, and A.H.Greenaway, "Combined temperature and strain measurement with a dispersive optical fiber Fourier-transform spectrometer", *Opt.Lett.*, **19**, 2167-2169 (1994)

236 M.Yamada, and K.Sakuda, "Analysis of almost-periodic distributed feedback slab waveguides via a fundamental approach", *Appl.Opt.*, **26**, 3474-3478 (1987)

237 S.Huang, M.LeBlanc, M.M.Ohn, and R.M.Measures, "Bragg intragrating sensing", *Appl.Opt.*, **34**, 5003-5009 (1995)